Fibrous biomimetic and biohybrid carbon scaffolds for 3D cell growth

A Dissertation by

Mohammadreza Taale

Submitted in Fulfillment of
the Requirements for the Degree of
Doctor of Engineering Science

Faculty of Engineering
Christian-Albrechts-Universität zu Kiel

2019

Declaration

I hereby declare that I wrote this dissertation by myself without improper external assistance and to the best of my knowledge and belief and that I have identified all quotations of other authors and used none but the indicated sources.

I declare that this dissertation has not been submitted either partially or wholly as part of a doctoral degree to another examining body and whether it has not been published or submitted for publications.

I declare that this dissertation has been prepared subject to the Rules of Good Scientific Practice of the German Research Foundation.

Mohammadreza Taale
Christian-Albrechts-Universität zu Kiel

Date: Signature:

Supervisor:

Prof. Dr. Christine Selhuber-Unkel

Reviewers:

Prof. Dr. Christine Selhuber-Unkel
Prof. Dr. Regine Willumeit-Römer

Date for the oral exam: 27.05.2019

Declaration of Authorship / Co-authorship

I, Mohammadreza Taale, state here the nature of my involvement to the work in the following publications which form this dissertation.

Publication 1

"A tunable scaffold of microtubular graphite for 3D cell growth", C. Lamprecht, **M. Taale**, I. Paulowicz, H. Westerhaus, C. Grabosch, A. Schuchardt, M. Mecklenburg, M. Böttner, R. Lucius, K. Schulte, R. Adelung, C. Selhuber-Unkel. *ACS Appl. Mater. Interfaces*, 8:24, 14980-14985, 2016.

I prepared the samples for cytotoxicity and cell adhesion assays, performed the cell adhesion and cytotoxicity investigations using fluorescence microscope, and prepared the related figures and graphs.

Publication 2

"Biomimetic carbon-fiber systems engineering : A modular design strategy to generate biofunctional composites from graphene and carbon nanofibers", **M. Taale**, F. Schütt, T. Carey, J. Marx, Y. K. Mishra, N. Stock, B. Fiedler, F. Torrisi, R. Adelung, C. Selhuber-Unkel. *ACS Appl. Mater. Interfaces*, 11:5, 5325-5335, 2019.

I prepared some of the samples for cytotoxicity and cell adhesion assays, and characterized the samples using SEM, and investigated cytotoxicity, cell adhesion, cell proliferation, protein adsorption capacity, and prepared the figures and graphs, and wrote the text.

Publication 3

"Bioactive carbon based hybrid 3D scaffolds for osteoblast growth", **M. Taale**, F. Schütt, K. Zheng, Y. K. Mishra, A. R. Boccaccini, R. Adelung, C. Selhuber-Unkel. *ACS Appl. Mater. Interfaces*, 10:50, 43874-43886, 2018.

I prepared some of the samples and synthesized hydroxyapatite nanoparticles. In addition, I characterized the samples using SEM, TEM, ICP-mass spectrometry, XRD, and investigated cytotoxicity, cell adhesion, protein adsorption capacity, and prepared the figures and graphs, and wrote the text.

Publication 4

"Systematically designed periodic electrophoretic deposition for decorating 3D carbon-based scaffolds with bioactive nanoparticles", **M. Taale**, D. Krüger, E. Ossei-Wusu, F. Schütt, M. A. U. Rehman, Y. K. Mishra, J. Marx, N. Stock, B. Fiedler, A. R. Boccaccini, R. Willumeit-Römer, R. Adelung, C. Selhuber-Unkel. *ACS Biomater. Sci. Eng.*, 5:9, 4393-4404, 2019.

I prepared all the samples and characterized using SEM, fluorescence microscope, and investigated cytotoxicity, cell proliferation, cell adhesion, protein adsorption capacity, and prepared the figures and graphs, and wrote the text.

To My Lovely Family

Abbreviations

μCT X-ray microcomputed tomography

2D two-dimensional

3D three-dimensional

AG aerographite

AG-CNTT aerographite-carbon nanotube tube

AG-G aerographite-graphene

ALP alkaline phosphatase

BCA bicinchoninic acid

BG bioactive glass

BGN bioactive glass nanoparticle

BSA bovine serum albumin

CaO calcium oxide

CBN carbon based nanomaterial

CNT carbon nanotube

CNTT carbon nanotube tubes

CNTT-BGN CNT-based tubes containing bioactive glass nanoparticles

CNTT-BGN/HA CNT-based tubes containing both bioactive glass and hydroxyapatite nanoparticles

CNTT-g carbon nanotube tubeglucose

CNTT-HA CNT-based tubes containing hydroxyapatite nanoparticles

CPD critical point drying

cRGD cyclic RGD

CVD chemical vapor deposition

D aspartic acid

DSPE-PEG2000-NH_2 Amine terminated PEG conjugated phospholipid

ECM extracellular matrix

EPD electrophoretic deposition

G graphene

GelMA gelatin methacrylate

GO graphene oxide

HA hydroxyapatite

HAn hydroxyapatite nanoparticles

HAn-AG hydroxyapatite nanoparticles decorated aerographite

ICP-MS inductively coupled plasma mass spectrometry

MTT methylthiazolyldiphenyl-

tetrazolium
bromide

MWCNT multiwalled carbon nanotube

PBS phosphate buffered saline

PEG poly(ethylene glycol)

PEG-lipid lipid poly(ethylene glycol) (PEG-lipid)

PEPD periodic electrophoretic deposition

*p***NPP** para-Nitrophenylphosphate

R L-amino acids arginin

REF YFP-Pax rat embryo fibroblast transfected with YFP-paxillin

REF52 rat embryonic fibroblast

REF52wt rat embryonic fibroblast wild type

ROI region of interest

SBF simulated body fluid

SEM scanning electron microscopy

TEM transmission electron microscopy

t-ZnO tetrapodal zinc oxide

WST-1 *((4-[3-(4-iodophenyl)-2-(4-nitrophenyl)-2H-5-tetrazolio]-1,3-benzene disulfonate)*

XRD X-ray diffraction

YFP yellow fluorescent protein

Zn Zinc

ZnO zinc oxide

TE tissue engineering

Abstract

The formation of three dimensional tissue (3D) in the laboratory highly depends on the biomimetic environment, the engineered extracellular matrix (scaffold), the cell type as well as the biologically active components. The scaffolds should resemble the structural and biochemical features of the natural extracellular environment in order to support and control the cell migration and growth. In particular, the microstructure and pore architecture significantly affect cell growth as they determine nutrient and oxygen diffusion, waste removal as well as spatially organized cell orientation. Open and interconnected pore architectures are strongly necessary to optimize these parameters for 3D cell growth. Zinc oxide (ZnO) networks, which consists of interconnected tetrapod-shaped ZnO micro particles, provide a highly porous (porosity $\geq$ 93%) framework with spaces of approximately 10 μm to 100 μm between filaments that is comparable to the fibrous microarchitecture of extracellular matrix (ECM). ZnO networks can serve as a sacrificial template for the fabrication of carbon-based scaffolds. After a desirable functionalization, such a highly porous carbon-based scaffold with its specific micro-structure can have a revolutionary impact on biomimetic scaffolds for 3D cell growth.

The primary focus of this study is to fabricate and functionalize these highly porous carbon-based scaffolds and to understand biological and cellular responses toward them. Therefore, ultra-light carbon-based scaffolds (aerographite), which consist of a self-supporting highly porous ($\geq$ 99.9% free volume) network of seamlessly interconnected hollow graphite tubes with micrometer-scale diameters and certain mechanical flexibilities, were functionalized with cyclic RGD (cRGD) peptides coupled to poly(ethylene glycol) (PEG) conjugated phospholipids. The PEG lipids render the hydrophobic aerographite (AG) hydrophilic and the cRGD enables fibroblast adhesion to the AG. However, stiffness and electrical conductivity of AG only can be tailored within small ranges (up to $\sim$ 100 kPa and between 0.2 and 0.5 S/m, respectively), limiting its applicability for cell culturing. Hence, a novel modular design strategy to generate biofunctional composite scaffolds based on ZnO templates infiltrated by graphene and carbon nanotubes (CNT) is presented. The resulting micro-fibrous scaffolds have high porosities (up to 93%), and can be produced with a wide range of Youngs moduli (from $\sim$ 0.027 to $\sim$ 22 MPa) as well as electrical conductivity (from $\sim$ 0.1 to $\sim$ 330 S/m) and different surface compositions. Furthermore, the micro-fibrous

scaffolds have a high protein adsorption capacity (up to 77.32±6.95 mg/cm^3), which enables them to resemble the ECM not only structurally, but also biochemically. In addition, the fibroblasts have been found to have the typical polygonal cell shape with elongated cytoplasm projections in-between the microtubes, revealing that the scaffolds support successful growth and adhesion of fibroblast cells.

To exploit the unique spatial features of the highly porous network for bone tissue engineering, bioactive ceramic nanoparticles (hydroxyapatite (HA), bioactive glass (BG)) are successfully incorporated into CNT-based scaffolds. The resulting 3D hybrid structures possess a hierarchical architecture, consisting of microfiber composites of self-entangled CNTs and bioactive nanoparticles. The incorporation of HA and BG nanoparticles into the porous network promotes the biomineralization ability and the protein adsorption capacity of the scaffolds significantly, as well as fibroblast and osteoblast adhesion. This strategy is a new approach for implementing low-dimensional bioactive materials into 3D carbon-based microfibrous networks. However, the incorporation of low-dimensional materials into AG structure depends on the immobilization of nanoparticles on the AG filaments. Therefore, the decoration of the AG scaffold with HA nanoparticles was done by a novel periodic electrophoretic deposition technique. The micro-filaments of the resulting network are homogeneously coated by HA nanoparticles on both internal and external areas of the network. Osteoblast proliferation and protein adsorption assays have revealed that the hydroxyapatite decorated AG scaffolds are biocompatible. A drastic increase in alkaline phosphatase (ALP) activity of osteoblasts up to about 300% was detected, showing that the scaffolds are able to promote osteoblastic activity as a result of HA nanoparticle decoration.

The methods presented in this thesis provide a novel concept to generate biocompatible and bioactive fibrous carbon scaffolds that mimic the ECM with the additional feature of conductivity. The generated scaffolds can serve as groundbreaking fiber systems for 3D cell growth, which pave the way toward further investigations of diverse tissue engineering and bioapplications.

Zusammenfassung

Die Entstehung eines dreidimensionalen (3D) Gewebes im Labor hängt stark von der biomimetischen Umgebung, der geformten extrazellulären Matrix (Gerüst), dem Zelltyp sowie von den biologisch aktiven Komponenten ab. Das Gerüst soll in Struktur und biochemischen Eigenschaften der extrazellulären Umgebung ähneln, da dies Zellmigration und -wachstum einerseits fördert und andererseits kontrollierbar macht. Insbesondere die Mikrostruktur und die Architektur der Hohlräume haben einen erheblichen Einfluss auf das Zellwachstum, da sie die Nährstoff- und Sauerstoffdiffusion, die Abfallentsorgung und die räumlich organisierte Zellorientierung beeinflussen. Um diese Prozesse sicher zu stellen, müssen die Poren offen und vernetzt sein. Zinkoxid(ZnO)-Netzwerke bestehen aus tetrapodförmigen, miteinander verbundenen ZnO-Mikropartikeln. Ihre hochporöse Struktur (Porosität $\geq 93\%$) mit Abständen von 10 μm bis 100 μm zwischen den Filamenten ist mit der faserförmigen Mikrostruktur der extrazellulären Matrix (ECM) vergleichbar. ZnO-Netzwerke können als Vorlagen zur Herstellung von kohlenstoffbasierten Gerüsten dienen und richtig funktionalisiert, kann solch ein hochporöses Kohlenstoffgerüst mit seiner spezifischen Mikrostruktur biomimetische Gerüste für 3D Zellwachstum revolutionieren.

Der Hauptschwerpunkt dieser Studie ist es, sowohl solche hochporösen kohlenstoffbasierten Gerüste herzustellen und zu funktionalisieren, als auch die biologischen und zellulären Reaktionen auf diese Gerüste verstehen zu lernen. Dazu wurden ultraleichte kohlenstoffbasierte Gerüste (Aerographite) mit zyklischen RGD (cRGD) Peptiden an poly(ethylene glycol) (PEG) konjugierten Phospholipiden funktionalisiert. Aerographite (AG) sind selbsttragende und hochporöse ($\geq$ 99.9% freies Volumen) Netzwerke aus nahtlos verbundenen, hohlen Graphitröhren, welche Durchmesser im Mikrometerbereich und eine bestimmte mechanische Stabilität aufweisen. Durch eine Funktionalisierung mit PEG Lipiden wird das hydrophobe AG hydrophil und cRGD ermöglicht die spezifische Adhäsion von Fibroblasten. Allerdings kann die Festigkeit von AG nur um wenige kPa (bis zu $\sim$ 100 kPa), und die elektrische Leitfähigkeit nur um wenige S/m ($\sim$ 0.2 bis 0.5 S/m) angepasst werden, was die Anwendbarkeit von AG als Substrat für Zellkultur mindert. Daher wird eine neue, bausteinartig konstruierte Strategie zur Herstellung biofunktionaler Verbundgerüste vorgestellt, die mit Graphen und Kohlenstoffnanoröhrchen infiltrierte ZnO Vorlagen nutzt. Die resultierenden mikrofaserförmigen Gerüste verfügen über hohe Porositäten (bis zu 93%) und

können mit einem breiten Spektrum an Elastizitätsmodulen (~ 0.027 bis 22MPa) und elektrischen Leitfähigkeiten (~ 0.1 bis 330 S/m), sowie mit verschiedenen Oberflächenkompositionen hergestellt werden. Außerdem haben diese neuen Verbundsgerüste ein hohe Proteinadsorptionskapazität (bis zu 77.32 ± 6.95 mg/cm^3), wodurch sie extrazellulären Matrixen nicht nur strukturell, sondern auch biochemisch ähneln. Zusätzlich weisen Fibroblasten in diesen Gerüsten eine typisch polygonale Zellform mit verlängerten Zytoplasmaprojektionen zwischen den Mikroröhrchen auf, was auf das erfolgreiche Wachstum und die Adhäsion der Fibroblasten hinweist.

Um die einzigartigen Eigenschaften dieser hochporösen Netzwerke für die Knochengewebezüchtung zu nutzen, wurden bioaktive, keramische Nanopartikel (Hydroxyapetite (HA), bioaktives Glass (BG)) erfolgreich in die CNT-basierten Gerüste eingebaut. Die resultierenden 3D Hybridstrukturen besitzen eine hierarchische Architektur aus Mikrofaserverbunden von verwobenen CNTs und bioaktiven Nanopartikeln. Die Einbettung von HA- und BG-Nanopartikeln in einem porösen Netzwerk begünstigt neben der Biomineralisierungsfähigkeit und der Proteinadsorptionskapazität der Gerüste auch die Fibroblast- und Osteoblast-Adhäsion erheblich. Diese Strategie bietet eine neue Möglichkeit, niederdimensionale, bioaktive Materialien in 3D kohlenstoffbasierte Mikrofasernetzwerke zu implementieren. Jedoch, hängt die Angliederung von niederdimensionalen Materialien in AG Strukturen von der Fixierung der Nanopartikeln auf den AG Filamenten ab. Deswegen wurde das Versetzen von AG Gerüsten mit HA Nanopartikeln mit einer neuen, periodisch elektrophoretischen Beschichtungstechnik durchgeführt. Die Mikrofilamente des resultierenden Netzwerks sind sowohl auf der Innen- als auch auf der Außenseite des Netzwerks homogen mit HA Nanopartikeln beschichtet. Das Proliferationsverhalten der Osteoblasten und die Proteinadsorption zeigen, dass die HA beschichten AG Gerüste biokompatibel sind. Es wurde ein drastischer Anstieg in der ALP Aktivität der Osteoblasten von bis zu etwa 300% festgestellt. Dies zeigt, dass das Beschichten der AG Gerüste mit HA Nanopartikeln osteoblastische Aktivitäten fördert.

Die hier präsentierten Methoden zeigen neue Konzepte der Herstellung von biokompatiblen und -aktiven Kohlenstoff Matrixen mit dem Vorteil der elektrischen Leitfähigkeit. Diese imitieren mit ihrer fibrösen Struktur die Extrazelluläre Matrix im Gewebe und generieren ein bahnbrechendes 3D Sytem für die Zellkultivierung. Im Bereich des Tissue Engineering und der biologischen Anwendungen können diese Strukturen somit als Grundlage zukünftiger Forschung dienen.

Contents

Chapter 1

Introduction

Artificial scaffolds that mimic the cell extracellular matrix (ECM) have evolved through demands in the field of tissue engineering, where they replicate the topographical environment of natural tissues[1]. Research on various synthetic materials that can resemble artificial scaffolds is ongoing to develop free-standing three-dimensional scaffolds[2], which provide better conditions for cell growth than two-dimensional ones[3]. In these scaffolds, the microstructure and porosity are key elements in providing a spatial organization for cell growth, as well as inducing various other biological functions[4]. The interconnectivity among the microscale-sized pores allows nutrient transport and cell migration. On the other hand, 2-20 μm thick fibrous microstructures arranged in filaments that provide a network mimicking intricate collagen fibers of ECM[5]. Highly porous ZnO templates, which consist of interconnected tetrapod-shaped ZnO particles[6], offer such a fibrous microstructure as a potential scaffold. Carbon-based scaffolds with 3D porous microstructure are promising candidates in tissue engineering due to their electrical conductivity and for their potential to convert into biofunctional[7], peptide- or protein-coated surfaces[8]. For instance, carbon-based nanomaterials e.g. carbon nanotube (CNT) or graphene, have a strong tendency to interact with peptides and proteins via physical or chemical bonds[8,9]. As the microarchitecture of the carbon-based scaffolds can maintain the spatial organization for cell growth[10], they can be suitable for biofunctionalization and addition of other biochemical cues.

The aim of this study is to develop carbon-based scaffolds, to design methods to biofunctionalize them and to investigate their interactions with living cells. The superposition of the microtetrapod-based scaffold structure and the different surface biofunctionalization techniques generates novel biocompatible scaffolds with diverse features, as depicted in Figure (1.1). As a primary focus, the feasibility of AG as a novel ultra-lightweight graphitic material for 3D cell growth was investigated. AG was functionalized with cRGD peptides coupled to poly(ethylene glycol) (PEG) conjugated phospholipids, promoting specific adhesion of fibroblast cells. In this study, I investigated fibroblasts adhesion on these scaffolds and the biocompatibility of AG according to the norm ISO 10993 (the data are available in chapter 3, based on publication 1).

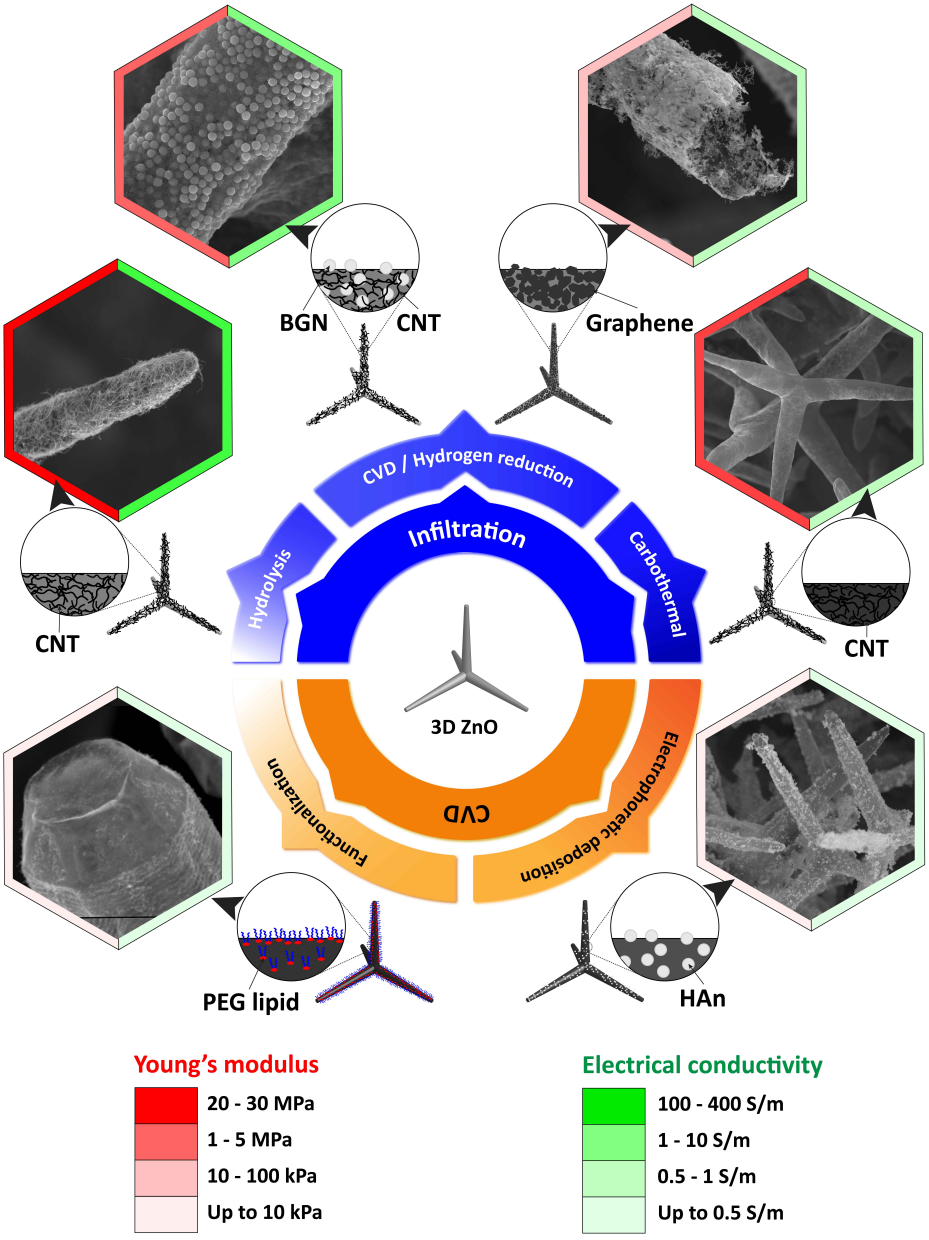

Figure 1.1: *Schematic of modular design strategy to generate biofunctional composites from aerographite, carbon nanotube, graphene and bioactive ceramic nanoparticles via implementing and combination of different procedures. The green and red stripes present the electrical conductivity and Young's modulus of the structures, respectively. (BGN: bioactive glass nanoparticles, CNT: carbon nanotube, HAn: hydroxyapatite nanoparticles)*

Additionally, I present a novel technique for preparing the scaffolds by removing the residual ZnO throughout washing cycles (Appendix-A). As described in chapter 4 (Based on publication 2), a variety of biomimetic carbon fiber scaffolds consisting of microtetrapods in close collaboration with the group of Prof. Dr. Rainer Adelung

(University of Kiel), Prof. Dr. Felice Torrisi (University of Cambridge) and Prof. Dr. Bodo Fielder (Hamburg University of Technology) were developed. Tailoring the features of fibrous scaffolds, a modular design strategy to generate biofunctional scaffolds from CNT and graphene was employed. I have also shown the scaffolds biocompatibility by investigating cell viability, fibroblast adhesion and proliferation rate, and protein adsorption capacity of the scaffolds. The scaffolds are able to resemble the extracellular matrix structurally and biochemically, successful cell adhesion and growth. This strategy leverages the possibilities of developing fibrous frameworks for 3D cell growth with diverse features, which opens up new avenues in tissue engineering, even for complex tissues.

To expand the applications of 3D carbon-based scaffolds in the field of bone tissue engineering upon specific cellular and biological responses, the bioactive materials were incorporated into the networks. In the first approach, novel bioactive carbon-based hybrid scaffolds were fabricated by the integration of BG and HA nanoparticles into microfibers of self-entangled CNTs (the results are available in Chapter 5, based on publication 3). The scaffolds were developed in collaboration with the group of Prof. Dr. Rainer Adelung (University of Kiel) and Prof. Dr. Aldo R. Boccaccini (University of Erlangen-Nuremberg) by the adoption of a recently presented infiltration process for fabrication of self-entangled carbon nanotube tube networks in the the group of Prof. Dr. Rainer Adelung (University of Kiel). I investigated the scaffolds bioactivity and biocompatibility in terms of fibroblast adhesion and proliferation, osteoblast growth, protein adsorption capacity and ion release. I demonstrated that hybrid carbon-based scaffolds successfully support 3D osteoblast growth and can enhance the biomineralization ability and protein adsorption capacity significantly. In addition, the hollow microtubes can allow nutrient transport while the osteoblasts and fibroblasts are stretched out along the fibers. In general, together with bioactivity tunable stiffness and porosity features, the bioactive hybrid scaffolds can be promising candidates for bone tissue engineering applications.

Despite the bioactive hybrid 3D scaffolds achieved by the infiltration approach, it is not possible to include bioactive nanoparticles such as hydroxyapatite nanoparticles (HAn) into AG, where indeed external forces are needed in order to immobilize the HAn in the scaffolds. To overcome this limitation, I presented a novel periodic electrophoretic deposition (PEPD) that allows a successful HAn coating on AG scaffolds, which are received from the group of Prof. Dr. Rainer Adelung (University of Kiel) and Prof. Dr. Bodo Fielder (Hamburg University of Technology), both internally and on the surface (the results are available in chapter 6, based on publication 4). The coating process was monitored *in situ*, which leads to better understanding of kinetics of nanoparticle deposition and allows finding out optimum parameters required for homogenous coating all over the scaffolds. The HAn coating significantly promoted osteoblast activity and increased protein adsorption capacity. The results from these studies provide a significant milestone in regulating 3D cell growth through carbon-based fibrous networks.

1.1 State-of-the-art

Employing the magnificent properties of carbon based nanomaterials in a macroscopic scale can improve function of the scaffolds, although assembly methods for converting Carbon based nanomaterials (CBN)s into a suitable 3D architecture for tissue engineering purposes are still challenging. Different assemblies such as CNT[11–14], graphene assemblies[15–18] and self-entangled CNT networks[19] have been reported. However, 3D CBN assemblies were rarely introduced in the tissue engineering field[20–22]. Broadly speaking, cells adhere and colonize into CNT assemblies according to *in vitro* studies[22]. Nevertheless, disassembly of CNT networks results in dispersion of scaffold components in the blood circulation system or surrounding tissue[23], which is considered a drawback for CNT assemblies.

Application of meso- and macroporous 3D CBN assemblies as a scaffold for cell growth has been shown in many studies[24]. The architecture of CNT and graphene macroporous 3D assemblies has been reported in the form of aligned CNT scaffolds[25,26], textile containing nano-fibers[27], self-assembled CNT sheets, CNT or graphene foam[28]. Among the others, the latest (CNT or graphene foam) possesses the highest porosity and accessibility from all sides. 3D macroporous scaffolds with foam architecture are widely used as bone replacement grafts as well[29].

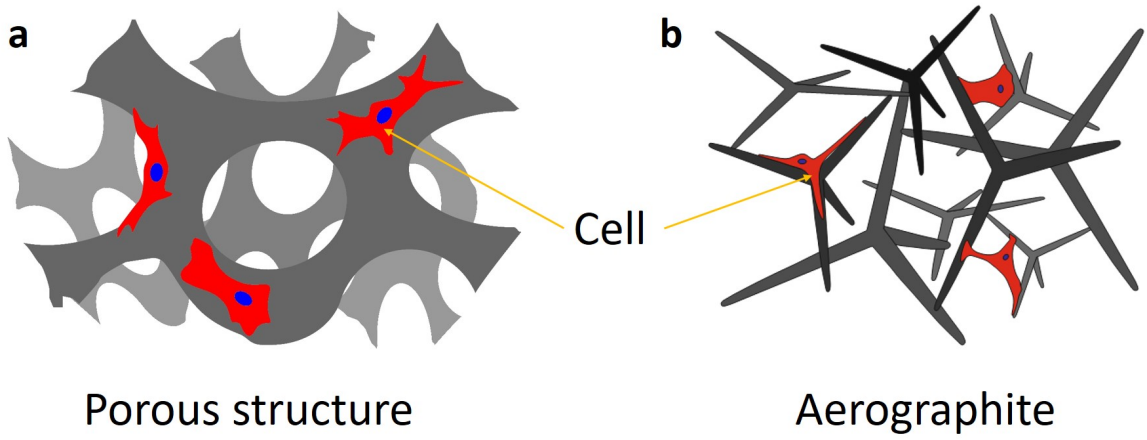

Figure 1.2: *Schematic of cell adhesion on scaffolds with foam (a) and aerographite (b) architecture, illustrating the cell adhesion difference on the filaments of CNT/graphene foam and aerograohite microstructure. Due to the small surface of one single filament for cell adhesion and the short distance between two neighboring filaments, a cell for a stable attachment, adheres to more than one filament of aerographite. Thus, the cells seem to bridge the filaments while adhering to aerographite.*

This 3D macroporous architecture consists of interconnected pores and uniform solid parts. In this work, super porous microstructures, made of micro-tetrapods with framework architecture, were used. The microstructures presented here (e.g.

aerographite) have a large free space (up to 99.99% of scaffold) that exist between the micro-tetrapods. The spatial arrangement of carbon micro-tubes provides large interstitial space where the cells are supposed to be accommodated. Figure (1.2) schematically compares cell adhesion on scaffolds with foam or aerographite architecture, suggesting that cells adhere to foam scaffolds by spreading over the substrate, whereas the cells span between the aerographite filaments.

CNT and graphene as the most well-known CBNs due to their unique features, such as high physical aspect ratios and electrical conductivity. Both have attracted significant attention in tissue engineering[30–32]. As it was discussed earlier, the biocompatibility of CBNs and CBNs containing scaffolds is an important requirement for their application in the field of tissue engineering. The biocompatibility of CNTs depends on different parameters such as their degree of purification and the synthetic method[33]. Although the biocompatibility of CNTs has been confirmed[34], the cytotoxicity of CNTs is still a concern[35]. On the contrary, Graphene has been reported to be biocompatible and is readily applicable for tissue engineering applications[32]. Therefore, the biocompatibility and cell responses of incorporated or self-standing CNT and graphene scaffolds with novel microarchitecture are investigated in this thesis.

The bioactive characteristics of a scaffold is a key property for enhancing bone regeneration[36]. Bioactive ceramics such as HA and BG are commonly used materials in the field of bone tissue engineering[37,38]. In principle, the bioactivity of this type of ceramics is based on the formation of a hydroxycarbonate apatite layer at the ceramic-bone interface upon interaction of calcium phosphate contents[39]. In case of inherently non-bioactive materials, different strategies, such as electrophoresis[40,41], entrapment[42], adsorption[43], Longmuir-Blodgett[44,45], layer-by-layer[46,47], and convective self-assembly[48,49] can be potentially used to incorporate bioactive ceramic nanoparticles for promoting their bioactivity. The capability of electrophoretic deposition (EPD) in coating the complex shapes with no requirement for binder has led to distinguished applications of EPD in the biomedical field[40,50]. EPD has been implemented for the deposition of a wide range of nanoparticles of almost any material class including ceramics[40,51], polymers[41,52,53], carbon-based materials[50,54–57], metals[58–60], and glasses[52,61], specifically bioactive ceramics such as HA and BG[40]. The thickness and morphology of HAn or BGN deposited film on a conductive substrate can be easily modified through parameter adjustment of the process[41]. In addition, EPD offers possibilities to coat fibers and porous substrates with bioactive ceramic nanoparticles. For instance, Zhitomirsky demonstrated the HAn-decorated carbon fibers using an EPD process[62]. Employing EPD to coat rapid prototyped 3D Ti6Al4V scaffolds[63] and 3D porous bioglass-scaffold with carbon nanotubes[64] resulted in inhomogeneous distribution of deposited ceramic nanoparticles throughout the scaffolds. Such inhomogeneities in particle deposition has led to thicker coatings on the outer surface of the scaffolds, which limits the applications of EPD for coating 3D scaffolds[63,64]. Therefore, more precise information of deposition phenomena during the EPD process, are needed for a full and quantitative fundamental understanding of mechanisms to optimize the EPD working parameters in order to broaden the application of EPD in coating 3D scaffolds. Thus, in regard to this thesis the HAn deposition was monitored by observation of fluorescently labeled HAn during the deposition process. In addition, the distribu-

tion of HAn on the AG scaffolds was investigated in 3D using X-ray microcomputed tomography (μCT).

Chapter 2

Basics

2.1 Tissue engineering

2.1.1 Principles of Tissue engineering

Initially, regenerative medicine was defined in the field of health science to describe the restoration and regeneration of damaged or diseased human tissue by natural human substances such as cells, genes or proteins and biomaterials[65,66]. The regeneration process can occur *in vivo* or *ex vivo* through cell seeding on artificial scaffold materials, with the addition of growth factors or combinations of them[66]. Over the past few years, reconstruction and implantation of various tissues and organs such as bioengineered vessels[67,68], functioning heart[69] and kidney[70,71] have been reported. Tissue engineering and newly emerging regenrative medicine field are often used interchangeably, though some experts argue that they represent different conceptual entities[72]. For instance, tissue engineering is restricted to the use scaffolding materials for the promotion of cell and tissue growth, while regenerative medicine includes the transplant of genetically modified cells without the specific need for scaffolds[73]. Hence, tissue engineering can be categorized as a subbranch in the field of regenerative medicine.

Tissue engineering is an interdisciplinary field that bridges life science and engineering. This field implements engineering principles and methods to regenerate function and structure of mammalian tissues while also providing the chance for a deeper fundamental understanding of biological systems[74]. Tissue engineering aims to overcome the limitations of conventional biomaterial or organ transplantation therapies, via the regeneration of entire biological components of a tissue outside the body for eventual transplantion. In order to guide cell ingrowth into a three-dimensional matrix or scaffold, new and functional tissues are fabricated. In some trials, decellularized vital organs with preserved natural architecture are implemented to be associated with cells before or after implantation[75]. Conceptually, in the field of tissue engineering the necessary cells are introduced into the artificial scaffold to replace the injured tissue. Therefore, the artificial scaffolds should be developed by mimicking the natural archi-

tecture and composition of tissue for optimized cell accommodation. Moreover, tissue engineering offers the opportunity to develop and design a functional three-dimensional tissue[65].

2.1.2 Graft and scaffold materials

The tissue engineering field requires vast knowledge of materials science and chemical engineering to develop desirable scaffolds with the essential features of engineered tissue. Crucially, the materials need to be compatible with biological environments (see section 2.5) as they interact directly with living cells. The compatible scaffolds can be natural or synthetic materials, which are permanent or degradable. The cell-scaffold interface has significant impact on cellular activities, which has to be considered and optimized at the molecular level for scaffold designing. Biological signaling should be involved in the materials development. Incorporating growth factors, specific adhesion sites, or releasing specific ions can be mentioned as some important examples[76].

Broadly speaking, the new generation of synthesized biomaterials for tissue engineering purposes are highly specialized in structure and composition with regard to the targeted tissue or organ[77]. For instance, natural and synthesized polymers are currently used widely as biomaterials with a direct contact to the cells and biological systems[78]. In addition, biodegradability and tunable features of polymers, have attracted considerable interest for imitating analogs for ECM replacement. Nevertheless, other materials such as bioactive ceramics[79] and carbon-based materials[7,10] have overcome the limitations of polymers e.g. being neither electrically conductive nor bioactive. Bioactive ceramics such as three-calcium phosphate, hydroxyapatite, bioactive glass and glass-ceramics (see section 2.4) with certain compositions of silicate and phosphate enhance the hard tissue and in some cases soft tissue restoration via reaction with physiological fluid and increase of cellular activity[80,81]. In addition, carbon based materials, due to their very specific nature, can be used as conductive matrices with the great potential to bond covalently or non-covalently with a wide range of molecules[82]. In this dissertation, a variety of carbon-based scaffolds with unique architecture and tunable features for tissue engineering purposes are presented. Figure (1.1) illustrates the schematic of the here implemented modular design strategy to generate biofunctional composites from aerographite, carbon nanotube, graphene and bioactive ceramic nanoparticles via implementation and combination of infiltration[19], chemical vapor deposition[83] and electrophoretic deposition methods.

2.1.3 Cells in tissue engineering

Cells as basic building blocks in tissue inevitably play a key role in tissue engineering. Cells are composed of a variety of components[84]. What follows is a very brief account of the cell cytoskeleton, nucleus and adhesion molecules, which will be highlighted in this dissertation.

The cytoskeleton is an important part of cells, that orients cell division, controls

cells movement individually or as a part of a cell sheet, and defines the shape of cells as an essential aspect of their function. The cytoskeleton mainly consists of microfilaments, microtubules and intermediate filaments. Microfilaments are polymers made of actin, which have different gene products such as α actin in muscle and β/γ actin in non-muscle cells. Microfilaments are associated with stress fibers, which exert traction on their substratum.

The nucleus is an organelle that controls the life of a cell. It contains the majority of genes, that are located in the nuclear chromosomes. A gene is organized as a sequence of DNA that codes for proteins and non-translated RNA.

Adhesion molecules are primarily located in the cell membrane as transmembrane molecules to interact with other cells or ECM components. Among all the cell adhesion molecules, integrin contributes in cell adhesion to the ECM and cadherin to cell to cell adhesion. Integrins are glycoproteins that are made of α and β subunit chains. The actin fibers are bound to cytoplasmic domains of the integrins through adhesion cluster[85]. The adhesion cluster forms upon initial clustering of integrin and the accumulation of secondary proteins such as talin, vinculin, and α-actinin[86]. In this work, the actin fibers and the adhesion clusters were investigated via fluorescent staining in order to study cell adhesion on the presented scaffolds.

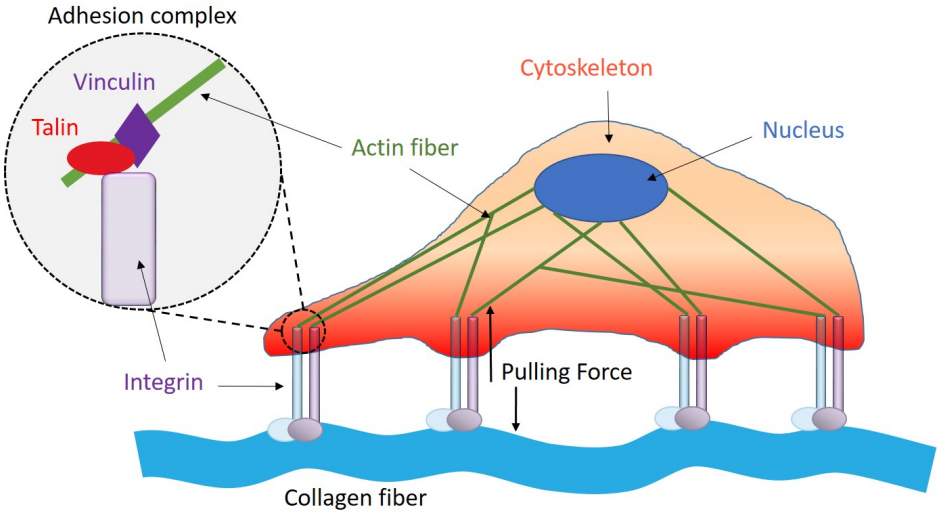

Figure 2.1: *Schematic of a eukaryotic cell structure. The visualized actin stress fibers are necessary to determine the cell shape and movements as well as the mechanical supports. The cytoskeleton of the cell connects to the ECM through the adhesion clusters which are large dynamic protein clusters on the cell membrane. Mechanosensing and transmission of the mechanical tension occurs through the connection of adhesion clusters and stress fibers. In this thesis, the adhesion cluster, actin fibers and nucleus of the cells were studied via fluorescent labeling.*

2.2 Extra cellular matrix (ECM)

2.2.1 Role and importance

The ECM as a heterogeneous non-cellular compartment of tissues, maintains the structure of tissues and organs. Mostly the ECM has a fibrous structure with large inerstitial spaces to accomodate the cells[87]. Basically, ECM is a connective network which provides mechanical stability and biochemical cues for tissue morphogenesis and formation. Hence, the physical, mechanical and biochemical properties of tissues are defined by characteristics of the ECM. For instance, the stiffness as well as the elasticity of a tissue is dictated by physical and biochemical characteristics of ECM[88]. Moreover, biochemistry and mechanical properties of ECM regulate the cell function and motility by interacting with cytoskeletal networks[89]. The ECM is dynamically remodeled as cells deposit or reassemble ECM during tissue development. For that reason each tissue possesses ECMs with different features and specification.

2.2.2 Molecular component, structure and features

ECM possesses a hierarchical structure made of protein fibers and glycosaminoglycans as water capacitors in gel form[76].The twisting of three alpha chains, produces triple helices, which creates the collagen fibrils that are the main constituent of the ECM. Different types of collagen are incorporated in different tissues, for instance collagen II in cartilage and collagen IV in basal lamina can found. Another important constituent protein is elastin, which dictates the elasticity of a tissue. Fibronectin, which consists of disulfide-bonded dimers, meditates cell adhesion by binding to integrins on the surface of cells. However, since ECM possesses a hierarchical architecture, it is implied that scaffolds with hierarchical architecture would have higher similarity to ECM.

2.2.3 Cell adhesion to ECM

Extracellular matrix has large effects on cell behavior such as migration, differentiation and most importantly adhesion[90]. Many of these events occur through ECM receptors on the cells. Integrin as the main mediator of cell adhesion, interacts with different ECM components, in particular, collagen, fibronectin and vitronectin. Integrin clusters are aggregated at adhesion sites which are called focal adhesions[91]. Integrins can also bind to bundles of cytoplasmic actin filaments via interaction with the two skeletal proteins, talin and α-actin[92]. In addition, focal adhesions contain a variety of components such as paxillin. Paxillin is a key component for integration and processing of adhesion and adhesion-related signals. This component is activated by engagement of integrins with ECM[93]. In order to detect and quantify the focal adhesions with fluorescence microscopy, paxillin can be transfected with YFP chimaeras. The YFP-paxillin transfected fibroblasts regularly have been used in this work.

2.2.4 Cell lines

REF52 is a fibroblast derived from rat embryo. Fibroblasts are the most common cells in connective tissues. They preserve the structural integrity of connective tissue by secreting ECM precursors, and therefore play a key role in tissue development. REF52 cells are isolated from 14 day old rat embryos[94].

Saso-2 was originally derived from the primary osteosarcoma of an 11-year-old Caucasian girl in 1973 by Fogh et al[95]. Later, scientists illustrated the osteoblastic features of Saso-2[96] with the ability to fully differentiate to osteoblast cells. Saos-2 have been widely used in *in vitro* assays, especially in the field of bone tissue engineering to show the potential and feasibility of a scaffold as a bone substitute.

MCT3T-E1 is an osteoblast precursor derived from mouse calvaria. As a result of their high alkaline phosphatase activity in the resting state and formation of calcified bone tissue[97], they have been used to study physiologically relevant systems.

2.3 Carbon based materials and nanomaterials in tissue engineering

2.3.1 Carbon based materials and scaffold features and their impacts on cellular behavior

Due to their unique chemical and physical properties such as electrical conductivity, optical properties and thermal and chemical stability, CBN have attracted extensive attention in various fields. Due to the multifunctional nature of CBNs, several areas of biomedical engineering use them as implants either individually or in composites in order to enhance biomaterial properties and function[7]. A growing body of literature has shown a great potential for fabrication of artificial scaffolds with similar chemical and physical features as ECM through using CBNs[98]. What follow is an account of the most prominent carbon based biomaterials which were used in this work as well.

Carbon nanotube (CNT): Despite the controversial emerging history of CNTs[99], their extraordinary properties are clearly disclosed to many of researchers. The secret behind the remarkable thermal and electrical conductivity as well as the mechanical and optical properties of CNTs is the chemical binding of nanotubes. The binding is mediated by sp^2-hybrid carbon atoms, as is the case in graphene[100]. As for the number of rolled-up graphene sheets, they fall under the two different categories of single-walled and multi-walled carbon nanotubes. Additionally, the CNTs electrical conductivity provides a chance to carry out electrical stimulation on artificial scaffolds. Furthermore, the most interesting feature of CNTs for tissue engineering is the scale of their dimensions. The flexible fiber-shaped CNTs with a great tensile strength are considered a physical analogue to ECM components such as collagen fibers[101].

Graphene: With their discovery of graphene as the thinnest material with usable properties, Geim and co-workers received the Nobel Prize in Physics in 2004. Graphene consists of a single layer of sp^2 carbon atoms as a two-dimensional sheet that can be considered as a basic structural element of other carbon allotropes such as CNT, graphite and fullerenes[102]. Graphene owes its unique mechanical, physiochemical, thermal, optical and biomedical properties to a specific atomic arrangement. Strong carbon-carbon bonds in a hexagonal lattice can explain its mechanical features, and the presence of free π electrons and reactive sites for surface reactions, its physiochemical properties[9]. Due to the surface properties of graphene, it has been shown that strong interactions with biomolecules can develop. Therefore, graphene has contributed to the implementation of many biomedical applications[32].

Aerographite (AG): When it comes to the lightest structural materials with super elastic deformability, aerographite shines brightest among all black carbon-based materials. In 2012, a team of researchers at the University of Kiel and the Technical University of Hamburg reported on areographite as a porous interconnected network

of graphitic microtubes[83] Figure (2.2). The AG network consists of micron-scale carbon tubes with wall thickness of about 15 nm. Similar to CNT and graphene, carbon bonding in AG has a sp^2 character as well. However, highly porous 3D interconnected networks can be considered as the greatest distinguishing feature of AG in comparison to other carbon-based materials in the fabricating of ECM-mimicking artificial scaffolds.

The AG synthesis process is based on zinc oxide reduction to zinc, graphite deposition and simultaneous zinc evaporation via a chemical vapor deposition process. The sacrificial ZnO template consists of micron-size tetrapods or often multipods[6]. However, AG inherits the pristine shape of sacrificial ZnO tetrapods without any adverse changes. The unique ZnO micro structure provides the physical cues for imitation of the ECM architecture as a scaffold.

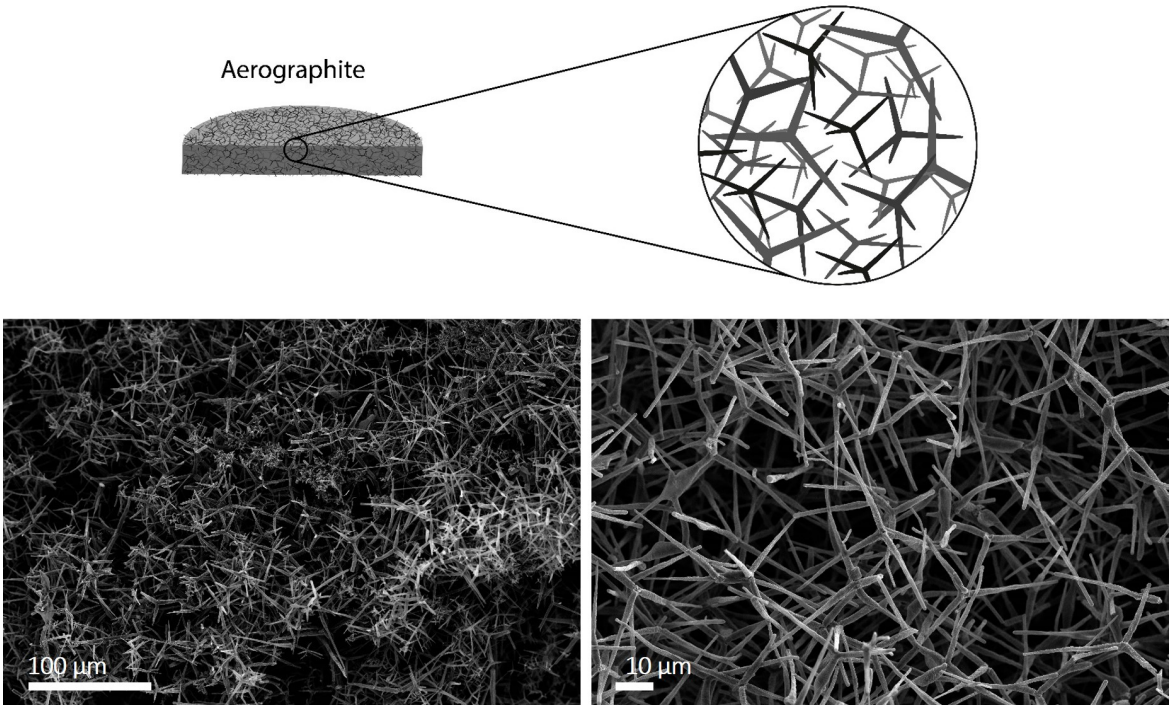

Figure 2.2: *Scanning electron microscope images and schematic of aerographite network, showing the arrangement of graphitic micro tetrapods next to each other, which forms a framework with vast free space in between of tetrapods.*

Chemical vapor deposition (CVD) is the most popular technique for CBN fabrication. CVD is a versatile process to fabricate broad range of carbon-based powders, coatings, components, fibers etc.[103]. Deposition of a solid phase derived from decomposition or reaction of a vapor phase or precursors onto a heated surface might be a proper definition for CVD. Many interactions, namely thermal decomposition, reduction, hydrolysis, and carburization are involved in the CVD technique. Despite the disciplinary thermodynamic fundamental of CVD, most of CVD processes have a simple operation, which can be readily optimized experimentally. However, the sequence of events in CVD is initiated by diffusion of the reactant through the boundary layers and subsequent contact with a surface. Then, the gaseous by-products of the

deposition reactions are carried away from the reactive surface via an inert gas[104].

CVD processes fall into different categories based on the purpose of use and the type of chemical reactions that are taking place[105]. Aerographite, CNT and graphene are mainly fabricated by a thermal CVD or catalytic CVD. In this type of CVD, CNT and graphene fabrication occurs through deposition of thermally decomposed hydrocarbon elements in the presence of metal catalysts. Thermal-decomposition and hydrogen reduction are the most prominent interactions in thermal CVD. The molecules of the introduced precursor gas are decomposed to elementary molecules. For instance the following reaction is one typical examples of hydrocarbon decomposition[103]

$$CH_4(g) \rightarrow C(s) + 2H_2(g) \tag{2.1}$$

This can become even more complex in case of toluene[106]:

$$C_6H_5CH_3 \rightarrow C_6H_5CH_2 + H \tag{2.2}$$

$$C_6H_5CH_3 \rightarrow C_6H_5 + CH_3 \tag{2.3}$$

Hydrogen reduction is the other important and widely used chemical reaction that takes place in a CVD reactor. Reaction at lower temperature in comparison to equivalent decomposition reactions is the major advantage of this reaction. In the presence of hydrogen the metal oxides are reduced to metal elements, which are normally volatile in the decomposition reaction.

Hydrocarbon decomposition and reduction interactions are the key reactions in the aerographite fabrication process. ZnO micro-tetrapods serve as the sacrificial template. ZnO is reduced to Zn, which due to the high temperature of the reactor is volatile and thus evaporates. The evaporated gaseous Zn is removed from the chamber with other by-product gases through an exhaust outlet. Simultaneously, the carbon molecules from the toluene decomposition are replaced by reduced ZnO (Figure 2.3).

2.3.2 Carbon-based nanomaterials functionalization

The biomedical application of CBNs is hampered by their physicochemical properties[107]. The highly hydrophobic nature of CNTs and bound functional groups[108] limit their solubility and, in the worse cases, elicit cytotoxic effects of CBTs through cellular damages[109]. The surface modification of CNTs can increase their solubility in aqueous solutions or relevant biological serums and solvents, leading to an improvement of their biocompatibility[107,108]. In this regard, various modification methods have been presented that can be in general categorized as covalent and non-covalent functionalizations.

Covalent functionalization: Solubility of CBNs can be achieved via the introduction of reactive species by covalent functionalization, mainly through acid oxidation[110] or cycloaddition[111]. Although the introduction of functional groups on CBNs

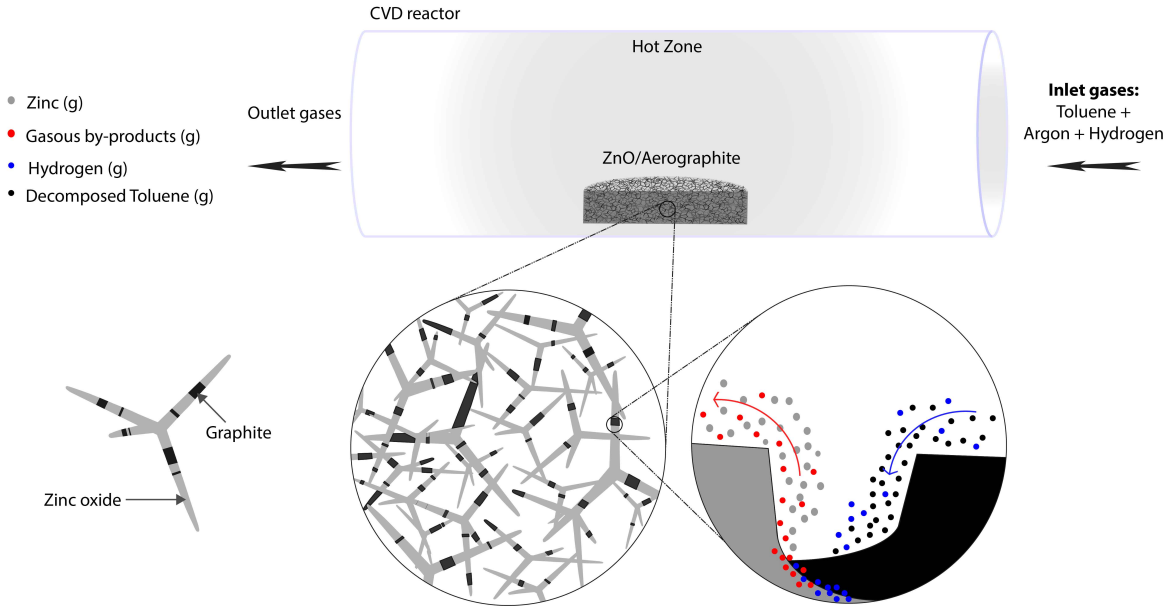

Figure 2.3: *Schematic of aerographite evolution via a CVD process. The conversion process occurs in a tube furnace while a mixture of argon, hydrogen and toluene gases are purged into the reactor. Initially the ZnO conversion starts as small ribbons and grows along the ZnO filaments. The schematic illustrates that the conversion that takes place via ZnO reduction and simultaneous replacement by carbon atoms.*

surfaces enhances their biocompatibility, such treatments alters the surface composition of CBNs.

Non-covalent functionalization: To avoid any alteration in the CBNs surface composition, various molecules can be introduced to their surface through weak and non-covalent interactions including π-π stacking, van der Waals or electrostatic interactions[108]. Noncovalent functionalization offers several advantages such as low cost, being quickness, efficacy, and the potential to include pharmaceutical products[82].

In order to disperse the CBNs, various amphiphilic molecules such as surfactants, synthetic or natural polymers, proteins and poly(ethylene glycol)(PEG)-compositions have been introduced[112]. Basically, amphiphilic molecules like surfactants or PEG compositions consist of a hydrophobic region where the surfactant physically via π-π stacking, van der Waals or electrostatic interactions is adsorbed to the surface of CBNs, and a hydrophilic region contributes to immerse in aqueous media[113].

PEG phospholipid is used as an amphipilic molecule to functionalize the CBNs non-covalently[114]. PEG lipids can densely coat the surface of nanomaterials, enhancing their water solubility[115]. This lipid binds to CBNs via van der Waals interaction[114], while the hydrophilic regions provide the solubility. In addition, amine-terminated PEG lipid can be conjugated to biologically relevant molecules[116] where the hydrophilic branches of PEG lipid improve CBNs solubility and the biological molecules enhance the biocompatibility of CBNs. Figure 2.4 illustrates a schematic of PEG lipids and their binding to CNTs. In this thesis to use AG as a scaffold for cell growth purposes,

PEG lipids were employed to overcome the super hydrophobic nature of AG. In addition, to promote cell adhesion and cell proliferation, cRGD peptides were coupled to PEG conjugated phospholipids as well.

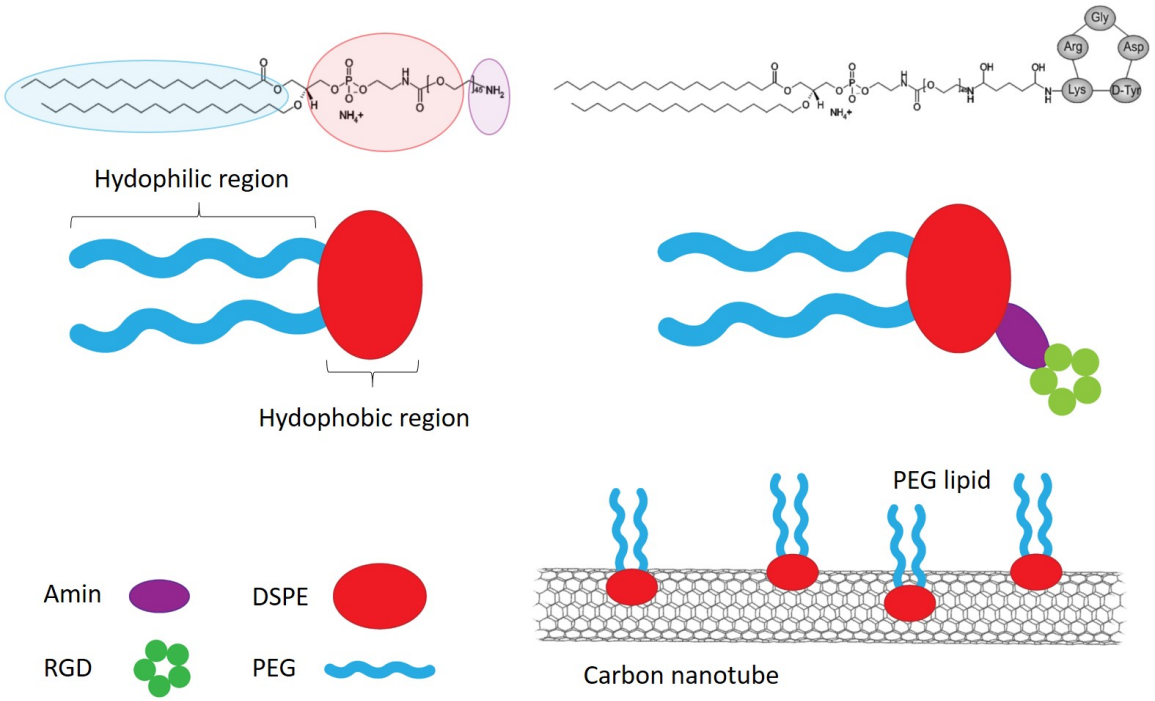

Figure 2.4: *Schematic of PEG lipid, illustrating the hydrophilic and hydrophobic regions of PEG molecules. The PEG lipid adheres to hydrophobic substrates (e.g. CNT or graphene) through its hydrophobic regions.*

2.3.3 Protein adsorption by CBN

Most of the scaffolds for tissue engineering purposes react and stabilize the blood clots, promoting the ECM organization that allows the cell ingrowth from neighboring tissue. In principle, achieving this biological reaction requires a favorable microenvironment for cell adhesion and proliferation. Generally, the synthesized scaffolds do not possess all the complex ECM features. Therefore, most strategies are aimed at guiding the adhesive protein such as fibronectin, fibrinogen or vitronectin as an initial mediating layer between the scaffolds and cells during implantation[117,118]. Clinically useful adherent proteins such as fibronectin play a crucial role in the adhesion process of different types of cells[119] as well as wound contraction. The V-region of fragmented fironectin contains specific sites for $\alpha 4\beta 1$ integrin expressing a receptor for fibronectin's RGD cell-binding domain, which provides a framework for cell adhesion[120], which is located in cell adhesion clusters (Figure 2.1). In addition, other types of adherent proteins like vitronectin are abundantly found in the ECM. Vitronectin

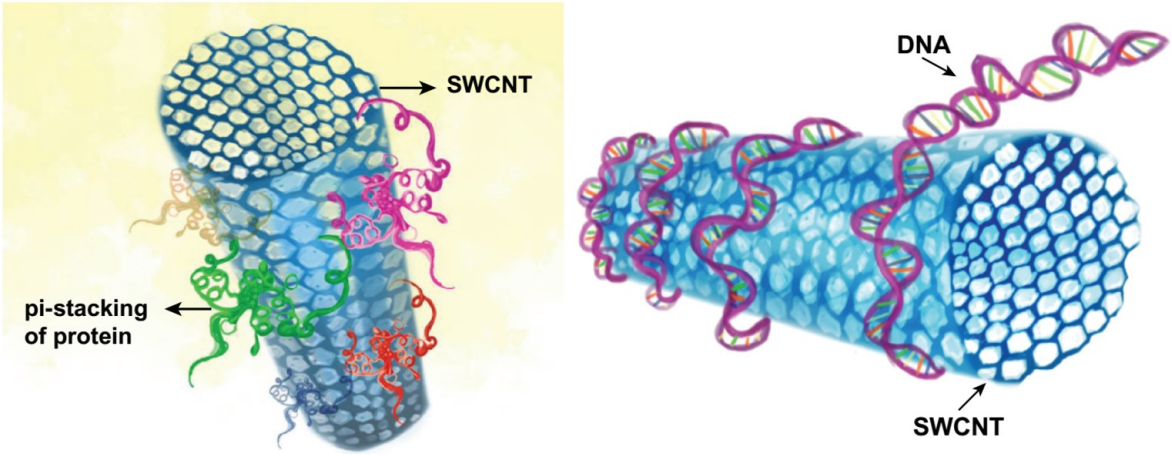

Figure 2.5: *Schematic of protein and DNA adsorption on CNTs, showing the non-covalent interaction of protein molecules and DNA with CNT's surface. Protein molecule retention on the surface is governed by π-π stacking. DNA molecules are immobilized by being wrapped around the CNTs. Figure is modified from Vardharajula et al*[107].

contains RGD sequences that promote cell adhesion via $\alpha v\beta 3$ integrin[121]. However, other types of adherent proteins such as albumin that do not contribute in cell adhesion should be considered as well. Albumin is the most abundant blood plasma serum protein. Albumin as a model adhesive protein has extensively been used to check the protein adsorption capacity of biomaterials[122]. Here in this thesis, using bovine serum albumin, the protein adsorption capacity of fabricated carbon-based scaffolds was determined.

An understanding of the CBNs interaction with proteins is crucial in the development of artificial organs. It is believed that protein adsorption occurs at the earliest stage when a biomaterial is implanted. The initially-adsorbed proteins in general are considered a surface modification, influencing cell adhesion and interactions. In addition, cellular interaction with CBNs is highly effected by the CBNs' surface properties[123]. Therefore, the surface properties of CBNs have a significant impact on cell interactions and *in vivo* performance of implants. In principle, the protein adsorption phenomena on carbon-based materials occurs through a variety of mechanisms such as π-π stacking interaction, noncovalent bonding[107]. Beside the van der Waals attraction, CBNs noncovalently interact with various biomolecules via hydrophobic, electrostatic and hydrogen-bonding interactions[124]. For instance, graphene and CNTs interact with aromatic residues of proteins via π-π stacking[107,125]. The capability of CBNs (e.g. graphene, CNT) to readily interact with proteins, contributes to them being functionalized with different biomolecules such as proteins and DNA (Figure 2.5). The protein functionalization of CBNs with fibronectin and bovine serum albumin (BSA) increases the cellular interaction[126,127].

2.4 Bioactivation of CBNs using nanoparticles

2.4.1 Bone tissue engineering

Bone as a dynamic tissue provides structural support for the body, protection of vital organs, environment for blood-forming system (marrow) and serves as reservoir of minerals and growth factors[128]. Bones are composed of two types of cortical (hard outer layer) and trabecular (spongy interior layer) tissues[129]. The trabecular bone consists of highly porous and rod-like network (Figure2.6), leading to a tissue with a lower density and higher flexibility than cortical bone[130]. The open sections of trabecular bone are filled with marrow and blood vessels mainly[131]. The non-mineral matrix of collagen protein forms the soft framework of bones. This is hardened by an inorganic crystal complex of calcium phosphate (hydroxyapatite) deposited within the matrix, which provides the strength and rigidity of the tissue[130]. Furthermore, the bone tissue consists of bone forming cells (i.e. osteoblasts and osteocytes) and resorbing cells (i.e. osteoclasts), which preserve it as a dynamic tissue[132].

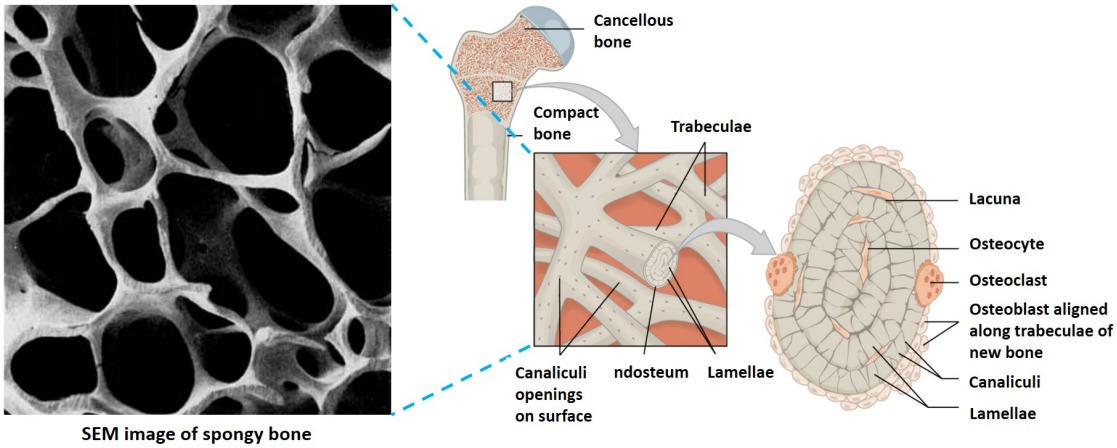

Figure 2.6: *Schematic of bone tissue, showing hierarchical microstructure of trabeculae tissue. Figure is reproduced from Whitehouse et al*[133] *and a figure* ***Authored by:*** *OpenStax College, licensed under CC-BY 4.0.*

Bone naturally has piezoelectric properties[134]. This results in an internal electrical field in response to strains, which influences cell proliferation in bone tissue[135]. This principle has been explored to expedite the bone regeneration by applying electrical stimuli[136]. It has been shown electrical stimulation has a significant progressive impact on osteoblastic activities such as proliferation[137], adhesion[137,138], and nodul formation[138,139]. Therefore, electrical conductivity of scaffolds can be the key parameter for transporting the electrical stimulation[140].

Large orthopedic defects can be reconstructed by traditional biological methods such as allografting or autografting spongy bone, or implanting bone cements[141]. Bone tissue engineering potentially provides an alternative bone reconstruction method without the limitations of the traditional methods e.g. risk of disease or infection[132].

The tissue-engineered scaffolds act as a matrix or carrier for bone forming and resorbing cells[142,143]. In addition, the scaffolds induce the bone formation and support the cell ingrowth from surrounding environment[143]. The ideal synthetic scaffold must be capable of presenting morphogenetic signals as well as a suitable matrix to accommodate bone cells. In principle, the ECM-mimetic scaffolds promote osteoblast proliferation and osteoblastic activity[144]. The fibrous microstructure of scaffolds based on sacrificial ZnO microtetrapods, highly mimics the filamentous microarchitecture of trabecular bone. Therefore, these scaffolds with a proper biofunctionalization can be potentially used for bone tissue engineering purposes.

Bioactivity is a critical issue for the application of biomaterials in the field of bone tissue engineering. In principle, bioactive materials are capable of eliciting specific biological responses from the living tissue and cells such as bone-like hydroxyapatite (HA) formation. Biomineralized HA on the surface of the bioactive material promotes osteoblast activity[145]. In case of inherently non-bioactive materials, different strategies, such as surface composition modification, have been presented[146]. Generally, unmodified CBNs hardly show bioactive behavior in a biological environment[7]. In order to avoid any composition change in the CBNs surface, it is possible to incorporate bioactive nanoparticles onto the surface of the CBNs. HA and BG are known as highly promising bioactive materials in bone tissue engineering[147]. Incorporation of HAn and BGN enhance the biomineralization[148] and osteoblast activities including proliferation[149], adhesion[150], and bone formation marker[151], hence leveraging the bone formation capacity in the scaffold. In principle, this attributes to the specific composition of HA and BG[150].

Hydroxyapatite with a nominal composition of $Ca_{10}(PO_4)_6(OH)_2$ being similar to the composition of bone tissue, HA has a broad range of application in the field of biomaterials and bone tissue engineering[152]. The high concentrations of Ca, P and Na ions on the surface of implanted-HA leads to intracellular and extracellular responses[153].

Bioactive glass with nominal composition of $70SiO_2$-30CaO, in particular silicate glass, is decisive for the formation of a bone-like calcium phosphate layer on the material which leads to strong bonds between the BG and bone or soft tissue. In case of incorporated Calcium oxide (CaO) BGs, the reactions on the surface of the BG increases the critical concentration of Ca and P ions, which in turn promotes the biomineralisation and bone formation[154].

2.4.2 Electrophoretic deposition

EPD as one of the most prominent and simple colloidal dispersion based techniques has been gaining interest in a wide range of applications to provide uniform ceramic nanoparticle coatings on surfaces[155]. In principle, EPD is the deposition of charged ceramic nanoparticles on the surface of an conductive electrode[156]. This is achieved by the introduction of an electric field into a dispersion of these nanoparticles via electrodes. Under the influence of the electric field, the charged nanoparticles move toward

the oppositely charged electrode where they are deposited as a dense and homogeneous coating layer on a flat surface. Depending on the nanoparticle surface charge, the deposition occurs at the anode electrode (negatively charged particles, anodic EPD) or cathode (positively charged particles, cathodic EPD). EPD offers nanoparticle deposition on complex shapes and surfaces and they can even be incorporated into a porous substrate[157]. In order to coat the geometrically complex shape of AG filaments, EPD was applied in this work. The porous structure of AG serves as an electrode during HAn deposition Figure (2.7). However, coating 3D porous structures via EPD processes still remains challenging[158,159]. It has been shown that the HAn deposition on 3D porous scaffolds mostly takes place on the outer surface of the scaffolds[160], which consequently leads to blockage of the pores. Therefore, avoiding a blocking of the outer pores by clustered HAn, it is necessary to study the kinetics of HAn deposition on 3D scaffold during EPD process.

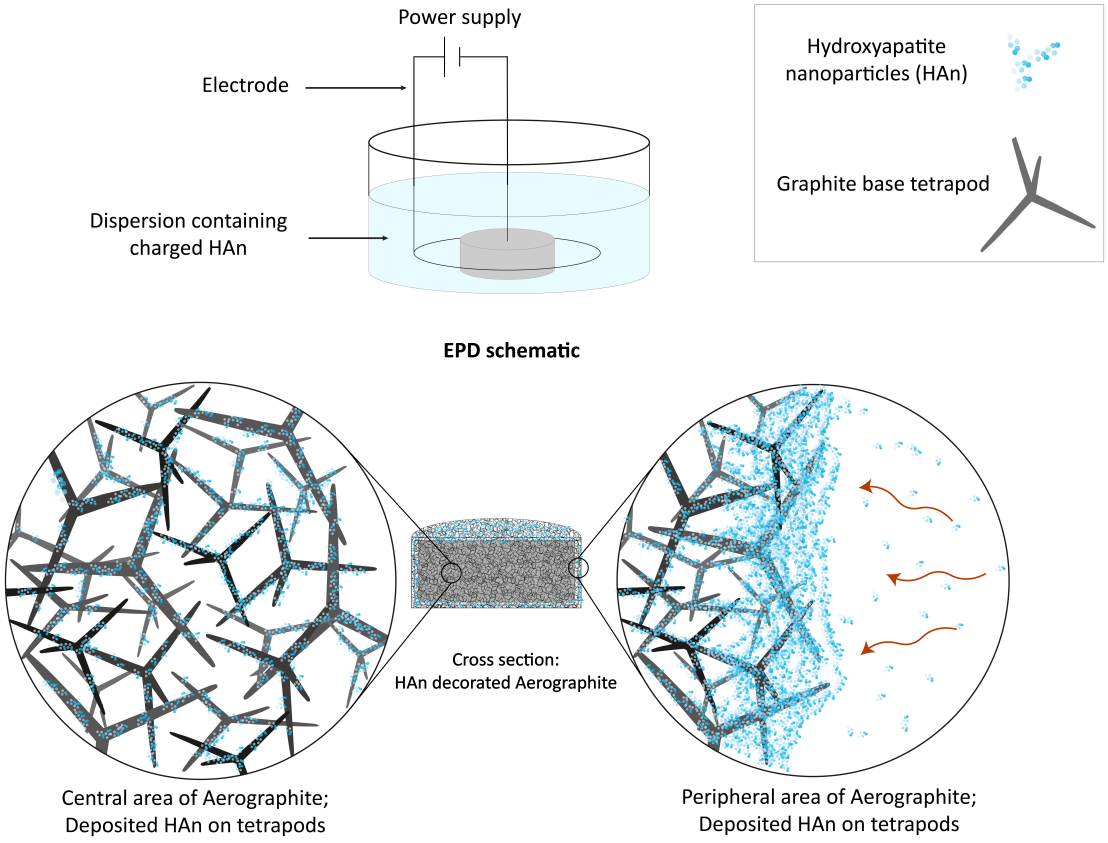

Figure 2.7: *Schematic of EPD process, illustrating the simple EPD cell for coating cylindrically shaped scaffolds. The EPD cell is connected to a power supplier providing the electrical potential for nanoparticle motion and electrodes, which serves as substrate for particle deposition. In addition, the schematic of HA nanoparticle deposition onto AG is presented. The schematic shows that the central area of the sample is partially covered with HAn, whereas the peripheral area of the sample is covered with a dense layer of HAn. This blocks the peripheral pores, leading to an agglomeration of HAn on the peripheral area of AG.*

In principle, the effective parameters of EPD are categorized into two groups of suspension- or process-related parameters such as electrodes or electrical conditions (e.g. deposition time, voltage, intensity). The parameters related to the suspension, such as particle size, dielectric constant of solution, conductivity of suspension, viscosity of suspension, concentration of ceramic nanoparticles in suspension, zeta potential and stability of suspension determine the weight and quality of the deposition. In addition, the parameters related to the process such as deposition time, applied voltage and conductivity of substrate define the weight and quality of the deposition [161]. Many attempts have been done to correlate the amount of deposited nanoparticles to different influencing parameters. For instance, Ishihara et al. have shown that the weight of deposited particles per unit area of the electrode is determined by the following equation:

$$W \propto C.\xi.\left(\frac{1}{\eta}\right).\left(\frac{E}{L}\right).t \tag{2.4}$$

Where C is the particle mass concentration in the suspension, ξ is the zeta potential, η is the viscosity of the solvent, E is the applied potential, L is the distance between the electrodes and t is the time of deposition [162]. The aforementioned equation suggests that weight deposition of particles is highly effected by the stated parameters. Therefore, here in this thesis the mentioned parameters are considered as the main ones. In order to focus on the monitoring EPD and the phenomena occurring during the process, the number of variables was lowered by fixing the suspension and process specifications according to the best of literature. All the parameters except the concentration of particles (C) and time of deposition (t) were fixed. In particular, Ethanol as a solvent with viscosity of (1.09 (cP)) and relative dielectric constant of (24.55) [163], the HA nanoparticles with average diameter of 200 nm, and electrical potential of 10 V were employed for all the experiments.

2.5 Biocompatibility of CBNs and cellular activities

The emergence of a variety of biomaterials as implantable medical devices in tissue engineering in the past decades has risen questions regarding the level of their safety and compatibility in biological environments. In principle, a wide range of interactive behaviors between the living unit and the materials occur. The interaction between non-living and living systems evokes either a host response, which can be a local or systemic, or a material response toward the biological process[72]. As a reputable definition, the materials that elicit minimal biological response and display good behavior in contact with tissue or body fluid are called biocompatible[66]. In other words, biocompatibility refers to the ability of a material to evoke an appropriate host response[123]. Based on the host response, the biocompatible implant materials are categorized in to four types: 1. With little or no host response (inert materials), 2. With specific and beneficial host and cellular response (Interactive materials), 3. With the ability to attract or incorporate cells, where they are treated as normal tissue matrices (Viable materials), 4. Originated from native tissue (Replant materials)[164]. Carbon-based nanomaterials are normally considered as inert materials[7]. With expansion of the application of materials in the tissue engineering and biomedical field and with the introduction of novel biomaterials, new paradigms have been emerged[165]. Particularly in the field of tissue engineering, *material* is replaced by *matrix* and *patient* by *cell*[164]. Thus, in this thesis, except for toxicology and proliferation studies, the material-cell interactions are studied.

2.5.1 Cytotoxicity

Cytotoxic components and materials are some of the most critical and effective parameters in the disruption of the biocompatibility of biomaterials. Depending on the toxicity level of exposed materials or components, cells respond differently. In case of lethal components, the cells undergo necrosis by loosing their membrane integrity. In the case of slightly lethal materials, cell proliferation may be stopped, which leads to apoptosis or autophagy[166]. However, nanomaterials can cause necrosis in a number of different ways[167]. In general, nanomaterials damage the cells physically due to their small size, specific shapes, and large surface area. For instance, many studies have shown the cytotoxic behavior of CNTs toward the cells, inducing oxidative stress and necrosis and inhibition of cell proliferation[35]. Due to the specific dimension of CNTs, they easily penetrate the cell membrane or even the centrosome. Thereby, CNTs physically interfere with cellular and extracellular constituents[168], leading to cellular injury and in severe cases to cell necrosis. It has been exhibited that well-dispersed CNTs can cause higher toxicity than agglomerated CNTs[169]. This is in agreement with the hereby presented results from CNT containing scaffolds, which show almost no cytotoxicity in the case of the entangled CNT microstructure. It can be speculated that the non-toxic behavior of CNT-incorporating scaffolds is attributed to the entanglement of the CNTs which limits the mobility of the CNTs.

Another proposed cytotoxicity mechanism relevant here is based on the effect of

released ion from the implanted materials to the cellular system. Specifically, it has been shown that small quantities of Zn ions (above 40 μg ml^{-1}) are strongly toxic. Papavlassopoulos et al. have demonstrated the toxic potential of ZnO nanoparticles and ZnO nano- and micro tetrapods on human dermal fibroblasts, where ZnO nanoparticles and ZnO tetrapods showed cytotoxic behavior above 15 μg ml^{-1} and 0.05 mg ml^{-1}, respectively[170]. Although it has been indicated that ZnO tetrapods are much more biocompatible compared to spherical ZnO nanoparticles, the cytotoxic effect of ZnO tetrapods should still not be ignored. Regarding this fact, in this work, the preliminary cytoctoxicity tests on AG have shown toxicity towards REF52 cells. In principle graphite is considered as an inert material. Thus, in order to understand the origin of the toxic effect, the amount of released ions from AG samples into the culture medium was measured every 3 days. Interestingly, the results indicated a high concentration of Zn ions in the medium during the first days of immersion as seen in Figure (Appendix-A.1). Continuing the immersion of AG in the medium, the concentration of released-Zn ions as well as the cytotoxic effect of AG drastically decreased to almost zero (Figure Appendix-A.1). This can be attributed to possible residual ZnO from the AG process (see section 2.3.1) which is released and removed from the AG's structure by immersion in culture medium. These results suggest a necessary pre-washing step prior to the use of AG in *in vitro* studies.

2.5.2 Proliferation

Cell proliferation is a process that increases the number of cells and replenish lost cells governed by the cell cycle. The cell cycle (division of cells, giving rise to two daughter cells) is crucial for the development and survival of cells and consequently keeps the balance between the dead and functional cells of a tissue. Determining the proliferation behavior of cells on a material, contributes to a better understanding on the biocompatibility of that material. For instance, interactive materials are designed to elicit specific cell responses, such as specific cell adhesion on the material, leading to an increase in cell growth. In comparison, cells show standard growth rates on inert materials. Thus, studying cell proliferation behavior reveals the biocompatibility level of a material which the cells are exposed to. In this work, in order to determine the capacity of the scaffolds to accommodate cells and support cell growth, cell proliferation on the fabricated carbon-based scaffolds was studied.

2.5.3 Colorimetric assays and reactions with CBNs

The biocompatibility of a material is extremely dependent on the cells' proliferation, interactions and enzymatic activities. Hence, many assay methods such as colorimetric, flow cytometry or high content imaging have been developed to estimate the number of viable cells on a sample. Among all these commonly used assays, colorimetric assays are widely used to quantify a variety of biological events including the number of viable cells, protein contents, enzyme activities or organelle functions. In principle, a colorimetric assay is based on changing a reagent to colored or fluorescent products

as a marker that can be detected and measured by a spectrophotometer or microplate reader[171]. In this study, the number of viable cells was measured via tetrazolium-based metabolic assays. In addition, the protein and the alkaline phosphatase enzyme concentration were calculated via bicinchoninic acid assay (BCA assay) and *para*-Nitrophenylphosphate (*p*NPP), respectively.

Metabolic assays

MTT (3-(4, 5-dimethylthiazolyl-2)-2, 5-diphenyltetrazolium bromide) assay: MTT is a sensitive and reliable tetrazolium-based metabolic assay for the indication of the population of dividing cells. MTT is a yellow color water soluble dye that undergoes a measurable color change via tetrazolium reduction in the mitochondrial activity to a purple color formazan crystal[172]. Thus, the quantity of formazan crystals is proportional to the number of viable cells. MTT tetrazolium reduction as the first developed cell viability assay for 96-well format has been used extensively to generate proliferative and toxicity profiles of CBNs[167]. In this thesis, MTT tetrazolium reduction assay based on a detailed ISO (ISO 10993-12:2012) protocol was used to determine the toxicity profile of fabricated scaffolds. However,the positively charged MTT tetrazolium compound might interact with ECM components[171]. Therefore, in this work for confirming the MTT results and determining the proliferation profile, other categories of tetrazolium compounds which are negatively charged (WST-1) were considered as well.
The application of tetrazolium assays in determining the cytotoxicity of CBNs is hampered by the interaction of insoluble formazan with CBNs. As it has been described by other studies, CNTs bind to insoluble MTT-formazan which leads to a stabilization of the chemical structure of formazan[173]. This interference results in a false strong cytotoxicity effect. Therefore, in this work, avoiding the possible interaction of CNTs with MTT-fromazan, the cytotoxic effect of fabricated scaffolds was investigated via an indirect test using the scaffold's extractions.

WST-1 ((4-[3-(4-iodophenyl)-2-(4-nitrophenyl)-2H-5-tetrazolio]-1,3-benzene disulfonate)) assay: WST-1 is an another type of metabolic assay based on negatively charged tetrazolium molecules, which monitors the proliferation profile of mammalian cells. In principle, WST-1 works similarly to the MTT assay by mitochondrical reduction of the WST-1 reagent into the water-soluble formazan product rather than the water-insoluble product of the MTT reagent[174].

Chapter 3

A tunable scaffold of microtubular graphite for 3D cell growth

Constanze Lamprecht, Mohammadreza Taale, Ingo Paulowicz, Hannes Westerhaus, Carsten Grabosch, Arnim Schuchardt, Matthias Mecklenburg, Martina Böttner, Ralph Lucius, Karl Schulte, Rainer Adelung, Christine Selhuber-Unkel

ACS APPLIED MATERIALS & INTERFACES

Letter

www.acsami.org

A Tunable Scaffold of Microtubular Graphite for 3D Cell Growth

Constanze Lamprecht,*[,†,#] Mohammadreza Taale,[†] Ingo Paulowicz,[†] Hannes Westerhaus,[†] Carsten Grabosch,[†] Arnim Schuchardt,[†] Matthias Mecklenburg,[‡] Martina Böttner,[§] Ralph Lucius,[§] Karl Schulte,[‡] Rainer Adelung,[†] and Christine Selhuber-Unkel[†]

[†]Institute for Materials Science, University of Kiel, 24143 Kiel, Germany

[‡]Institute of Polymers and Composites, Hamburg University of Technology, 21073 Hamburg, Germany

[§]Institute of Anatomy, University of Kiel, 24118 Kiel, Germany

Supporting Information

ABSTRACT: Aerographite (AG) is a novel carbon-based material that exists as a self-supportive 3D network of interconnected hollow microtubules. It can be synthesized in a variety of architectures tailored by the growth conditions. This flexibility in creating structures presents interesting bioengineering possibilities such as the generation of an artificial extracellular matrix. Here we have explored the feasibility and potential of AG as a scaffold for 3D cell growth employing cyclic RGD (cRGD) peptides coupled to poly(ethylene glycol) (PEG) conjugated phospholipids for surface functionalization to promote specific adhesion of fibroblast cells. Successful growth and invasion of the bulk material was followed over a period of 4 days.

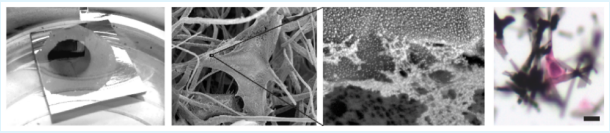

KEYWORDS: *aerographite, tissue engineering, 3D scaffold, cyclic RGD, fibroblasts*

Developing novel materials for tissue regeneration requires the consideration of principles of engineering and life sciences. The natural extracellular matrix (ECM) provides a network of intricate collagen fibers that arrange in filaments of 2−20 μm thickness to support cells, and guide their growth as well as their behavior.[1] In order to imitate this topographical environment naturally derived and synthetic materials have been explored that are beginning to show notable progress.[2−5] More recently, free-standing 3D scaffolds are increasingly favored over 2D materials to more accurately mimic the complex 3D cellular environment.[4−7] Early work has shown promising results using microfiber constructs for organ reconstruction[8] and neuronal regeneration in animal models.[9]

The macroscopic geometry is a key element in providing spatial organization for cell growth and appropriate nutritional conditions. Supplying oxygen and nutrients as well as waste removal by diffusion present growth constraints for cells in 3D. Thus, a conducive environment for cell growth and proliferation will be contingent on material porosity, pore size and interconnectivity of pores that allow cell migration and mass transport. The minimum pore size might be approximated by the diameter of cells in suspension, which depends on the cell type and varies broadly from 5 to 15 μm for fibroblasts of connective tissue up to 100−350 μm for bone.[10]

To mimic the ECM biochemically, cell-adhesive ligands, which are presented by the natural ECM in the form of fibronectin, vitronectin, and laminin, have to be included in the scaffold design.[1] These ligands recruit cell surface receptors of the integrin-family, which play an active role in biochemical and mechanical signaling.[11] A common motif of integrin-binding sites in fibronectin, vitronectin and laminin is the tripeptide RGD of the L-amino acids arginin (R), glycine (G), and aspartic acid (D). It is widely used in synthetic materials to promote adhesion of a variety of cells.[12−14]

Ultralightweight aerographite[15,16] (AG) inherently fulfills the geometrical requirements posed by natural ECM very well. This novel material consists of a self-supporting highly porous (>99.9% free volume) network of seamlessly interconnected hollow graphite tubes with micrometer-scale diameters and mechanical flexibility (kPa modulus). Via surface functionalization, various biochemical signals may be introduced to provide appropriate conditions for 3D mammalian cell culture applications. In this study we investigated the use of AG as a scaffold for 3D cell growth for the first time. We employed cyclic RGD (cRGD) peptides coupled to poly(ethylene glycol) (PEG) conjugated phospholipids to promote specific adhesion of REF52 fibroblast cells and followed cell growth and invasion into the bulk material over a period of 4 days.

Conventional methods to fabricate 3D fibrous matrices include the decellularization of donor-derived matrices[17] and electrospinning methods.[18] AG synthesis,[15] in contrast, is a one-step chemical vapor deposition (CVD) process. In brief, ZnO templates (Figure 1A, top panel) are produced from a loose powder of microsized ZnO tetra- and multipods that are compressed and heated for 3h at 1200 °C.[19] Under an argon and hydrogen atmosphere with toluene as a carbon source the templates are converted into AG at ∼760 °C. During

Received: January 20, 2016
Accepted: June 3, 2016
Published: June 3, 2016

DOI: 10.1021/acsami.6b00778
ACS Appl. Mater. Interfaces 2016, 8, 14980−14985

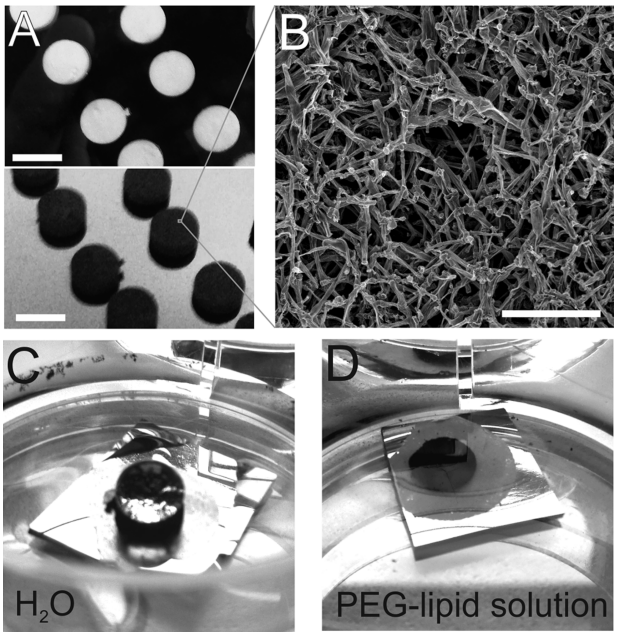

Figure 1. (A) White ZnO templates with a volume of 0.085 cm^3 (top) are converted into black AG (bottom) in a one step CVD process. The ZnO is removed completely during formation of AG filaments. Scale bar: 6 mm. (B) Scanning electron microscopy reveals the hierarchical scaffold of interconnected hollow carbon microtubules. Scale bar: 50 μm. (C) AG is inherently super hydrophobic as demonstrated by water forming a nearly perfect droplet on the surface of the black AG disk, which is fixed to a small Si-chip with double-sided adhesive tape. (C) An aqueous solution of DSPE-PEG2000-NH_2 is a well-suited wetting agent and the Si-chip with the AG disk readily submerges in the liquid.

deposition and formation of tubular graphitic carbon the underlying ZnO network is reduced to elemental Zn and removed entirely by the gas flow, resulting in a black opaque material (Figure 1A, bottom panel). An injection rate of 6 mL/h per g(ZnO) yielded sample densities of 1.0−1.2 mg/cm^3 and a Young's modulus of about 1 kPa.

Because the conversion process follows the template exactly, the resultant scaffold exhibits the same architecture and porosity. Hence, pore size and macroscopic shape of AG can be freely tailored through manipulating the template. By adjusting CVD parameters it is possible to tune filament diameter, thickness and aspect ratio and yield elastic moduli from 1 kPa up to several 100 kPa,[15] which allows for a multitude of bioengineering possibilities.[20]

AG scaffolds in this study exhibited pore sizes varying from 10 μm to about 100 μm and filaments with diameters between 0.5 and 3 μm (Figure 1B), which compares well with natural ECM.[1] Other carbon-based templates, such as graphene-foams[21] or graphene oxide scaffolds[22] lack the fibrous nature and form much larger pores. Capillary force induced restructuring of carbon nanotube-based networks, on the other hand, leads to confined cavities that are not accessible from all sides,[23] whereas AG provides interconnected pores that afford penetrability and accessibility of all surfaces. In addition, the combination of ultralightweight and negligible volume fraction may prove advantageous for cells. After initial attachment to the scaffold, ECM producing cells may restructure and remodel their environment according to their adhesion needs through deposition of natural ECM. At the same time the hierarchical architecture of AG is able to withstand strong deformations making AG networks mechanically flexible.[15]

However, the application of AG in the biomedical field is initially hampered by its superhydrophobic nature (Figure 1C). To overcome this barrier, noncovalent functionalization schemes using amphiphilic molecules can be very attractive, as they do not require elaborate chemical modification that may alter the surface composition. Moreover, as pharmaceutical products often contain surfactants, a comprehensive library of approved agents is already available. In this study, we tested

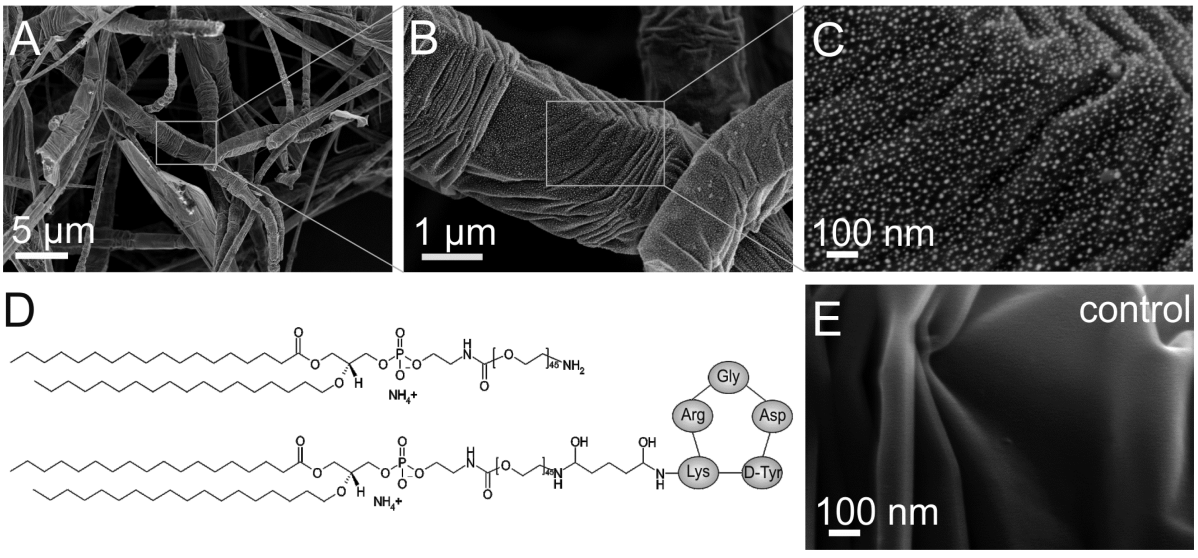

Figure 2. PEG-lipid functionalized AG was subjected to supercritical point drying followed by deposition of a thin layer of gold. (A−C) Gradual zoom-in reveals the adsorbed PEG-lipid molecules at high magnification. (D) A 4:1 mixture of amine terminated (top) and cyclic RGD peptide (cRGD) functionalized PEG-lipids (bottom) was used to promote cell attachment by integrin-mediated binding to cRGD. (E) Gold-coated pristine AG exhibits a smooth surface.

DOI: 10.1021/acsami.6b00778
ACS Appl. Mater. Interfaces 2016, 8, 14980−14985

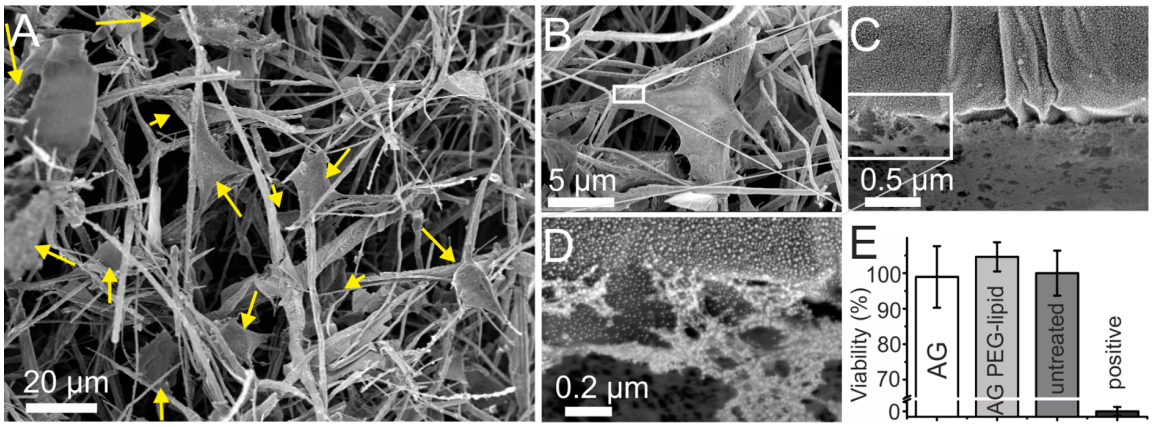

Figure 3. SEM images of REF 52 cells after 4 days of growth within cRGD functionalized AG with a 4:1 mixture of DSPE-PEG2000-NH_2/ DSPE-PEG2000-cRGD. (A) The medium sized overview scan shows growth of numerous cells (arrows) along fibers in different planes within the 3D network. (B–D) Zoom-in on the interface between cell and functionalized AG surface show a tight physical connection between cells and scaffold material. (E) Results of MTT-Formazan absorbance measurement, showing mean values of cell viability (two independent experiments, three technical repeats in each of them) and ± standard deviation for REF 52 cells treated with extracts of pristine (AG) and PEG-lipid conjugated (AG PEG-lipid) aerographite, as well as normal medium (untreated) and 15% DMSO (positive).

different agents (Supporting Information) including lipid–poly(ethylene glycol) (PEG-lipid) to improve the immersion properties of AG. In that regard the open mostly unconstrained interconnected pore space in AG should facilitate wetting of all surfaces within the bulk of the material. Amine terminated PEG conjugated phospholipid (DSPE-PEG2000-NH_2) yielded immediate and complete immersion of AG at a surfactant concentration of 1 mg/mL in distilled water (Figure 1C). PEG-lipids are widely used in medical products[24] and have been shown to successfully disperse various carbon based materials in aqueous media.[25] The hydrophobic alkyl chains of the lipid part adsorbs onto the strongly hydrophobic surface of the carbon material, whereas PEG extends into the aqueous phase to impart hydrophilicity.[24] Immersed samples were subjected to vacuum treatment to remove all air out from the bulk and ensure wetting of all surfaces.

Scanning electron microscopy (SEM) was performed to verify adsorption of PEG-lipids on the outer surface of the filaments (Figure 2). AG samples were dehydrated by super critical point drying (CPD) to avoid the destructive effect of surface tension on the network during evaporation of the liquid and a thin layer of gold was applied to improve visualization of biomolecules on the graphitic filaments. The PEG-lipids became visible at high magnification as bright dots (Figure 2B, C), and were found to decorate the surface as a dense and homogeneous monolayer of individual molecules. Control experiments with gold-coated pristine AG confirmed that the observed nanostructures were not artifacts of the coating procedure (Figure 2E).

Amine terminated PEG-lipids offer several advantages: long-chain PEG conveys inertness to the surfaces and prevents nonspecific binding of cells and proteins. The amine can be used for standard coupling of ligands, antibodies or therapeutic molecules to introduce specific functionalities, such as integrin mediated cell adhesion. Here we used cyclic RGD (cRGD) as ligand for the $\alpha_v\beta_3$ integrin in the plasma membrane of rat embryo fibroblasts (REF52). Fibroblasts were chosen in this pilot study, because this cell type synthesizes and deposits ECM to create an environment best suited to their function.[7] AG scaffolds were functionalized with a 4:1 mixture of DSPE-PEG2000-NH_2:DSPE-PEG2000-cRGD (Figure 2D). Assuming a uniform mixing of both types of PEG-lipids and taking into account a length of 9 nm for fully extended PEG2000, a ratio of 4:1 would yield a maximum spacing of integrin binding cRGD-sites of 45 nm. This is well within the range of distances that promote attachment and stable formation of focal adhesions by REF52 fibroblasts.[26]

REF52 were cultured for 4 days, then fixed with paraformaldehyde and prepared for SEM imaging by CPD. A thin layer of gold was applied for visualization of cells within the scaffolds and reduction of the destructive influence of the electron beam on biological samples. SEM images of fibroblasts near the surface of the AG bulk material (Figure 3) revealed the typical polygonal cell shape with elongated cytoplasm projections attaching to the scaffold. Images at higher magnification (Figure 3C,D) showed contact formation of the plasma membrane with the AG surface indicating the ability of cRGD functionalized AG to promote integrin mediated specific cell adhesion. The viability of cells upon exposure to pristine and DSPE-PEG2000-NH_2 functionalized AG was tested according to the norm ISO 10993, which proposes standardized conditions for biological evaluation of medical devices and materials. In particular, assay protocols outlined in parts 5 (ISO 10993–5:2009) and 12 (ISO 10993–12:2004) of this norm were applied. Briefly, REF52 cells were cultured for 24 h in extract medium that had been incubated with AG and PEG-lipid conjugated AG at 37 °C for 72 h. To determine cell viability the colorimetric MTT metabolic activity assay was used with cells incubated in untreated medium as negative control and cells incubated in 15% DMSO as positive control (Figure 3E). The results were normalized to the viability of the negative control and show neither a negative effect of functionalized AG nor pristine AG on REF 52 cells.

Next, we explored the colonization depth within AG scaffolds using inherently fluorescent REF52 cells, which express YFP-paxillin. Paxillin is mainly located in the focal contacts formed by fibroblast upon adhesion (Figure 4A). Despite the extreme low density and open porous structure, AG scaffolds are opaque and have tremendous light absorbing capacities.[15] Thus, fluorescence imaging proved most challenging and required extended illumination times of up to 5 s/frame. Optical image stacks were recorded up to a maximum penetration depth of

DOI: 10.1021/acsami.6b00778
ACS Appl. Mater. Interfaces 2016, 8, 14980–14985

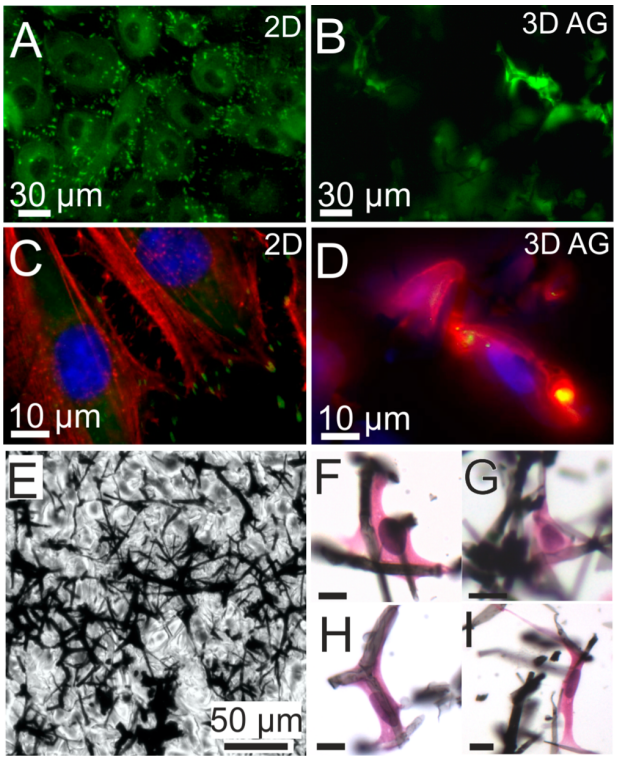

Figure 4. (A) YFP fluorescence (green) images of REF YFP-paxillin cells on a flat substrate, which have grown to a confluent layer. Bright fluorescent spots indicate focal adhesions of the cells. Intracellular homogeneous fluorescence originates in part from cytosolic paxillin. Dark circular regions indicate the area of cell nuclei. B) Optical section image approximately 100 μm from the surface. YFP-paxillin fluorescence appears to be associated with filament-like structures indicating cell growth along fibers of the scaffold. (C) Higher-magnification fluorescence image of REF YFP-paxillin cells on 2d substrate (focal adhesion sites; green) that were stained with DAPI (nuclei; blue) and RFP (stress fibers; red). (D) Optical section image approximately 50 μm from the surface, showing a mesh of actin (red) rather than stress fibers and smaller clusters of YFP-paxillin compared to the 2D substrate, which appear yellow due to overlap with red actin fluorescence. E) Bright field image of a 9 μm paraffin thin section from a position about 0.4 mm below the AG surface. Embedded in wax cells cannot be distinguished from the paraffin background. (F–I) Haematoxylin and eosin staining makes REF52 YFP Pax cells visible by coloring the nuclei blue (hematoxylin) and the cytosol pink (eosin). Due to vigorous dewaxing and staining treatment, the original AG section is highly fragmented. Nevertheless, higher-magnification reveals cells that are well-interfaced with AG filaments and illustrate morphologies typical for fibroblasts. Scale bars: 10 μm.

300 μm from the surface. Figure 4B shows an optical section image taken approximately 100 μm from the surface of an AG scaffold. In the image AG filaments are well visible as black fibers, as they absorbed all emitted light; fluorescence signals from embedded cells indicate progressive growth into the matrix. Figures 4C, D compare actin (red) and paxillin (green) distributions on 2D glass and in 3D AG. On a 2D substrate, actin assembles in stress fibers, and separate focal adhesion sites are clearly visible. In 3D, paxillin clusters are much smaller and actin forms more of a mesh. This is in agreement with previous studies that have shown that adhesion structures are quite different in 2D and 3D.[6,27−29]

Because of the obvious limitations of fluorescence microscopy due to the optical properties of AG, we prepared histological sections for bright-field microscopy. The samples were dehydrated, embedded in paraffin, and sections of 9 μm thickness were cut from the surface down to about half the sample height at 1.5 mm (see also Figure S4–S6). To visualize the embedded cells, we applied hematoxylin and eosin (HE) stain that color cell nuclei in blue and eosinophilic structures in the cytosol in shades of red and pink. AG scaffold fragments clearly show association with intact cells (Figure 4F–I). Through screening of all sections from multiple scaffolds we determined colonization depths of up to 580 μm. Higher-magnification images revealed fibroblasts of normal morphologies that were well interfaced with AG fragments (Figures 3F–L) and stretched out or spanned between adjacent filaments, in accordance with our observation from SEM.

In summary, we demonstrated the capacity of biofunctionalized AG as a novel ultra lightweight graphitic material to provide a scaffold conducive to directed three-dimensional cell growth. Cells were able to adhere, extend leading edges and elongate along the fibers of the matrix. The great advantages of AG compared to other porous 3D scaffolds are its extremely high porosity and the opportunity to tune the elastic modulus to accommodate different types of tissues.[20] Together with the material's excellent electrical properties (conductivity ~1 S/m) AG may prove very promising for applications where guidance cues and electrical conductivity within a 3D environment are vital for cell proliferation and stimulation, e.g., in cardiac tissue engineering[30,31] or regeneration of neural activity.[32] Thus, our findings commend AG with its extensive possibilities of tailoring for further investigations of other tissue engineering and bioapplications.

■ ASSOCIATED CONTENT

Supporting Information

The Supporting Information is available free of charge on the ACS Publications website at DOI: 10.1021/acsami.6b00778.

Materials and Methods, test series using different surfactants for AG immersion, additional SEM images of functionalized AG without Au coating and pristine AG with Au coating, images of paraffin embedded AG, and corresponding thin sections of three types of AG with different specific weight (PDF)

■ AUTHOR INFORMATION

Corresponding Author

*E-mail: constanze.lamprecht@jku.at.

Present Address

#C.L. is currently at Institute of Biophysics, Johannes Kepler University Linz, 4020 Linz, Austria

Author Contributions

The manuscript was written through contributions of all authors. All authors have given approval to the final version of the manuscript.

Notes

The authors declare no competing financial interest.

■ ACKNOWLEDGMENTS

This project was funded by the European Union's Framework Programme 7 (2007-2013) under the Marie Sklodowska-Curie Grant Agreement 330418. In addition, C.S. acknowledges

DOI: 10.1021/acsami.6b00778
ACS Appl. Mater. Interfaces 2016, 8, 14980−14985

funding from the European Research Council under ERC Starting Grant no. 336104. R.A., I.P., and A.S acknowledge support through German Research Foundation (DFG) grant AD 183/17-1. M.M. and K.S. received funding through the DFG SFB 986 M^3 project B1. and M.T. was supported by the Deutscher Akademischer Austauschdienst (DAAD) through a research grant for doctoral candidates (91526555-57048249). We gratefully acknowledge the help of Brook Shurtleff with English editing.

■ ABBREVIATIONS

AG, aerographite
CVD, chemical vapor deposition
CPD, super critical point drying
cRGD, cyclic RGD
DSPE-PEG2000-NH_2, 2-distearoyl-*sn*-glycero-3-phosphoethanolamine-N-[amine(PEG)2000]
ECM, extra cellular matrix
PEG, poly(ethylene glycol)
SEM, scanning electron microscopy

■ REFERENCES

(1) Alberts, B.; Johnson, A.; Lewis, J.; Raff, M.; Roberts, K.; Walter, P. The Extracellular Matrix of Animals. In *Molecular Biology of the Cell*, 4th ed.; Alberts, B, Johnson, A, Lewis, J, Raff, M, Roberts, K., Walter, P.., Eds.; Garland Science: New York, 2002; Chapter 19.
(2) Perez, R. A.; Won, J.-E.; Knowles, J. C.; Kim, H.-W. Naturally and Synthetic Smart Composite Biomaterials for Tissue Regeneration. *Adv. Drug Delivery Rev.* **2013**, *65* (4), 471−496.
(3) Lutolf, M. P.; Hubbell, J. A. Synthetic Biomaterials as Instructive Extracellular Microenvironments for Morphogenesis in Tissue Engineering. *Nat. Biotechnol.* **2005**, *23* (1), 47−55.
(4) Zorlutuna, P.; Annabi, N.; Camci-Unal, G.; Nikkhah, M.; Cha, J. M.; Nichol, J. W.; Manbachi, A.; Bae, H.; Chen, S.; Khademhosseini, A. Microfabricated Biomaterials for Engineering 3D Tissues. *Adv. Mater.* **2012**, *24* (14), 1782−1804.
(5) Bajaj, P.; Schweller, R. M.; Khademhosseini, A.; West, J. L.; Bashir, R. 3D Biofabrication Strategies for Tissue Engineering and Regenerative Medicine. *Annu. Rev. Biomed. Eng.* **2014**, *16*, 247−276.
(6) Cukierman, E.; Pankov, R.; Yamada, K. M. Cell Interactions with Three-dimensional Matrices. *Curr. Opin. Cell Biol.* **2002**, *14* (5), 633−639.
(7) Grinnell, F. Fibroblast Biology in Three-dimensional Collagen Matrices. *Trends Cell Biol.* **2003**, *13* (5), 264−269.
(8) Oberpenning, F.; Meng, J.; Yoo, J. J.; Atala, A. De Novo Reconstitution of a Functional Mammalian Urinary Bladder by Tissue Engineering. *Nat. Biotechnol.* **1999**, *17* (2), 149−155.
(9) Park, K. I.; Teng, Y. D.; Snyder, E. Y. The injured brain interacts reciprocally with neural stem cells supported by scaffolds to reconstitute lost tissue. *Nat. Biotechnol.* **2002**, *20* (11), 1111−1117.
(10) Yang, S. F.; Leong, K. F.; Du, Z. H.; Chua, C. K. The Design of Scaffolds for Use in Tissue Engineering. Part 1. Traditional Factors. *Tissue Eng.* **2001**, *7* (6), 679−689.
(11) van der Flier, A.; Sonnenberg, A. Function and Interactions of Integrins. *Cell Tissue Res.* **2001**, *305* (3), 285−298.
(12) Hersel, U.; Dahmen, C.; Kessler, H. RGD Modified Polymers: Biomaterials for Stimulated Cell Adhesion and Beyond. *Biomaterials* **2003**, *24* (24), 4385−4415.
(13) Rahmany, M. B.; Van Dyke, M. Biomimetic Approaches to Modulate Cellular Adhesion in Biomaterials: A Review. *Acta Biomater.* **2013**, *9* (3), 5431−5437.
(14) Battista, E.; Causa, F.; Lettera, V.; Panzetta, V.; Guarnieri, D.; Fusco, S.; Gentile, F.; Netti, P. A. Ligand Engagement on Material Surfaces is Discriminated by Cell Mechanosensoring. *Biomaterials* **2015**, *45*, 72−80.
(15) Mecklenburg, M.; Schuchardt, A.; Mishra, Y. K.; Kaps, S.; Adelung, R.; Lotnyk, A.; Kienle, L.; Schulte, K. Aerographite: Ultra Lightweight, Flexible Nanowall, Carbon Microtube Material with Outstanding Mechanical Performance. *Adv. Mater.* **2012**, *24* (26), 3486−3490.
(16) Schuchardt, A.; Braniste, T.; Mishra, Y. K.; Deng, M.; Mecklenburg, M.; Stevens-Kalceff, M. A.; Raevschi, S.; Schulte, K.; Kienle, L.; Adelung, R.; Tiginyanu, I. Three-dimensional Aerographite-GaN Hybrid Networks: Single Step Fabrication of Porous and Mechanically Flexible Materials for Multifunctional Applications. *Sci. Rep.* **2015**, *5*, 8839.
(17) Crapo, P. M.; Gilbert, T. W.; Badylak, S. F. An Overview of Tissue and Whole Organ Decellularization Processes. *Biomaterials* **2011**, *32* (12), 3233−3243.
(18) Sill, T. J.; von Recum, H. A. Electrospinning: Applications in Drug Delivery and Tissue Engineering. *Biomaterials* **2008**, *29* (13), 1989−2006.
(19) Mishra, Y. K.; Kaps, S.; Schuchardt, A.; Paulowicz, I.; Jin, X.; Gedamu, D.; Freitag, S.; Claus, M.; Wille, S.; Kovalev, A.; Gorb, S. N.; Adelung, R. Fabrication of Macroscopically Flexible and Highly Porous 3D Semiconductor Networks from Interpenetrating Nanostructures by a Simple Flame Transport Approach. *Part. Part. Syst. Charact.* **2013**, *30* (9), 775−783.
(20) Seidi, A.; Ramalingam, M.; Elloumi-Hannachi, I.; Ostrovidov, S.; Khademhosseini, A. Gradient biomaterials for soft-to-hard interface tissue engineering. *Acta Biomater.* **2011**, *7* (4), 1441−51.
(21) Li, N.; Zhang, Q.; Gao, S.; Song, Q.; Huang, R.; Wang, L.; Liu, L.; Dai, J.; Tang, M.; Cheng, G. Three-dimensional Graphene Foam as a Biocompatible and Conductive Scaffold for Neural Stem Cells. *Sci. Rep.* **2013**, *3*, 1604.
(22) Serrano, M. C.; Patino, J.; Garcia-Rama, C.; Ferrer, M. L.; Fierro, J. L. G.; Tamayo, A.; Collazos-Castro, J. E.; del Monte, F.; Gutierrez, M. C. 3D Free-standing Porous Scaffolds Made of Graphene Oxide as Substrates for Neural Cell Growth. *J. Mater. Chem. B* **2014**, *2* (34), 5698−5706.
(23) Correa-Duarte, M. A.; Wagner, N.; Rojas-Chapana, J.; Morsczeck, C.; Thie, M.; Giersig, M. Fabrication and Biocompatibility of Carbon Nanotube-based 3D Networks as Scaffolds for Cell Seeding and Growth. *Nano Lett.* **2004**, *4* (11), 2233−2236.
(24) Knop, K.; Hoogenboom, R.; Fischer, D.; Schubert, U. S. Poly(ethylene glycol) in Drug Delivery: Pros and Cons as Well as Potential Alternatives. *Angew. Chem., Int. Ed.* **2010**, *49* (36), 6288−6308.
(25) Yang, M.; Wada, M.; Zhang, M.; Kostarelos, K.; Yuge, R.; Iijima, S.; Masuda, M.; Yudasaka, M. A High Poly(ethylene glycol) Density on Graphene Nanomaterials Reduces the Detachment of Lipid−poly(ethylene glycol) and Macrophage Uptake. *Acta Biomater.* **2013**, *9* (1), 4744−4753.
(26) Cavalcanti-Adam, E. A.; Volberg, T.; Micoulet, A.; Kessler, H.; Geiger, B.; Spatz, J. P. Cell Spreading and Focal Adhesion Dynamics are Regulated by Spacing of Integrin Ligands. *Biophys. J.* **2007**, *92* (8), 2964−2974.
(27) Baker, B. M.; Chen, C. S. Deconstructing the third dimension - how 3D culture microenvironments alter cellular cues. *J. Cell Sci.* **2012**, *125* (13), 3015−3024.
(28) Cukierman, E.; Pankov, R.; Stevens, D. R.; Yamada, K. M. Taking cell-matrix adhesions to the third dimension. *Science* **2001**, *294* (5547), 1708−12.
(29) Kubow, K. E.; Horwitz, A. R. Reducing background fluorescence reveals adhesions in 3D matrices (vol 13, pg 3, 2011). *Nat. Cell Biol.* **2012**, *14* (12), 1344.
(30) Dvir, T.; Timko, B. P.; Brigham, M. D.; Naik, S. R.; Karajanagi, S. S.; Levy, O.; Jin, H. W.; Parker, K. K.; Langer, R.; Kohane, D. S. Nanowired Three-dimensional Cardiac Patches. *Nat. Nanotechnol.* **2011**, *6* (11), 720−725.
(31) Ganji, Y.; Li, Q.; Quabius, E. S.; Böttner, M.; Selhuber-Unkel, C.; Kasra, M. Cardiomyocyte Behavior on Biodegradable Polyurethane/Gold Nanocomposite Scaffolds Under Electrical Stimulation. *Mater. Sci. Eng., C* **2016**, *59*, 10−18.
(32) Fabbro, A.; Villari, A.; Laishram, J.; Scaini, D.; Toma, F. M.; Turco, A.; Prato, M.; Ballerini, L. Spinal Cord Explants Use Carbon

DOI: 10.1021/acsami.6b00778
ACS Appl. Mater. Interfaces 2016, 8, 14980−14985

Nanotube Interfaces To Enhance Neurite Outgrowth and To Fortify Synaptic Inputs. *ACS Nano* **2012**, *6* (3), 2041−2055.

DOI: 10.1021/acsami.6b00778
ACS Appl. Mater. Interfaces 2016, 8, 14980−14985

The Supporting Information is available in Appendix-B

Chapter 4

Biomimetic carbon-fiber systems engineering : A modular design strategy to generate biofunctional composites from graphene and carbon nanofibers

Mohammadreza Taale, Fabian Schütt, Tian Carey, Janik Marx, Yogendra Kumar Mishra, Norbert Stock, Bodo Fiedler, Felice Torrisi, Rainer Adelung, Christine Selhuber-Unkel

ACS APPLIED MATERIALS & INTERFACES

Research Article

Cite This: ACS Appl. Mater. Interfaces XXXX, XXX, XXX−XXX

www.acsami.org

Biomimetic Carbon Fiber Systems Engineering: A Modular Design Strategy To Generate Biofunctional Composites from Graphene and Carbon Nanofibers

Mohammadreza Taale,[†] Fabian Schütt,[‡] Tian Carey,[§] Janik Marx,[∥] Yogendra Kumar Mishra,[‡] Norbert Stock,[⊥] Bodo Fiedler,[∥] Felice Torrisi,[§] Rainer Adelung,[‡] and Christine Selhuber-Unkel*[,†]

[†]Biocompatible Nanomaterials, Institute for Materials Science and [‡]Functional Nanomaterials, Institute for Materials Science, Kiel University, Kaiserstraße 2, D-24143 Kiel, Germany

[§]Cambridge Graphene Centre, University of Cambridge, 9 JJ Thomson Avenue, Cambridge CB3 0FA, U.K.

[∥]Institute of Polymer and Composites, Hamburg University of Technology, Denickestraße 15, D-21073 Hamburg, Germany

[⊥]Institute of Inorganic Chemistry, Kiel University, Max-Eyth Straße 2, D-24118 Kiel, Germany

Supporting Information

ABSTRACT: Carbon-based fibrous scaffolds are highly attractive for all biomaterial applications that require electrical conductivity. It is additionally advantageous if such materials resembled the structural and biochemical features of the natural extracellular environment. Here, we show a novel modular design strategy to engineer biomimetic carbon fiber-based scaffolds. Highly porous ceramic zinc oxide (ZnO) microstructures serve as three-dimensional (3D) sacrificial templates and are infiltrated with carbon nanotubes (CNTs) or graphene dispersions. Once the CNTs and graphene coat the ZnO template, the ZnO is either removed by hydrolysis or converted into carbon by chemical vapor deposition. The resulting 3D carbon scaffolds are both hierarchically ordered and free-standing. The properties of the microfibrous scaffolds were tailored with a high porosity (up to 93%), a high Young's modulus (ca. 0.027−22 MPa), and an electrical conductivity of ca. 0.1−330 S/m, as well as different surface compositions. Cell viability, fibroblast proliferation rate and protein adsorption rate assays have shown that the generated scaffolds are biocompatible and have a high protein adsorption capacity (up to 77.32 ± 6.95 mg/cm^3) so that they are able to resemble the extracellular matrix not only structurally but also biochemically. The scaffolds also allow for the successful growth and adhesion of fibroblast cells, showing that we provide a novel, highly scalable modular design strategy to generate biocompatible carbon fiber systems that mimic the extracellular matrix with the additional feature of conductivity.

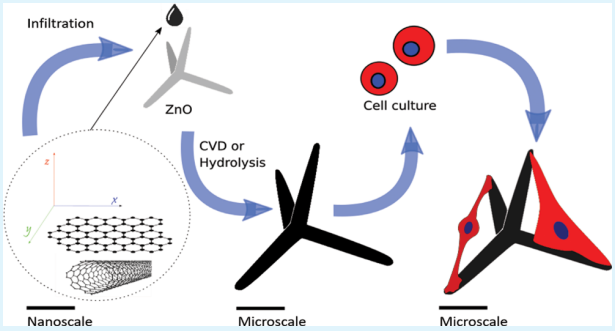

KEYWORDS: *tissue engineering, CNT, graphene, aerographite, ZnO, three-dimensional scaffold, cell adhesion*

1. INTRODUCTION

Regenerative medicine aims at developing microenvironments for the regrowth of damaged or dysfunctional tissue and organs. New promising strategies of regenerative medicine make use of biomaterial scaffolds that resemble the chemical composition,[1] the topographical structure, and the three-dimensional (3D) micro- and nanoenvironments of extracellular matrix (ECM).[2] The ECM consists of interwoven protein fibers, such as collagens, in different ranges of diameters varying from a few (<5 nm) up to several hundred nanometers for bundled collagen fibrils.[3] The chemical, structural, and mechanical features of the ECM significantly control cell migration, as well as tissue development and maintenance[4] such that finding novel ways to mimic the ECM is a highly important task in biomaterials science. As the diameter (<5 nm) and length (<500 nm) of unbundled collagen fibrils are in the range of those of carbon nanotubes (CNTs),[3] CNTs present an interesting substitute for collagen fibrils.

A general goal of artificially fabricated biomaterial scaffolds is to promote cells to differentiate and proliferate in three dimensions so that they fulfill their functions in the artificial tissue and integrate well after implantation.[5] Particularly, the microstructure and porosity of a scaffold are the key to achieve spatially organized cell growth, besides the induction of specific biological functions in the regenerated tissue. Tailoring pore size, shape, and interconnectivity of a scaffold ensures that cell migration, as well as oxygen and nutrient contribution are similar to the conditions of natural tissues.[6] Often, a large pore size in

Received: October 11, 2018
Accepted: January 2, 2019
Published: January 2, 2019

DOI: 10.1021/acsami.8b17627
ACS Appl. Mater. Interfaces XXXX, XXX, XXX−XXX

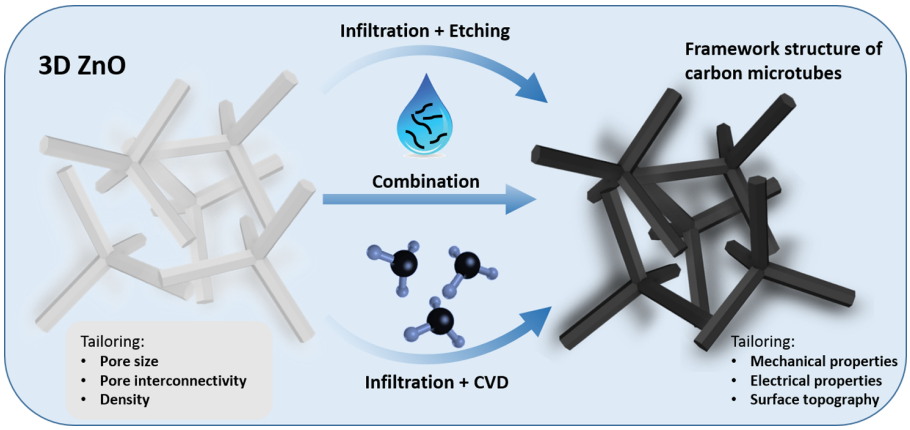

Figure 1. Schematic illustration of different 3D carbon tube structures. The highly porous ZnO template can be either infiltrated with a nanoparticle dispersion (e.g., graphene, CNT) leading to a homogeneous coating around the tetrapodal particles or converted to a graphitic structure using a chemical vapor deposition (CVD) process (aerographite). The combination of both processes leads to a modular design strategy, especially in terms of conductivity, mechanical stiffness, and surface topography.

the range of a few micrometers supports cell migration and ensures the transport of nutrition and waste products.[7]

In neural implants and heart tissue engineering, the electrical conductivity of a scaffold material is often a further requirement necessary for cellular signaling and function.[8] For example, conductivities of 0.03−0.6 S/m have been reported for cardiac muscles.[9] Carbon-based nanomaterials can in principle fulfill such requirements for 3D assemblies.[10,11] CNTs have a high electrical conductivity (up to 67 000 S/cm)[12] and chemical stability (e.g., against acids);[13] while graphene (G) offers high surface area (2630 m^2/g)[14] and high electrical conductivity (10^7−10^8 S/m).[15] Both CNTs and graphene have attracted significant attention in biomedical applications, ranging from biosensors[16] and drug/gene delivery[17] to targeted bioimaging.[17] In addition, compared to other carbon-based nanomaterials, the high physical aspect ratio of CNTs (up to 3750 length/diameter) and graphene provides a sufficient surface area for the attachment of adhesion ligands and cells.[14,18] Regarding neural tissue engineering, 3D graphene foams[19] and graphene films[18] have contributed to enhance neural stem cell differentiation toward astrocytes and neurons.[20]

An important requirement for such carbon-containing scaffolds is biocompatibility. The biocompatibility of CNTs depends on the concentration of CNTs,[21] their degree of purification, synthesis method,[22] aspect ratio, diameter and number of CNT walls,[23] and their surface functionalization.[24] Although many studies have proven the feasibility of CNTs as biocompatible material,[25] the cytotoxicity of CNTs is still a concern due to residual metal catalysts, amorphous carbon, and CNT aggregation that can occur within the cell.[26] In contrast, graphene has been reported to be biocompatible and is readily applicable for a variety of biological applications, including the use of neuronal cells,[18] cardiomyocytes,[27] and osteoblast[28] cells. Graphene oxide (GO) is an interesting graphene derivative, as it consists of a single atomic carbon layer decorated with hydrophilic functional groups such as carboxylic acid, hydroxyl, and epoxide.[29] In particular, GO has shown a strong tendency to interact with peptides and proteins via physical or chemical bonds.[30] Therefore, graphene and GO have great potential in biomedical applications as they can easily be converted into biofunctional, peptide- or protein-coated surfaces. Moreover, carbon microtube materials, specifically aerographite (AG), are of further interest as biomaterials due to their electrical conductivity (0.2−0.8 S/m)[31] and highly porous (up to 99.99%)[32] 3D interconnected network. A recent study has demonstrated the feasibility of AG as a suitable 3D matrix for cell migration and proliferation.[33] However, a clear pathway to generate a highly porous biocompatible ECM-mimetic scaffold with tunable porosity, electrical conductivity, and suitable mechanics for biomedical applications has so far been missing.

Here we demonstrate a novel modular design strategy to generate hierarchically structured carbon-based, microfibrous scaffold materials with adjustable electrical and mechanical properties that mimic the structure of the extracellular matrix. The materials investigated here are biocompatible, support cell proliferation and adhesion, and open the gateway to future biomaterial development, where biocompatibility and electrical conductivity are vital for cell proliferation and stimulation.

2. RESULTS AND DISCUSSION

2.1. Novel Types of Graphitic Scaffolds by CNT and Graphene Infiltration. Different types of fibrous 3D carbon scaffolds have been prepared based on our modular template-mediated method. Figure 1 shows the modular design strategy of our fabrication method. The fabrication uses presintered highly porous (porosity > 93%) ceramic ZnO templates as a sacrificial material.[32] These ZnO templates themselves consist of interconnected tetrapod-shaped ZnO particles. Representative scanning electron microscopy (SEM) images of the ZnO templates are shown in the Supporting Information Figure S2. The highly porous ZnO templates have an interstitial space of approximately 10−100 μm between ZnO filaments, which in turn have diameters between 0.5 and 5 μm. Therefore, the spatial geometry and organization of the microtube-shaped structures of the ZnO template are comparable to that of the ECM.[34]

The coating of ZnO templates with carbon nanomaterials (e.g., CNTs, graphene) is performed via a simple process to infiltrate the entire 3D template with a CNT dispersion as described by Schütt et al.[35] In addition, here we demonstrate that the feasibility of this technique can be extended also to graphene dispersions. The infiltration process relies on the superhydrophilicity of the ZnO template,[36] which is a direct result of the combination of the hydrophilic character of the

DOI: 10.1021/acsami.8b17627
ACS Appl. Mater. Interfaces XXXX, XXX, XXX−XXX

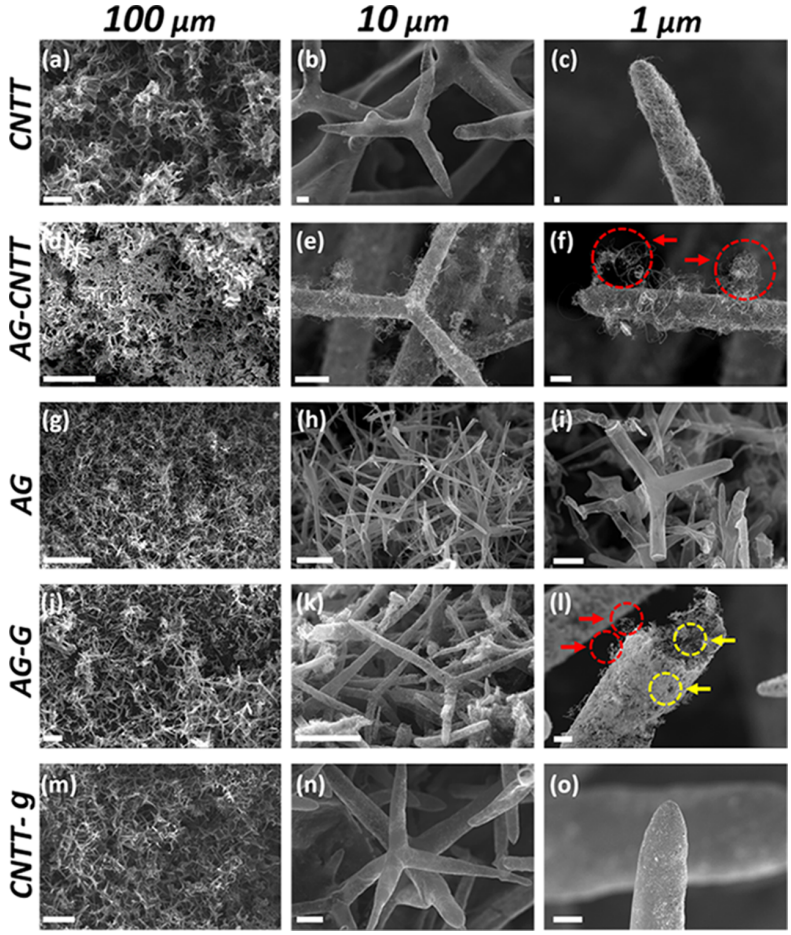

Figure 2. SEM images from low to high magnification of the different 3D carbon structures. (a–c) Carbon nanotube tubes (CNTTs), (d–f) aerographite with incorporated CNTs (AG–CNTT) (the red arrows show the grown CNTs during the CVD process), (g–i) aerographite (AG), (j–l) aerographite with incorporated graphene (AG–G) (the yellow arrows point to nanopores on the surface of aerographite), and (m–o) carbon nanotube tubes incorporated into a thick carbon layer (CNTT–g).

individual tetrapod-shaped ZnO microparticles and the high porosity (>93%) of the template. During water evaporation, the nanomaterials form a widely homogeneous coverage[35] around the ZnO microrods (Supporting Information Figures S3 and S4). The amounts of CNTs and graphene flakes covering the ZnO template can be controlled by cyclically repeating the infiltration process several times (Supporting Information, Figures S3 and S4). SEM images revealed that the infiltrated CNTs form a layer made of self-entangled CNTs around the ZnO network (Supporting Information Figure S4). Similarly to CNTs, a dispersion of graphene flakes also forms a homogeneous layer around the ZnO (Supporting Information Figure S3).

To generate freestanding scaffolds from the ZnO templates after coating them with carbon nanomaterials, the ZnO must be carefully removed. We have used three different processes to remove the sacrificial ZnO network after infiltration (Figure 1): (i) hydrolyzing the sacrificial ZnO template by a HCl solution[35] (Supporting Information Figure S5a), (ii) converting the ZnO template via a CVD process[31] (Supporting Information Figure S5b,c), and (iii) using a carbothermal reduction process[37] in combination with glucose (g) as a carbon source. Each of these processes leads to a specific type of carbon-based scaffold. Therefore, the results of these processes (Supporting Information Figure S5) are discussed in the following sections.

2.2. Freestanding Carbon Nanotube Network (CNTT) Scaffolds from Hydrolysis of the Sacrificial ZnO Template by HCl. When HCl is used to dissolve the ZnO in CNT-coated ZnO templates, hierarchically structured CNTT scaffolds are formed. These structures consist of interconnected hollow tubes, which are composed of self-entangled CNT networks, as reported previously.[35] SEM images of the resulting CNTT scaffolds are presented in Figure 2a–c. The presented structures demonstrate a hierarchical architecture, where the porous scaffold are composed of microtetrapods (Figure 2a,b), which in turn consist of nanoscale CNTs (Figure 2c). The HCl-based ZnO dissolution can only be applied for templates infiltrated with CNTs. Templates infiltrated with graphene only led to collapsing structures (data not shown), presumably as the graphene flakes cannot interweave.

2.3. ZnO Conversion to AG via CVD Forms Composites with Embedded Nanoparticles. We also use a CVD process to remove the ZnO, resulting in a thin (~15 nm) film of graphite around the entire template similar to the graphitic shells in AG.[31] The CVD process can be applied if the ZnO is coated with either CNTs or graphene (Supporting Information Figure S6). Then, the AG serves as an additional backbone. This is the case in all of

DOI: 10.1021/acsami.8b17627
ACS Appl. Mater. Interfaces XXXX, XXX, XXX–XXX

our CVD-based scaffolds, i.e., in composites of graphene and aerographite (AG−G) and in composites of multiwalled CNTs and aerographite (AG−CNTT) (Figure 2d−l). The modular design of the fabrication process allows us to change and tailor the surface topography of the hollow graphitic microtubes. Up to 5 μm long CNTs are formed perpendicular to the surface of microtubes on AG−G and AG−CNTT during the CVD process (Figure 2f). Such CNTs are not formed on pure AG (Figure 2i).[31] The growth of new carbon nanotubes on AG−G networks (Figure 2l, red arrows) is most likely attributed to the adsorption of carbon atom clusters on the active sites of the graphene surface during the CVD process.[38]

2.4. Carbothermal Reduction Process Leads to Novel Types of Graphitic Structures with Embedded CNTs. In the carbothermal reduction reaction,[37] glucose acts as the carbon source enabling the reduction of ZnO in a quartz tube furnace at 950 °C under argon atmosphere. To do so, ZnO templates were infiltrated with a mixture of glucose and CNTs. The carbothermal reduction of ZnO to Zn(g)[37] leads to ZnO removal and to the formation of graphitic shells, thus resulting in the so-called CNTT−g structure (Figure 2m−o). We have confirmed the removal of ZnO by Raman spectroscopy (Figure 3, CNTT−g graph) (see next paragraph). Furthermore, this

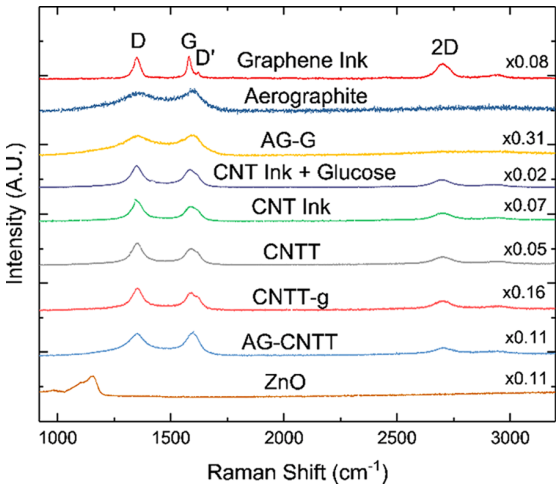

Figure 3. Raman spectroscopy of aerographite, ZnO, CNTT, AG−CNTT, CNTT−g, AG−G, graphene, and CNT inks.

process results in a scaffold with a microstructure that is comparable to that of the AG−CNTT scaffold (Figure 2e,n). However, the graphitic shells of the CNTT−g scaffold appear to be thicker than those of the AG−CNTT scaffold (Figure 2n,o). Additionally, in contrast to the AG−CNTT structures, no additional CNTs are grown (Figure 2n) in the CNTT−g case.

Figure 3 shows Raman spectra (Renishaw 1000 InVia) of all of the carbon-based structures. Raman spectroscopy is used to examine the structural fingerprint of each material at a wavelength of 514.5 nm with an incident power of ∼0.1 mW. The graphene and CNT inks were drop-cast onto Si/SiO_2 substrates before measurement. For the graphene ink (red curve), the G peak (∼1586) corresponds to the E_{2g} phonon at the Brillouin zone center, and the D peak located at ∼1350 cm^{-1} corresponds to the breathing modes of the sp^2 carbon atoms and requires a defect for its activation.[39] Our graphene inks are produced by liquid-phase exfoliation; therefore we attribute this peak to edge defects rather than to defects in the basal plane.[40] The two-dimensional (2D) peak located at ∼2700 cm^{-1} is the D peak overtone and can be fitted by a single Lorentzian, indicating electronically decoupled graphene monolayers.[41]

The aerographite (dark blue curve) shows a G peak position Pos(G) ∼ 1600 cm^{-1} and the absence of a distinct 2D peak, indicating the more defective nature of this sample and a lack of structural order in the aerographite.[42] The AG−G (yellow curve) structure has a similar spectrum to that of aerographite with D and G peaks located at ∼1350 and ∼1600 cm^{-1}, respectively, indicating that the material is mostly composed of aerographite and graphene, given the selective etching of the ZnO scaffold during the CVD reduction.[31] The spectra of the CNT ink (green curve) and CNT ink with glucose (purple curve) show D, G, and 2D peaks at ∼1350, ∼1580, and ∼2700 cm^{-1}, respectively. The peaks from the glucose residue are too weak to be observed. Moreover, the CNTT spectra (gray curve), AG−CNTT (blue curve), and CNTT−g (pink curve) have D, G, and 2D peaks that demonstrate the presence of the CNTs, respectively. Finally, the ZnO spectra (brown curve) display several peaks below 1200 cm^{-1}, predominately created from the intense peak at 1158 cm^{-1} attributed to the $2A_1(LO)$ and $2E_1(LO)$ modes at the Brillouin zone center.[43] However, no peaks attributed to ZnO are observed in any of the CNTTs or aerographite scaffolds, proving the complete removal of the ZnO template.

2.5. Scaffold Mechanics can be Tailored Over Several Orders of Magnitudes. Figure 4 shows Young's moduli and

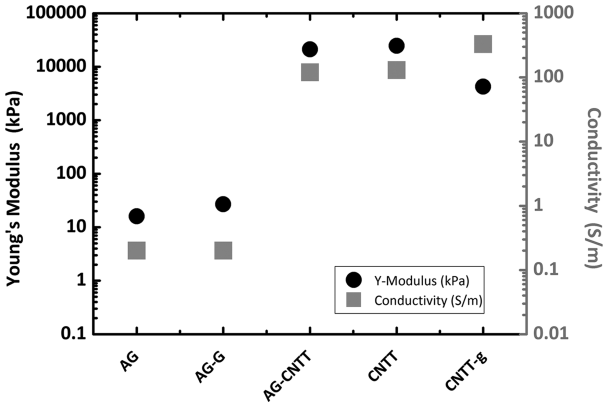

Figure 4. Young's modulus (measured under compression) and electrical conductivity of the 3D CNTT, AG−CNTT, CNTT−g, and AG−G scaffolds. All structures containing CNTs have a higher Young's modulus and conductivity compared to those without CNTs. The values for pure AG and CNTTs were taken from the corresponding publications,[31,35] whereas the other values were measured using a self-built electromechanical testing setup.

electrical conductivities of CNTT, AG−CNTT, CNTT−g, AG, and AG−G. The scaffold with the lowest stiffness is AG with a Young's modulus of 16 kPa, which is comparable to previously reported values.[31] AG−G has a Young's modulus of up to 27 kPa, thus adding graphene into the graphitic shells of AG results in a mechanical reinforcement of the scaffold (∼170%). This reinforcement is in a similar range to that of other graphene-reinforced porous networks, e.g., graphene/chitosan composites[44] (∼200%). In contrast to AG−G, AG−CNTT is much stiffer (Figure 4), with Young's modulus reaching ∼22 MPa.

This reinforcement by a factor of about 1000 is presumably due to the reinforcement of CNTs on the nanoscale by self-

DOI: 10.1021/acsami.8b17627
ACS Appl. Mater. Interfaces XXXX, XXX, XXX−XXX

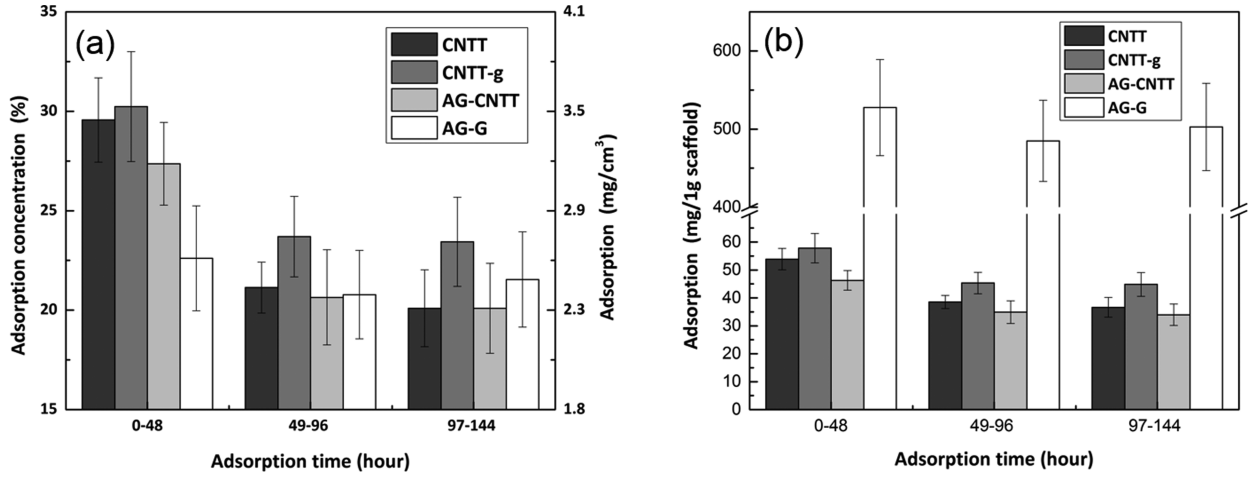

Figure 5. Protein adsorption on CNTT, AG−CNTT, CNTT−g, and AG−G during 0−48, 49−96, and 97−144 h of incubation with albumin solution (1 mg/mL). (a) Absolute protein adsorption amount per scaffold volume. (b) Absolute protein adsorption amount per scaffold weight.

Table 1. Full Names and Abbreviations of Fabricated Materials and Scaffolds in Our Study

full name	abbreviation	density (g/cm^3)	porosity (%)
aerographite	AG	~200 × 10^{-6} [31]	up to ~99.9[31]
carbon nanotube tube	CNTT	~0.064	~94
carbon nanotube tube−glucose	CNTT−g	~0.061	~90
aerographite−carbon nanotube tube	AG−CNTT	~0.069	~95
aerographite−graphene	AG−G	~0.005	~96

entanglement.[35] Hence, the mechanical reinforcement of AG by CNTs is higher than in other CNT-reinforced porous biomaterials, including gelatin methacrylate (GelMA)−CNT composites[45] and poly(propylenefumarate)−CNT composites.[46] Young's modulus of CNTT−g (~4 MPa) is in between the moduli of AG−G and AG−CNTT. These results confirm that the incorporation of CNTs and graphene into 3D scaffolds compensates for the typically low mechanical Young's moduli of porous structures[47] and that AG provides a stable backbone for CNTT scaffolds. In addition, the structural integrity of AG−G scaffolds is demonstrated during a long-cycle compression test (Figure S7) (Supporting Information Video S1).

2.6. Tailoring Scaffold Conductivity. We also investigated the electrical properties of our scaffolds (Figure 4, gray squares). AG−G and AG have similar electrical conductivities of around 0.5 and 0.2 S/m, whereas the conductivities of AG−CNTT and CNTT−g are about 120 and 130 S/m, respectively (Figure 4). Hence, AG−CNTT and CNTT−g clearly have higher electrical conductivities than CNT-containing electrospun fibrous composites (3.5 S/m),[48] which are applied in cardiac tissue engineering. The increase in conductivity of the scaffolds can be mainly attributed to the high conductivity of CNTs that are embedded in the graphitic shells of AG. This effect is more pronounced in the case of AG−CNTT and CNTT−g, presumably as a result of the conductive pathways formed by the self-entangled CNT networks. It has already been shown that by adjusting the CNT concentration during the infiltration process, the conductivity of CNTT can be tailored between 10^{-6} and 130 S/m.[35] Indeed, CNTT−g has the highest conductivity (330 S/m) of our scaffolds.

2.7. Scaffolds Strongly Adsorb Proteins. Albumin is an adhesive protein in plasma and can non-specifically bind to low-dimensional carbon-based materials via electrostatic interactions.[49] Therefore, we checked the albumin adsorption capacity of the scaffolds using the bicinchoninic acid (BCA) assay. As shown in Figure 5, within the first 48 h, albumin adsorption is smaller on AG−G than on AG−CNTT, whereas its adsorption is very similar on all scaffolds later on. The highest absolute protein adsorption mass (30.23−22.6 ± 2.76 mg/cm^3) was detected during the first 2 days of incubation, and the adsorption amount reduced to approximately two-thirds (23.69−20.64 ± 2.39 mg/cm^3) during the third to fourth day of incubation. Overall, protein adsorption is very similar on all tested scaffolds, although CNTT, CNTT−g, and AG−CNTT scaffolds adsorb slightly higher protein amounts (CNTT−g: 77.32 ± 6.95 mg/cm^3; CNTT: 70.77 ± 5.33 mg/cm^3; AG−CNTT: 68.08 ± 6.73 mg/cm^3) than AG−G (64.92 ± 7.2 mg/cm^3) (Figure 5a). This might be attributed to the higher protein adsorption capacity of CNTs than graphene flakes due to van der Waals forces and electrostatic interactions.[30]

To compare our results of protein adsorption with other studies, we needed to relate them to the weight of the scaffolds by taking into account their density (Table 1). Figure 5b shows that protein adsorption per weight of CNTT, CNTT−g, and AG−CNTT scaffolds is different for different scaffold types (CNTT−g: 147.9 ± 13.42 mg/g; CNTT: 128.9 ± 9.69 mg/g; AG−CNTT: 115.14 ± 11.38 mg/g). It is also higher than on single-walled CNTs and graphene (~100 mg/g)[30] and on nanoporous silica (~70 mg/g).[50] In addition, due to its low density, AG−G adsorbs even more protein per weight (1512.25 mg/g) after 144 h, e.g., about 10 times more than our other scaffolds. The albumin adsorption on AG−G even after 48 h (527 mg/g) is comparable to that of graphene oxide (~500 mg/g).[30]

2.8. Biocompatibility of the Carbon-Based Scaffolds. Biocompatibility of the scaffolds is investigated by methylthiazolyldiphenyl-tetrazolium bromide (MTT) metabolic activity and WST-1 assays, as well as by proliferation studies. Figure 6

DOI: 10.1021/acsami.8b17627
ACS Appl. Mater. Interfaces XXXX, XXX, XXX−XXX

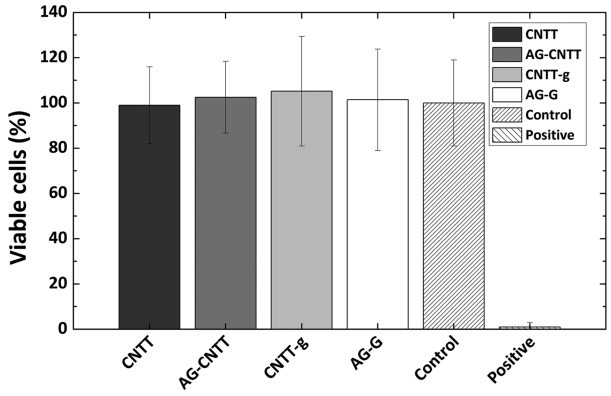

Figure 6. Percentage of viable cells (rat embryonic fibroblasts wild type, REF52wt) relative to the negative control, as determined in an MTT assay (four independent experiments, five technical repeats in each of them). The error bars denote standard deviation.

shows the results for CNTT, CNTT−g, AG−CNTT, and AG−G samples using an MTT assay, demonstrating that all scaffolds are biocompatible, hosting a similar number of viable cells as the negative control. As cell adhesion is not possible on pristine AG without functionalization,[33] biocompatibility of AG is not investigated again in this study.

Figure 7 shows the proliferation rate of rat embryonic fibroblast cells (REF52wt) cultured on CNTT, CNTT−g, AG−

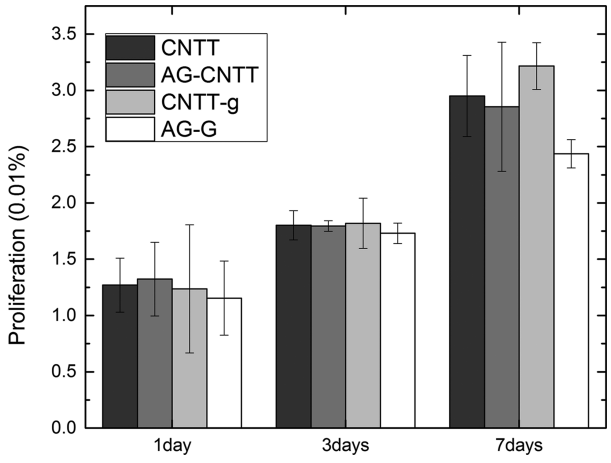

Figure 7. Results of WST-1 metabolic tests of cell proliferation rate (REF52wt). Mean values were determined from four independent experiments, each including five technical repeats. The error bars denote standard deviation, the raw data were normalized to the control, and a correction factor was applied to account for unspecific adsorption (see Materials and Methods).

CNTT, and AG−G samples relative to cells cultured on a culture dish. CNT-containing scaffolds (CNTT, CNTT−g, and AG−CNTT) lead to higher proliferation rates (ca. 300−320%) than graphene-containing structures (AG−G) (∼240%) after 7 days in culture. As fibroblast proliferation depends on matrix stiffness,[51] an increase in stiffness might also lead to an increase in fibroblast proliferation,[52] which can be attributed to the translation of mechanical cues from the matrix into a biochemical one via mechanosensory receptors such as focal adhesions.[53] Specifically, it has been reported that fibroblasts need substrates with a minimum Young's modulus of 20−30 kPa to spread and 2 MPa to spread and polarize perfectly.[51] Hence, the huge difference in Young's moduli between CNT-reinforced scaffolds (between 4 MPa in CNTT−g and 23 MPa in CNTT) and graphene-reinforced scaffolds (27 kPa in AG−G) can explain the higher proliferation rate of fibroblast cells on CNTT, AG−CNTT, and CNTT−g compared to AG−G.

2.9. Carbon-Based Scaffolds as Porous Structures for Cell Growth. Fibroblast cells (REF52wt) were cultured for 7 days on the scaffolds to investigate cellular growth at the surface and inside. SEM images of critically point-dried cells (Figure 8) revealed that cells (highlighted in green) are attached to the surface of the scaffolds. Fibroblasts do not migrate strongly within a 3D network[54] but proliferate so that we typically observe several cells at one location. Cells are sprawled and elongated between the filaments of scaffolds and have a polygonal shape on all four scaffold types. Close-up images on the adhesion sites reveal tightly anchored membranes of cells to CNTs and graphene on the surface of structures, comparable to fibroblasts on AG functionalized with cyclic arginylglycylaspartic acid (RGD) peptides.[33]

To investigate cell adhesion at the molecular level, we studied the presence of paxillin in adhesion structures. Paxillin is a component of focal adhesion clusters;[55] therefore, it can be assumed that more paxillin in contact with our scaffolds is related to stronger cell adhesion. We used cells that were stably transfected with yellow fluorescent protein (YFP)-paxillin and imaged the paxillin in fluorescence microscopy. Imaging fluorescence in 3D matrices compared to 2D is challenging.[56] Due to the low intensity of paxillin in the cells and the high light absorbance of our scaffolds,[31] imaging the paxillin adhesion sites was only possible by using long acquisition times (5 s), which resulted in background signals. Nevertheless, paxillin-containing adhesion sites can be distinguished around the filaments of the scaffolds. Based on the fluorescence images (Figures 9a−d and S8), more adhesion clusters can be detected on CNT-reinforced scaffolds than on graphene-reinforced scaffolds. This could again result from the different mechanical properties of the scaffolds, but it is also in agreement with cell studies on multiwalled CNTs showing that NIH-3T3 fibroblasts form larger adhesion clusters on CNTs than on graphene.[57]

A further important contribution to cell adhesion is the cytoskeleton, where networks of actin fibers determine cell shape and movements.[58] To investigate cellular actin networks on our scaffolds, we investigated the fluorescence of phalloidin to detect actin fibers. Again, imaging deeply inside the scaffolds was impaired by the strong light absorbance of CNTs and graphene, restricting it to the first 300 μm from the surface. As shown in Figure 9, well-developed actin fibers (in red) are indeed present within the fibroblasts. Furthermore, the cells are polarized and have oriented actin bundles. Figure 9a−c also shows that actin fibers on CNT-reinforced scaffolds (CNTT, AG−CNTT, and CNTT−g) are mainly oriented in the direction of fibroblast protrusions. Although many actin fibers can be detected in cells grown on AG−G (Figure 9d), they are neither well polarized nor elongated like the actin fibers in the cells on CNT-reinforced scaffolds (CNTT, AG−CNTT, and CNTT−g). These results could again originate from the mechanical properties of our materials, similarly to proliferation rate and paxillin clusters.

2.10. ECM-Mimetic Scaffolds. The open porous structure of our scaffolds with large free volumes (>95%) should be highly beneficial for the growth and migration of cells, as the open pores allow the cells to freely migrate and proliferate within the

DOI: 10.1021/acsami.8b17627
ACS Appl. Mater. Interfaces XXXX, XXX, XXX−XXX

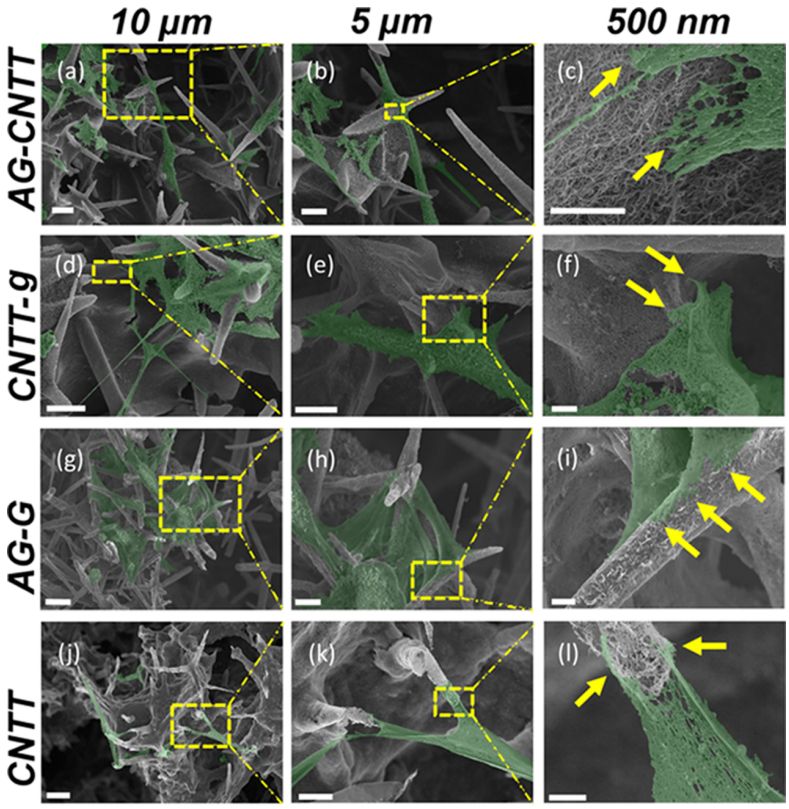

Figure 8. SEM images of REF52wt cells after 7 days of culturing within (a−c) AG−CNTT, (d, e) CNTT−g, (g−i) AG−G, and (j−l) CNTT scaffolds. Left: Medium-sized overview images illustrating the growth of cells between the fibers in different directions and planes; middle: zoomed-in images showing well-stretched cells along the fibers and their elongation; and right: close-up images on the adhesion sites, proving the presence of strong contacts between the materials and the cell membrane (yellow arrows).

scaffolds.[2] Moreover, in contrast to other studies on 3D porous structures, in which the alignment of CNTs[24] or graphene sheets[59] confined the accessibility of cavities, our carbon framework structures provide accessible interconnected pores from all sides (Figure 2). In addition, the hierarchical organization of structural elements, specifically self-entangled CNTs in the form of microtubes, is reminiscent of the hierarchical nano- and microstructure of the ECM. It should therefore in principle be possible to employ our modular design strategy to generate different composition-dependent structural and mechanical features similar to collagen[60] in the ECM. As our scaffolds strongly adsorb proteins, it should also be possible to adsorb adhesion ligands typically present in ECM proteins, such as RGD.[61] In this way, the scaffolds can be modified such that they finally mimic the ECM structurally and biochemically, but with the additional feature of conductivity.

3. CONCLUSIONS

In summary, we have introduced a novel modular design strategy to produce carbon-based scaffolds that mimic the ECM and allow 3D cellular growth. Biocompatibility studies revealed a high proliferation rate of fibroblasts as well as the ability of fibroblasts to develop paxillin-containing adhesion sites. In addition, the cells sprawl and elongate between single filaments of the scaffolds. Tuning electrical conductivity (ca. 0.1−330 S/m), stiffness (ca. 10^{-3}−0.7 MPa), and protein adsorption and porosity (up to ∼99%) of the scaffold provides great possibilities for culturing cells. Based on the proven protein adsorption capacity of the scaffolds, they are suitable for biofunctionalization and addition of other biochemical cues. This is particularly relevant in tissue engineering of electrically excitable tissue, e.g., heart tissue, as our scaffolds have tunable electrical conductivity. In addition, the fabrication procedure is very simple and can in principle be adopted to develop 3D assemblies from other low-dimensional nanomaterials (e.g., bioactive ceramic nanoparticles, polymeric nanofibers) by only changing the nanoparticle dispersion, as long as the nanoparticles are connected via strong physical contacts such as entanglement, fusion, or physical locks. This makes the scaffolds promising candidates as conductive ECM-mimetic materials in many applications from regenerative medicine to 3D cell culture.

4. MATERIALS AND METHODS

4.1. Fabrication of 3D Carbon Scaffold Materials. Templates of tetrapod-shaped ZnO were fabricated by a previously developed flame transport synthesis method.[32] The resulting loose powder was pressed into a cylindrical shape (h = 3 mm, d = 6 mm) at a density of 0.3 g/cm^3. The pellets were subsequently sintered for 5 h at 1150 °C to obtain an interconnected 3D ZnO network.[32] This structure is the sacrificial template used for fabrication of carbon-based scaffolds, i.e., free-standing CNTT, AG−CNTT, and AG−G.

For the fabrication of the CNTT scaffolds, the porous ZnO templates were infiltrated with an aqueous dispersion of multiwalled CNTs (1 wt %, CARBOBYK-9810, BYK Additives & Instruments) using a self-built computer-controlled syringe. The length of the CNTs can be on the order of a few micrometers, with diameters in the range of 20−60 nm.[34] After infiltration of ∼90 μL of the CNT solution, the samples were dried under ambient conditions for at least 1 h. The process was repeated six times so that CNTs covered the ZnO template.

DOI: 10.1021/acsami.8b17627
ACS Appl. Mater. Interfaces XXXX, XXX, XXX−XXX

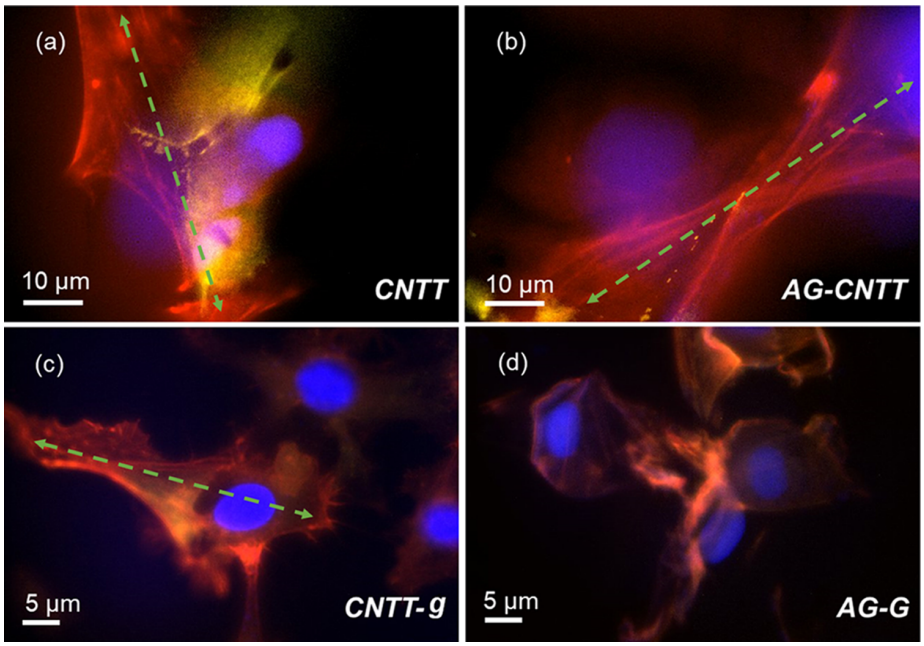

Figure 9. High-magnification fluorescence images of REF52 YFP-paxillin cells on 3D scaffolds: (a) CNTT, (b) AG−CNTT, (c) CNTT−g, and (d) AG−G. YFP-paxillin is mainly distributed in small clusters (YFP; yellow), the nucleus was stained with Hoechst (4′,6-diamidino-2-phenylindole, DAPI; blue), and actin fibers were visualized by phalloidin (red). Fluorescence imaging took place in optical sections approximately between 50 and 100 μm from the surface of the material. Adhesion sites are detectable (a, b) as tiny yellow spots mainly around the tube-shaped filaments of CNTT and AG−CNTT structures. Due to the low intensity and small size of YFP-paxillin (c, d), they are not clearly observed, which is also obscured by red (actin fibers) and blue (nucleus) channels in multichannel images. The green dashed arrows illustrate the protrusion direction of the cells.

Then, the ZnO backbone was removed by immersing the composite in a 1 M HCl solution overnight. The HCl solution was replaced by washing with pure ethanol (five times). Finally, the etched structures were dried in a critical point dryer (EMS 3000) by using the automatic mode. The purge time was set to 15 min to ensure that all ethanol was washed out, leaving freestanding CNTTs.[3]

To alter the CNTT structures further, we added glucose (1 wt %) to the CNT ink used for infiltration. The infiltration into a ZnO template was then repeated four times. After that, the samples were transferred into a quartz tube furnace and heated to 950 °C under argon atmosphere for 2 h. During this process, the ZnO was removed by carbothermal reduction,[45] leading to CNTT−g, which contains both the remnants of the glucose and embedded CNTs.

For the synthesis of AG−CNTT scaffolds, the CNT-coated ZnO templates were exposed to a CVD process, as reported previously.[31] Briefly, the ZnO template was replicated into aerographite at ∼760 °C under a hydrogen and argon atmosphere in the presence of toluene as the source of carbon.[62] Thereby, the CNTs were embedded into the graphite microtubes of aerographite while the ZnO was simultaneously etched by H_2.

A similar process was used to generate composites of graphene and aerographite (AG−G). The graphene ink was made by dispersing graphite flakes (12 mg/mL, Sigma-Aldrich No. 332461) and Triton X-100 stabilization agent (1.7 mg/mL) in deionized water, followed by sonication (Fisherbrand FB15069, Max power 800 W) for 9 h.[63,64] The dispersion was then centrifuged (Sorvall WX100 mounting a TH-641 swinging bucket rotor) at 5k rpm for 1 h to remove the thick flakes. The supernatant (i.e., the top 70%) of the dispersion was then decanted to produce the final graphene ink. In Figure S1, optical absorption spectroscopy (Cary 7000) is used to estimate the flake concentration.[65] The flake concentration in the graphene ink is obtained via the Beer−Lambert law, which links the absorbance $A = \alpha c l$ with the beam path length l (m), the flake concentration c (g/L), and the absorption coefficient α (L/(g m)). The graphene ink was diluted 1:20 with water/Triton X-100. An absorption coefficient of $\alpha \sim 1390$ L/(g m) for the graphene ink at 660 nm was utilized,[66] estimating a graphene flake concentration of ∼0.09 mg/mL, consistent with previous reports of graphene-based inks.[40,67] The spectrum of the graphene ink is mostly featureless due to the linear dispersion of the Dirac electrons, while the peak in the UV region is a signature of the van Hove singularity in the graphene density of states.[68] The ZnO scaffold was infiltrated 50 times to achieve coverage of graphene around the ZnO tetrapods, due to the low concentration of the ink (0.09 mg/mL). After infiltration, the CVD process (see process specification above) was used to embed the graphene flakes into aerographite microtubes and to remove the ZnO template.

4.2. Mechanical and Electrical Characterizations of 3D Carbon Scaffold Materials. Mechanical and electrical characterizations were performed using a self-built setup consisting of a Maerzhaeuser Wetzlar HS 6.3 micromanipulator, which is driven by a stepper motor, a Kern PLE 310-3N precision balance, and a Keithley 6400 source meter. A self-written LabView program controls all components. To avoid any vibration damping, the whole setup is located on a very rigid aluminum plate in a box filled with sand, which is mounted on a vibration-isolated table. Stress−strain curves were measured by placing the sample in between the micromanipulator and the precision balance. For compression tests, the micromanipulator deforms the sample by a user-defined step size. After each step, the program measures the force of the balance after a short settling time has been elapsed. These steps are repeated until the maximum deformation defined by the user is reached. Afterwards, the direction of the deformation is inverted until the micromanipulator comes back to its original position. Finally, the stress−strain curves are evaluated and Young's modulus is determined. With respect to the cyclic compression test, the same procedure was repeated several times. The wait time between each compression step was set to 0 s, and the deformation speed was set to 40 μm/s. To demonstrate the structural integrity, a video was recorded during the long-cycle compression test with a USB camera. Furthermore, the same setup also allows to record the current−voltage characteristics using a Keithley 6400 source meter in the four-wire sense mode. For electrical measurements, the carbon structures were connected to thin copper plates on both sides by using conductive

DOI: 10.1021/acsami.8b17627
ACS Appl. Mater. Interfaces XXXX, XXX, XXX−XXX

silver paste. It is noteworthy that only a thin layer of paste was needed to ensure good electrical connection of the porous material to the measurement setup. Current−voltage curves were measured in a voltage range of up to 5 V. Finally, the resistance was calculated from the obtained data and converted to conductivity to give meaningful values for each structure.

4.3. Cell Culture and Cell Seeding on Scaffolds. Rat embryonic fibroblasts (REF52), both as wild type and stably transfected with YFP-paxillin (REF YFP-Pax),[69] were cultured in Dulbecco's modification of Eagle medium (Biochrom, Germany) at 37 °C, 5% CO_2 at ∼90% humidity. The medium was supplemented with 10% fetal bovine serum (Biochrom, Germany) and 1% penicillin/streptomycin (Sigma-Aldrich, Germany). To expel any traces of remaining zinc from the scaffold fabrication process prior to cell experiments, all samples were immersed in culture medium for 14 days after autoclaving at 121 °C. Shortly before the cell experiments, the cells were immersed in a fresh culture medium, counted with a cell counter (Scepter, Merck Millipore, Germany), and ∼20 000 cells were seeded on each scaffold in 24-well plates. The cells were incubated on the scaffolds for 1, 3, or 7 days.

4.4. Cell Staining. To investigate the cell morphology, proliferation, and adhesion on the scaffolds, cell nuclei were stained with DAPI (Thermo Fisher, Germany), and actin stress fibers were stained with phalloidin (Alexa Fluor 647 phalloidin, Thermo Fisher, Germany). Imaging was carried out using fluorescence microscopy (IX81, Olympus, Germany), and images were processed with cellSens Dimension (Olympus, Germany). For electron microscopy investigations, the cells were fixed by paraformaldehyde (Thermo Fisher, Germany) and dried using critical point drying (EMS 3000). A thin layer of gold was sputtered (Bal-Tec SCD 050, 30 mA, 30 s) onto the sample prior to scanning electron microscopy (SEM) (Ultra Plus Zeiss SEM, 5 kV). The cells in SEM images were highlighted in green (via Adobe Photoshop CC 2017) to distinguish them more easily.

4.5. Viability and Proliferation Assay. The number of living cells on the scaffolds was quantified by a WST-1 proliferation assay after 1, 3, and 7 days of incubation. In this assay, the number of living cells can be acquired from the amount of dye produced via bioreduction of stable tetrazolium salt WST-1 (Sigma-Aldrich, Germany). The amount of formazan is proportional to the number of cells (Cell Proliferation Reagent WST-1 Protocol, Sigma-Aldrich, Germany). The experiments were carried out as follows: After seeding the cells onto each sample (see specification above), the scaffolds were first washed with phosphate buffered saline and then incubated with a WST-1-containing medium for 4 h. The concentration of the formazan dye was quantified by a multiwell spectrophotometer (Bio-Tek μQuant) after removal of the samples from the wells. CNTs tend to react with tetrazolium salts;[70] thus, the proliferation rates were normalized to the absorption of the detected tetrazolium on control samples without cells. The amount of tetrazolium reacting with the scaffolds was determined for each sample as explained in the following: 10 000 cells were cultured for 24 h in 96-well plates prior to adding scaffolds to half of the wells, with the other half serving as scaffold-free control. Then, all of the wells were incubated for an additional time of 4 h with the WST-1 reagent before quantification of the formazan (i.e., product of tetrazolium cell reaction) amount in each well by a multiwell spectrophotometer. The amount of tetrazolium that reacted with the scaffold was calculated for each specimen by subtracting the amount of formazan of scaffold-containing wells from scaffold-free control wells. The difference in absorbance between the scaffolds and controls was used as a correction factor for the data generated with the WST-1 assay.

In addition, the viability of cells was tested according to the ISO 10993 norm. Briefly, 10 000 cells/100 μL REF52 cells were cultured in a 96-well plate for 24 h. For medium extraction, the scaffolds were incubated in a culture medium at 37 °C for 72 h. The cultured cells were incubated with either untreated medium or extracted medium for a further 24 h. To determine cell viability, the colorimetric methylthiazolyldiphenyl-tetrazolium bromide metabolic activity assay (MTT; Sigma-Aldrich, Germany) was used. The cells in untreated medium served as the negative control, and the cells in 20% dimethyl sulfoxide were the positive control. The absorbance was measured at 490 nm (absorption wavelength of formazan) and 600 nm as a reference. The results from the cultured cells with extracted medium were normalized to the values measured for the negative control.

4.6. Protein Adsorption Rate. The protein adsorption rate on the scaffolds was measured by using bovine serum albumin (Pierce; Thermo Fisher, Germany) as a model protein. Protein solution (1 mL, 1 mg/mL) was added per scaffold and incubated at 37 °C in a humidified incubator (CO_2 5%, humidity 95%). After 48 h, nonadhered proteins were carefully removed by a pipette and saved for recording. The scaffolds were washed with saline and incubated for a further 48 h after addition of 1 mL of protein solution. The same procedure was repeated after 48 h. The concentration of protein in the supernatant was measured using a Micro BCA protein assay (Pierce; Thermo Fisher, Germany). To do so, 10 μL of supernatant was mixed with 200 μL of working reagent and incubated for 30 min. The absorbance was measured using a microplate reader (Bio-Tek μQuant) at 570 nm. After calibrating the results with a standard curve provided by the BCA protein assay kit (Pierce; Thermo Fisher, Germany), the protein adsorption rate was calculated by subtracting the residual protein concentration from the initial protein concentration.

■ ASSOCIATED CONTENT

Supporting Information

The Supporting Information is available free of charge on the ACS Publications website at DOI: 10.1021/acsami.8b17627.

Optical absorption spectrum of graphene ink (Figure S1); SEM images of ZnO templates (Figures S2−S4); different 3D carbon tube structures (Figure S5); SEM images of AG−CNTT structures (Figure S6); long-cycle compression test graph of AG−G scaffold (Figure S7); high-magnification fluorescence image of REF52 YFP-paxillin cells (Figure S8); supporting discussion (PDF)

Structural integrity of AG−G scaffold (AVI)

■ AUTHOR INFORMATION

Corresponding Author

*E-mail: cse@tf.uni-kiel.de.

ORCID

Fabian Schütt: 0000-0003-2942-503X
Yogendra Kumar Mishra: 0000-0002-8786-9379
Norbert Stock: 0000-0002-0339-7352
Felice Torrisi: 0000-0002-6144-2916
Christine Selhuber-Unkel: 0000-0002-5051-4822

Notes

The authors declare no competing financial interest.

■ ACKNOWLEDGMENTS

R.A. gratefully acknowledges partial project funding by the Deutsche Forschungsgemeinschaft under contract FOR2093. This project has received funding from the European Union's Horizon 2020 research and innovation programme under grant agreement No. GrapheneCore2 785219. C.S.-U. was supported by the European Research Council (ERC StG 336104 CELLINSPIRED, ERC PoC 768740 CHANNELMAT) and the German Research Foundation (RTG 2154, SFB 1261 project B7). M.T. acknowledges support from the German Academic Exchange Service (DAAD) through a research grant for doctoral candidates (91526555-57048249). The authors acknowledge funding from EPSRC grants EP/P02534X/1, ERC grant 319277 (Hetero2D), the Trinity College, Cambridge, and the Isaac Newton Trust. We also acknowledge Galen Ream for critical proofreading.

DOI: 10.1021/acsami.8b17627
ACS Appl. Mater. Interfaces XXXX, XXX, XXX−XXX

REFERENCES

(1) O'Brien, F. J. Biomaterials & Scaffolds for Tissue Engineering. *Mater. Today* **2011**, *14*, 88−95.

(2) Yang, S.; Leong, K.-F.; Du, Z.; Chua, C.-K. The Design of Scaffolds for Use in Tissue Engineering. Part I. Traditional Factors. *Tissue Eng.* **2001**, *7*, 679−689.

(3) Shoulders, M. D.; Raines, R. T. Collagen Structure and Stability. *Annu. Rev. Biochem.* **2009**, *78*, 929−958.

(4) Friedl, P.; Wolf, K. Plasticity of Cell Migration: A Multiscale Tuning Model. *J. Cell Biol.* **2010**, *188*, 11−19.

(5) Langer, R.; Vacanti, J. P. Tissue Engineering. *Science* **1993**, *260*, 920−926.

(6) Place, E. S.; Evans, N. D.; Stevens, M. M. Complexity in Biomaterials for Tissue Engineering. *Nat. Mater.* **2009**, *8*, 457−470.

(7) Loh, Q. L.; Choong, C. Three-Dimensional Scaffolds for Tissue Engineering Applications: Role of Porosity and Pore Size. *Tissue Eng., Part B* **2013**, *19*, 485−502.

(8) Ganji, Y.; Li, Q.; Quabius, E. S.; Böttner, M.; Selhuber-Unkel, C.; Kasra, M. Cardiomyocyte Behavior on Biodegradable Polyurethane/Gold Nanocomposite Scaffolds under Electrical Stimulation. *Mater. Sci. Eng., C* **2016**, *59*, 10−18.

(9) Potse, M.; Dubé, B.; Vinet, A. Cardiac Anisotropy in Boundary-Element Models for the Electrocardiogram. *Med. Biol. Eng. Comput.* **2009**, *47*, 719−729.

(10) Fang, B.; Yang, J.; Chen, C.; Zhang, C.; Chang, D.; Xu, H.; Gao, C. Carbon Nanotubes Loaded on Graphene Microfolds as Efficient Bifunctional Electrocatalysts for the Oxygen Reduction and Oxygen Evolution Reactions. *ChemCatChem* **2017**, *9*, 4520−4528.

(11) Li, Z.; Liu, Z.; Sun, H.; Gao, C. Superstructured Assembly of Nanocarbons: Fullerenes, Nanotubes, and Graphene. *Chem. Rev.* **2015**, *115*, 7046−7117.

(12) Lekawa-Raus, A.; Patmore, J.; Kurzepa, L.; Bulmer, J.; Koziol, K. Electrical Properties of Carbon Nanotube Based Fibers and Their Future Use in Electrical Wiring. *Adv. Funct. Mater.* **2014**, *24*, 3661−3682.

(13) Sahebian, S.; Zebarjad, S. M.; vahdati Khaki, J.; Lazzeri, A. A Study on the Dependence of Structure of Multi-Walled Carbon Nanotubes on Acid Treatment. *J. Nanostruct. Chem.* **2015**, *5*, 287−293.

(14) Aliofkhazraei, M.; Ali, N.; Milne, W. I.; Ozkan, C. S.; Mitura, S.; Gervasoni, J. L. *Graphene Science Handbook: Electrical and Optical Properties*; CRC Press, 2016; p 715.

(15) Chen, J. H.; Jang, C.; Xiao, S.; Ishigami, M.; Fuhrer, M. S. Intrinsic and Extrinsic Performance Limits of Graphene Devices on SiO2. *Nat. Nanotechnol.* **2008**, *3*, 206−209.

(16) Gorityala, B. K.; Ma, J.; Wang, X.; Chen, P.; Liu, X. W. Carbohydrate Functionalized Carbon Nanotubes and Their Applications. *Chem. Soc. Rev.* **2010**, *39*, 2925−2934.

(17) Bhunia, S. K.; Saha, A.; Maity, A. R.; Ray, S. C.; Jana, N. R. Carbon Nanoparticle-Based Fluorescent Bioimaging Probes. *Sci. Rep.* **2013**, *3*, 1473.

(18) Fabbro, A.; Scaini, D.; León, V.; Vázquez, E.; Cellot, G.; Privitera, G.; Lombardi, L.; Torrisi, F.; Tomarchio, F.; Bonaccorso, F.; Bosi, S.; Ferrari, A. C.; Ballerini, L.; Prato, M. Graphene-Based Interfaces Do Not Alter Target Nerve Cells. *ACS Nano* **2016**, *10*, 615−623.

(19) Call, T. P.; Carey, T.; Bombelli, P.; Lea-Smith, D. J.; Hooper, P.; Howe, C. J.; Torrisi, F. Platinum-Free, Graphene Based Anodes and Air Cathodes for Single Chamber Microbial Fuel Cells. *J. Mater. Chem. A* **2017**, *5*, 23872−23886.

(20) Li, N.; Zhang, Q.; Gao, S.; Song, Q.; Huang, R.; Wang, L.; Liu, L.; Dai, J.; Tang, M.; Cheng, G. Three-Dimensional Graphene Foam as a Biocompatible and Conductive Scaffold for Neural Stem Cells. *Sci. Rep.* **2013**, *3*, 1604.

(21) Mooney, E.; Dockery, P.; Greiser, U.; Murphy, M.; Barron, V. Carbon Nanotubes and Mesenchymal Stem Cells: Biocompatibility, Proliferation and Differentiation. *Nano Lett.* **2008**, *8*, 2137−2143.

(22) Yang, S. T.; Luo, J.; Zhou, Q.; Wang, H. Pharmacokinetics, Metabolism and Toxicity of Carbon Nanotubes for Bio-Medical Purposes. *Theranostics* **2012**, *2*, 271−282.

(23) Jia, G.; Wang, H.; Yan, L.; Wang, X.; Pei, R.; Yan, T.; Zhao, Y.; Guo, X. Cytotoxicity of Carbon Nanomaterials: Single-Wall Nanotube, Multi-Wall Nanotube, and Fullerene. *Environ. Sci. Technol.* **2005**, *39*, 1378−1383.

(24) Correa-Duarte, M. A.; Wagner, N.; Rojas-Chapana, J.; Morsczeck, C.; Thie, M.; Giersig, M. Fabrication and Biocompatibility of Carbon Nanotube-Based 3D Networks as Scaffolds for Cell Seeding and Growth. *Nano Lett.* **2004**, *4*, 2233−2236.

(25) Edwards, S. L.; Church, J. S.; Werkmeister, J. A.; Ramshaw, J. A. M. Tubular Micro-Scale Multiwalled Carbon Nanotube-Based Scaffolds for Tissue Engineering. *Biomaterials* **2009**, *30*, 1725−1731.

(26) Liu, Y.; Zhao, Y.; Sun, B.; Chen, C. Understanding the Toxicity of Carbon Nanotubes. *Acc. Chem. Res.* **2013**, *46*, 702−713.

(27) Cohen-Karni, T.; Qing, Q.; Li, Q.; Fang, Y.; Lieber, C. M. Graphene and Nanowire Transistors for Cellular Interfaces and Electrical Recording. *Nano Lett.* **2010**, *10*, 1098−1102.

(28) Akhavan, O.; Ghaderi, E.; Shahsavar, M. Graphene Nanogrids for Selective and Fast Osteogenic Differentiation of Human Mesenchymal Stem Cells. *Carbon* **2013**, *59*, 200−211.

(29) Shin, S. R.; Li, Y. C.; Jang, H. L.; Khoshakhlagh, P.; Akbari, M.; Nasajpour, A.; Zhang, Y. S.; Tamayol, A.; Khademhosseini, A. Graphene-Based Materials for Tissue Engineering. *Adv. Drug Delivery Rev.* **2016**, *105*, 255−274.

(30) Smith, S. C.; Ahmed, F.; Gutierrez, K. M.; Frigi Rodrigues, D. A Comparative Study of Lysozyme Adsorption with Graphene, Graphene Oxide, and Single-Walled Carbon Nanotubes: Potential Environmental Applications. *Chem. Eng. J.* **2014**, *240*, 147−154.

(31) Mecklenburg, M.; Schuchardt, A.; Mishra, Y. K.; Kaps, S.; Adelung, R.; Lotnyk, A.; Kienle, L.; Schulte, K. Aerographite: Ultra Lightweight, Flexible Nanowall, Carbon Microtube Material with Outstanding Mechanical Performance. *Adv. Mater.* **2012**, *24*, 3486−3490.

(32) Mishra, Y. K.; Kaps, S.; Schuchardt, A.; Paulowicz, I.; Jin, X.; Gedamu, D.; Freitag, S.; Claus, M.; Wille, S.; Kovalev, A.; Gorb, S. N.; Adelung, R. Fabrication of Macroscopically Flexible and Highly Porous 3D Semiconductor Networks from Interpenetrating Nanostructures by a Simple Flame Transport Approach. *Part. Part. Syst. Charact.* **2013**, *30*, 775−783.

(33) Lamprecht, C.; Taale, M.; Paulowicz, I.; Westerhaus, H.; Grabosch, C.; Schuchardt, A.; Mecklenburg, M.; Böttner, M.; Lucius, R.; Schulte, K.; Adelung, R.; Selhuber-Unkel, C. A Tunable Scaffold of Microtubular Graphite for 3D Cell Growth. *ACS Appl. Mater. Interfaces* **2016**, *8*, 14980−14985.

(34) Mouw, J. K.; Ou, G.; Weaver, V. M. Extracellular Matrix Assembly: A Multiscale Deconstruction. *Nat. Rev. Mol. Cell Biol.* **2014**, *15*, 771−785.

(35) Schütt, F.; Signetti, S.; Krüger, H.; Röder, S.; Smazna, D.; Kaps, S.; Gorb, S. N.; Mishra, Y. K.; Pugno, N. M.; Adelung, R. Hierarchical Self-Entangled Carbon Nanotube Tube Networks. *Nat. Commun.* **2017**, *8*, No. 1215.

(36) Feng, X.; Feng, L.; Jin, M.; Zhai, J.; Jiang, L.; Zhu, D. Reversible Super-Hydrophobicity to Super-Hydrophilicity Transition of Aligned ZnO Nanorod Films. *J. Am. Chem. Soc.* **2004**, *126*, 62−63.

(37) Chen, H.-K. Kinetic Study on the Carbothermic Reduction of Zinc Oxide. *Scand. J. Metall.* **2001**, *30*, 292−296.

(38) Zhao, J.; Xing, B.; Yang, H.; Pan, Q.; Li, Z.; Liu, Z. Growth of Carbon Nanotubes on Graphene by Chemical Vapor Deposition. *New Carbon Mater.* **2016**, *31*, 31−36.

(39) Ferrari, A. C.; Robertson, J. Resonant Raman Spectroscopy of Disordered, Amorphous, and Diamondlike Carbon. *Phys. Rev. B: Condens. Matter Mater. Phys.* **2001**, *64*, 075414.

(40) Carey, T.; Cacovich, S.; Divitini, G.; Ren, J.; Mansouri, A.; Kim, J. M.; Wang, C.; Ducati, C.; Sordan, R.; Torrisi, F. Fully Inkjet-Printed Two-Dimensional Material Field-Effect Heterojunctions for Wearable and Textile Electronics. *Nat. Commun.* **2017**, *8*, 1202.

(41) Ferrari, A. C.; Meyer, J. C.; Scardaci, V.; Casiraghi, C.; Lazzeri, M.; Mauri, F.; Piscanec, S.; Jiang, D.; Novoselov, K. S.; Roth, S.; et al. Raman Spectrum of Graphene and Graphene Layers. *Phys. Rev. Lett.* **2006**, *97*, 187401.

DOI: 10.1021/acsami.8b17627
ACS Appl. Mater. Interfaces XXXX, XXX, XXX−XXX

(42) Ferrari, A.; Robertson, J. Interpretation of Raman Spectra of Disordered and Amorphous Carbon. *Phys. Rev. B: Condens. Matter Mater. Phys.* **2000**, *61*, 14095−14107.
(43) Cuscó, R.; Alarcón-Lladó, E.; Ibáñez, J.; Artús, L.; Jiménez, J.; Wang, B.; Callahan, M. Temperature Dependence of Raman Scattering in ZnO. *Phys. Rev. B: Condens. Matter Mater. Phys.* **2007**, *75*, 165202.
(44) Fan, H.; Wang, L.; Zhao, K.; Li, N.; Shi, Z.; Ge, Z.; Jin, Z. Fabrication, Mechanical Properties, and Biocompatibility of Graphene-Reinforced Chitosan Composites. *Biomacromolecules* **2010**, *11*, 2345−2351.
(45) Ahadian, S.; Ramón-Azcón, J.; Estili, M.; Liang, X.; Ostrovidov, S.; Shiku, H.; Ramalingam, M.; Nakajima, K.; Sakka, Y.; Bae, H. H.; Matsue, T.; Khademhosseini, A. Hybrid Hydrogels Containing Vertically Aligned Carbon Nanotubes with Anisotropic Electrical Conductivity for Muscle Myofiber Fabrication. *Sci. Rep.* **2015**, *4*, 4271.
(46) Shi, X.; Sitharaman, B.; Pham, Q. P.; Liang, F.; Wu, K.; Edward Billups, W.; Wilson, L. J.; Mikos, A. G. Fabrication of Porous Ultra-Short Single-Walled Carbon Nanotube Nanocomposite Scaffolds for Bone Tissue Engineering. *Biomaterials* **2007**, *28*, 4078−4090.
(47) Chen, Z.; Ren, W.; Gao, L.; Liu, B.; Pei, S.; Cheng, H. M. Three-Dimensional Flexible and Conductive Interconnected Graphene Networks Grown by Chemical Vapour Deposition. *Nat. Mater.* **2011**, *10*, 424−428.
(48) Zhao, G.; Zhang, X.; Lu, T. J.; Xu, F. Recent Advances in Electrospun Nanofibrous Scaffolds for Cardiac Tissue Engineering. *Adv. Funct. Mater.* **2015**, *25*, 5726−5738.
(49) Zuo, G.; Kang, S. G.; Xiu, P.; Zhao, Y.; Zhou, R. Interactions between Proteins and Carbon-Based Nanoparticles: Exploring the Origin of Nanotoxicity at the Molecular Level. *Small* **2013**, *9*, 1546−1556.
(50) Suh, C. W.; Kim, M. Y.; Choo, J. B.; Kim, J. K.; Kim, H. K.; Lee, E. K. Analysis of Protein Adsorption Characteristics to Nano-Pore Silica Particles by Using Confocal Laser Scanning Microscopy. *J. Biotechnol.* **2004**, *112*, 267−277.
(51) Prager-Khoutorsky, M.; Lichtenstein, A.; Krishnan, R.; Rajendran, K.; Mayo, A.; Kam, Z.; Geiger, B.; Bershadsky, A. D. Fibroblast Polarization Is a Matrix-Rigidity-Dependent Process Controlled by Focal Adhesion Mechanosensing. *Nat. Cell Biol.* **2011**, *13*, 1457−1465.
(52) El-Mohri, H.; Wu, Y.; Mohanty, S.; Ghosh, G. Impact of Matrix Stiffness on Fibroblast Function. *Mater. Sci. Eng., C* **2017**, *74*, 146−151.
(53) Sun, Y.; Chen, C. S.; Fu, J. Forcing Stem Cells to Behave: A Biophysical Perspective of the Cellular Microenvironment. *Annu. Rev. Biophys.* **2012**, *41*, 519−542.
(54) Moreno-Arotzena, O.; Borau, C.; Movilla, N.; Vicente-Manzanares, M.; García-Aznar, J. M. Fibroblast Migration in 3D Is Controlled by Haptotaxis in a Non-Muscle Myosin II-Dependent Manner. *Ann. Biomed. Eng.* **2015**, *43*, 3025−3039.
(55) Turner, C. E. Paxillin and Focal Adhesion Signalling. *Nat. Cell Biol.* **2000**, *2*, E231−E236.
(56) Chiu, C.-L.; Aguilar, J. S.; Tsai, C. Y.; Wu, G.; Gratton, E.; Digman, M. M. A.; Kuo, J.; Han, X.; Hsiao, C.; Iii, J. Y.; et al. Nanoimaging of Focal Adhesion Dynamics in 3D. *PLoS One* **2014**, *9*, e99896.
(57) Ryoo, S. R.; Kim, Y. K.; Kim, M. H.; Min, D. H. Behaviors of NIH-3T3 Fibroblasts on Graphene/Carbon Nanotubes: Proliferation, Focal Adhesion, and Gene Transfection Studies. *ACS Nano* **2010**, *4*, 6587−6598.
(58) Cooper, G. M. *The Cell: A Molecular Approach*; ASM Press, 2000; Vol. *10*.
(59) Serrano, M. C.; Patiño, J.; García-Rama, C.; Ferrer, M. L.; Fierro, J. L. G.; Tamayo, A.; Collazos-Castro, J. E.; Del Monte, F.; Gutiérrez, M. C. 3D Free-Standing Porous Scaffolds Made of Graphene Oxide as Substrates for Neural Cell Growth. *J. Mater. Chem. B* **2014**, *2*, 5698−5706.
(60) Avery, N. C.; Bailey, A. J.; Fratzl, P. *Collagen: Structure and Mechanics*; Springer, 2008.
(61) LeBaron, R. G.; Athanasiou, K. A. Extracellular Matrix Cell Adhesion Peptides: Functional Applications in Orthopedic Materials. *Tissue Eng.* **2000**, *6*, 85−103.
(62) Marx, J.; Lewke, M. R. D.; Smazna, D.; Mishra, Y. K.; Adelung, R.; Schulte, K.; Fiedler, B. Processing, Growth Mechanism and Thermodynamic Calculations of Carbon Foam with a Hollow Tetrapodal Morphology − Aerographite. *Appl. Surf. Sci.* **2019**, *470*, 535−542.
(63) Wang, F.; Torrisi, F.; Jiang, Z.; Popa, D.; Hasan, T.; Sun, Z.; Cho, W.; Ferrari, A. C. Graphene Passively Q-Switched Two-Micron Fiber Lasers. In *Conference on Lasers and Electro-Optics (CLEO); OSA Technical Digest* (Optical Society of America): San Jose, CA, 2012; p JW2A 72.
(64) Purdie, D. G.; Popa, D.; Wittwer, V. J.; Jiang, Z.; Bonacchini, G.; Torrisi, F.; Milana, S.; Lidorikis, E.; Ferrari, A. C. Few-Cycle Pulses from a Graphene Mode-Locked All-Fiber Laser. *Appl. Phys. Lett.* **2015**, *106*, 253101.
(65) Bianchi, V.; Carey, T.; Viti, L.; Li, L.; Linfield, E. H.; Davies, A. G.; Tredicucci, A.; Yoon, D.; Karagiannidis, P. G.; Lombardi, L.; Tomarchio, F.; Ferrari, A. C.; Torrisi, F.; Vitiello, M. S. Terahertz Saturable Absorbers from Liquid Phase Exfoliation of Graphite. *Nat. Commun.* **2017**, *8*, 15763.
(66) Lotya, M.; Hernandez, Y.; King, P. J.; Smith, R. J.; Nicolosi, V.; Karlsson, L. S.; Blighe, F. M.; De, S.; Wang, Z.; McGovern, I. T.; Duesberg, G. S.; Coleman, J. N. Liquid Phase Production of Graphene by Exfoliation of Graphite in Surfactant/Water Solutions. *J. Am. Chem. Soc.* **2009**, *131*, 3611−3620.
(67) Carey, T.; Jones, C.; Le Moal, F.; Deganello, D.; Torrisi, F. Spray Coating Thin Films on Three-Dimensional Surfaces for a Semi-Transparent Capacitive Touch Device. *ACS Appl. Mater. Interfaces* **2018**, *10*, 19948−19956.
(68) Kravets, V. G.; Grigorenko, A. N.; Nair, R. R.; Blake, P.; Anissimova, S.; Novoselov, K. S.; Geim, A. K. Spectroscopic Ellipsometry of Graphene and an Exciton-Shifted van Hove Peak in Absorption. *Phys. Rev. B: Condens. Matter Mater. Phys.* **2010**, *81*, 155413.
(69) Selhuber-Unkel, C.; Erdmann, T.; López-García, M.; Kessler, H.; Schwarz, U. S.; Spatz, J. P. Cell Adhesion Strength Is Controlled by Intermolecular Spacing of Adhesion Receptors. *Biophys. J.* **2010**, *98*, 543−551.
(70) Wörle-Knirsch, J. M.; Pulskamp, K.; Krug, H. F. Oops They Did It Again! Carbon Nanotubes Hoax Scientists in Viability Assays. *Nano Lett.* **2006**, *6*, 1261−1268.

DOI: 10.1021/acsami.8b17627
ACS Appl. Mater. Interfaces XXXX, XXX, XXX−XXX

The Supporting Information is available in Appendix-C

Chapter 5

Bioactive carbon based hybrid 3D scaffolds for osteoblast growth

Mohammadreza Taale, Fabian Schütt, Kai Zheng, Yogendra Kumar Mishra, Aldo R Boccaccini, Rainer Adelung, Christine Selhuber-Unkel

ACS APPLIED MATERIALS & INTERFACES

Research Article

Cite This: ACS Appl. Mater. Interfaces 2018, 10, 43874−43886

www.acsami.org

Bioactive Carbon-Based Hybrid 3D Scaffolds for Osteoblast Growth

Mohammadreza Taale,[†] Fabian Schütt,[‡] Kai Zheng,[§] Yogendra Kumar Mishra,[‡] Aldo R. Boccaccini,[§] Rainer Adelung,[‡] and Christine Selhuber-Unkel*[,†]

[†]Biocompatible Nanomaterials, Institute for Materials Science and [‡]Functional Nanomaterials, Institute for Materials Science, Kiel University, Kaiserstr. 2, 24143 Kiel, Germany

[§]Institute of Biomaterials, Department of Materials Science and Engineering, University of Erlangen-Nuremberg, Cauerstr. 6, 91058 Erlangen, Germany

Supporting Information

ABSTRACT: Bone, nerve, and heart tissue engineering place high demands on the conductivity of three-dimensional (3D) scaffolds. Fibrous carbon-based scaffolds are excellent material candidates to fulfill these requirements. Here, we show that highly porous (up to 94%) hybrid 3D framework structures with hierarchical architecture, consisting of microfiber composites of self-entangled carbon nanotubes (CNTs) and bioactive nanoparticles are highly suitable for growing cells. The hybrid 3D structures are fabricated by infiltrating a combination of CNTs and bioactive materials into a porous (~94%) zinc oxide (ZnO) sacrificial template, followed by the removal of the ZnO backbone via a H_2 thermal reduction process. Simultaneously, the bioactive nanoparticles are sintered. In this way, conductive and mechanically stable 3D composites of free-standing CNT-based microfibers and bioactive nanoparticles are formed. The adopted strategy demonstrates great potential for implementing low-dimensional bioactive materials, such as hydroxyapatite (HA) and bioactive glass nanoparticles (BGN), into 3D carbon-based microfibrous networks. It is demonstrated that the incorporation of HA nanoparticles and BGN promotes the biomineralization ability and the protein adsorption capacity of the scaffolds significantly, as well as fibroblast and osteoblast adhesion. These results demonstrate that the developed carbon-based bioactive scaffolds are promising materials for bone tissue engineering and related applications.

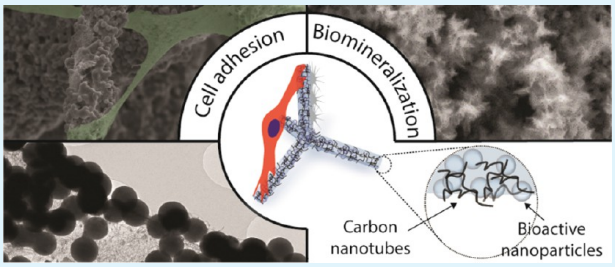

KEYWORDS: *carbon nanotubes, 3D scaffolds, bioactive glass, hydroxyapatite, osteoblasts*

1. INTRODUCTION

Bioactive materials are highly important for inducing specific cellular responses, particularly in tissue engineering.[1] A highly promising bioactive material in bone tissue engineering is silicate bioactive glass (BG).[2] In particular, the presence of CaO in silicate BG is decisive in the formation of a bone-like calcium phosphate layer on the material.[3] This surface layer results in a strong connection between the biomaterial and both bone and soft tissue.[4] To expand the interface between BG and tissue, BG can be prepared as scaffolds or incorporated into scaffolds. Depending on the microstructure and fabrication method of the BG, the Young's modulus of porous scaffolds made of BG can be varied between 1 and 22 MPa.[3] In addition, BG can be degraded by releasing ions into the environment so that a main component of bone, hydroxyapatite (HA), is formed.[3,5] BG is also known to support the adhesion and proliferation of osteoblast cells, such as MC3T3-E1[6−9] and MLO-A5.[1,10] In addition, many studies have shown that the ions released from BG, including Si, Ca, P, and Cu, play an important role in enhancing osteoblast proliferation and bone formation.[4] Another important bioactive material is hydroxyapatite, as it is a main component of bone within the human body. It has frequently been used as a coating to promote bone ingrowth or as a bone graft substitute.[11]

BG is often implemented in biomaterials in the form of composites. Out of such composite systems, BG and carbon nanotubes (CNTs) have shown to be most promising due to a mutually beneficial modification of the features and functionality of each other.[12] On the one hand, CNTs enhance the features of BG such as stiffness, electrical conductivity, and surface roughness in several ways: (i) the mechanical properties, such as stiffness and fracture toughness, are improved by the CNTs,[13−15] (ii) the local and overall electrical conductivity is increased by CNTs,[16,17] (iii) CNTs lead to a rougher surface on the nanoscale and consequently to an improvement of cell attachment and proliferation.[18] On the other hand, BG makes CNTs more appropriate for biomedical applications by accelerating biomineralization[19] and increasing the concentration of physiologically relevant ions, thus resulting in higher cell proliferation rates and faster regeneration of soft tissue.[20]

Received: August 9, 2018
Accepted: November 5, 2018
Published: November 5, 2018

DOI: 10.1021/acsami.8b13631
ACS Appl. Mater. Interfaces 2018, 10, 43874−43886

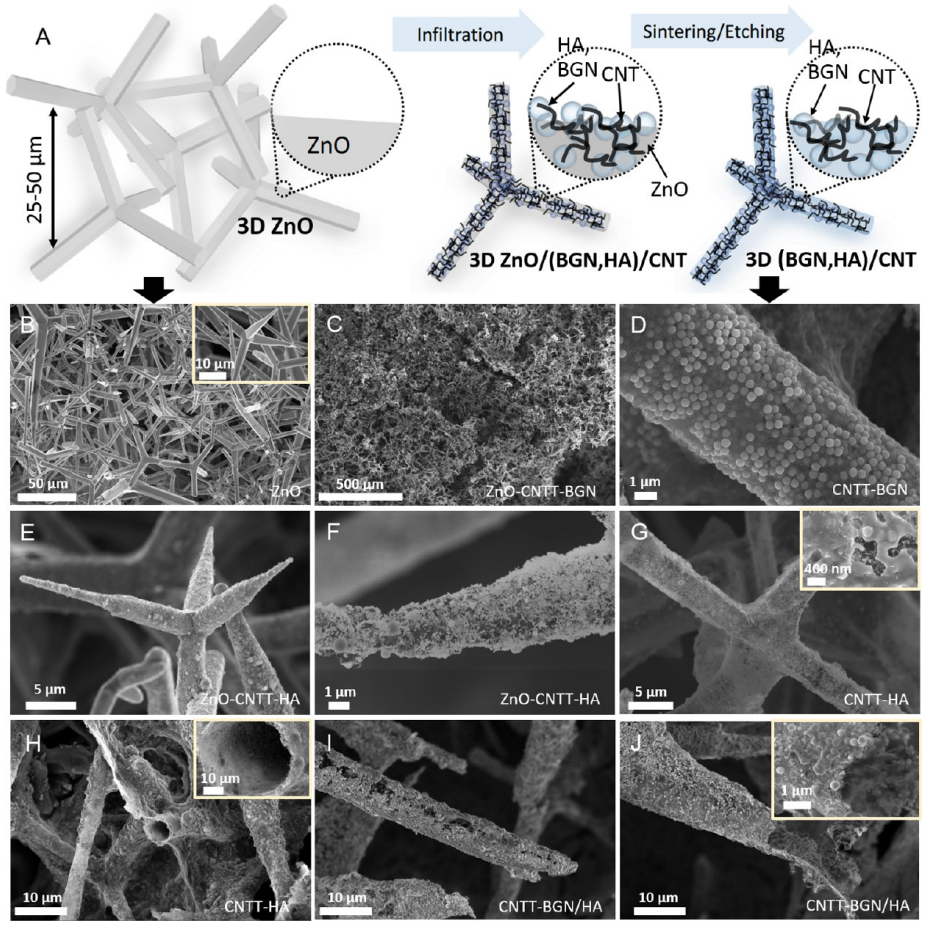

Figure 1. (A) Sketch of the fabrication process: the porous ZnO templates are infiltrated with HA nanoparticles or BGN and CNT dispersions. Due to the strong capillary forces and superhydrophilic properties of ZnO, the micro-tetrapods are entirely covered with a layer of CNTs and BGN. Later, the sacrificial ZnO template is removed via H_2 etching at 900 °C. The remaining structure consists of self-entangled CNTs as a backbone and sintered BGN as a bioactive material. (B–J) Scanning electron micrographs: (B) the 3D ZnO sacrificial template consisting of micron-sized ZnO tetrapods, (C) the ZnO–CNTT–BGN (entangled CNTs + BGN) structure before H_2 etching/sintering process, (D) the CNTT–BGN (entangled CNTs + BGN) structure after H_2 etching/sintering, (E, F) the CNTT–HA (entangled CNTs + HA) structure before H_2 etching/sintering, (G, H) the CNTT–HA structure (entangled CNTs + HA) after the H_2 etching/sintering. (H) The broken filament of the CNTT–HA scaffold showing that the structures are made of hollow tubes, (I, J) the CNTT–BGN/HA (entangled CNTs + BGN + HA) structure after H_2 etching/sintering (BGN: bioactive glass nanoparticles, CNT: carbon nanotube, HA: hydroxyapatite).

To exploit the unique properties of composites made of CNTs and bioactive materials (such as BG and HA) for tissue engineering, three-dimensional (3D) scaffold fabrication methods are needed that provide a mechanically stable 3D environment that supports cell proliferation.[21] In such 3D environments, the pore architecture is one of the most decisive parameters as it affects cell growth by determining nutrient and oxygen diffusion, waste removal, as well as the growth rate of the cells. Open porous and interconnected pore architectures are strongly necessary to facilitate these parameters.[22] Commonly used techniques to generate pores in materials, such as salt-leaching, freeze-drying, gas foaming, sol–gel crosslinking, and phase separation only provide very limited control of the internal pore architecture of the scaffold material for tissue engineering.[23] Therefore, rapid prototyping techniques have been employed recently, which enable the fabrication of scaffolds with control over pore size and architecture together with good design reproducibility.[24] Nevertheless, rapid prototyping techniques are limited with respect to the biomaterials that can be printed and they cannot be used to fabricate 3D structures from nanomaterials only.[25]

Recently, an infiltration-based synthesis method for the fabrication of porous, 3D scaffolds consisting of interconnected CNT-based microtubes has been reported.[26] With this method, open porous scaffolds with total dimensions on the cm^3 scale can be fabricated, resulting in a 3D hierarchical CNT tube (CNTT) structure with improved mechanical and electrical properties compared to other 3D assemblies prepared by wet chemistry. As the reported fabrication method relies on the infiltration of nanoparticle dispersions into sacrificial ZnO templates, in principle, also other nanoparticle types besides CNTs can be embedded. Therefore, this method is a great and versatile starting point for fabricating hybrid 3D scaffold materials with properties that can be tailored towards specific, electronic, catalytic, or biomedical applications, e.g., by the incorporation of bioactive nanoparticles.

We show here that low-dimensional bioactive materials in the form of bioactive glass and hydroxyapatite nanoparticles can be integrated into CNTT materials, to make it bioactive and

DOI: 10.1021/acsami.8b13631
ACS Appl. Mater. Interfaces 2018, 10, 43874–43886

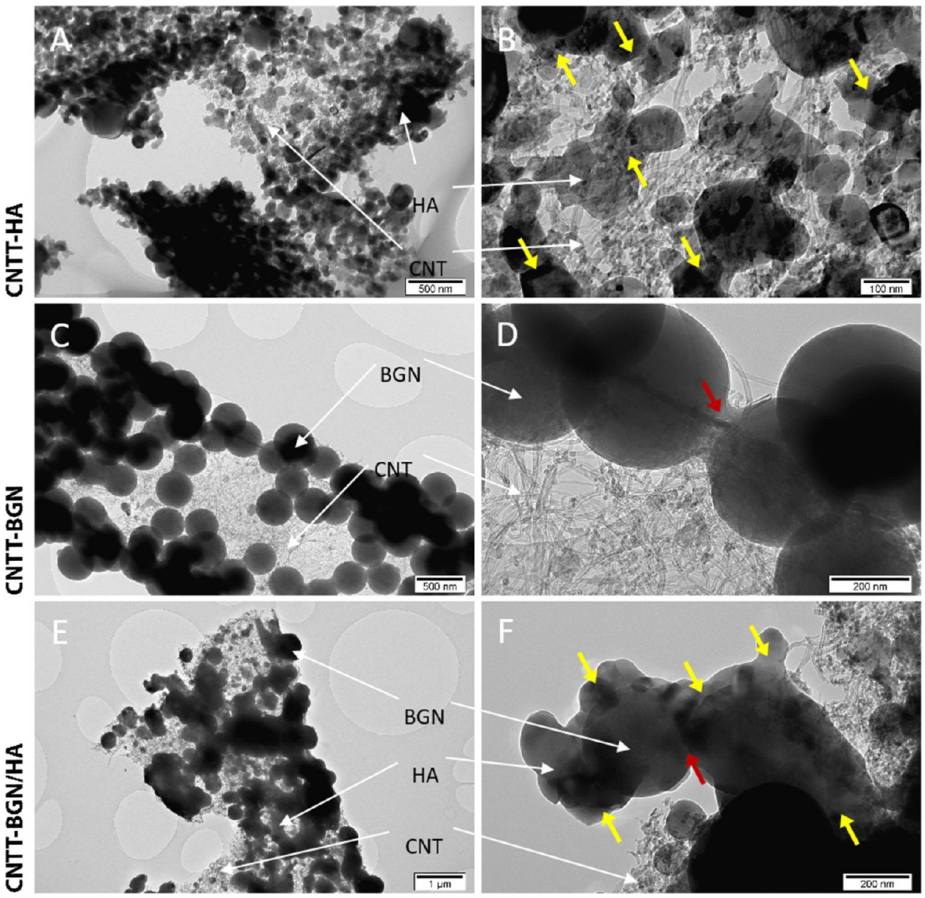

Figure 2. TEM images of CNTT−BGN, CNTT−BGN/HA, and CNTT−HA scaffolds. (A, B) The CNTT−HA structure (entangled CNTs + HA), (C, D) CNTT−BGN structure (entangled CNTs + BGN), and (E, F) CNTT−BGN/HA structure (entangled CNTs + BGN and HA). Yellow and red arrows point at fused particles. BGN are partially fused to the particles in their vicinity (red arrows) and probably to the CNT matrix, whereas HA nanoparticles underwent a greater sintering deformation (yellow arrows). HA particles bridge the gaps between BG nanoparticles in the combined structure (CNTT−BGN/HA) during the etching/sintering process. HA nanoparticles and BGN in CNTT−BGN/HA scaffolds were distinguished by their shape in the CNTT−BGN and CNTT−HA scaffolds.

supportive for cell growth. The bioactive nanoparticles incorporated into the scaffolds are sintered during a single step etching/sintering process. The structure of the resulting material was characterized with scanning electron microscopy (SEM), transmission electron microscopy (TEM), and X-ray diffraction (XRD). To prove the bioactivity of the scaffolds, we investigated biomineralization as well as their protein adsorption capacity. In vitro studies demonstrate that fibroblasts and osteoblasts can adhere to the fibrous structures of the hybrid CNT network, demonstrating the feasibility of this 3D composite material for bone tissue engineering.

2. RESULTS AND DISCUSSION

2.1. Bioactive Carbon-Based Scaffolds. The successful fabrication of free-standing, fibrous 3D composite scaffolds, consisting of CNTs and a nanoscale bioactive ceramic biomaterial has been achieved via a very simple strategy based on a ceramic template. Figure 1A shows a schematic representation of the fabrication process, in which compressed and sintered ZnO tetrapods (Figure 1B) serve as sacrificial materials. To generate free-standing carbon-based and bioactive composite structures these 3D and porous (porosity ∼94%) ZnO templates were infiltrated with an aqueous dispersion of CNTs and either BGN, HA nanoparticles or both of them. Due to the strong capillary forces and the superhydrophilic properties of the ZnO template,[27] the dispersion is rapidly soaked into the template during the infiltration process. Figure 1C shows an SEM image of a ZnO template after infiltration with CNTs and BGN. Figure 1E,F show SEM images of the templates after infiltration with CNTs and HA nanoparticles. In the experiments, it is in principle also possible to tailor the amount of CNTs as well as the amount of BGN and HA nanoparticles added on the template by controlling the volume of the injected nanoparticle dispersion into the ZnO network.

To generate free-standing hybrid structures, we needed to remove the ZnO. This is also necessary to make the materials biocompatible, as a high amount of ZnO is toxic for cells.[28] Most methods to remove ZnO are based on wet chemistry, e.g., using diluted HCl. However, since an acidic treatment would also dissolve the incorporated bioactive materials, a H_2 etching process was used to remove the ZnO.[29] At 900 °C, ZnO is completely reduced by H_2, evaporated to Zn (gas) without the presence of a carbon source, and removed by the employed carrier gas (argon). In Figure 1D−J, SEM images of the resulting structures are shown. Figure 1D shows CNT and BGN scaffolds after etching of the ZnO template. Figure 1H,1J show that broken microtubes are hollow, proving that the entire ZnO template has been removed during the etching process. The free-

DOI: 10.1021/acsami.8b13631
ACS Appl. Mater. Interfaces 2018, 10, 43874−43886

Table 1. Conductivity and Compressive Strength of CNTT−HA and CNTT−BGN Scaffolds[a]

scaffold	specific conductivity (S/m)	compressive strength (kPa)	compressive strength/density (kPa cm^3/g)	Young's modulus (MPa)
CNTT−HA	∼0.88	∼7.2	∼27	∼0.4
CNTT−BGN	∼12.7	∼32	∼118	∼1

[a]The large discrepancy in conductivity between CNTT−HA and CNTT−BGN is most probably a result of clamping difficulties, as the surface of the material is covered with HA and BGN, respectively. Still, the conductivity is in the range of that of CNTTs without incorporated ceramic nanoparticles.[26]

standing composites are denoted as CNTT−BGN (CNT-based tubes containing BGN), CNTT−HA (CNT-based tubes containing HA nanoparticles), and CNTT−BGN/HA (CNT-based tubes containing both BGN and HA nanoparticles). In general, the process described here can be easily scaled-up as it is based on commercially available materials that can all be mass-produced.

Initially, the CNTs in our scaffolds form interwoven layers of self-entangled CNTs with high mechanical stability similar to the ones shown in previous work.[26] Most importantly, the high temperature during the ZnO template removal fuses the ceramic nanoparticles to each other and leads to a physical interaction with the CNTs, resulting in a hollow free-standing entangled CNT architecture combined with sintered ceramic nanoparticles (Figure 2). These ceramic nanoparticles are believed to contribute to a further reinforcement of the mechanical properties of the scaffold (Table 1). Moreover, the geometry of the networks provides highly accessible interconnected pores from all sides, whereas the preferential alignment of CNTs in other 3D assemblies confines the accessibility of cavities.[30]

In addition, the porous structure of our scaffolds leads to a large free volume, which should in turn result in higher bioactivity.[31] The scaffolds possess up to 94% porosity (Table S1), thus being in the range of that of other highly porous BG-containing scaffolds.[31,32] The porosity of the scaffolds presented is higher than that of 3D printed biomaterials that contain HA nanoparticles, including HA nanoparticle incorporated poly(lactide-*co*-glycolide) with up to 63.33% of porosity.[33,34] Furthermore, due to the interwoven arrangement of CNTs in the microtubes, we assume that the scaffolds possess a similar conductivity (Table 1) as the recently reported self-entangled CNT assemblies,[26] but with the additional feature that the incorporated ceramic nanoparticles make the material bioactive.

It is important to note that our scaffolds are not intended to replace bone in load-bearing areas, as their compressive strength (Table 1) is smaller than that of trabecular bone.[35] Instead, the idea of tissue engineering in this context is to generate scaffolds, which induce the formation of new bone tissue based on the bioactivity of the scaffold.[5,11] If the scaffold exhibits bioactivity, the mechanical properties will strengthen upon implantation so that a new bone is formed.[36] The suitability of soft materials for bone tissue engineering has recently been shown by Huebsch et al.,[37] who used soft hydrogels to induce bone formation. As our scaffolds are bioactive (see Section 2.5) and support osteoblast growth (see Section 2.6), we are convinced that they are suitable for bone tissue engineering.

2.2. Morphology and Composition of Ceramic Nanoparticles on CNTT Scaffolds. Figure 2 shows TEM images of CNTT−BGN, CNTT−HA, and CNTT−BGN/HA. The most striking result from these images is that all generated structures are free-standing and the ZnO template has been completely removed. Furthermore, the images show that the ceramic nanoparticles were fused to each other in the etching/sintering procedure. In addition, HA and BGN were fused to each other in CNTT−BGN/HA composites. Interestingly, BGN mainly retain their spherical shape and are only slightly fused together. In contrast, the initially also spherical HA nanoparticles were deformed to flakes or unevenly shaped particles during the etching/sintering procedure.

This allowed us to distinguish the particle types even in CNTT−BGN/HA scaffolds (Figure 2E,F). Furthermore, these images suggest that the HA particles bridged the gaps between the BGN in CNTT−BGN/HA samples (Figure 2E,F, yellow arrows). This difference in the sintering behavior is probably due to the lower effective sintering point of HA nanoparticles (700 °C) compared to silicate-based BGN (950−1000 °C),[38,39] thus the deformation and fusion of HA particles is more pronounced. A further interesting result is that the CNTs in the structures do not seem to be altered by the sintering procedure, even in the presence of hydrogen.

To check the crystallinity of the ceramic nanoparticles after the fabrication process, we carried out an XRD study. The XRD pattern (Figure 3) of a CNTT−HA sample revealed diffraction peaks of HA. In contrast, the XRD pattern of a CNTT−BGN sample revealed no diffraction peaks related to BGN, but diffraction peaks related to α-quartz are recognized. Pristine BGN are amorphous and only possess broad peaks in the range of 2θ = 20−35°.[40] Since the incorporated BGN had the

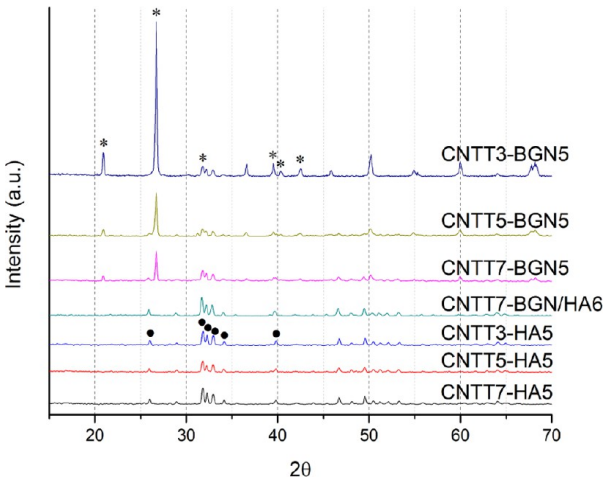

Figure 3. XRD patterns of CNTT−BGN, CNTT−HA, and CNT−BGN/HA scaffolds. CNTT*y*−BGN*x*: *y* and *x* correspond to the number of infiltrations of CNTs and ceramic (HA or BG) nanoparticles, respectively (as an example CNTT3−BGN5 means a ZnO template was infiltrated five times with BG nanoparticles and three times with CNT dispersion). Due to the smaller diffraction of X-rays by CNTs, the intensity of ceramic peaks is more pronounced in structures with a lower amount of infiltrated CNTs. The XRD patterns of the CNTT−BGN structures are in conformity with α-quartz peaks, and CNTT−HA structures mostly with hydroxyapatite (•hydroxyapatite, *α-quartz). Interestingly, the combined structure (CNTT−BGN/HA) only reveals the hydroxyapatite XRD pattern.

DOI: 10.1021/acsami.8b13631
ACS Appl. Mater. Interfaces 2018, 10, 43874−43886

composition $92SiO_2-8CaO$ (in mol %),[40] their crystallization behavior is similar to that of pure silica nanoparticles. However, in this study the processing temperature (900 °C) used for the fabrication of the scaffolds was high enough to cause the crystallization of silica-based nanoparticles,[41] which explains the appearance of the diffraction peaks of α-quartz in CNTT−BGN. For the CNTT−BGN/HA structure, the diffraction pattern only correlates to that of crystallized HA. In addition, SiO_2−CaO-based BGN sintered at 900 °C should be partially crystallized according to previous work.[41] Importantly, Figure 3 also shows the effect of different amounts of infiltrated CNTs: the intensity of the ceramic peaks decreased if more CNTs had been infiltrated.

The XRD results of the HA-containing scaffolds show no change of the crystalline phase of HA. As the first phase transformation of HA occurs at 1000−1100 °C.[42] we assume that our HA particles are not decomposed at our sintering temperature (900 °C). Furthermore, in a previous study, no reaction of multiwalled CNTs (MWCNTs) with glass matrices to form SiC or other reaction phases in response to sintering between 850 and 1000 °C was detected by powder X-ray diffraction.[43]

2.3. Protein Adsorption on Scaffolds. The adsorption of proteins on bioceramics is essential because it influences cell adhesion and can facilitate scaffold integration into tissues.[44] To investigate the protein adsorption capacity of CNTT−BGN and CNTT−HA scaffolds, we used bovine serum albumin (BSA) as a model protein. The adsorption capacity of the scaffolds was quantified for 4, 8, 12, 24, 48, and 72 h of scaffold incubation with protein solution. The bicinchoninic acid (BCA) assay (Figure 4) shows that the protein adsorption is higher on CNTT−BGN scaffolds than on CNTT−HA scaffolds.

This difference in adsorbing proteins is highest during the first 4 h of incubation with proteins and levels out after 8 h of incubation. Despite the fact that there was a slight difference regarding the protein adsorption ratio between the two scaffold types, both exhibited a similar temporal progression of protein adsorption. This can be explained by the fact that CNTs presumably play the main role in protein adsorption due to the high amount of CNTs in the matrix in both the CNTT−HA and CNTT−BGN scaffolds (Figure 1). It is also important to mention here that the protein adsorption capacity of scaffolds is a decisive parameter for osteoblast attachment.[45] As the CNT matrix can serve as an attachment site for a variety of extracellular matrix molecules, biomolecules, proteins, and growth factors, it can further mediate cell proliferation and adhesion.[46] Interestingly, in the present study CNTT−BGN has a higher adsorption capacity than CNTT−HA (Figure 4).

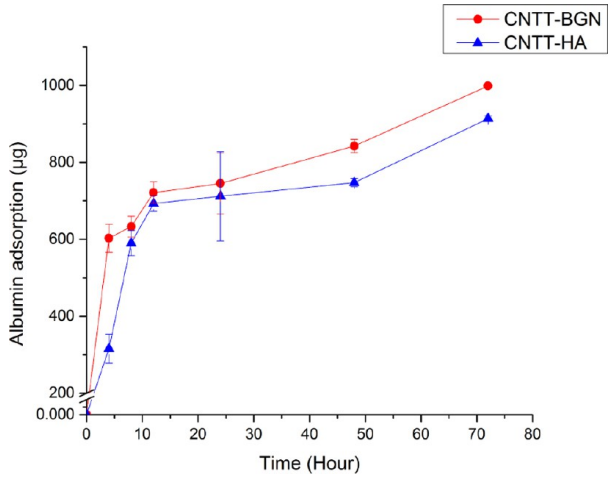

Figure 4. Bovine serum albumin adsorption (mean values) on CNTT−BGN and CNTT−HA scaffolds, measured with a BCA colorimetric assay. BGN containing structures have a slightly higher protein adsorption capacity compared to CNTT−HA scaffolds. (Each experiment was carried out on three samples and three replicates each. Error bars: standard deviation.)

This result could be due to an electrostatic interaction between the highly polar BSA and the BGN surface,[44] which might be a result of the etching/sintering process, as explained in the following: at the sintering temperature of 900 °C, H_2 reacts with silica to form SiOx on the surface of BGN.[47] The presence of SiOx on the surface of BGN can alter the surface charge density of BGN.[48] Therefore, due to a change in surface charge, the BGN surface might have the potential to bind more BSA proteins. In addition, previous studies indicated that surface-modified bioactive glass adsorbs a higher amount of serum protein than hydroxyapatite.[49]

2.4. Ion Release from Scaffolds in Phosphate Buffered Saline (PBS). To explore the ion release capability of the fabricated hybrid scaffolds within biologically relevant media, we measured the concentration of Ca, Si, and Zn ions in phosphate buffered saline (PBS) after 4, 8, 12, 24, 96, 158, 230, 302, and 398 h of incubation with the scaffolds using inductively coupled plasma-mass spectrometry (ICP-MS) (Figure 5). Clearly, the amount of ions released from the scaffolds increased with incubation time. The release of Zn ions is almost zero (~5 μg after 400 h), even after 16 days of immersing CNTT−BGN or CNTT−HA scaffolds in PBS. This proves again that the sacrificial ZnO templates had been entirely removed during the H_2 etching process. Hence, the hydrogen etching process at elevated temperatures provides a clear improvement compared to previously reported methods used for ZnO removal.[50] As shown in Figure 5, a high amount of Ca^{2+} ions was released into the PBS from CNTT−HA and CNTT−BGN structures during the first 24 h of immersion (Figure 5). Afterwards, the release rate of Ca^{2+} ions was decreased. The high accessibility of Ca^{2+} ions on the surface of BG and HA nanoparticles leads to a high Ca^{2+} ion concentration gradient between PBS and the ceramic nanoparticles, presumably resulting in a high initial release rate and a smaller and more stable release rate for longer immersion times. As expected, we did not measure any Si ion release from the CNTT−HA scaffolds (Figure 5A). In contrast, CNTT−BGN scaffolds released Si ions (Figure 5B) and the release rate has a similar temporal progression as the one reported on pure BGN by Zheng et al.,[40] though with a slightly lower release rate than our scaffolds. Zheng at al. carried out their experiments in Dulbecco's modified Eagle's medium (DMEM), whereas we used PBS. The ions in DMEM could cause the formation of an amorphous Ca-P layer on the surface of BGN,[40] thus leading to a decreased release rate.

2.5. In Vitro Bioactivity. A highly important indicator for the ability of scaffolds to integrate with bone is the formation of hydroxyapatite on the scaffolds. On our samples, needle-shaped crystals are formed on CNTT−BGN scaffolds after immersion in a simulated body fluid (SBF) for 7 days (Figure 6A), whereas such crystals are neither observed on CNTT−HA nor on CNTT−BGN/HA scaffolds after immersion in the SBF. (Figure 6B,C). To explain this, we checked the results from energy dispersive X-ray spectroscopy (EDS). Our EDS results

DOI: 10.1021/acsami.8b13631
ACS Appl. Mater. Interfaces 2018, 10, 43874−43886

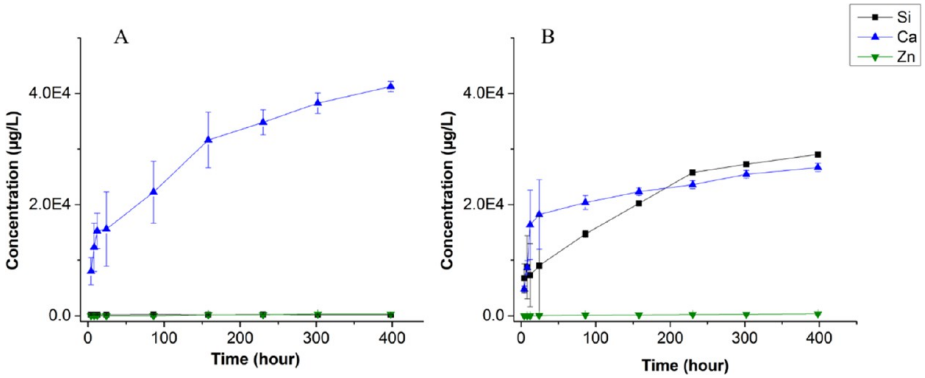

Figure 5. Mean values of ion release from CNTT−HA (A) and CNTT−BGN (B), measured by ICP-mass spectrometry (mean values). The concentration of released Zn, Ca, and Si ions from immersed CNTT−HA and CNTT−BGN structures in phosphate buffer saline represents the degradation rate of the bioactive ceramics. The concentration of Zn ions was measured to quantify the amount of residual ZnO from the fabrication process. (Each experiment was carried out using three samples. Error bars: standard deviation.)

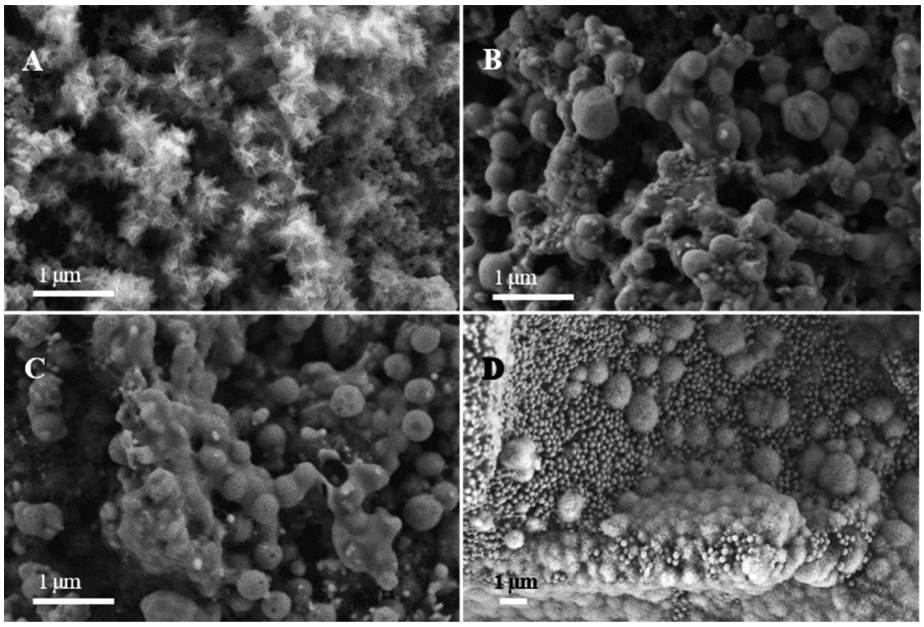

Figure 6. SEM images of the scaffolds after immersion in the SBF. (A) CNTT−BGN in SBF for 7 days; (B) CNTT−HA in SBF for 7 days; (C) CNTT−BGN/HA in SBF for 7 days; (D) CNTT−BGN in SBF for 14 days. SEM images plus EDS results (Supporting Information, Figure S1) confirm the formation of biomineralized hydroxyapatite.

(Supporting Information, Figure S1) show that phosphorus is present on the surface of CNTT−BGN filaments after immersion in the SBF for 7 days, which indicates the formation of calcium phosphate species.

Additionally, silicon is still present according to the EDS spectrum of CNTT−BGN indicating that BGN have not completely dissolved yet after 7 days of immersion in SBF. After immersion in SBF for 14 days, cauliflower-like crystals are present on CNTT−BGN scaffolds (Figure 6D). This is a typical morphology of hydroxyapatite crystals formed on BG scaffolds after immersion in SBF.[51] In addition, spherical BGN are still present on these scaffolds, showing that the time until full dissolution of the BGN is longer than 14 days. In general, BG is more surface reactive and has a higher dissolvability than other bioceramics (e.g., HA).[52] Therefore, the formation of bone-like apatite crystals, which is a result of surface dissolution and ion exchange, occurs faster on BG surfaces than on HA surfaces in body fluids. In the study presented here, the apatite forming ability of the scaffolds was improved after coating of BGN in comparison with HA nanoparticles, considering that the apatite crystals were observed on CNTT−BGN scaffolds after 7 days of soaking in SBF, whereas no crystals were present on CNTT−HA. As shown in Figure 6C, the situation for CNTT−BGN/HA is similar as for CNTT−HA. Inhibited apatite formation occurs when BGN are mixed with non-reactive or less reactive materials.[53] Our composite coating is like a glass-ceramic phase with less reactive surfaces, thus reducing the dissolution and ion exchange. The presence of HA in the coating also reduces the number of sites for apatite nucleation. Hence, apatite formation was inhibited in CNTT−BGN/HA scaffolds compared to CNTT−BGN. Interestingly, the formation of apatite crystals on our CNTT−BGN composite scaffolds took longer than when using pure BGN in SBF, where crystals had formed after 3 days of immersion.[40] This result can be explained

DOI: 10.1021/acsami.8b13631
ACS Appl. Mater. Interfaces 2018, 10, 43874−43886

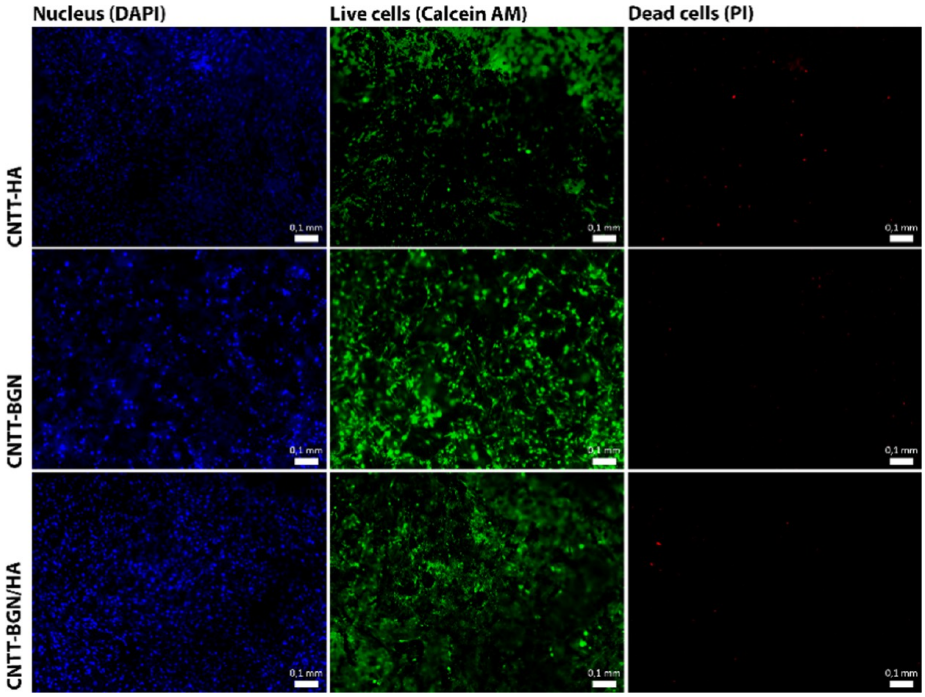

Figure 7. Fluorescence images of pre-osteoblast cells (MC3T3-e1) cultured for 21 days on CNTT−HA, CNTT−BGN, and CNTT−BGN/HA structures. The nucleus of the cells was stained with 4,6-diamidino-2-phenylindole (DAPI) (Hoechst), live cells with calcein AM (green), and dead cells with propidium iodide (red). All the scaffolds support osteoblast adhesion and proliferation. There is only a small number of dead cells after 21 days of cultivation (scale bars: 0.1 mm).

by the etching/sintering process that is necessary to remove the ZnO templates and caused the partial crystallization of BGN. The XRD result (Figure 3) shows the formation of α-quartz phase in BGN. Such a partial crystallization should not eliminate the biodegradability and bioactivity of BGN.[54] BGN maintain their bioactivity and biodegradability, though these properties could be inhibited.[55] Nevertheless, the BGN coating promotes the bioactivity and can therefore also be expected to improve the osteogenesis and osseointegration of our scaffolds.

2.6. Osteoblast and Fibroblast Growth on the Composite Scaffolds. The proliferation and adhesion of rat embryonic fibroblast and pre-osteoblastic cells (MC3T3-E1) on CNTT−HA, CNTT−BGN, and CNTT−BGN/HA were assessed individually using fluorescence microscopy. As the CNTT scaffolds absorb light almost completely,[56] optical imaging was restricted to approximately the first 200 μm from the surface. A long-term (21 days) in vitro study of MC3T3-E1 cells with our fabricated scaffolds revealed a surprisingly low number of dead cells in comparison to live cells (Figure 7) and that the scaffolds support osteoblast growth and adhesion. In addition, pre-osteoblasts appear to be well supported by all the scaffolds as well.

To investigate cell adhesion further, we also checked the adhesion of REF52 cells stably transfected with YFP-paxillin.[57] Paxillin is an essential part of the fibroblast adhesion machinery.[58] After 4 days of cultivation, fibroblast cells had well-adhered on all scaffold types (CNTT−BGN, CNTT−HA, CNTT−BGN/HA) (Figure 8). Imaging the paxillin fluorescence from adhesion clusters shows tiny and blurry spots (Figure 8A3−F3). Actin fibers are arranged in a meshed-form fibroblast cytoskeleton rather than stress fibers on all of our scaffolds (Figure 8A1−F1). Such a mesh-like arrangement of actin is typical for fibroblast adhesion in three dimensions.[50,59−61]

To investigate cell morphology in our 3D scaffold materials, we studied cell shape and morphology via SEM (Figure 9). SEM micrographs reveal that the cells were stretched and spanned between filaments on all scaffolds. Interestingly, most of the fibroblast cells are stretched between two or three filaments, leading to large cell membrane extensions. A comparison of the SEM images with fluorescence images shows that the cells within the scaffolds are associated with scaffold microtubes and developed physical contact with scaffold filaments (Figure 9, right column), especially with the CNT matrix. In addition, the actin fiber meshes are elongated between microtubes of the scaffolds (Figure 8). This is in agreement with SEM images (Figure 9) of fibroblasts on all scaffold types, as membrane projections attach to the microtubes of the scaffold. Despite the ability of the fibroblasts to adhere to the scaffolds, an methylthiazolyldiphenyl-tetrazolium bromide (MTT) assay (Figure 10) revealed a 5−20% lower growth rate for fibroblasts compared to the negative control after 1 day of incubation. Fibroblasts and fibroblast growth factors have an ambivalent impact on bone growth and osteogenesis. On the one hand, fibroblast growth factors increase the proliferation of immature osteoblasts,[62] whereas fibroblast growth factors cause apoptosis in differentiated osteoblasts and block mineralization,[62−64] and fibroblasts inhibit biomineralized bone nodule formation.[65] As fibroblasts adhere very well to our materials (Figures 8 and 9), we assume that our material is feasible for tissue engineering applications.

3. CONCLUSIONS

In summary, we have demonstrated a simple and efficient strategy to fabricate highly porous composite scaffolds made of self-entangled CNTs in microtube structures with incorporated bioactive ceramic nanoparticles (BGN and HA). These

DOI: 10.1021/acsami.8b13631
ACS Appl. Mater. Interfaces 2018, 10, 43874−43886

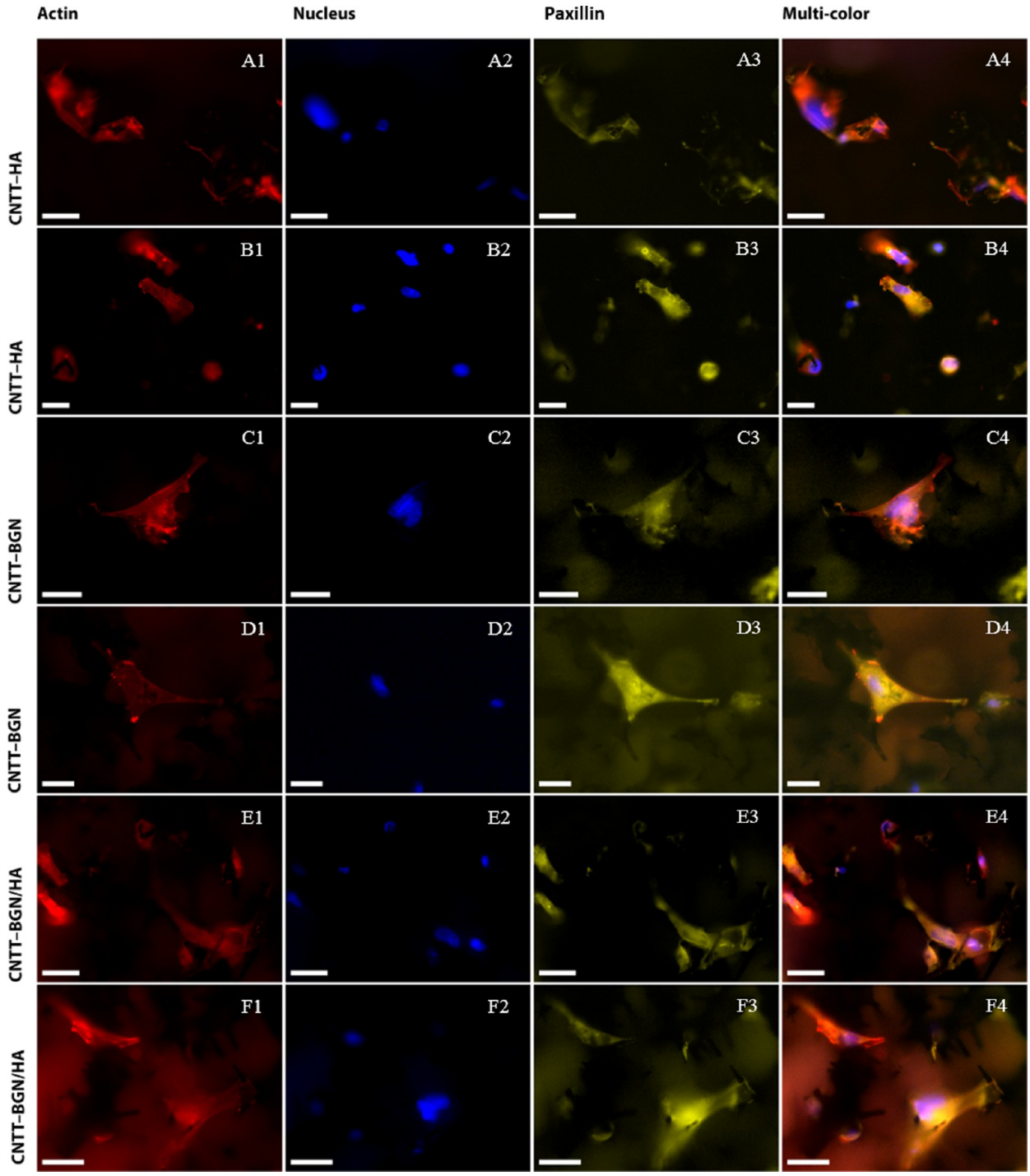

Figure 8. Fluorescence images of rat embryonic fibroblasts cultivated for 4 days on CNTT−HA (row A, B), CNTT−BGN (row C, D), and CNT−BGN/HA (row E, F) scaffolds. YFP-paxillin transfected REF cells (focal adhesion sites; yellow) were stained with DAPI (nuclei; blue) and phalloidin (actin filament; red). Fluorescence imaging took place in optical sections of 200 μm from the surface inside the material. Small paxillin clusters are visible in each optical focal plane. Imaging of actin reveals spanned cells with actin meshes. To show more details, fluorescence images of two different regions of each scaffold are shown in two rows (scale bars: 10 μm).

nanoparticles have been chosen to promote bone tissue ingrowth. To prepare the scaffolds, we have employed a H_2 thermal reduction process to etch ZnO and sinter BG or HA nanoparticles in a single step. The preferential removal of the ZnO template by the H_2 etching/sintering process offers the opportunity of implementing a variety of ceramic nanoparticles into the highly porous 3D networks for the fabrication of diverse hybrid composite structures. Moreover, we have proven that the incorporation of BGN and HA nanoparticles leads to biomineralization of the scaffolds. Apart from its bioactivity, the great advantage of our scaffolds compared to other 3D carbon-based porous structures is that its stiffness and porosity

DOI: 10.1021/acsami.8b13631
ACS Appl. Mater. Interfaces 2018, 10, 43874−43886

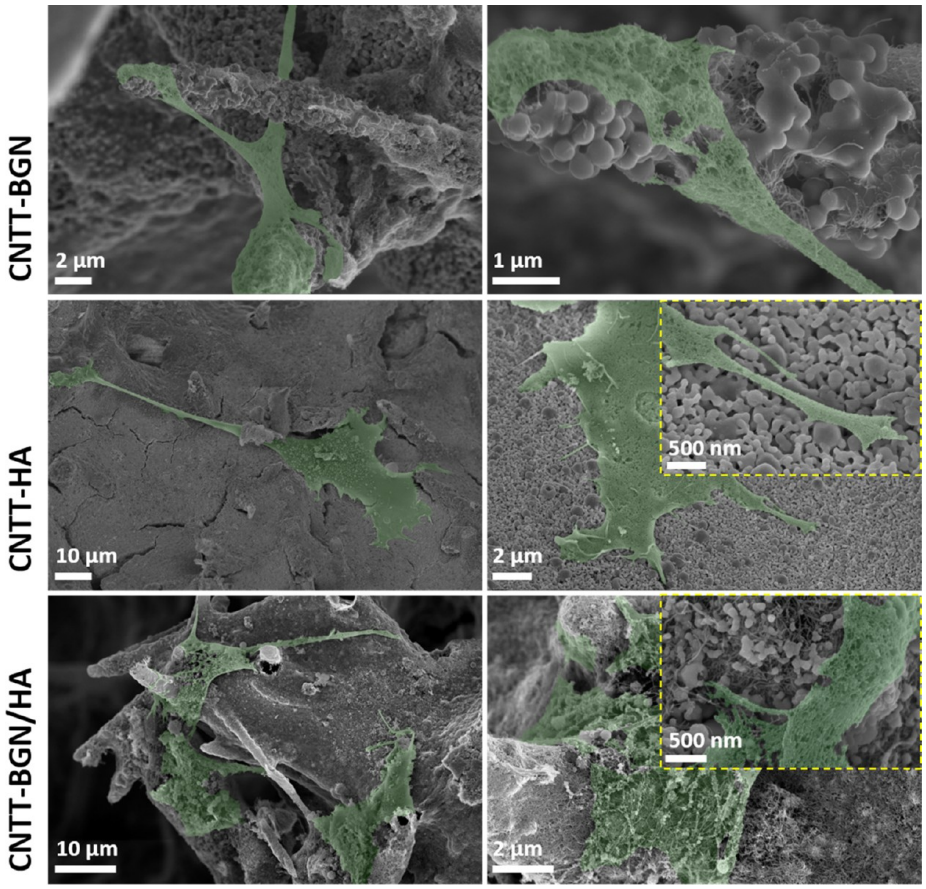

Figure 9. SEM micrographs of rat embryonic fibroblasts (colored in green) cultivated for 4 days on CNTT−BGN, CNTT−HA, and CNTT−BGN/HA scaffolds. Onto all types of structures cell membranes are extended and many adhesion sites are developed. The cells are mainly isolated and stretched. In the top right image, the fibroblast cell adhered preferentially to CNTs in the presence of CNT and BGN. Nevertheless, they adhered to HA even in those areas where CNTs are locally covered with HA nanoparticles (image to the right, middle row).

can in principle be tuned. The hollow microtubes lead to a low density of the scaffolds, and thus to an increase in ion release and electrical conductivity per scaffold weight. In addition, the hollow microtubes can serve as channels for nutrient transport and in future studies might also be filled with drugs or growth factors. The spatial architecture of fibers in the fabricated structures provides large free space for cell adhesion and both osteoblasts and fibroblasts were capable of adhesion to the scaffolds and stretched out along the fibers. The bioactivity of the scaffolds together with the electrical conductivity of the CNTT backbone makes them promising candidates for applications where porous 3D architectures are essential for cell growth, stimulation, function, or biomineralization, e.g., in bone tissue engineering.

4. MATERIALS AND METHODS

4.1. Fabrication of Bioactive Scaffolds. The fabrication of the bioactive cell scaffold materials is based on infiltrating the bioactive material into a highly porous (~94%) ceramic sacrificial template. For fabricating this template, tetrapodal-shaped ZnO microparticles (t-ZnO) were prepared using a flame transport approach as described by Mishra et al.[66] To interconnect the microparticles, the loose powder was pressed into a cylindrical cast (diameter: 12 mm; height: 2 mm) and sintered at around 1150 °C for 5 h to form a 3D template.[27]

BGN with a nominal composition of $70SiO_2$−30CaO (in mol %) and a particle diameter of ~400 nm were synthesized by a sol−gel method as described by Zheng et al.[40] Hydroxyapatite (HA) nanoparticles were bought from Sigma (nanopowder, <200 nm). CNTs were purchased from Carbobyk (CARBOBYK-9810). The zinc oxide (ZnO) templates were coated with such nanoparticles using an infiltration process recently described by Schütt et al.[26] The ceramic nanoparticles (BGN and HA) with a concentration of 214.28 ± 11.9 mg/cm^3 were dispersed in absolute ethanol (Sigma, Germany). Due to the high porosity (~94%) of the template and its superhydrophilic properties, nanoparticle dispersions are rapidly sucked into the template and a homogenous coverage is achieved after evaporation of the solvent. This process can be repeated several times to increase the amount of infiltrated nanoparticles. It is also possible to infiltrate different nanoparticle types in sequence so that a composite layer is formed around the template structure. Here, the templates were alternately infiltrated with a 1 wt % aqueous carbon nanotube (CNT) dispersion and a 4 wt % ceramic nanomaterial (HA or BGN) dispersion (in ethanol). The concentration of the ceramic nanoparticles was the same both for HA and BGN 214.28 ± 11.9 mg/cm^3, whereas different CNT concentrations between 32.14 ± 1.78 and 75.00 ± 4.16 mg/cm^3 were tested. After finishing the infiltration procedure, the ZnO template was removed by H_2 etching. To do so, the samples were placed in a sealed quartz tube furnace and the air was replaced by pure argon. The pressure was adjusted to 200 mbar. Subsequently, the temperature was increased to 900 °C. Then, an evaporator (170 °C) was used to decompose urea into ammonia (NH_3).[67] At 900 °C ammonia decomposes to N and H_2, thereby etching the ZnO template, resulting in free-standing, fibrous composite structures of CNTs with bioactive nanoparticles. Depending on the content of the composite scaffolds, they are called CNTT−BGN (free-standing CNT networks with BGN), CNTT−HA (free-standing CNT networks with hydroxyapatite

DOI: 10.1021/acsami.8b13631
ACS Appl. Mater. Interfaces 2018, 10, 43874−43886

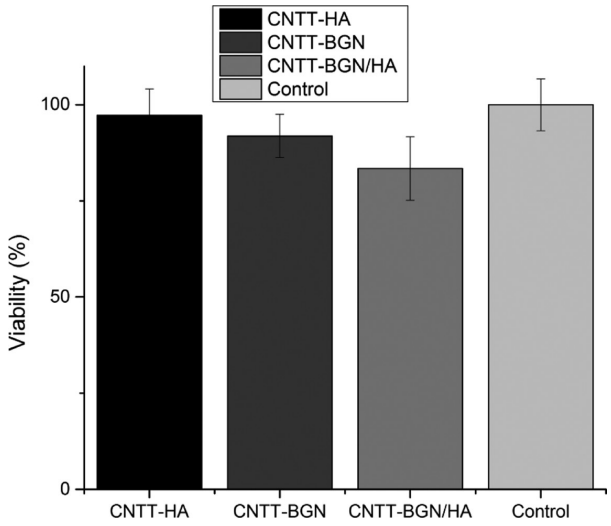

Figure 10. Cell viability of rat embryonic fibroblasts (REF52wt) treated with extractions of CNTT−BGN, CNTT−HA, and CNTT−BGN/HA, measured via an MTT−formazan absorbance assay. Fresh and untreated culture medium served as control. The result of this MTT assay reveals a small decrease in the fibroblast proliferation rate on CNTT−BGN and CNTT−HA, which is more pronounced for the combined structure containing both HA and BGN (CNTT−BGN/HA). (Each experiment was carried out in five technical repeats with three extractions for each sample. Error bars: standard deviation.)

nanoparticles), CNTT−BGN/HA (free-standing CNT networks with both BG and hydroxyapatite nanoparticles).

4.2. Characterization. The porosity of the scaffolds is obtained as follows: a defined amount of tetrapodal ZnO powder (here: 0.068 g) is pressed into a cylindrical shape (12 mm diameter; 6 mm height). The resulting volume is ∼0.226 cm^3 and leads to a density of around 0.3 g/cm^3. Since the bulk density of ZnO is 5.61 g/cm^3, the porosity is ∼94% for the ZnO template. For the preparation of the bioactive scaffolds, a CNT dispersion of 1 wt % and a BGN or HA dispersion of 4 wt % were used and infiltrated into the ZnO templates. The amount of infiltrated dispersion was adjusted to the amount, which was needed to completely fill the free volume of the template (∼230 μL).

The porosities of the final scaffold materials were calculated as follows: by adding 230 μL of a 1 wt % CNT dispersion, around 2.3 mg of CNTs are added to the network. Considering the density for CNTs to be 1.4 g/cm^3 (which is already quite a high value for MWCNTs) the additional volume is around 0.0016 cm^3 for each infiltration. By the addition of 230 μL HA or BGN dispersion 9.2 mg are added. Considering the densities of BG and HA to be in the range of 2−6 g/cm^3, we obtain an additional volume of 0.0015−0.0046 cm^3. Therefore, in the case of a template that was infiltrated five times with a 1 wt % CNT dispersion and five times with a 4 wt % HA or BGN dispersion, we obtain a porosity between 86 and 93% (depending on the density of HA, as given by the manufacturer). More information is shown in the Supporting Information (Table S1).

Electrical characterization was performed using a Keithley 6400 source-meter, which is controlled by a self-written LabView program, capable of measuring *IV* curves. Therefore, a sample holder was used in which the flat sides of the cylindrical samples (d = 6 mm, h = 3 mm) were connected to copper plates. To ensure a good contact between the copper plates and the sample surface, conductive silver paste was used at the interface. To avoid any electrical contact between the sample holder and the copper plates, Kapton tape was used as an insulator (Figure S2). The current was measured as a function of applied voltage (from −1 to +1 V using a step size of 0.1 V).

Mechanical characterization was performed with a self-built setup consisting of a Märzhäuser Wetzlar HS 6.3 micromanipulator, which is driven by a stepper motor and a load cell (Burster präzisionsmestechnik GmbH & Co KG, type 8523-5050). A self-written LabView program is used to control all components and measure the force. To avoid any vibration damping, the whole setup is located on a very rigid aluminum plate in a box filled with sand, which is mounted on a vibration isolated table. For the compression tests, the samples were placed in between the micromanipulator and the load cell. The samples were compressed by 2000 μm with a rate of ∼66.67 μm/s and the force was measured using the load cell. Finally, the stress−strain curves are evaluated and the compressive strength was determined (Figure S3).

4.3. Protein Adsorption Rate. Bovine serum albumin (Pierce; Thermo Fisher, Germany) was used to test the protein adsorption capacity of the scaffolds. Quantification was carried out using bicinchoninic acid (BCA; Thermo Fisher, Germany) in a colorimetric detection assay. For this, each scaffold type was immersed and incubated with 200 μL of bovine serum albumin (BSA) solution (1 mg/mL) for 4, 8, 12, 24, 48, and 72 h. Next, the supernatant was removed and mixed with 200 μL working reagent (Pierce; Thermo Fisher, Germany 23225). After 30 min of incubation, the protein concentration in the supernatant was quantified by a colorimetric microplate reader (BioTek uQuant) at 570 nm. Adsorption values were calculated by subtracting the measured protein concentration in the supernatant from the initial protein concentration in the protein solution before adding to the samples (1 mg/mL).

4.4. In Vitro Apatite Formation. The ability of the scaffolds to form apatite in vitro was evaluated by immersing the scaffolds into the simulated body fluid (SBF) according to the protocol proposed by Kokubo et al.[68] Briefly, the scaffolds were incubated in the SBF at a ratio of 1 mg/mL at 37 °C and stirred at 90 rpm for up to 14 days. The SBF was replaced once a week during the incubation period. At every predetermined time point, the scaffolds were removed from the SBF, gently rinsed with deionized water, dehydrated with acetone, and dried at 60 °C for 12 h. The apatite formation on the scaffolds was assessed by field emission scanning electron microscopy (FE-SEM; Auriga, Carl Zeiss) and energy dispersive X-ray spectroscopy (EDS; X-Max^N Oxford Instruments).

4.5. Quantification of Ion Release. The concentration of ions released from the scaffolds during incubation in PBS (Biochrom, Germany) at different time points was analyzed with inductively coupled plasma mass spectrometry (ICP-MS). In brief, 15 mg of scaffold material was placed in 1× PBS for 4, 8, 12, and 24 h at 37 °C as a short-term experiment. In a long-term experiment the amount of released ions was measured every 3 days under the same conditions. For measuring ion release, PBS was extracted and the samples were immersed in fresh PBS. The extracts were acidified by 20 μL of nitric acid (Sigma, Germany). Acidified pure PBS was used as the control and the ion concentrations in pure PBS were subtracted from the ion concentrations measured in extractions to receive the ions released from the scaffolds.

4.6. Sample Preparation for Transmission Electron Microscopy (TEM). A tiny piece of a scaffold was crushed and dispersed in butanol prior to dropping small crumbs on TEM grids. Then the micrographs of structures were taken by TEM (JEOL JEM-2100) at 200 kV.

4.7. Cell Adhesion Assays. *4.7.1. Fibroblasts.* The scaffolds (CNTT−BGN, CNTT−HA, CNTT−BGN/HA) were autoclaved at 121 °C and afterwards soaked in DMEM supplemented (Biochrom, Germany) with 10% fetal bovine serum (FBS, Biochrom, Germany) and 1% penicillin/streptomycin (Sigma, Germany). Approximately 10 000 rat embryonic fibroblast cells were seeded on each sample. The cells were incubated on the scaffolds for 4 days at 37 °C and 5% CO_2. Afterwards, they were fixed by paraformaldehyde (Thermo Fisher, Germany) and dried using critical point drying (EMS 3000). Prior to scanning electron microscopy (Ultra Plus Zeiss SEM, 5 kV), the cells were coated with a thin sputtered gold layer (Bal-Tec SCD 050, 30 mA, 30 s).

Cell morphology, adhesion, and cytoskeleton were investigated by fluorescently staining cell nuclei and stress fibers. Cell nuclei were stained with DAPI (Thermo Fisher, Germany), which binds to DNA, and stress fibers were stained with Phalloidin (Alexa Fluor 647 Phalloidin, Thermo Fisher, Germany), which binds to the F-actin of the

DOI: 10.1021/acsami.8b13631
ACS Appl. Mater. Interfaces 2018, 10, 43874−43886

cytoskeleton. Images of the stained cells were recorded using a fluorescence microscope (Olympus IX81, camera: Hamamatsu, UV lamp: Lumencor).

4.7.2. Osteoblasts. The adhesion of osteoblast-like MC3T3-E1 to the scaffolds was visualized by detecting the filamentous actin of the cytoskeleton of cells on the scaffolds. Live/dead staining was carried out to assess the cytotoxicity of the scaffolds. In brief, the scaffolds were immersed into MEM (Biochrom, Germany) to stabilize the pH value prior to the seeding of cells on the scaffolds. After the pre-treatment, 0.2 mL of MC3T3-E1 cell suspension (2×10^5 cells/mL) was added on the scaffolds (in 24-well plates). After 3 h of incubation, an additional 1.8 mL of MEM was added. The culture medium was changed every 2 days. To minimize the influence of cells adhering to the bottom surface of the well during cultivation, the scaffolds were placed into new wells of a 24-well-plate when exchanging the medium. After 21 days of culture, cell adhesion on the scaffolds was visualized by staining. Cell nuclei were stained by 4,6-diamidino-2-phenylindole (DAPI, dilactate, Invitrogen), whereas the live/dead assay was carried out using calcein (Thermo Fisher, Germany) and propidium iodide (Thermo Fisher, Germany), according to the manufacturer's protocol. Images of the fluorescently stained MC3T3-E1 cells were taken by a fluorescence microscope (Axio Scope A.1, Carl Zeiss Microimaging GmbH, Germany).

4.8. MTT Assay. The viability of fibroblast cells on the scaffolds was quantified according to the ISO 10993 norm. In brief, extractions were prepared by incubating the scaffolds at 37 °C in 1 mL culture medium (DMEM supplemented with 10% FBS and 1% penicillin/streptomycin) for 72 h. 10 000 REF52wt cells were cultured with 100 μL of medium for 24 h. The supernatant was replaced with 100 μL of extraction medium, then the cells were incubated for 24 h at 37 °C again. The number of vital cells incubated with the extraction medium was measured by adding 50 μL of methylthiazolyldiphenyl-tetrazolium bromide (MTT; Sigma-Aldrich, Germany) solution. After 4 h of incubation the absorbance was measured at 570 and 620 nm as a reference. Fresh and untreated culture medium was used as a negative control and medium containing 20% dimethyl sulfoxide as a positive control. The results were normalized to the absorbance measured in the controls. Five technical repeats were carried out in three independent experiments.

■ ASSOCIATED CONTENT

Supporting Information

The Supporting Information is available free of charge on the ACS Publications website at DOI: 10.1021/acsami.8b13631.

EDS results of the scaffolds after immersion in simulated body fluid, further data on the scaffolds (e.g., density, porosity) (PDF)

■ AUTHOR INFORMATION

Corresponding Author

*E-mail: cse@tf.uni-kiel.de.

ORCID

Fabian Schütt: 0000-0003-2942-503X
Kai Zheng: 0000-0002-2573-6677
Yogendra Kumar Mishra: 0000-0002-8786-9379
Aldo R. Boccaccini: 0000-0002-7377-2955
Christine Selhuber-Unkel: 0000-0002-5051-4822

Notes

The authors declare no competing financial interest.

■ ACKNOWLEDGMENTS

C.S.-U. and M.T. acknowledge funding from the European Research Council (Proof of Concept Grant 768740, Starting Grant 336104) and the German Research Foundation (SFB 1261, Project B7). M.T. was supported by the Deutscher Akademischer Austauschdienst (DAAD) through a research grant for doctoral candidates (91526555-57048249). In addition, R.A. gratefully acknowledges partial project funding by the Deutsche Forschungsgemeinschaft in the scope of contract Ad 183-17/1 and the research training group GRK 2154, as well. We gratefully acknowledge support from Prof. Dr. Dieter Garbe-Schönberg and Ulrike Westernströer in the ICP-mass spectrometry measurements. We also acknowledge Galen Ream for critical proofreading.

■ ABBREVIATIONS

3D, three-dimensional
CNT, carbon nanotube
ZnO, zinc oxide
HA, hydroxyapatite
BGN, bioactive glass nanoparticles
BG, bioactive glass
CaO, calcium oxide
CNTT, hierarchical carbon nanotube tube networks
SEM, scanning electron microscopy
TEM, transmission electron microscopy
XRD, X-ray diffraction
CNTT−BGN, CNT-based tubes containing bioactive glass nanoparticles
CNTT−HA, CNT-based tubes containing hydroxyapatite nanoparticles
CNTT−BGN/HA, CNT-based tubes containing both bioactive glass and hydroxyapatite nanoparticles
t-ZnO, tetrapodal zinc oxide
BSA, bovine serum albumin
SBF, simulated body fluid
ICP-MS, inductively coupled plasma mass spectrometry
PBS, phosphate buffered saline
REF52wt, rat embryonic fibroblasts 52 wild type

■ REFERENCES

(1) Gu, Y.; Wang, G.; Zhang, X.; Zhang, Y.; Zhang, C.; Liu, X.; Rahaman, M. N.; Huang, W.; Pan, H. Biodegradable Borosilicate Bioactive Glass Scaffolds with a Trabecular Microstructure for Bone Repair. *Mater. Sci. Eng., C* **2014**, *36*, 294−300.

(2) Gerhardt, L.-C.; Boccaccini, A. R. Bioactive Glass and Glass-Ceramic Scaffolds for Bone Tissue Engineering. *Materials* **2010**, *3*, 3867−3910.

(3) Rahaman, M. N.; Day, D. E.; Sonny Bal, B.; Fu, Q.; Jung, S. B.; Bonewald, L. F.; Tomsia, A. P. Bioactive Glass in Tissue Engineering. *Acta Biomater.* **2011**, *7*, 2355−2373.

(4) Hoppe, A.; Güldal, N. S.; Boccaccini, A. R. A Review of the Biological Response to Ionic Dissolution Products from Bioactive Glasses and Glass-Ceramics. *Biomaterials* **2011**, *32*, 2757−2774.

(5) Roether, J. A.; Boccaccini, A. R.; Hench, L. L.; Maquet, V.; Gautier, S.; Jérôme, R. Development and in Vitro Characterisation of Novel Bioresorbable and Bioactive Composite Materials Based on Polylactide Foams and Bioglass for Tissue Engineering Applications. *Biomaterials* **2002**, *23*, 3871−3878.

(6) Turk, M.; Deliormanlı, A. M. Electrically Conductive Borate-Based Bioactive Glass Scaffolds for Bone Tissue Engineering Applications. *J. Biomater. Appl.* **2017**, *32*, 28−39.

(7) Lin, Y.; Xiao, W.; Bal, B. S.; Rahaman, M. N. Effect of Copper-Doped Silicate 13−93 Bioactive Glass Scaffolds on the Response of MC3T3-E1 Cells in Vitro and on Bone Regeneration and Angiogenesis in Rat Calvarial Defects in Vivo. *Mater. Sci. Eng., C* **2016**, *67*, 440−452.

(8) Axrap, A.; Wang, J.; Liu, Y.; Wang, M.; Yusuf, A. Study on Adhesion, Proliferation and Differentiation of Osteoblasts Promoted by New Absorbable Bioactive Glass Injection in Vitro. *Eur. Rev. Med. Pharmacol. Sci.* **2016**, *20*, 4677−4681.

DOI: 10.1021/acsami.8b13631
ACS Appl. Mater. Interfaces 2018, 10, 43874−43886

(9) Yu, C.; Zhuang, J.; Dong, L.; Cheng, K.; Weng, W. Effect of Hierarchical Pore Structure on ALP Expression of MC3T3-E1 Cells on Bioglass Films. *Colloids Surf., B* **2017**, *156*, 213−220.
(10) Bellucci, D.; Sola, A.; Anesi, A.; Salvatori, R.; Chiarini, L.; Cannillo, V. Bioactive Glass/Hydroxyapatite Composites: Mechanical Properties and Biological Evaluation. *Mater. Sci. Eng., C* **2015**, *51*, 196−205.
(11) Suchanek, W.; Yoshimura, M. Processing and Properties of Hydroxyapatite-Based Biomaterials for Use as Hard Tissue Replacement Implants. *J. Mater. Res.* **1998**, *13*, 94−117.
(12) Venkatesan, J.; Kim, S. K. Carbon Nanotube for Bone Repair. In *Handbook of Polymer Nanocomposites. Processing, Performance and Application*; Springer: Berlin, 2015; pp 511−526.
(13) Schausten, M. C.; Meng, D.; Telle, R.; Boccaccini, A. R. Electrophoretic Deposition of Carbon Nanotubes and Bioactive Glass Particles for Bioactive Composite Coatings. *Ceram. Int.* **2010**, *36*, 307−312.
(14) Touri, R.; Moztarzadeh, F.; Sadeghian, Z.; Bizari, D.; Tahriri, M.; Mozafari, M. The Use of Carbon Nanotubes to Reinforce 45S5 Bioglass-Based Scaffolds for Tissue Engineering Applications. *Biomed. Res. Int.* **2013**, *2013*, No. 465086.
(15) Gao, C.; Feng, P.; Peng, S.; Shuai, C. Carbon Nanotube, Graphene and Boron Nitride Nanotube Reinforced Bioactive Ceramics for Bone Repair. *Acta Biomater.* **2017**, *61*, 1−20.
(16) Porwal, H.; Estili, M.; Grünewald, A.; Grasso, S.; Detsch, R.; Hu, C.; Sakka, Y.; Boccaccini, A. R.; Reece, M. J. 45S5 Bioglass−MWCNT Composite: Processing and Bioactivity. *J. Mater. Sci.: Mater. Med.* **2015**, *26*, 199.
(17) Doostmohammadi, A.; et al. Fabrication of Chitosan/Poly (Vinyl Alcohol)/Carbon Nanotube/Bioactive Glass Nanocomposite Scaffolds for Neural Tissue Engineering. *J. Nanomed. Res.* **2016**, *4*, No. 00088.
(18) Chen, Q.; Garcia, R. P.; Munoz, J.; Pérez De Larraya, U.; Garmendia, N.; Yao, Q.; Boccaccini, A. R. Cellulose Nanocrystals-Bioactive Glass Hybrid Coating as Bone Substitutes by Electrophoretic Co-Deposition: In Situ Control of Mineralization of Bioactive Glass and Enhancement of Osteoblastic Performance. *ACS Appl. Mater. Interfaces* **2015**, *7*, 24715−24725.
(19) Han, B.; Zhang, X.; Liu, H.; Deng, X.; Cai, Q.; Jia, X.; Yang, X.; Wei, Y.; Li, G. Improved Bioactivity of PAN-Based Carbon Nanofibers Decorated with Bioglass Nanoparticles. *J. Biomater. Sci., Polym. Ed.* **2014**, *25*, 341−353.
(20) Miguez-Pacheco, V.; Hench, L. L.; Boccaccini, A. R. Bioactive Glasses beyond Bone and Teeth: Emerging Applications in Contact with Soft Tissues. *Acta Biomater.* **2015**, *13*, 1−15.
(21) Newman, P.; Lu, Z.; Roohani-Esfahani, S. I.; Church, T. L.; Biro, M.; Davies, B.; King, A.; Mackenzie, K.; Minett, A. I.; Zreiqat, H. Porous and Strong Three-Dimensional Carbon Nanotube Coated Ceramic Scaffolds for Tissue Engineering. *J. Mater. Chem. B* **2015**, *3*, 8337−8347.
(22) Hollister, S. J. Porous Scaffold Design for Tissue Engineering. *Nat. Mater.* **2005**, *4*, 518−524.
(23) Loh, Q. L.; Choong, C. Three-Dimensional Scaffolds for Tissue Engineering Applications: Role of Porosity and Pore Size. *Tissue Eng., Part B* **2013**, *19*, 485−502.
(24) Mota, C.; Puppi, D.; Chiellini, F.; Chiellini, E. Additive Manufacturing Techniques for the Production of Tissue Engineering Constructs. *J. Tissue Eng. Regener. Med.* **2015**, *9*, 174−190.
(25) Chia, H. N.; Wu, B. M. Recent Advances in 3D Printing of Biomaterials. *J. Biol. Eng.* **2015**, *9*, 4.
(26) Schütt, F.; Signetti, S.; Krüger, H.; Röder, S.; Smazna, D.; Kaps, S.; Gorb, S. N.; Mishra, Y. K.; Pugno, N. M.; Adelung, R. Hierarchical Self-Entangled Carbon Nanotube Tube Networks. *Nat. Commun.* **2017**, *8*, No. 1215.
(27) Mishra, Y. K.; Adelung, R. ZnO Tetrapod Materials for Functional Applications. *Mater. Today* **2018**, *21*, 631−651.
(28) Papavlassopoulos, H.; Mishra, Y. K.; Kaps, S.; Paulowicz, I.; Abdelaziz, R.; Elbahri, M.; Maser, E.; Adelung, R.; Röhl, C. Toxicity of Functional Nano-Micro Zinc Oxide Tetrapods: Impact of Cell Culture Conditions, Cellular Age and Material Properties. *PLoS One* **2014**, *9*, No. e84983.
(29) Mecklenburg, M.; Schuchardt, A.; Mishra, Y. K.; Kaps, S.; Adelung, R.; Lotnyk, A.; Kienle, L.; Schulte, K. Aerographite: Ultra Lightweight, Flexible Nanowall, Carbon Microtube Material with Outstanding Mechanical Performance. *Adv. Mater.* **2012**, *24*, 3486−3490.
(30) Correa-Duarte, M. A.; Wagner, N.; Rojas-Chapana, J.; Morsczeck, C.; Thie, M.; Giersig, M. Fabrication and Biocompatibility of Carbon Nanotube-Based 3D Networks as Scaffolds for Cell Seeding and Growth. *Nano Lett.* **2004**, *4*, 2233−2236.
(31) Rezwan, K.; Chen, Q. Z. Z.; Blaker, J. J. J.; Boccaccini, A. R. Biodegradable and Bioactive Porous Polymer/Inorganic Composite Scaffolds for Bone Tissue Engineering. *Biomaterials* **2006**, *27*, 3413−3431.
(32) Wu, Z. Y.; Hill, R. G.; Yue, S.; Nightingale, D.; Lee, P. D.; Jones, J. R. Melt-Derived Bioactive Glass Scaffolds Produced by a Gel-Cast Foaming Technique. *Acta Biomater.* **2011**, *7*, 1807−1816.
(33) Kankala, R. K.; Xu, X.-M.; Liu, C.-G.; Chen, A.-Z.; Wang, S.-B. 3D-Printing of Microfibrous Porous Scaffolds Based on Hybrid Approaches for Bone Tissue Engineering. *Polymers* **2018**, *10*, No. 807.
(34) Helguero, C. G.; Mustahsan, V. M.; Parmar, S.; Pentyala, S.; Pfail, J. P.; Kao, I.; Komatsu, D. E.; Pentyala, S. Biomechanical Properties of 3D-Printed Bone Scaffolds Are Improved by Treatment with CRFP. *J. Orthop. Surg. Res.* **2017**, *12*, No. 195.
(35) Rho, J. Y.; Kuhn-Spearing, L.; Zioupos, P. Mechanical Properties and the Hierarchical Structure of Bone. *Med. Eng. Phys.* **1998**, *20*, 92−102.
(36) Livingston, T.; Ducheyne, P.; Garino, J. In Vivo Evaluation of a Bioactive Scaffold for Bone Tissue Engineering. *J. Biomed. Mater. Res.* **2002**, *62*, 1−13.
(37) Huebsch, N.; Lippens, E.; Lee, K.; Mehta, M.; Koshy, S. T.; Darnell, M. C.; Desai, R. M.; Madl, C. M.; Xu, M.; Zhao, X.; Chaudhuri, O.; Verbeke, C.; Kim, W.; Alim, K.; Mammoto, A.; Ingber, D.; Duda, G. N.; Mooney, D. J. Matrix Elasticity of Void-Forming Hydrogels Controls Transplanted-Stem-Cell-Mediated Bone Formation. *Nat. Mater.* **2015**, *14*, 1269−1277.
(38) Fathi, M. H.; Hanifi, A. Evaluation and Characterization of Nanostructure Hydroxyapatite Powder Prepared by Simple Sol-Gel Method. *Mater. Lett.* **2007**, *61*, 3978−3983.
(39) Chen, Q. Z.; Thompson, I. D.; Boccaccini, A. R. 45S5 Bioglass-Derived Glass-Ceramic Scaffolds for Bone Tissue Engineering. *Biomaterials* **2006**, *27*, 2414−2425.
(40) Zheng, K.; Taccardi, N.; Beltrán, A. M.; Sui, B.; Zhou, T.; Marthala, V. R. R.; Hartmann, M.; Boccaccini, A. R. Timing of Calcium Nitrate Addition Affects Morphology, Dispersity and Composition of Bioactive Glass Nanoparticles. *RSC Adv.* **2016**, *6*, 95101−95111.
(41) Drisko, G. L.; Carretero-Genevrier, A.; Perrot, A.; Gich, M.; Gàzquez, J.; Rodriguez-Carvajal, J.; Favre, L.; Grosso, D.; Boissière, C.; Sanchez, C. Crystallization of Hollow Mesoporous Silica Nanoparticles. *Chem. Commun.* **2015**, *51*, 4164−4167.
(42) Liao, C. J.; Lin, F. H.; Chen, K. S.; Sun, J. S. Thermal Decomposition and Reconstruction of Hydroxyapatite in Air Atmosphere. *Biomed. Sci. Instrum.* **1999**, *35*, 99−104.
(43) Giovanardi, R.; Montorsi, M.; Ori, G.; Cho, J.; Subhani, T.; Boccaccini, A. R.; Siligardi, C. Microstructural Characterisation and Electrical Properties of Multiwalled Carbon Nanotubes/Glass-Ceramic Nanocomposites. *J. Mater. Chem.* **2010**, *20*, 308−313.
(44) Wang, K.; Zhou, C.; Hong, Y.; Zhang, X. A Review of Protein Adsorption on Bioceramics. *Interface Focus* **2012**, *2*, 259−277.
(45) Webster, T. J.; Ergun, C.; Doremus, R. H.; Siegel, R. W.; Bizios, R. Specific Proteins Mediate Enhanced Osteoblast Adhesion on Nanophase Ceramics. *J. Biomed. Mater. Res.* **2000**, *51*, 475−483.
(46) Lamprecht, C.; Huzil, J. T.; Ivanova, M. V.; Foldvari, M. Non-Covalent Functionalization of Carbon Nanotubes with Surfactants for Pharmaceutical Applications - A Critical Mini-Review. *Drug Delivery Lett.* **2011**, *1*, 45−57.
(47) Tso, S. T.; Pask, J. A. Reaction of Fused Silica With Hydrogen Gas. *J. Am. Ceram. Soc.* **1982**, *65*, 457−460.

DOI: 10.1021/acsami.8b13631
ACS Appl. Mater. Interfaces 2018, 10, 43874−43886

(48) El-Ghannam, A.; Hamazawy, E.; Yehia, A. Effect of Thermal Treatment on Bioactive Glass Microstructure, Corrosion Behavior ζ Potential, and Protein Adsorption. *J. Biomed. Mater. Res.* **2001**, *55*, 387−395.
(49) El-Ghannam, A.; Ducheyne, P.; Shapiro, I. M. Effect of Serum Proteins on Osteoblast Adhesion to Surface-Modified Bioactive Glass and Hydroxyapatite. *J. Orthop. Res.* **1999**, *17*, 340−345.
(50) Lamprecht, C.; Taale, M.; Paulowicz, I.; Westerhaus, H.; Grabosch, C.; Schuchardt, A.; Mecklenburg, M.; Böttner, M.; Lucius, R.; Schulte, K.; Adelung, R.; Selhuber-Unkel, C. A Tunable Scaffold of Microtubular Graphite for 3D Cell Growth. *ACS Appl. Mater. Interfaces* **2016**, *8*, 14980−14985.
(51) Zheng, K.; Wu, J.; Li, W.; Dippold, D.; Wan, Y.; Boccaccini, A. R. Incorporation of Cu-Containing Bioactive Glass Nanoparticles in Gelatin-Coated Scaffolds Enhances Bioactivity and Osteogenic Activity. *ACS Biomater. Sci. Eng.* **2018**, *4*, 1546−1557.
(52) Roohani-Esfahani, S. I.; Nouri-Khorasani, S.; Lu, Z. F.; Appleyard, R. C.; Zreiqat, H. Effects of Bioactive Glass Nanoparticles on the Mechanical and Biological Behavior of Composite Coated Scaffolds. *Acta Biomater.* **2011**, *7*, 1307−1318.
(53) Bellucci, D.; Desogus, L.; Montinaro, S.; Orrù, R.; Cao, G.; Cannillo, V. Innovative Hydroxyapatite/Bioactive Glass Composites Processed by Spark Plasma Sintering for Bone Tissue Repair. *J. Eur. Ceram. Soc.* **2017**, *37*, 1723−1733.
(54) Filho, O. P.; Latorre, G. P.; Hench, L. L. Effect of Crystallization on Apatite-Layer Formation of Bioactive Glass 45S5. *J. Biomed. Mater. Res.* **1996**, *30*, 509−514.
(55) Clupper, D. C.; Mecholsky, J. J.; LaTorre, G. P.; Greenspan, D. C. Bioactivity of Tape Cast and Sintered Bioactive Glass-Ceramic in Simulated Body Fluid. *Biomaterials* **2002**, *23*, 2599−2606.
(56) Popov, V. N. Carbon Nanotubes: Properties and Application. *Mater. Sci. Eng., R* **2004**, *43*, 61−102.
(57) Selhuber-Unkel, C.; Erdmann, T.; López-García, M.; Kessler, H.; Schwarz, U. S.; Spatz, J. P. Cell Adhesion Strength Is Controlled by Intermolecular Spacing of Adhesion Receptors. *Biophys. J.* **2010**, *98*, 543−551.
(58) Balaban, N. Q.; Schwarz, U. S.; Riveline, D.; Goichberg, P.; Tzur, G.; Sabanay, I.; Mahalu, D.; Safran, S.; Bershadsky, A.; Addadi, L.; Geiger, B. Force and Focal Adhesion Assembly: A Close Relationship Studied Using Elastic Micropatterned Substrates. *Nat. Cell Biol.* **2001**, *3*, 466−472.
(59) Fraley, S. I.; Feng, Y.; Wirtz, D.; Longmore, G. D. Reply: Reducing Background Fluorescence Reveals Adhesions in 3D Matrices. *Nat. Cell Biol.* **2011**, *13*, 5−7.
(60) Miyamoto, S.; Akiyama, S. K.; Yamada, K. M. Synergistic Roles for Receptor Occupancy and Aggregation in Integrin Transmembrane Function. *Science* **1995**, *267*, 883−885.
(61) Baker, B. M.; Chen, C. S. Deconstructing the Third Dimension − How 3D Culture Microenvironments Alter Cellular Cues. *J. Cell Sci.* **2012**, *125*, 3015−3024.
(62) Mansukhani, A.; Bellosta, P.; Sahni, M.; Basilico, C. Signaling by Fibroblast Growth Factors (FGF) and Fibroblast Growth Factor Receptor 2 (FGFR2)-Activating Mutations Blocks Mineralization and Induces Apoptosis in Osteoblasts. *J. Cell Biol.* **2000**, *149*, 1297−1308.
(63) Marie, P. J. Fibroblast Growth Factor Signaling Controlling Osteoblast Differentiation. *Gene* **2003**, *316*, 23−32.
(64) Debiais, F.; Hott, M.; Graulet, A. M.; Marie, P. J. The Effects of Fibroblast Growth Factor-2 on Human Neonatal Calvaria Osteoblastic Cells Are Differentiation Stage Specific. *J. Bone Miner. Res.* **1998**, *13*, 645−654.
(65) Ogiso, B.; Hughes, F. J.; Melcher, A. H.; McCulloch, C. A. G. Fibroblasts Inhibit Mineralised Bone Nodule Formation by Rat Bone Marrow Stromal Cells in Vitro. *J. Cell. Physiol.* **1991**, *146*, 442−450.
(66) Mishra, Y. K.; Modi, G.; Cretu, V.; Postica, V.; Lupan, O.; Reimer, T.; Paulowicz, I.; Hrkac, V.; Benecke, W.; Kienle, L.; Adelung, R. Direct Growth of Freestanding ZnO Tetrapod Networks for Multifunctional Applications in Photocatalysis, UV Photodetection, and Gas Sensing. *ACS Appl. Mater. Interfaces* **2015**, *7*, 14303−14316.
(67) Schaber, P. M.; Colson, J.; Higgins, S.; Thielen, D.; Anspach, B.; Brauer, J. Thermal Decomposition (Pyrolysis) of Urea in an Open Reaction Vessel. *Thermochim. Acta* **2004**, *424*, 131−142.
(68) Kokubo, T.; Takadama, H. How Useful Is SBF in Predicting in Vivo Bone Bioactivity? *Biomaterials* **2006**, *27*, 2907−2915.

DOI: 10.1021/acsami.8b13631
ACS Appl. Mater. Interfaces 2018, 10, 43874−43886

The Supporting Information is available in Appendix-D

Chapter 6

Systematically designed periodic electrophoretic deposition for decorating 3D carbon-based scaffolds with bioactive nanoparticles

Mohammadreza Taale, Diana Krüger, Emmanuel Ossei-Wusu, Fabian Schütt, Muhammad Atiq Ur Rehman, Yogendra Kumar Mishra, Janik Marx, Norbert Stock, Bodo Fiedler, Aldo R Boccaccini, Regine Willumeit-Römer, Rainer Adelung, Christine Selhuber-Unkel

ACS Biomaterials SCIENCE & ENGINEERING
Cite This: ACS Biomater. Sci. Eng. XXXX, XXX, XXX−XXX
Article
pubs.acs.org/journal/abseba

Systematically Designed Periodic Electrophoretic Deposition for Decorating 3D Carbon-Based Scaffolds with Bioactive Nanoparticles

Mohammadreza Taale,[†] Diana Krüger,[‡] Emmanuel Ossei-Wusu,[§] Fabian Schütt,[§] Muhammad Atiq Ur Rehman,[∥,⊥] Yogendra Kumar Mishra,[§] Janik Marx,[#] Norbert Stock,[▽] Bodo Fiedler,[#] Aldo R. Boccaccini,[∥] Regine Willumeit-Römer,[‡] Rainer Adelung,[§] and Christine Selhuber-Unkel*[,†]

[†]Biocompatible Nanomaterials, Institute for Materials Science, Kiel University, Kaiserstr. 2, D-24143 Kiel, Germany
[‡]Helmholtz-Zentrum Geesthacht, Institute of Materials Research, Division Metallic Biomaterials, Max-Planck-Str. 1, D-21502 Geesthacht, Germany
[§]Functional Nanomaterials, Institute for Materials Science, Kiel University, Kaiserstr. 2, D-24143 Kiel, Germany
[∥]Institute of Biomaterials, University of Erlangen-Nuremberg, Cauerstrasse 6, 91058 Erlangen, Germany
[⊥]Department of Materials Science and Engineering, Institute of Space Technology Islamabad, 1, Islamabad Highway, Islamabad 44000, Pakistan
[#]Institute of Polymer and Composites, Hamburg University of Technology, Denickestr. 15, D-21073 Hamburg, Germany
[▽]Institute of Inorganic Chemistry, Kiel University, Max-Eyth Straße 2, D-24118 Kiel, Germany

Supporting Information

ABSTRACT: The coating of porous scaffolds with nanoparticles is crucial in many applications, for example to generate scaffolds for catalysis or to make scaffolds bioactive. A standard and well-established method for coating surfaces with charged nanoparticles is electrophoresis, but when used on porous scaffolds, this method often leads to a blockage of the pores so that only the outermost layers of the scaffolds are coated. In this study, the electrophoretic coating process is monitored in situ and the kinetics of nanoparticle deposition are investigated. This concept can be extended to design a periodic electrophoretic deposition (PEPD) strategy, thus avoiding the typical blockage of surface pores. In the present work we demonstrate successful and homogeneous electrophoretic deposition of hydroxyapatite nanoparticles (HAn, diameter ≤200 nm) on a fibrous graphitic 3D structure (ultralightweight aerographite) using the PEPD strategy. The microfilaments of the resulting scaffold are covered with HAn both internally and on the surface. Furthermore, protein adsorption assays and cell proliferation assays were carried out and revealed that the HAn-decorated aerographite scaffolds are biocompatible. The HAn decoration of the scaffolds also significantly increases the alkaline phosphatase activity of osteoblast cells, showing that the scaffolds are able to promote their osteoblastic activity.

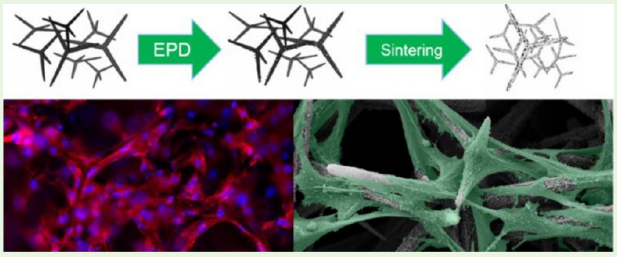

KEYWORDS: *tissue engineering, aerographite, hydroxyapatite, 3D scaffold, electrophoretic deposition, osteoblasts*

1. INTRODUCTION

Designing porous scaffolds with a high surface to weight ratio is important in many disciplines, including catalysis[1] and tissue engineering.[2] The functionality of such scaffolds could often be enhanced by integrating nanoparticles on their surfaces: For example, bioactive nanoparticles, such as hydroxyapatite nanoparticles (HAn), enhance bioactivity as well as osteogenic activity of biomaterials.[3,4]

When used in the context of tissue engineering, it is very important that the used scaffold structurally resembles tissue architecture and functionality. Therefore, biomaterial scaffolds that mimic the structure of extracellular matrix are highly promising candidates.[5] An example of such a biomaterial scaffold is aerographite (AG), which is a highly porous (up to 99.99%) fibrous carbon-based scaffold with a microstructure similar to that of collagen.[6] Furthermore, it can easily be biofunctionalized with cell adhesion ligands,[7] it is electrically conductive (0.5−3.5 S/m),[8] and of ultralight weight (<200 $\mu g/cm^3$).[9] Its fabrication is based on the usage of a sacrificial and highly porous (∼94%) zinc oxide (ZnO) tetrapod network, where a chemical vapor deposition process (CVD) adds a graphitic layer on the surface of the ZnO tetrapods and

Received: January 23, 2019
Accepted: June 13, 2019
Published: June 13, 2019

DOI: 10.1021/acsbiomaterials.9b00102
ACS Biomater. Sci. Eng. XXXX, XXX, XXX−XXX

the underneath ZnO is simultaneously removed by the precursor gases at high temperature in a CVD chamber.[9] When the surfaces of ZnO tetrapods are covered with nanoparticles in the template prior to the CVD procedure, the underlying ZnO is removed, but the integrated nanoparticles remain intact at the inner surface of hollow arms in the aerographite structure. Therefore, these remnant nanoparticles get covered with a thin graphite layer and would presumably lose their actual surface properties. Alternatively, to access the real surface properties of integrated nanoparticles, it would be practical to coat such porous scaffolds homogeneously with nanoparticles after their fabrication.

In our research we aimed at the incorporation of bioactive nanoparticles, such as HAn, into AG, as HAn are prominent bioactive nanoparticles that promote osteoblast alkaline phosphatase activity,[10] as well as biomineralization on composites.[11,12] Different strategies have been developed to fabricate 3D composite scaffolds that contain HAn, for example polymer scaffolds with incorporated HAn,[13−15] surface coatings with HAn of Ti_6Al_4V scaffolds,[16,17] or electrospun composites containing HAn.[18] Electrophoretic deposition (EPD) as one of the effective coating techniques based on colloidal dispersions has been used extensively to provide uniform HAn coatings on surfaces.[19] In principle, EPD is carried out in a two-electrode cell. The dispersed dielectric or charged nano- or microparticles are driven toward the working electrode by electrophoresis and deposited on the electrode via particle coagulation.[20] Particle deposition during EPD is generally influenced by parameters related to suspension and process.[21] As described by Hamaker's law[22] (eq 1), the deposit yield (w) is related to the electrophoretic mobility (μ), the electric field (E), and the particle concentration in the suspension (C).

$$w \propto \int_{t_1}^{t_2} \mu C E \, dt \tag{1}$$

Here, the correlation between electrophoretic mobility (μ), zeta potential (ξ), viscosity of suspension (η), and permittivity (ε)[21] is given through

$$\mu = \frac{\varepsilon \xi}{6\pi\eta} \tag{2}$$

when assuming stable suspension parameters that lead to a constant electrophoretic mobility (μ). Therefore, the deposit yield, w, is only influenced by particle concentration (C) and electrical field strength (E). Ethanol as a solvent with a viscosity of 1.09 cP and a relative permittivity of 24.55[23] provides a stable HAn dispersion with sufficient electrical conductivity and leads to homogeneous deposition.[24]

The capability of the EPD process in the fabrication of uniform coatings with adequate thickness control on different and complex material shapes has led to distinguished applications of EPD in the biomedical field.[19,21,25] Although EPD can be successfully applied to generate inorganic bioactive nanoparticle coatings on metallic substrates,[19,26] the coating of porous 3D structures remains challenging.[27] For instance, exploring HAn deposition on 3D Ti_6Al_4V scaffolds fabricated by rapid prototyping[27] or 3D porous bioglass-scaffold with carbon nanotubes[28] using EPD has revealed that the deposition of nanoparticles mostly occurs on the outer surface of these scaffolds, because their outer pores are quickly blocked with nanoparticles, thus blocking further nanoparticle transport into the inner parts of the scaffolds. Hence, the advantages of EPD have so far not been realized for the coating of 3D scaffolds. This is partly due to the so far insufficient understanding of the EPD process in 3D structures.

In the present work, we have systematically designed a novel periodic electrophoretic method (PEPD) to homogeneously integrate HAn into a 3D porous scaffold. HAn deposition was explored by monitoring fluorescently labeled HAn during the EPD process as well as by determining the kinetics of HAn deposition and its distribution via X-ray microcomputed tomography (μCT). A homogeneous HAn distribution throughout the scaffold was achieved by PEPD, where the parameters defining the different deposition periods were determined by μCT. Our results demonstrate that PEPD contributes to a deeper nanoparticle transport into the scaffold and limits pore blockage on the surface of the scaffold. In addition, the adhesion and enzymatic activity of osteoblasts suggest that the generated HAn decorated AG (HAn-AG) scaffolds have the potential to serve as 3D materials in tissue engineering applications.

2. EXPERIMENTAL SECTION

2.1. Preparation of Aerographite (AG) Samples. AG was fabricated based on a well-known one step conversion of tetrapod shaped ZnO templates via a CVD process.[9] Briefly, the loose powder of tetrapod-shaped ZnO templates was synthesized by a flame transport synthesis.[29] The ZnO tetrapods were then pressed into tablets of cylindrical shape (height = 3 mm, diameter = 6 mm) at a density of 0.3 g/cm^3 and subsequently heated for 5 h at 1150 °C to form interconnected networks. These 3D ZnO templates were then replicated into interconnected graphitic microtube structures, called aerographite, by CVD at ∼760 °C under an argon and hydrogen atmosphere and toluene as carbon source.[30] The obtained interconnected graphitic microtube structure is known and referred to as AG in this study.

2.2. Electrophoretic Deposition of HAn. HAn dispersions were prepared at different concentrations by adding 0.2, 1, and 2 g/L hydroxyapatite powder (≤200 nm, Sigma, Germany) to 50 mL of absolute ethanol (analytical grade, Sigma, Germany). The pH of these dispersions was adjusted to approximately 4 by gradually adding HCl (Sigma, Germany). Prior to EPD, the dispersions were sonicated (Bandelin electronics, Germany) for 1 h at room temperature. In order to sediment larger particles, the dispersion was kept stable for 15 min before running the EPD process. In the electrophoresis setup, a cylindrical stainless-steel electrode (diameter: 26 mm, height: 10 mm) was used as a counter electrode. The AG samples served as the working electrodes and were connected to a power supply by a platinum wire. The distance between the counter electrode and the working electrode was 10 mm. The EPD process was performed at a constant voltage of 10 V, and current changes were simultaneously recorded by a potentiostat instrument (ET&TE Etch and Technology GmbH, Germany). The samples were dried using critical point drying (CPD, instrument: EMS 3000) after finishing EPD. Afterward, the HAn decorated AG (unsintered HAn) scaffolds were heated in a highly vacuumed (1.0×10^{-7} Torr) quartz tube furnace at 1100 °C for 5 h at a heating rate of 2 °C/min. The scaffolds were studied using a scanning electron microscope (Ultra Plus Zeiss SEM, 5 kV).

In PEPD, the EPD (1 min at the above-mentioned specifications) and CPD processes were repeated three times. After the final CPD process, the scaffolds were heated as described before.

HAn deposit yield was measured by subtracting the weight of the AG scaffold before and after the EPD process.

2.3. Monitoring the EPD Process with Fluorescence Microscopy. In order to image the temporal progression of HAn deposition on AG, the HAn were labeled with a fluorescent dye (OsteoImage, Lonza, Germany). Briefly, a dispersion of 0.2 g/L HAn in OsteoImage dilution buffer (Lonza, Germany) was prepared. The

DOI: 10.1021/acsbiomaterials.9b00102
ACS Biomater. Sci. Eng. XXXX, XXX, XXX−XXX

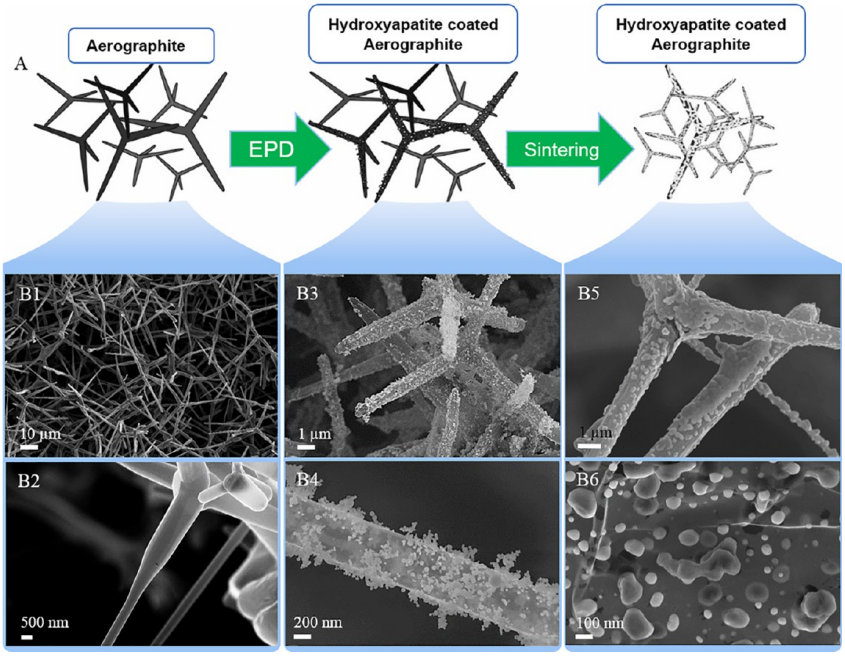

Figure 1. Schematic (A) and SEM micrographs (B1−6) of AG and HAn deposition on AG. (A) Ceramic HAn are electrophoretically deposited on the graphitic 3D network of AG and sintered to form a homogeneous layer. (B1−B2) Pure aerographite scaffold; (B3−B4) HAn-decorated microfilaments of AG before sintering, revealing a homogeneous distribution of HAn; (B5−B6) HA nanoparticles on AG after sintering.

staining reagent was diluted 1:100 in the dispersion to the final calculated volume. After 30 min incubation at room temperature, the HAn were removed from the dilution buffer by centrifuging the dispersion. The HAn were washed 3 times with washing buffer (Lonza, Germany) for 5 min in each round. The stained HAn were dispersed at a concentration of 0.2 g/L in absolute ethanol. The EPD setup was placed on a fluorescence microscope so that an *in situ* recording of HAn deposition was possible. Also here, a constant voltage of 10 V and a distance of 10 mm between the electrodes were used. The deposition of fluorescently labeled HAn was recorded *in situ* (Olympus IX81, camera: Hamamatsu, UV lamp: Lumencor). The recorded videos were analyzed frame by frame by the cellSens Dimension 1.16 software (Olympus). Each frame was image processed by thresholding. Thresholding was done by considering the background intensity as a fixed constant and replacing each pixel with a red pixel if the intensity is higher than this constant.

2.4. Mechanical Characterizations of Scaffolds. Mechanical characterizations of the scaffolds were performed using a self-built setup consisting of a Maerzhaeuser Wetzlar HS 6.3 micromanipulator, which is driven by a stepper motor and a Kern PLE 310−3N precision balance. The whole setup is located on a very rigid aluminum plate in a box filled with sand, which is mounted on a vibration-isolated table. Stress−strain curves were measured by placing the sample in between the micromanipulator and the balance. For compression tests, the micromanipulator deforms the sample by a user-defined step-size (here 25 μm) and deformation (here 2 mm), and the force is measured by the precision balance at each step with a settling time of 4 s. From the obtained stress−strain curves the Young's modulus is determined.

2.5. Cell Experiments. Preosteoblast cells (MC3T3- E1) were cultured in αMEM (Sigma, Germany) at 37 °C, 5% CO_2 and 90% humidity. The medium was supplemented with 10% Fetal Bovine Serum (FBS; Biochrom, Germany), 2 mM Glutamine (Sigma, Germany) and 1% penicillin/streptomycin (Sigma, Germany). Prior to any cell experiments, the samples (AG, 1 min EPD, 30 min EPD, PEPD 2 g/l) were autoclaved at 121 °C and immersed into fresh culture medium. To check the recrystallization of HAn during the autoclave process, the crystallinity of HAn were studied by X-ray diffraction (XRD). Approximately 20,000 cells were seeded on each scaffold in a 24 well plate (SARSTEDT, Germany). Cells were grown on the scaffolds for 4 days. To investigate cell morphology, proliferation and adhesion on the scaffolds, cell nuclei were stained with DAPI (ThermoFisher, Germany), which binds to DNA, and actin stress fibers were stained with Phalloidin (Alexa Fluor 647 Phalloidin, ThermoFisher, Germany). Imaging was carried out using fluorescence microscopy (IX81, Olympus, Germany). For electron microscopy, cells were first fixed by paraformaldehyde (ThermoFisher, Germany) and then dried using critical point drying (EMS 3000). A thin layer of gold was sputtered (Bal-Tec SCD 050, 30 mA, 30 s) onto the samples prior to scanning electron microscopy (SEM) imaging (Ultra Plus Zeiss SEM, 5 kV).

The viability of preosteoblast cells (MC3T3-E1) on the scaffolds was quantified according to the ISO 10993 norm. Briefly, 10,000 preosteoblast cells were cultured with 100 μL culture medium (αMEM supplemented with 10% FBS and 1% penicillin/streptomycin) for 24 h. The medium was replaced with extract medium (prepared by incubation of 1 mL culture medium with the scaffold for 72 h at 37 °C) for 24 h. To determine the number of viable cells the methylthiazolyldiphenyl-tetrazolium bromide (MTT; Sigma-Aldrich, Germany) metabolic activity assay was used with cells incubated in untreated medium as negative control and cells incubated in 20% DMSO as positive control. The results were normalized to the absorbance measured in the negative control.

2.6. Protein Adsorption Rate. To quantify the protein adsorption rate on the scaffolds we used bovine serum albumin (Pierce; ThermoFisher, Germany) as a model protein. One mL of protein solution (1 mg/mL in bidest. water) was added per sample and incubated at 37 °C, 5% CO_2 and 90% humidity. After 24 h, the amount of nonadhered proteins was measured using a micro bicinchoninic acid (BCA) protein assay (Pierce; ThermoFisher, Germany). Ten μL of supernatant of nonadhered protein solution were mixed with 200 μL working reagent and incubated for 30 min. The absorbance was measured with a microplate reader (Bio-Tek μQuant, USA) at 570 nm. The results were calibrated/normalized with a standard curve and the amount of protein adsorption was calculated by subtracting the residual protein concentration from the initial protein concentration. In order to demonstrate the statistical

DOI: 10.1021/acsbiomaterials.9b00102
ACS Biomater. Sci. Eng. XXXX, XXX, XXX−XXX

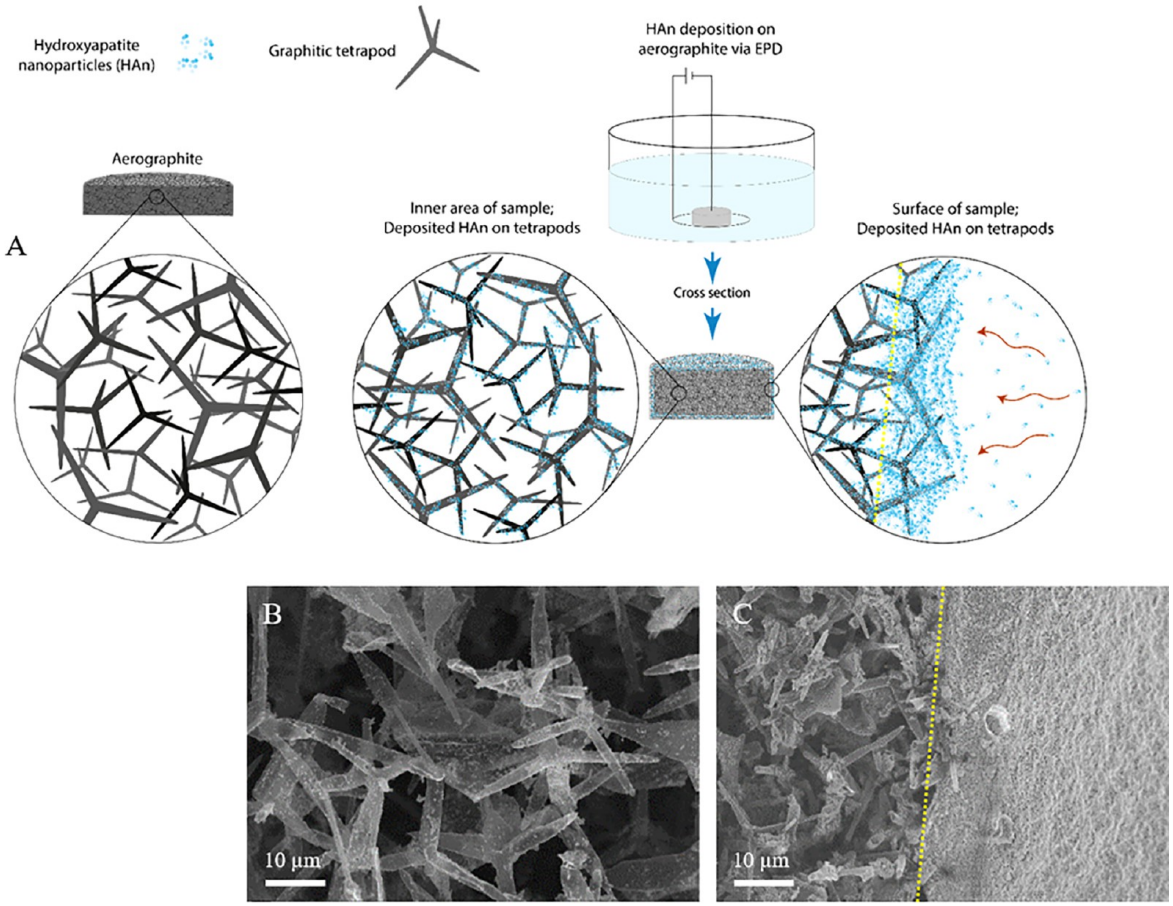

Figure 2. Overview of HAn deposition on AG. (A) EPD process for HAn deposition on AG. Schematic representation of a highly porous AG network consisting of graphitic micrometer-sized tetrapods before EPD (left scheme). Sketch of the HAn-AG sample after EPD, the inner area of the sample is partially covered with HAn. EPD process for HAn deposition on the AG (middle scheme). The surface is covered with a dense layer of HA nanoparticles. EPD process for HAn deposition on the AG (right scheme) (B) Higher magnification SEM image of an inner area in the 3D HAn-AG scaffold. (C) SEM image of the surface of HAn-coated AG, showing a dense layer of deposited HAn on the outer part of AG that blocks the inflow of further HA nanoparticles and dispersant (right of the yellow line).

significance for protein adsorption, a student's *t* test (Origin software) was carried out.

2.7. Alkaline Phosphatase Enzyme Activity Measurement. 20,000 MC3T3-E1 cells were seeded on each scaffold in a 24 well plate. After 4 days the medium was removed and the samples were gently rinsed with ice-cold 1x PBS. One mL of lysis buffer at 4 °C (0.1% Triton-X 100 in PBS) was added to each well and the samples were kept at 0 °C with constant shaking at 200 rpm. The lysates were transferred to microcentrifuge tubes and centrifuged at 20,000 rpm for 10 min. Thirty µL aliquot supernatant taken from each sample was mixed with 50 µL p-Nitrophenyl Phosphate (pNPP) and incubated for 1 h at 37 °C. The reaction was stopped by adding 20 µL of 3N NaOH. The absorbance was measured at 405 nm. Two independent experiments, each in three technical repeats, were carried out. All the results were normalized to the protein content of the cells, which was measured using the Pierce BCA protein assay kit. In order to demonstrate the statistical significance for alkaline phosphatase (ALP) activity, a student's *t* test (Origin software) was carried out.

2.8. X-ray Microcomputed Tomography and Image Processing. µCT data were acquired and reconstructed using a GE/Phoenix Nanotom benchtop µCT with a voxel size of 3.5−3.7 µm. In the obtained images the connected bright pixels represent areas with more absorption, hence the areas with more HAn. A "mean" filter with a pixel amount of 3 × 3 × 3 was applied to the original data to enhance the contrast between the background and the sample (ImageJ (Fiji)). The improved data set was segmented with Ilastik. Whereby, the partition of an image into multiple segments/objects is called "segmentation". As the results of the segmentation, the HAn-AG scaffolds (mostly consisting of the shell) and the background were set to the labels with values 1 and 0 accordingly. To minimize the calculation time, a region of interest (ROI) was defined. The final graph was generated with Matlab (Matlab R2015a, R2016a). The thickness distribution of the deposited layer was measured via ImageJ (Fiji).

3. RESULTS AND DISCUSSION

AG is a highly porous example of a filamentous network of carbon-based microtubes[9] (Figure 1A,B1). Due to its structural features, it is highly interesting for bone tissue engineering, particularly as an artificial substitute for spongy bone. Representative SEM images of the AG network are shown in Figure 1(B1,B2). The AG has an interstitial space of 10 to 100 µm between filaments and filaments with diameters between 0.5 and 3 µm. However, the inert and superhydrophobic nature of bare AG[7,9] hampers its application in tissue engineering. To improve cell adhesion, one can either choose to chemically biofunctionalize the AG[7] or to coat the AG filaments with bioactive substances, as these should promote biomineralization and osteogenesis.[31,32]

DOI: 10.1021/acsbiomaterials.9b00102
ACS Biomater. Sci. Eng. XXXX, XXX, XXX−XXX

To include bioactive nanoparticles, such as HAn, into AG, they need to be incorporated after the fabrication of the porous scaffold, and electrostatic forces appear to be perfect as external mediators to immobilize the HAn in the scaffold. Therefore, we implemented EPD as a simple and low-cost method to decorate the AG scaffolds with HAn. Figure 2A shows the EPD method to cover the AG filaments with HAn. The decoration process is based on the mobility of charged HAn (≤200 nm) in an ethanol-based HAn dispersion. Since ethanol is an amphiphilic molecule,[33] the superhydrophobic AG is readily immersed into the ethanol-based HAn dispersion and the HAn dispersion (0.2 g/L) can freely and without constraints pass through the open interconnected structure of the AG framework. After immersion of AG in the HAn dispersion, the EPD process was carried out for 2 h at 10 V. The HAn decorated AG (HAn-AG) scaffolds were dried by CPD to avoid destructive influences of surface tension during ethanol evaporation. We assume that the charged HAn are immobilized on the filaments via electrostatic and van der Waals forces, as they are not removed during the CPD process. SEM was performed to study the deposited particles on the surface of AG filaments (Figure 2B−C). The SEM images show that the inner parts of the scaffolds are not covered densely (Figure 2B), whereas a dense coverage is clearly visible on the outer areas of the HAn-AG scaffold (Figure 2C). This is a typical phenomenon observed when coating porous scaffolds with nanoparticles using EPD, which is likely attributed to the electrical potential and suspension flow difference between the surface of the scaffolds and inside the scaffolds.[27,28,34] During the immersion of AG into the HAn dispersion, the initially trapped particles are presumably deposited on the nearest surface of the graphitic filament as shown in Figure 2A. By continuing EPD, the HAn are fed from the suspension reservoir between the AG network and the cylinder counter electrode. These particles are electrostatically deposited on the closest filament to them, which is located on the outer area of AG network. This is due to higher accessibility to the dispersion flow (Figure 2A,C), thereby forming a dense coverage on the outer surface of HAn-AG scaffolds. Similar deposition phenomena on 3D structures have been reported on other types of scaffolds, such as HAn coated Ti_6Al_4V scaffolds with fiber spacings between about 700 and 1050 μm[27,34] or carbon nanotubes on porous bioglass scaffolds.[28] It was also suggested that the electrical potential difference between the surface and the center of scaffolds would increase the deposit yield on the outer surface of 3D networks.[27]

In principle the deposit yield is a function of the applied potential.[21] Higher applied voltages (>100 V) result in a higher deposit yield, but the deposition of the particles in the coating does not occur in a close-packed manner. In addition, high fields increase electrophoretic mobility, leading to movement and deposition of huger particles as well.[21] To avoid an inhomogeneous coating as much as possible, all of our experiments were carried out at low applied fields (10 V) to improve the inhomogeneity of coating. At a constant applied voltage (10 V), initially the current is decreased drastically within 1 min right after running the EPD process and then is maintained relatively constant (Figure 3). The deposited particles appear to form an insulating layer on the AG surface (Figure 2A,C), which can lead to a decrease in electrophoresis.[35] In addition, the deposit yield is increased while the deposition current is decreased asymptotically (Figure 3). The HAn concentration in the suspension is reduced during the EPD process, as more and more particles are added to the scaffold. Consequently, a decreasing deposit yield with deposition time can be attributed to the formation of an insulation layer (i.e., deposited HAn) on the surface and the decrease in particle concentration in the suspension.

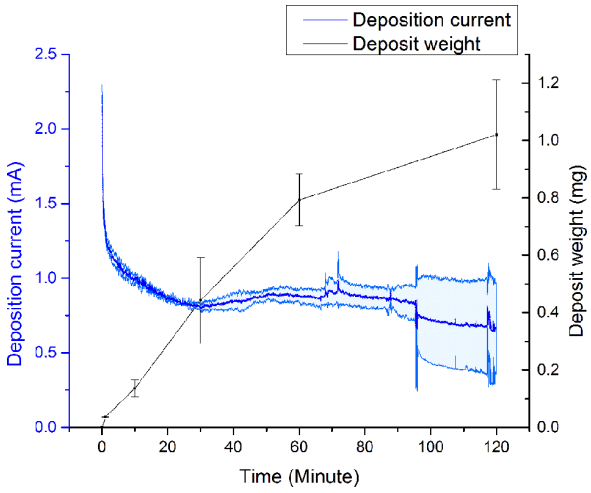

Figure 3. Deposition current (blue) of the EPD process (10 V) and deposit weight, the light blue curve represents the error bar. Deposit weight (black) of HA (0.2 g/L HA in ethanol) on AG. Error bars denote standard deviation; each data point of deposit weight is the average of five experiments. (Error bars represent ± standard deviation, n = 5).

Our main goal was to avoid a blockage of the outer pores by clustered HAn. This was achieved by stopping the EPD process before the pores were blocked, and periodically repeating it several times. For this it is necessary to have detailed knowledge about the deposition kinetics of HAn on AG. Therefore, the distribution of HAn on the HAn-AG scaffolds was investigated in 3D after 30, 60, and 120 min EPD using μCT (Figure 4). The 3D reconstruction of deposited HAn (Figure 4A−C, Supporting Information, Video S1) reveals an inhomogeneous thickness of the deposited HAn layer (shell) on the surface of AG. In contrast, less dense HAn distributions are present on the inner parts of AG (Figure 4B,D). In most of the investigated areas, there is a thick layer of HAn, whereas in some areas there is almost no coverage (Figures 4E−H). The distribution of deposition thickness reveals an average shell thickness of 62 ± 7 μm for 30 min EPD, 81 ± 21 μm for 60 min EPD, and 134 ± 70 μm for 120 min EPD samples (Figure 4H). These results suggest that the deposition of HAn preferentially occurred on specific areas of the AG as is explained in the following: AG consists of micron-sized graphitic tetrapods (Figure 1A, 1B, 2A), which lead to an uneven surface on the micron scale. Consequently, we assume that the uneven surface of AG leads to a higher electrical charge density or depletion zones in different areas during the EPD process, resulting in different HAn deposit yields on different parts of the AG surface. The relevance of surface structure on the results of EPD has recently been demonstrated for hydroxyapatite deposition on Ti_6Al_4V scaffolds.[27]

In order to identify the dynamics of HAn deposition on the AG scaffolds during EPD, we used a method to fluorescently label HAn and then investigated its deposition using a combined setup of EPD and a fluorescence microscope. As

DOI: 10.1021/acsbiomaterials.9b00102
ACS Biomater. Sci. Eng. XXXX, XXX, XXX−XXX

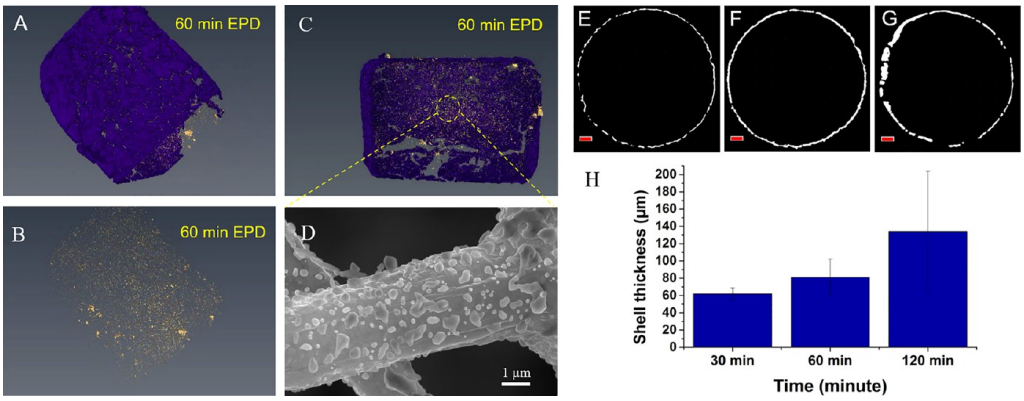

Figure 4. 3D reconstruction of μCT data of HAn deposition on AG after sintering. (A–C) Partial/different views on segmented data of HAn deposition on AG scaffolds after 60 min EPD. In order to distinguish the HAn on different parts of the scaffold more easily, the HAn on the shell and on inner parts are colored as blue and yellow, respectively. The images show a dense layer of deposited HAn on the outer surface of AG (blue shell) (A,C), and the distribution of less dense HAn structures on the inner parts of AG (yellow dots) (B). (D) SEM image of an inner area in the 3D HAn-AG scaffold. (E–G) Representative longitudinally sectioned slices of tomography 3D reconstructed data of HAn deposition on AG scaffolds after 30 min EPD (E), 60 min EPD (F), and 120 min EPD (G). Red scale bars represent 500 μm. (H) Layer thickness measurement of deposited HAn on the outer area of AG scaffolds after vacuum sintering. Error bars represent ± standard deviation, n = 3.

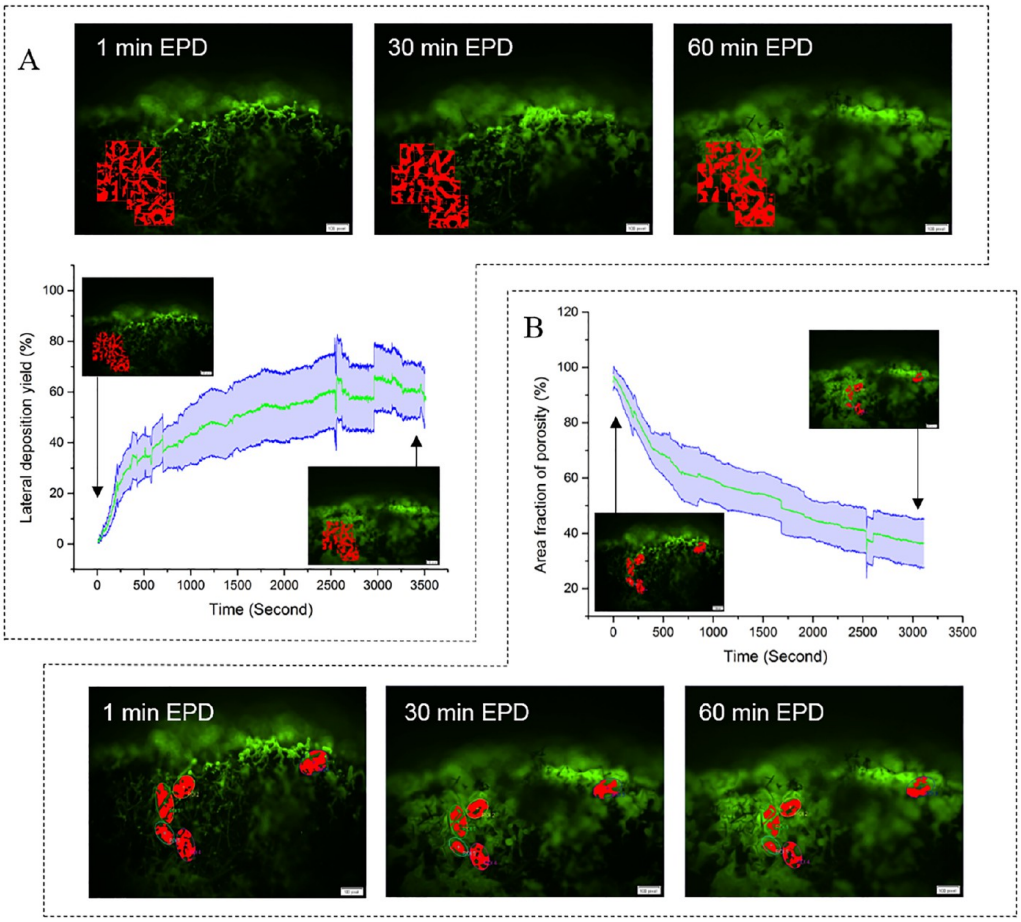

Figure 5. HAn deposition on the surface of AG in EPD. The deposition of fluorescently labeled HAn on the surface of AG was observed and recorded in situ with a fluorescence microscope. (A) The lateral deposition of HAn (green) on the AG filaments shows the increase of the area covered with HAn over time. (B) Area fraction of porosity, revealing a decreasing pore size with EPD time. (Mean value: green line, error bar: blue line). The images show the fluorescently labeled HAn on the surface of AG after three different EPD times (1, 30, and 60 min). The HAn deposit on the AG filaments (box A) and area fraction of porosity (box B) is illustrated in red after image thresholding. (Error bars represent the mean ± standard deviation, n = 4).

DOI: 10.1021/acsbiomaterials.9b00102
ACS Biomater. Sci. Eng. XXXX, XXX, XXX–XXX

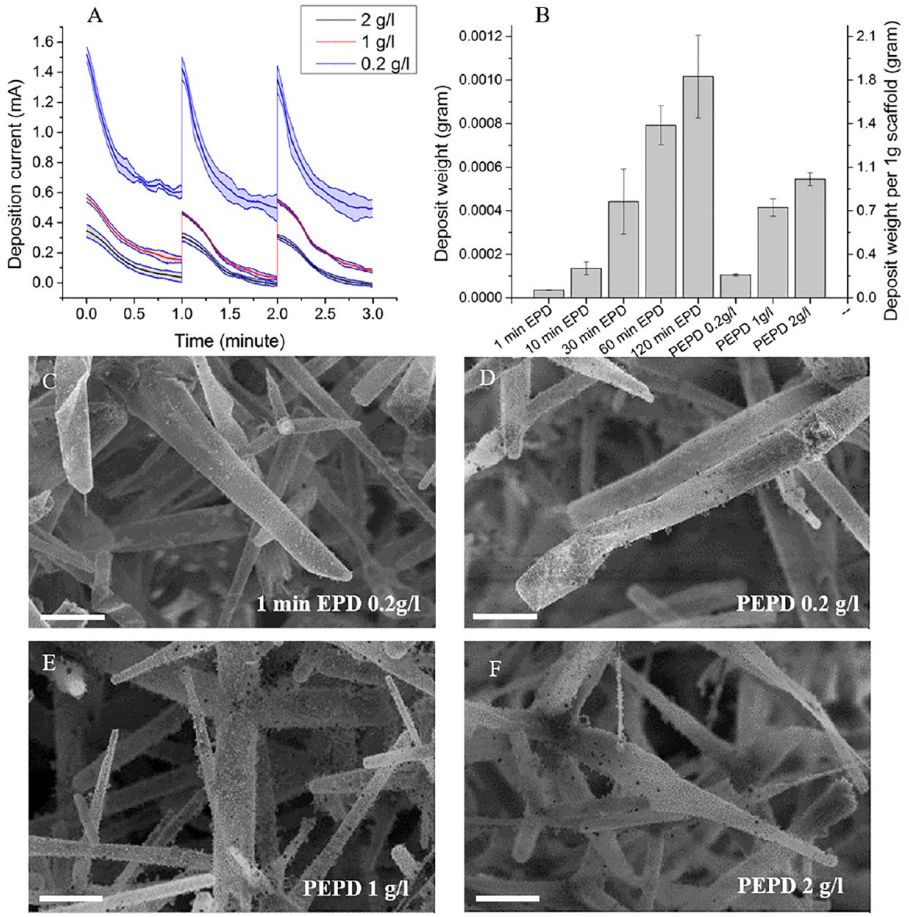

Figure 6. Overview of HAn deposition on AG for different dispersion concentrations. (A) Deposition current of the EPD process for different dispersion concentrations. After 1 min, the EPD process was stopped and each sample was dried using CPD. This cycle was repeated three times. (B) Deposit weight of HAn for different EPD parameters. (C–F) SEM images of the inner parts (almost middle) of the HAn-AG scaffolds. (C) After 1 min EPD (dispersion concentration: 0.2 g/L, 10 V). (D) After PEPD (dispersion concentration: 0.2 g/L, 10 V). (E) After PEPD (dispersion concentration: 1 g/L, 10 V). (F) After PEPD (dispersion concentration: 2 g/L, 10 V). (Error bars: ± standard deviation, n = 5, scale bars: 10 μm).

AG is opaque and a good light absorber,[9] the recorded images show the AG filament in black and the fluorescently labeled HAn in green. The deposition was recorded as a video with illumination time of 1 s (Supporting Information, Video S2a). The fraction of porosity in a predefined area is calculated by normalizing the gained fluorescent area to the first frame, where basically no HAn coverage can be seen. After running the EPD process for a few seconds, AG filaments are well visible as green fibers, as they are all covered with fluorescently labeled HAn, which emit green light (Figure 5). The increasing thickness of green filaments indicates the progressive deposition of HAn on the outer surface of AG. According to the direction of imaging, which is perpendicular to the surface of AG, only lateral changes of HAn deposition on the filaments in the focal plane (Supporting Information, Figure S1) are detectable. The lateral increase in HAn thickness on the filaments and the simultaneous decrease in the porosity of the AG are clearly visible within the 60 min of recording EPD (Figure 5B). The frame by frame analysis of the recorded movies proves the lateral growth of the deposited HAn (Figure 5A) whereas the lateral deposition rate is reduced asymptotically, which is in agreement with the results of deposit yield (Figure 3). The closure of pores on the surface of AG appears to have slightly the same trend as the deposition itself. After 60 min EPD, about 60% of the pores are blocked by HAn (Figure 5B).

From these results, it is clear that the classical application of EPD for coating 3D scaffolds by HAn is limited, as pores are blocked and the HAn cannot reach deeper areas of the AG. To overcome this problem, we designed a periodic EPD (PEPD) process, which stops EPD before the pores are blocked and restarts several times. In our experiments, the EPD process was stopped after 1 min, which is the time at which the deposition current turns into a steady state (Figure 6A). Then, the HAn-AG scaffolds were dried with CPD and reimmersed into the HAn dispersion. Then, EPD is restarted. Due to the formation of the insulation layer, the deposition current is reduced after each periodic step (Figure 6A). This is in agreement with SEM images of HAn-AG (Figure 6C,D) that also show a denser coating layer of HAn on AG filaments after 3 times of periodic 1 min EPD compared to the single EPD process that ran for 1 min. In order to check the potential of PEPD to also coat interior volumes of the AG with HAn, we tested the periodic process with higher concentrations of HAn dispersions, i.e. a 5

DOI: 10.1021/acsbiomaterials.9b00102
ACS Biomater. Sci. Eng. XXXX, XXX, XXX–XXX

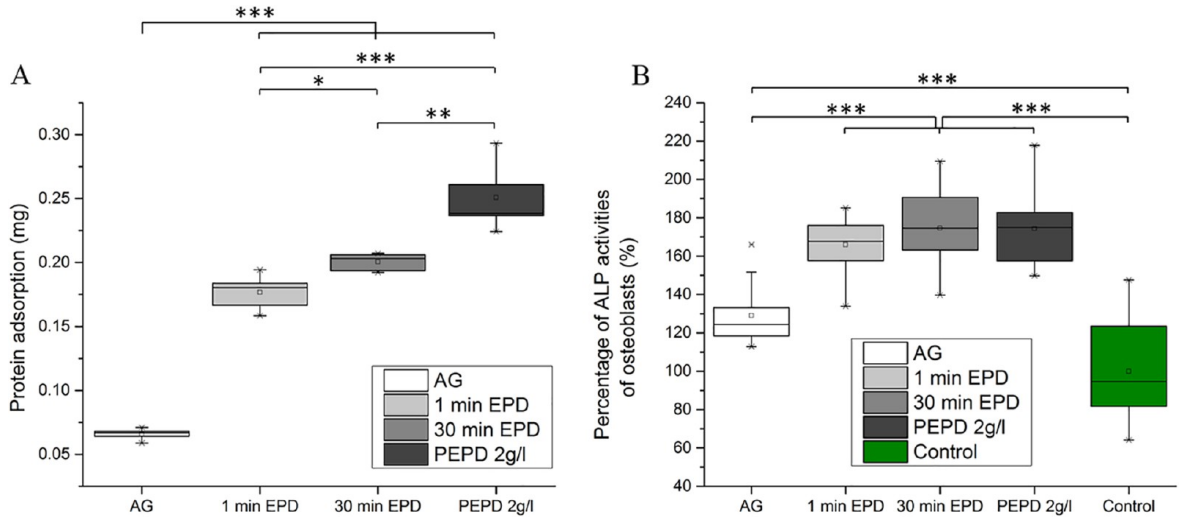

Figure 7. Overview of bioactivity and protein adsorption of HAn-AG scaffolds. (A) Albumin adsorption on the HAn-AG scaffolds. (B) ALP enzyme activity of preosteoblast cells (MC3T3-E1) on the AG and HAn-AG scaffolds. In order to demonstrate the statistical significance, a student's *t* test was carried out. The significance level was set as $*p < 0.05$, $**p < 0.01$, and $***p < 0.001$.

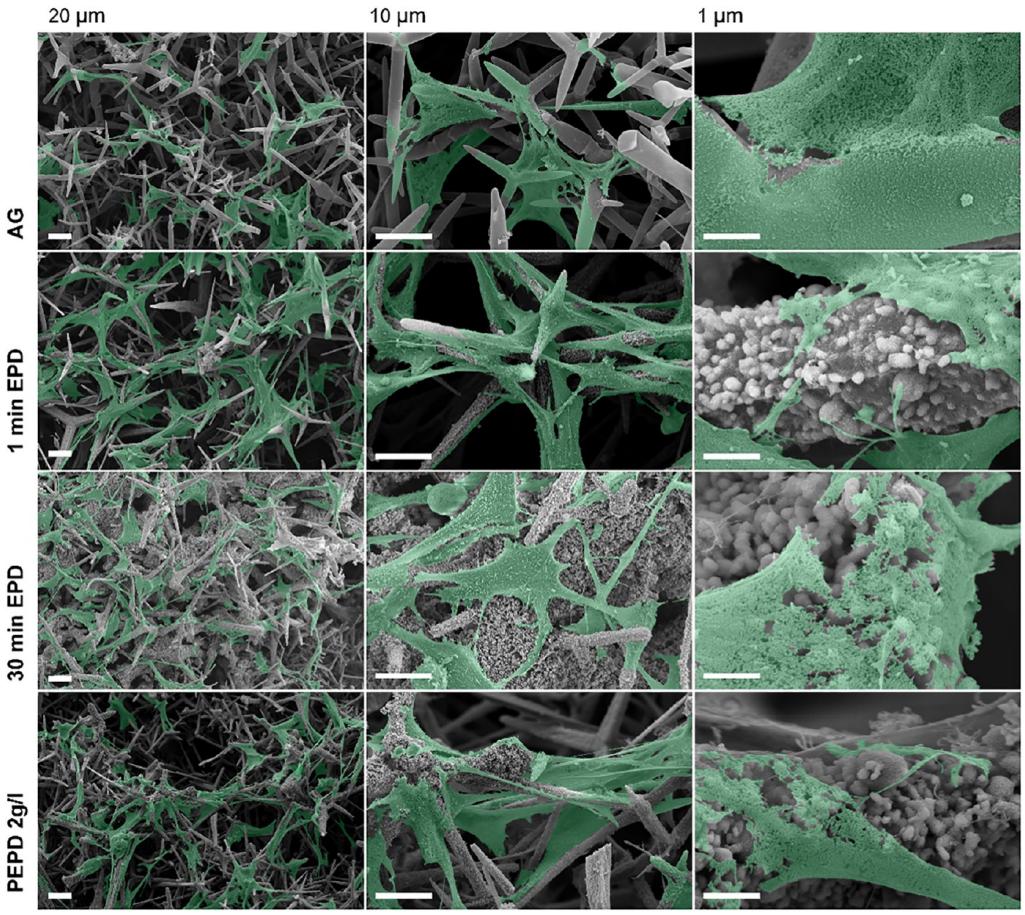

Figure 8. SEM micrographs of preosteoblast cells (MC3T3-E1) cultivated for 4 days on AG and HAn-AG scaffolds. Scale bars are 20 μm for the column to the left, 10 μm for the central column, and 1 μm for the column to the right. SEM imaging took place approximately up to 300 μm from the surface of the scaffolds and shows that cells are homogeneously covering these areas. In addition, cells spanned and stretched along the tube-shaped filaments of AG networks. All the structures support preosteoblast growth. The cells in SEM images were highlighted with green color (Photoshop) in order to distinguish them more easily.

DOI: 10.1021/acsbiomaterials.9b00102
ACS Biomater. Sci. Eng. XXXX, XXX, XXX−XXX

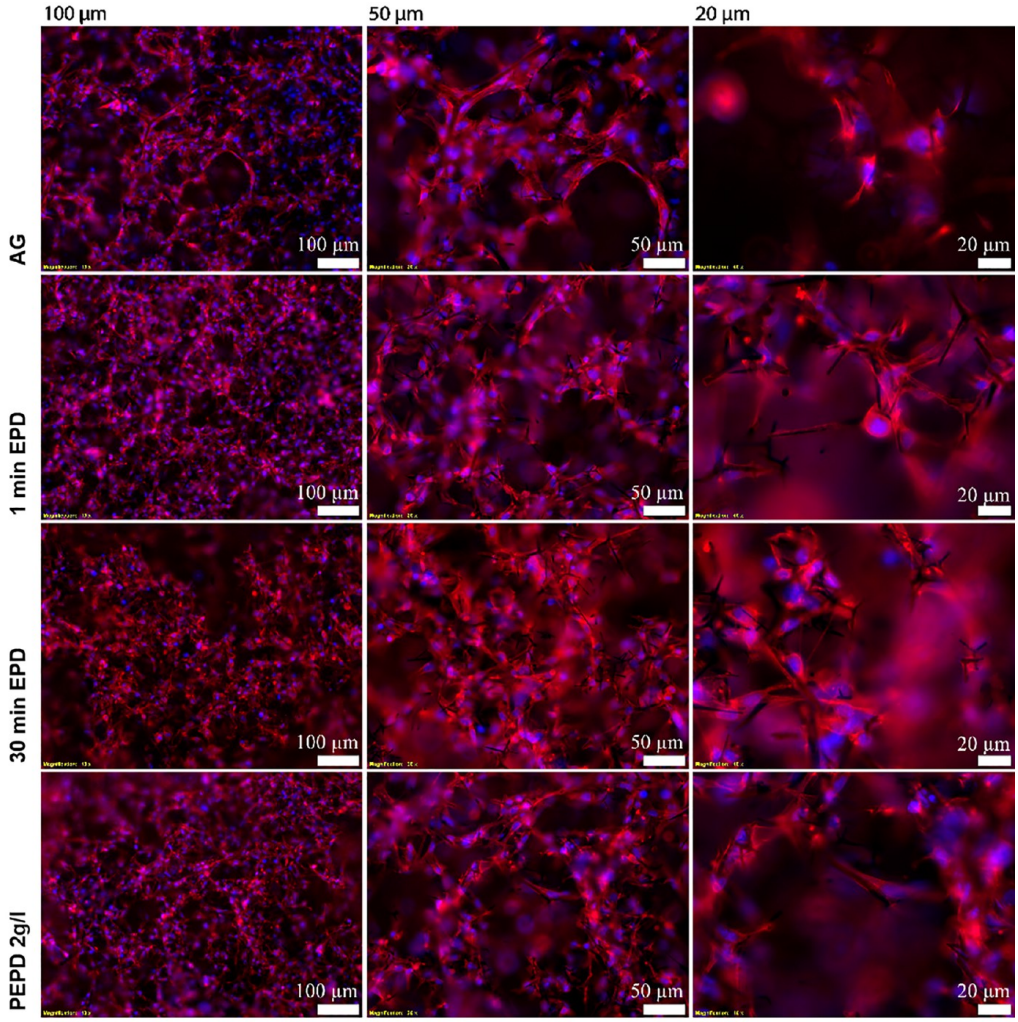

Figure 9. Representative fluorescence images of preosteoblast cells (MC3T3-E1) cultivated for 4 days on AG and HAn-AG. Scale bars are 100 μm for the column to the left, 50 μm for the central column, and 20 μm for the column to the right. MC3T3-E1 cells were stained with DAPI (nuclei; blue) and phalloidin (actin; red). Fluorescence imaging took place in optical sections of up to 200 μm from the surface of the scaffolds. The images reveal the adhesion and growth of preosteoblast cells on all scaffolds.

times (1 g HAn/L) and 10 times (2 g HAn/L) more concentrated dispersion. A denser coating layer was deposited on the AG filaments when a higher HAn concentration was used in the dispersion (Figure 6B,E,F), which can be attributed to the deposition of a denser coating by using the more concentrated dispersions.[21] Interestingly, based on SEM observations from the HAn decorated-scaffolds via PEPD for all investigated concentrations (0.2, 1, 2 g HAn/L) (Figure 6C−F), the outer pores of the scaffold were not blocked using this procedure. To stabilize the HAn further on the AG, a sintering process was applied, which slightly deformed the HAn and fused them to each other (Figure 1B5,B6).

Figure S3 shows Young's moduli of AG, 1 min EPD, 30 min EPD, and PEPD 2g/L. AG has the lowest Young's modulus with ~22 kPa, which is in the range of previously reported values.[9] 1 min EPD and 30 min EPD scaffolds have Young's moduli of ~27 kPa and ~35 kPa, respectively. Thus, coating the scaffolds with HAn results in mechanical reinforcement of bare AG, and the reinforcement is higher the longer EPD takes place. This can be attributed to a thicker HAn shell on the surface of the 30 min EPD scaffold (Figure 4). Interestingly, the PEPD 2g/L scaffold is much stiffer than the other scaffolds (AG, 1 min EPD, 30 min EPD), with a Young's modulus of ~59 kPa. Presumably, the more homogeneous and higher amount of deposited HAn (Figure 6) on the PEPD 2g/L scaffold is the reason for this reinforcement. These results confirm that PEPD is a successful strategy to also increase the Young's modulus of the AG scaffold.

To prove the applicability of the HAn-AG scaffolds in bioengineering applications, we investigated the protein adsorption capacity of AG and HAn-AG prepared with 1 min, 3 min EPD (10 V, dispersion concentration 0.2 g/L), and PEPD (10 V, dispersion concentration 2 g/L, 1 min). The protein adsorption capacity of these scaffolds was investigated by immersion in bovine serum albumin (BSA) as a model protein for 24 h. For quantifying protein adsorption, a BCA assay was used. The PEPD at 2g/L, 30 min EPD, and 1 min EPD samples show higher protein adsorption than AG, respectively (Figure 7A). Furthermore, the protein adsorption capacity of the scaffolds is proportional to deposit yield, where the pure AG scaffold has the lowest amount of adsorbed proteins and the HAn-AG scaffold prepared with PEPD

DOI: 10.1021/acsbiomaterials.9b00102
ACS Biomater. Sci. Eng. XXXX, XXX, XXX−XXX

adsorbs the highest amount of proteins (Figure 7A). This effect can be explained by the fact that HA has a greater protein adsorption capacity compared to graphite,[36] so that the scaffold with the highest amount of deposited HAn can be expected to have the highest protein adsorption capacity. An additional contribution to the increased protein adsorption capacity of HAn-AG compared to AG might be the increase in surface area due to HAn coating, as the diameter of the microfilaments increases. Protein adsorption of specific adherent proteins onto bioceramics facilitates osteoblasts adhesion;[37] hence, our HAn-AG scaffolds should be suitable for promoting osteoblast adhesion as well.

To further prove the ability of the HAn-AG scaffolds to serve as materials for bone cell growth, we investigated the growth of preosteoblast cells (MCT3T3-E1) on the different types of AG-derived scaffolds. MTT tests (Figure S5) show a negative effect of neither HAn-AG nor pristine AG on MCT3T-E1 cells. SEM images taken up to 300 μm sample depth reveal that all the scaffolds support the growth of osteoblast cells (Figure 8). Preosteoblast cells grow densely on the HAn-AG scaffolds and are elongated on the scaffold filaments (Figure 8). This is supported by contact formation of the cellular plasma membranes with the HAn (Figures 8, right column) and the high density of osteoblasts on all the scaffolds (PEPD 2g/l, 1 min EPD, 30 min EPD, AG). The SEM images shown in Figure 8 demonstrate the potential AG to support the growth of osteoblasts and adhesion on its network. These results are in good agreement with earlier findings, where a graphene substrate promoted the adhesion of osteoblasts.[38] Additional SEM images of preosteoblast cells deeply inside (up to 3 mm) the scaffolds without HAn shell (AG, 1 min EPD, PEPD 2g/L) (Figure S6) reveal cell colonization inside the structures, not only on their surface. To prove the influence of HAn on osteoblast activity further, the ALP (alkaline phosphatase) activity of osteoblasts on the different scaffolds after 4 days of culturing was tested using a pNPP based ALP activity assay. Interestingly, the ALP activity of osteoblasts was enhanced by ~30% on the bare AG scaffold and significantly ($p \leq 0.001$) up to two times on HAn-AG scaffolds (Figure 7B) compared to the control on a plastic dish. In the presence of HAn, the enzyme activity was significantly increased with a slight dependence on the concentration of HAn on the scaffolds compared to bare AG. This indicates that the HAn-AG scaffolds improve the functional activity of osteoblast cells. In addition, adsorbed proteins from FBS in the medium might also contribute to the functional activity of osteoblasts. Furthermore, released ions from HAn during the culturing period, as previously demonstrated by Gustavsson et al. for the release of Ca^{2+} and P_i in culture media,[39] can significantly enhance osteoblastic phenotype expression levels (e.g., ALP activity) by affecting extracellular signaling.[40] Although graphene substrates promote the adherence of human osteoblasts and mesenchymal stromal cells,[38] for CNT-based and other graphene-based material it appears useful to add HAn for increasing osteoblast adhesion.[4,41] Therefore, PEPD is a suitable coating technique used for 3D scaffolds to extend bioapplications of AG by a homogeneous incorporation of bioactive nanoparticles (e.g., HAn) into its structure.

Actin fiber bundles as small compartments of stress fibers have a key role in cell motility.[42] To investigate the formation of stress fibers in osteoblasts on bare AG and HAn-AG scaffolds, actin fibers were investigated via phalloidin staining (red). In addition, nuclei of preosteoblast cells were stained using DAPI (blue). However, as imaging in AG is limited, only cells located up to 200 μm from the surface of the scaffolds were imaged. Interestingly, all types of scaffolds are fully covered with osteoblasts after 4 days (Figure 9, left column) and the osteoblasts are stretched between and along the filaments of the scaffolds (Figure 9, middle column). Osteoblast elongation is presumed to enhance their migration into 3D networks by providing coherent interfaces between cells and the scaffolds.[40] Images at higher magnification (Figure 9, right column) (Supporting Information, Figure S2) reveal dense actin networks in the cytoplasm of attached osteoblasts, as they are typical in these cells.[43] This is in agreement with a previous study of rat bone mesenchymal stem cells on HAn and a reduced graphene oxide composite.[44] The interstitial space of AG at the first glance appears to be smaller than the recommended pore size for bone regeneration (e.g., >300 μm) based on studies on porous blocks of hydroxyapatite and pores laser-textured Ti6Al4 V scaffolds.[45] Although Karageorgiou et al. stated a pore size of 100 μm as minimum requirement, the fibrous network of AG provides more free spatial microstructure for 3D osteoblasts growth[4] compared to porous block materials.

4. CONCLUSIONS

In summary, we have developed a periodic EPD process that allows for coating porous scaffolds with ceramic HAn. Whereas the standard EPD process led to a thick surface layer of HAn on fibrous aerographite, thus blocking the pores and hindering the homogeneous coating of the whole scaffold, our period procedure allowed for the homogeneous coating of the full scaffold. The *in situ* monitoring of HAn deposition on the AG scaffolds revealed the high tendency of HAn to deposit on the outer areas of the AG network in the standard EPD process but not in the PEPD process. The PEPD technique presented here is therefore a simple and practical method that can be adopted to decorate different types of 3D porous scaffolds with a wide variety of charged nanoparticles for diverse applications. In our specific example, we could demonstrate the bioactivity of the HAn-AG scaffolds as well as their ability to support osteoblast cell growth, so that they are promising candidates for bone tissue engineering.

■ ASSOCIATED CONTENT

Supporting Information

The Supporting Information is available free of charge on the ACS Publications website at DOI: 10.1021/acsbiomaterials.9b00102.

Figures S1. In situ monitoring of fluorescently labeled HAn deposition via EPD. The schematic reveals the meaning of lateral deposition. Figure S2. High magnification fluorescence image of preosteoblast cells (MC3T3-E1) on 3D AG and HAn-AG scaffolds. Figure S3. Young's moduli of AG and HAn-AG scaffolds. Figure S4. XRD patterns of 1 min EPD and 30 min EPD scaffolds after and before autoclaving. Figure S5. Cell viability of preosteoblast cells (MC3T3-E1) treated with extractions of AG and HAn-AG scaffolds. Figure S6. SEM micrographs of preosteoblast cells (MC3T3-E1) cultivated for 4 days on AG and HAn-AG scaffolds. (PDF)

Video S1. 3D reconstruction of deposited HAn on a HAn-AG scaffold using μCT images. (MP4)

DOI: 10.1021/acsbiomaterials.9b00102
ACS Biomater. Sci. Eng. XXXX, XXX, XXX−XXX

Video S2. Dynamics of HAn deposition on AG scaffolds during EPD using fluorescently labeled HAn. (MP4)

AUTHOR INFORMATION

Corresponding Author

*E-mail: cse@tf.uni-kiel.de.

ORCID

Mohammadreza Taale: 0000-0003-2033-3294
Fabian Schütt: 0000-0003-2942-503X
Muhammad Atiq Ur Rehman: 0000-0001-5201-973X
Yogendra Kumar Mishra: 0000-0002-8786-9379
Norbert Stock: 0000-0002-0339-7352
Aldo R. Boccaccini: 0000-0002-7377-2955
Christine Selhuber-Unkel: 0000-0002-5051-4822

Notes

The authors declare no competing financial interest.

ACKNOWLEDGMENTS

CS is supported by the European Research Council (ERC StG 336104 CELLINSPIRED, ERC PoC 768740 CHANNEL-MAT) and by the German Research Foundation (RTG 2154, SFB 1261 project B7). MT acknowledges support from the German Academic Exchange Service (DAAD) through a research grant for doctoral candidates (91526555-57048249) and Constanze Lamprecht support during the initial phase of the project. This project has received funding from the European Union's Horizon 2020 research and innovation program under grant agreement No. GrapheneCore2 785219.

ABBREVIATIONS

μCT, X-ray microcomputed tomography
AG, aerographite
ALP, alkaline phosphatase
BCA, bicinchoninic acid
BSA, bovine serum albumin
CPD, critical point drying
CVD, chemical vapor deposition
EPD, electrophoretic deposition
HAn, hydroxyapatite nanoparticles
HAn-AG, HAn decorated AG
MTT, methylthiazolyldiphenyl-tetrazolium bromide
PEPD, periodic electrophoretic deposition
pNPP, p-nitrophenyl phosphate
ROI, region of interest
SEM, scanning electron microscopy
XRD, X-ray diffraction
ZnO, zinc oxide

REFERENCES

(1) Perego, C.; Millini, R. Porous Materials in Catalysis: Challenges for Mesoporous Materials. *Chem. Soc. Rev.* **2013**, *42* (9), 3956−3976.
(2) O'Brien, F. J. Biomaterials & Scaffolds for Tissue Engineering. *Mater. Today* **2011**, *14* (3), 88−95.
(3) Zheng, K.; Wu, J.; Li, W.; Dippold, D.; Wan, Y.; Boccaccini, A. R. Incorporation of Cu-Containing Bioactive Glass Nanoparticles in Gelatin-Coated Scaffolds Enhances Bioactivity and Osteogenic Activity. *ACS Biomater. Sci. Eng.* **2018**, *4* (5), 1546−1557.
(4) Taale, M.; Schütt, F.; Zheng, K.; Mishra, Y. K.; Boccaccini, A. R.; Adelung, R.; Selhuber-Unkel, C. Bioactive Carbon Based Hybrid 3D Scaffolds for Osteoblast Growth. *ACS Appl. Mater. Interfaces* **2018**, *10*, 43874.
(5) Lutolf, M. P.; Hubbell, J. A. Synthetic Biomaterials as Instructive Extracellular Microenvironments for Morphogenesis in Tissue Engineering. *Nat. Biotechnol.* **2005**, *23* (1), 47−55.
(6) Taale, M.; Schütt, F.; Carey, T.; Marx, J.; Mishra, Y. K.; Stock, N.; Fiedler, B.; Torrisi, F.; Adelung, R.; Selhuber-Unkel, C. Biomimetic Carbon Fiber Systems Engineering: A Modular Design Strategy to Generate Biofunctional Composites from Graphene and Carbon Nanofibers. *ACS Appl. Mater. Interfaces* **2019**, *11* (5), 5325−5335.
(7) Lamprecht, C.; Taale, M.; Paulowicz, I.; Westerhaus, H.; Grabosch, C.; Schuchardt, A.; Mecklenburg, M.; Böttner, M.; Lucius, R.; Schulte, K.; Adelung, R.; Selhuber-Unkel, C. A Tunable Scaffold of Microtubular Graphite for 3D Cell Growth. *ACS Appl. Mater. Interfaces* **2016**, *8* (24), 14980−14985.
(8) Marx, J.; Brouschkin, A.; Roth, S.; Smazna, D.; Mishra, Y. K.; Wittich, H.; Schulte, K.; Adelung, R.; Fiedler, B. Fundamentals of the Temperature-Dependent Electrical Conductivity of a 3D Carbon Foam—Aerographite. *Synth. Met.* **2018**, *235*, 145−152.
(9) Mecklenburg, M.; Schuchardt, A.; Mishra, Y. K.; Kaps, S.; Adelung, R.; Lotnyk, A.; Kienle, L.; Schulte, K. Aerographite: Ultra Lightweight, Flexible Nanowall, Carbon Microtube Material with Outstanding Mechanical Performance. *Adv. Mater.* **2012**, *24* (26), 3486−3490.
(10) Shu, R.; McMullen, R.; Baumann, M. J.; McCabe, L. R. Hydroxyapatite Accelerates Differentiation and Suppresses Growth of MC3T3-E1 Osteoblasts. *J. Biomed. Mater. Res. - Part A* **2003**, *67* (4), 1196−1204.
(11) Lobo, A. O.; Corat, M. A. F.; Ramos, S. C.; Matsushima, J. T.; Granato, A. E. C.; Pacheco-Soares, C.; Corat, E. J. Fast Preparation of Hydroxyapatite/Superhydrophilic Vertically Aligned Multiwalled Carbon Nanotube Composites for Bioactive Application. *Langmuir* **2010**, *26* (23), 18308−18314.
(12) Li, M.; Liu, Q.; Jia, Z.; Xu, X.; Cheng, Y.; Zheng, Y.; Xi, T.; Wei, S. Graphene Oxide/Hydroxyapatite Composite Coatings Fabricated by Electrophoretic Nanotechnology for Biological Applications. *Carbon* **2014**, *67*, 185−197.
(13) Gonçalves, E. M.; Oliveira, F. J.; Silva, R. F.; Neto, M. A.; Fernandes, M. H.; Amaral, M.; Vallet-Regí, M.; Vila, M. Three-Dimensional Printed PCL-Hydroxyapatite Scaffolds Filled with CNTs for Bone Cell Growth Stimulation. *J. Biomed. Mater. Res., Part B* **2016**, *104* (6), 1210−1219.
(14) Zhang, H.; Mao, X.; Du, Z.; Jiang, W.; Han, X.; Zhao, D.; Han, D.; Li, Q. Three Dimensional Printed Macroporous Polylactic Acid/Hydroxyapatite Composite Scaffolds for Promoting Bone Formation in a Critical-Size Rat Calvarial Defect Model. *Sci. Technol. Adv. Mater.* **2016**, *17* (1), 136−148.
(15) Wang, X.; Jiang, M.; Zhou, Z.; Gou, J.; Hui, D. 3D Printing of Polymer Matrix Composites: A Review and Prospective. *Composites, Part B* **2017**, *110*, 442−458.
(16) Li, Y.; Yang, W.; Li, X.; Zhang, X.; Wang, C.; Meng, X.; Pei, Y.; Fan, X.; Lan, P.; Wang, C.; Li, X.; Guo, Z. Improving Osteointegration and Osteogenesis of Three-Dimensional Porous Ti6Al4V Scaffolds by Polydopamine-Assisted Biomimetic Hydroxyapatite Coating. *ACS Appl. Mater. Interfaces* **2015**, *7* (10), 5715−5724.
(17) Yuan, W.; He, X.; Zhou, X.; Zhu, Y. Hydroxyapatite Nanoparticle-Coated 3D-Printed Porous Ti6Al4V and CoCrMo Alloy Scaffolds and Their Biocompatibility to Human Osteoblasts. *J. Nanosci. Nanotechnol.* **2018**, *18* (6), 4360−4365.
(18) Kim, H.; Che, L.; Ha, Y.; Ryu, W. Mechanically-Reinforced Electrospun Composite Silk Fibroin Nanofibers Containing Hydroxyapatite Nanoparticles. *Mater. Sci. Eng., C* **2014**, *40*, 324−335.
(19) Boccaccini, A. R.; Keim, S.; Ma, R.; Li, Y.; Zhitomirsky, I. Electrophoretic Deposition of Biomaterials. *J. R. Soc. Interface* **2010**, *7* (SUPPL. 5), S581−S613.
(20) Sarkar, P.; Nicholson, P. S. Electrophoretic Deposition (EPD): Mechanisms, Kinetics, and Application to Ceramics. *J. Am. Ceram. Soc.* **1996**, *79* (8), 1987−2002.

DOI: 10.1021/acsbiomaterials.9b00102
ACS Biomater. Sci. Eng. XXXX, XXX, XXX−XXX

(21) Besra, L.; Liu, M. A Review on Fundamentals and Applications of Electrophoretic Deposition (EPD). *Prog. Mater. Sci.* **2007**, *52* (1), 1−61.
(22) Hamaker, H. C. Formation of a Deposit by Electrophoresis. *Trans. Faraday Soc.* **1940**, *35*, 279−287.
(23) Mazurkiewicz, J.; Tomasik, P. Viscosity and Dielectric Properties of Liquid Binary Mixtures. *J. Phys. Org. Chem.* **1990**, *3* (8), 493−502.
(24) Xiao, X. F.; Liu, R. F. Effect of Suspension Stability on Electrophoretic Deposition of Hydroxyapatite Coatings. *Mater. Lett.* **2006**, *60* (21−22), 2627−2632.
(25) Corni, I.; Ryan, M. P.; Boccaccini, A. R. Electrophoretic Deposition: From Traditional Ceramics to Nanotechnology. *J. Eur. Ceram. Soc.* **2008**, *28* (7), 1353−1367.
(26) Simchi, A.; Tamjid, E.; Pishbin, F.; Boccaccini, A. R. Recent Progress in Inorganic and Composite Coatings with Bactericidal Capability for Orthopaedic Applications. *Nanomedicine: Nanotechnology, Biology, and Medicine*; Elsevier: February 1, 2011; pp 22−39. DOI: 10.1016/j.nano.2010.10.005.
(27) Ozhukil Kollath, V.; Chen, Q.; Mullens, S.; Luyten, J.; Traina, K.; Boccaccini, A. R.; Cloots, R. Electrophoretic Deposition of Hydroxyapatite and Hydroxyapatite−alginate on Rapid Prototyped 3D Ti6Al4V Scaffolds. *J. Mater. Sci.* **2016**, *51* (5), 2338−2346.
(28) Meng, D.; Ioannou, J.; Boccaccini, A. R. Bioglass®-Based Scaffolds with Carbon Nanotube Coating for Bone Tissue Engineering. *J. Mater. Sci.: Mater. Med.* **2009**, *20* (10), 2139−2144.
(29) Mishra, Y. K.; Kaps, S.; Schuchardt, A.; Paulowicz, I.; Jin, X.; Gedamu, D.; Wille, S.; Lupan, O.; Adelung, R. Versatile Fabrication of Complex Shaped Metal Oxide Nano-Microstructures and Their Interconnected Networks for Multifunctional Applications. *KONA* **2014**, *31* (1), 92−110.
(30) Marx, J.; Lewke, M. R. D.; Smazna, D.; Mishra, Y. K.; Adelung, R.; Schulte, K.; Fiedler, B. Processing, Growth Mechanism and Thermodynamic Calculations of Carbon Foam with a Hollow Tetrapodal Morphology − Aerographite. *Appl. Surf. Sci.* **2019**, *470*, 535−542.
(31) Yu, C.; Zhuang, J.; Dong, L.; Cheng, K.; Weng, W. Effect of Hierarchical Pore Structure on ALP Expression of MC3T3-E1 Cells on Bioglass Films. *Colloids Surf., B* **2017**, *156*, 213−220.
(32) Roether, J. A.; Boccaccini, A. R.; Hench, L. L.; Maquet, V.; Gautier, S.; Jérôme, R. Development and in Vitro Characterisation of Novel Bioresorbable and Bioactive Composite Materials Based on Polylactide Foams and Bioglass® for Tissue Engineering Applications. *Biomaterials* **2002**, *23* (18), 3871−3878.
(33) Fernandes, L. M. P.; de Andrade, E. F.; Monteiro, M. C.; Cartágenes, S. C.; Lima, R. R.; Prediger, R. D.; Maia, C. S. F. Ethanol. In *Addictive Substances and Neurological Disease*; Academic Press, 2017; pp 201−215. DOI: 10.1016/B978-0-12-805373-7.00020-7.
(34) Seuss, S.; Lehmann, M.; Boccaccini, A. R. Alternating Current Electrophoretic Deposition of Antibacterial Bioactive Glass-Chitosan Composite Coatings. *Int. J. Mol. Sci.* **2014**, *15* (7), 12231−12242.
(35) Zhitomirsky, I.; Gal-Or, L. Electrophoretic Deposition of Hydroxyapatite. *J. Mater. Sci.: Mater. Med.* **1997**, *8* (4), 213−219.
(36) Wang, K.; Zhou, C.; Hong, Y.; Zhang, X. A Review of Protein Adsorption on Bioceramics. *Interface Focus* **2012**, *2* (3), 259−277.
(37) Webster, T. J.; Ergun, C.; Doremus, R. H.; Siegel, R. W.; Bizios, R. Specific Proteins Mediate Enhanced Osteoblast Adhesion on Nanophase Ceramics. *J. Biomed. Mater. Res.* **2000**, *51* (3), 475−483.
(38) Kalbacova, M.; Broz, A.; Kong, J.; Kalbac, M. Graphene Substrates Promote Adherence of Human Osteoblasts and Mesenchymal Stromal Cells. *Carbon* **2010**, *48* (15), 4323−4329.
(39) Gustavsson, J.; Ginebra, M. P.; Engel, E.; Planell, J. Ion Reactivity of Calcium-Deficient Hydroxyapatite in Standard Cell Culture Media. *Acta Biomater.* **2011**, *7* (12), 4242−4252.
(40) Kim, H. W.; Kim, H. E.; Salih, V. Stimulation of Osteoblast Responses to Biomimetic Nanocomposites of Gelatin-Hydroxyapatite for Tissue Engineering Scaffolds. *Biomaterials* **2005**, *26* (25), 5221−5230.
(41) Zhang, L.; Liu, W.; Yue, C.; Zhang, T.; Li, P.; Xing, Z.; Chen, Y. A Tough Graphene Nanosheet/Hydroxyapatite Composite with Improved in Vitro Biocompatibility. *Carbon* **2013**, *61*, 105−115.
(42) Pellegrin, S.; Mellor, H. Actin Stress Fibres. *J. Cell Sci.* **2007**, *120* (20), 3491−3499.
(43) Danilevicius, P.; Georgiadi, L.; Pateman, C. J.; Claeyssens, F.; Chatzinikolaidou, M.; Farsari, M. The Effect of Porosity on Cell Ingrowth into Accurately Defined, Laser-Made, Polylactide-Based 3D Scaffolds. *Appl. Surf. Sci.* **2015**, *336*, 2−10.
(44) Nie, W.; Peng, C.; Zhou, X.; Chen, L.; Wang, W.; Zhang, Y.; Ma, P. X.; He, C. Three-Dimensional Porous Scaffold by Self-Assembly of Reduced Graphene Oxide and Nano-Hydroxyapatite Composites for Bone Tissue Engineering. *Carbon* **2017**, *116*, 325−337.
(45) Karageorgiou, V.; Kaplan, D. Porosity of 3D Biomaterial Scaffolds and Osteogenesis. *Biomaterials* **2005**, *26* (27), 5474−5491.

DOI: 10.1021/acsbiomaterials.9b00102
ACS Biomater. Sci. Eng. XXXX, XXX, XXX−XXX

The Supporting Information is available in Appendix-E

Chapter 7

Conclusion

In my thesis, novel fibrous biomimetic and biohybrid carbon scaffolds that ensure an optimal environment for 3D fibroblast and osteoblast growth, have been developed. These fibrous structures offer intriguing 3D biomimetic network to promote cell proliferation and adhesion, so that cells stretch between the fibrous filaments of the scaffolds. Promoting cell proliferation and adhesion in this work was conducted by both compositional alteration and functionalization. The functionalization approaches for enhancing fibroblast adhesion and growth are presented in publication 1 and 4, respectively. On the other hand, the fibroblast and osteoblast adhesion and proliferation on the biohybrid scaffolds with tunable features are presented in publication 2 and 3. In addition, the biocompatibility of the scaffold is discussed in all the publications accordingly. The combination of the two approaches enabled the development of a variety of scaffolds with an unique fibrous biomimetic architecture.

In the first approach, AG as a novel ultraweight graphitic material has been functionalized using cRGD peptides coupled to PEG conjugated phospholipids. Using these networks as a conductive scaffold for 3D cell growth revealed the high capacity of biofunctionalized AG for fibroblast adhesion and proliferation. The biocompatibility of the developed scaffolds was proven through MTT metabolic activity assay according to the norm ISO 10993. The great advantages of AG compared to other porous 3D scaffolds are its unique fibrous microstructure and high porosity to accommodate fibroblasts. This microstructure provides large free space for cell adhsion and growth. Thus, cells were able to adhere and elongate between the filaments of AG scaffolds. In addition, fluorescence microscopy showed that fibroblasts develop actin fibers and focal complexes growing on the AG matrix. Functionalized AG with its extensive possibilities of tailoring is applicable for further bioapplications.

To extend the possibilities of AG microstructure for further tissue engineering and bioapplications, a novel modular design strategy to develop fibrous biomimetic carbon scaffolds with remarkable and tunable features, is introduced. Carbon-based scaffolds that mimic the ECM, with tuning electrical conductivity (ca. 0.1330 S/m), stiffness (ca. 1030.7 MPa), have been successfully fabricated. Biocompatibility studies revealed high protein adsorption capacity and fibroblast proliferation. Accordingly, the scaf-

folds are capable for biofunctionalization and addition of other biochemical cues. In addition, fibroblasts sprawl and elongated along the fiber of the matrices. The developed paxillin-containing adhesion sites as well as actin fibers reveal that fibroblasts are able to adhere and extend leading edges. In addition, the fabrication procedure is very simple and can in principle be adopted to develop 3D assemblies from other low-dimensional nanomaterials e.g. bioactive nanoparticles. This is particularly relevant in bone tissue engineering.

In the other study in my thesis, a simple and efficient strategy to fabricate highly porous composite scaffolds made of self-entangled CNTs in microtube structures with incorporated bioactive ceramic nanoparticles (BGN and HAn) is demonstrated. The incorporation of BGN and HAn resulted in biomineralization of the scaffolds, which possibly leads to promote bone ingrowth. Biocompatibility of the scaffolds was confirmed by showing that both fibroblasts and osteoblasts are capable of adhesion and stretching out between the fibers beside high protein adsorption capacity of the scaffolds. In addition, the hollow microtubes lead to an increase in ion release and low density of the scaffolds. This strategy can provide high-throughput method for implementing a variety of ceramic nanoparticles into the highly porous 3D networks upon the preferential removal of the ZnO by H_2 etching/sintering process. This in combination of tunable features e.g. stiffness and porosity, offers the opportunity of fabricating diverse hybrid composite structures.

In another attempt to achieve bioactive AG scaffolds, a novel periodic EPD process to coat the highly porous network of AG is presented. If the AG scaffolds were coated with a standard EPD process, an inhomogeneous distribution of deposited HAn throughout the 3D network has been demonstrated by μCT investigation. This result is supported by *in situ* monitoring of fluorescently labeled HAn during EPD process. The *in situ* monitoring revealed the high tendency of HAn to deposit on the outer areas of the AG network forming a shell during the standard EPD process. On the contrary, a homogeneous distribution of deposited HAn was obtained by using the here presented periodic EPD. Biocompatibility studies revealed a high proliferation rate of osteoblasts as well as the ability of osteoblasts to develop actin fibers. The scaffolds are fully covered with osteoblasts, the osteoblasts are stretched and elongated between and along the filaments of the scaffolds. In addition, the incorporation of HAn into the AG network led to an increase in both protein adsorption capacity and ALP enzyme activity of osteoblasts. The experimental outcome suggests that HAn coated AG scaffolds provide a suitable network with astonishing features for 3D osteoblast growth. The coating strategy presented here can be easily applied to many different 3D scaffolds.

The spatial architecture of fibers in the fabricated structures presented in this thesis provides a large free space for 3D cell growth and cell adhesion. In addition, the fabrication procedure can in principle be adopted to develop 3D assemblies such that they finally mimic the ECM structurally and biochemically, but with the additional feature of conductivity. This allows several degrees of freedom in the design of such fibrous carbon scaffolds and provides unique properties for controlling cell growth and adhesion in 3D.

Appendix-A

A.1 Overcoming the cytotoxic effect of AG by a washing process

The preliminary cytoctoxicity tests on AG have shown toxicity towards REF52 cells. In principle graphite is considered as an inert material. Thus, in order to understand the origin of the toxic effect, the amount of released ions from AG samples into the culture medium was measured every 3 days. Interestingly, the results indicated a high concentration of Zn ions in the medium during the first days of immersion as seen in Figure (Appendix-A.1). Continuing the immersion of AG in the medium, the concentration of released-Zn ions as well as the cytotoxic effect of AG drastically decreased to almost zero (Figure Appendix-A.1). This can be attributed to possible residual ZnO from the AG process (see section 2.3) which is released and removed from the AG's structure by immersion in culture medium. These results suggest a necessary pre-washing step prior to the use of AG in *in vitro* studies.

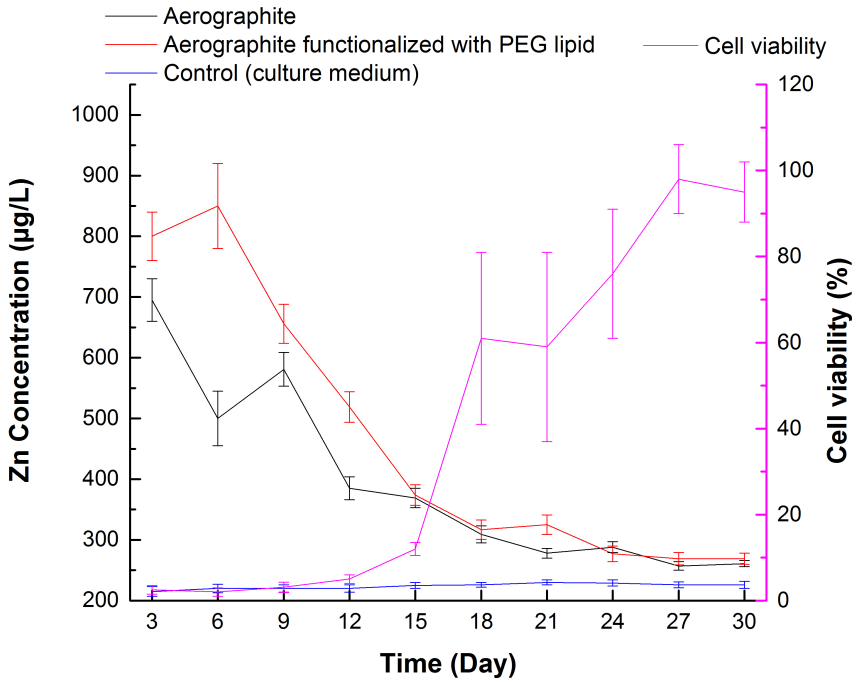

Figure Appendix-A.1: *Concentration of Zn ions released into the culture medium and its cytotoxic effect by immersion the AG scaffold in culture medium. The blue, red and black graphs illustrate the Zn ion concentration in culture medium: after immersing AG (black graph), and AG that was functionalized with PEG lipid (red graph) every 3 days in fresh culture medium. The blue graph represents the situation for untreated culture medium. The purple graph illustrates the viability percentage of REF52 cells exposed to culture medium after immersion an AG sample. The medium was refreshed every 3 days and the treated medium was used for a MTT assay.*

Appendix-B

B.1 Supporting information on publication 1

A tunable scaffold of microtubular graphite for 3D cell growth

Constanze Lamprecht, Mohammadreza Taale, Ingo Paulowicz, Hannes Westerhaus, Carsten Grabosch, Arnim Schuchardt, Matthias Mecklenburg, Martina Böttner, Ralph Lucius, Karl Schulte, Rainer Adelung, Christine Selhuber-Unkel

Corresponding Author

E-mail: constanze.lamprecht@jku.at

Present Addresses

Institute of Biophysics, Johannes Kepler University Linz, 4020 Linz, Austria

MATERIALS AND METHODS

Biofunctionalization: A 4:1 mixture of 2-distearoyl-sn-glycero-3-phosphoethanolamine-N- [amine(PEG)2000] (DSPE-PEG2000-NH_2; Avanti Polar Lipids) and DSPE-PEG2000-cRGD was prepared in ultrapure water with a PEG-lipid concentration of 1mg/ml. AG samples were placed into a 12-well plate and 500 μl of PEG-lipid mixture were carefully pipetted into each well. The well-plate was covered with a lid and placed into a desiccator, which was evacuated and purged with nitrogen twice. Then samples remained under nitrogen atmosphere for 24 hours. Afterwards, the samples were washed twice with ultrapure water and left to soak in ultrapure water for another 24 h to remove unbound PEG-lipids. Finally, the solution was exchanged for cell culture medium and AG samples were directly used for cell seeding.

Covalent coupling of cRGD to amine terminated PEG-lipids: Cyclo(Arg-Gly-Asp-D-Tyr-Lys) (c(RGDyK); EUROGENTEC) was coupled via the amine terminus to DSPE-PEG2000-NH_2 (M=2,790 g/mol) according to following procedure. 10 mg of PEG-lipids were dissolved in 3 ml standard PBS containing 8% glutaraldehyde (Sigma) assisted by brief (4sec) sonication and 10 min treatment in a thermoshaker at 1500 rpm and 40°C. The solution was allowed to incubate over night at room temperature. Activated PEG-lipids were concentrated and washed 3 times with 200 μl ultrapure water using centrifugal filters (Vivacon 500, 2,000 MWCO; Sartorius) at 10,000 g for 90 min. For reductive amination of activated PEG-lipids (DSPE-PEG2000- glutaraldehyde), 2.5 mg c(RGDyK) (1.1 eq; 4mol) were dissolved in 500 μl carbonate buffer pH 8.3. Then 236 mg of sodium cyanoborohydride NaCNBH 3 (M=62.8 g/mol) were dissolved in 200 μl carbonate buffer pH 8.3, of which 20 μl were added to the recovered DSPE-PEG2000- glutaraldehyde solution together with the dissoveld c(RGDyK). The solution was briefly sonicated (4sec), then placed in a thermoshaker for 15 min at 40°C and 1500 rpm, and left for incubation over night at room temperature. The solution was then filtered using vivacon 500 centrifugal filters at 10,000 g for 120 min to remove carbonate buffer followed by 3 washing steps with ultrapure water (200 μl) at 10,000 g for 40 min for purification of the resulting DSPE-PEG2000-cRGD. The recovered concentrated cRGD-PEG-lipids were stored at -20°C until use.

Cell culture and cell seeding: Rat embryonic fibroblasts (REF52) and fluorescent rat embryonic fibroblasts (REF52 YFP Pax), were cultured in Dulbeccos modified Eagles medium (DMEM; Gibco Laboratories) supplemented with 10% fetal calf serum, 1% penicillin/streptomycin, and 2 mM L-glutamine (all from Gibco Laboratories) in an incubator at 37°C and 5% CO 2 level. About 20,000 cells were seeded on functionalized AG and 10,000 cells were seeded into empty control wells. Growth was visually inspected until control cells reached confluence after day 4. Then the cells were fixed with 4% paraformaldehyde (PFA) in Hanks buffered salt solution (both Sigma) for 20 min and washed with PBS.

Actin fiber and nuclear staining with Phalloidin and Hoechst: PFA fixed control cells and AG/cell samples were washed with PBS three times and 0.1% Triton X-100 in PBS was added for 5 min followed by three times washing with PBS. Next 20 μl PBS and 5 μl Phalloidin and 0.2 μl Hoechst (10 μg/ml) were mixed. Phalloidin stains

actin fibers, and Hoechst stains the nucleus of a cell. Four μl of staining solution were added to each sample and incubated for 20 min at 37°C. Afterward, the solution was removed and the wells were washed with PBS three times and transferred to an IX81 microscope to examine them.

Fluorescence microscopy: Fluorescence imaging was done on an Olympus IX81 inverted microscope equipped with a metal halide lamp, and a monochrome CCD camera (Hamamatsu C9300). In order to observe the different fluorescently labeled cell features the following filters were used: YFP to observe YFP conjugated paxillin that marks adhesion complexes, DAPI for nuclear staining with Hoechst, and RFP to visualize phalloidin stained actin fibers. Setup control and image recording were assisted by Olympus CellSense Dimension software. Control cells were recorded in epi-fluorescence configuration at 0.1 sec illumination. Images of AG bulk samples were taken as optical image stacks of 20 to 80 sections in epi-fluorescence by motor-stage assisted change of the focal plane in 5 μm-steps. Illumination was set to 5 sec per image to provide enough fluorescence signals at reasonable signal to noise ratio. Image processing of monochrome images was done using CellSense Dimension software. Composite images of all three channels were done in Image J with adjustment of contrast and brightness.

MTT based viability assay: In accordance with protocols in part 12 of ISO 10993 (ISO 10993- 12:2004) Sample preparation and reference materials, we have prepared extracts from three PEG-lipid functionalized and three pristine AG samples in cell culture medium with a mass/volume ratio of sample and medium of 0.1 g/ml taking into consideration the standard surface areas and extract liquid volumes outlined in Table 1 of the ISO 10993:12:2004. The immersed samples were gently agitated at 37°C over a period of 72 h. Following protocols in part 5 of ISO 10993 (ISO 10993-5:2009) Tests for in vitro cytotoxicity the viability of REF 52 fibroblasts was tested with an MTT metabolic activity assay after 24 hours of exposure of seeded cells to the extracts. REF cells were cultured for 24 h at 37°C with the undiluted extracted medium. Cells treated with 15% DMSO served as positive control, and cells incubated in untreated culture medium were used as negative control. After 24 h incubation the medium was exchanged to 3-(4.5-dimethylthiazol-2-yl)-2.5-diphenyltetrazolium bromide (MTT) (Sigma- Aldrich, Germany) solution in Eagle minimum essential medium (Biochrom, Germany) without supplements and phenol red (at concentration of 1mg/ml) followed by 4 h incubation at 37°C. The MTT converted to formazan was extracted by adding isopropanol alcohol, and the optical density of formazan was measured in a plate reader (Bio-Tek instruments, Quant) (at 570 nm).

Super critical point drying and scanning electron microscopy: PFA fixed AG/cell samples were dehydrated stepwise in graded ethanol (EtOH) of increasing alcohol concentrations starting at 60% EtOH and incubation period of 30 min followed by 80% (30 min), 90% (30 min), 95% (1 h) and 100% (>1 h). Thereafter, EtOH was substituted against acetone and the samples were transferred into the chamber of the critical point dryer (CPD, BAL-Tec CPD030). For SEM imaging a 7,5 nm layer of gold was applied directly after CPD. Imaging was done in Supra 55VP field emission SEM (Zeiss) applying an acceleration voltage of 2 kV. SEM images have been cropped but

are otherwise displayed as recorded. Scale bars have been included using CorelDraw X7.

Preparation of AG sections: PFA fixed AG/cell samples were dehydrated in graded EtOH. Concentrated EtOH was then substituted against xylene, which was changed 3 times with 1 h settling time for each step. Afterwards samples were soaked in paraffin of 56°C for 1.5 hours, drained and immersed again for embedding into blocks of solidified paraffin. After complete hardening, paraffin was trimmed down to the sample surface and sections of 9 μm thickness were prepared with a microtome. Sections were placed onto glass slides and dried at 37°C. Prior to hematoxylin/eosin (HE) staining with Mayers Haemalaun and 0.1 % Eosin-B solution (both from Merck) paraffin was removed and sections were rehydrated by reversal of the dehydration procedure.

Dewaxing of AG/cell sections and haematoxylin/eosin staining. Dewaxing was done by placing glass slides with paraffin sections in xylene three times for 3 min. Then the glass slides were passed through ethanol solutions of decreasing concentrations (100% EtOH 3 x 3 min, 90% 2 x 3 min, 80% 2 x 3 min, 70% 1 x 3 min, 50% 1 x 3) and finally into deionized water for two times 3 min. After rehydration glass slides were incubated in Mayers Haemalaun solution (Merck) for 3 min, rinsed with 0.1% HCl for 2 sec and washed under running water for 1 min. Next, glass slides were placed in 0.1% Eosin-B solution (Merck) for 3 min followed by 30 sec rinsing with water. Lastly, samples were dehydrated again in an ascending graded ethanol series, soaked in xylene two times, and then covered with Neo-Mount (Merck) and a cover slip.

Optical bright field microscopy was done on an Olympus BX43 equipped with a color CCD camera (ImagingSource). Final image contrast and brightness of presented micrographs were adjusted using CorelDraw X7.

SI APPENDIX I: Surfactants for immersion of AG in aqueous media test series A vast number of molecules have been investigated for dispersion of carbon based materials. We have chosen amphiphilic agents that were successfully tested for large diameter CNTs, as AG filaments range from several 100 nm up to a few micrometers. We have tested the following agents at different concentrations in aqueous solution:

1. Bovine serum albumin (BSA), a serum albumin protein derived from cows, which is a standard low cost protein in lab experiments and cell culture, and shows no adverse effects.

2. Carboxymethyl cellulose (CBMC) is used in detergents and in purified form for food and pharmaceutical applications.

3. Amine terminated poly(ethylene glycol) conjugated phospholipids (e.g. DSPE-PEG2000- NH_2), are engineered biopolymers that have been proven to successfully disperse CNTs and graphene. The hydrophobic tails of the phospholipid DSPE (1,2-distearoyl-sn- glycero-3-phosphoethanolamine) are assumed to attach non-covalently to the AG surface via hydrophobic interactions, whereas PEG extends into the aqueous phase imparting hydrophilicity to AG. Applications of PEG in medicine are manifold. It is used to increase blood circulation times of therapeutics and prevent rapid renal clearance, serves as coating and lubricant for pharmaceutical products and in eye

drops.

4. Cell culture medium supplemented with 10% fetal bovine serum (FBS) is used for eukaryotic in vitro cell culture. Apart from BSA as the major component, FBS contains a rich variety of proteins including growth factors. The nutrients and proteins of FBS may adsorb onto the AG surface and facilitate AG immersion in aqueous solutions as well as afford a suitable matrix for cell adhesion

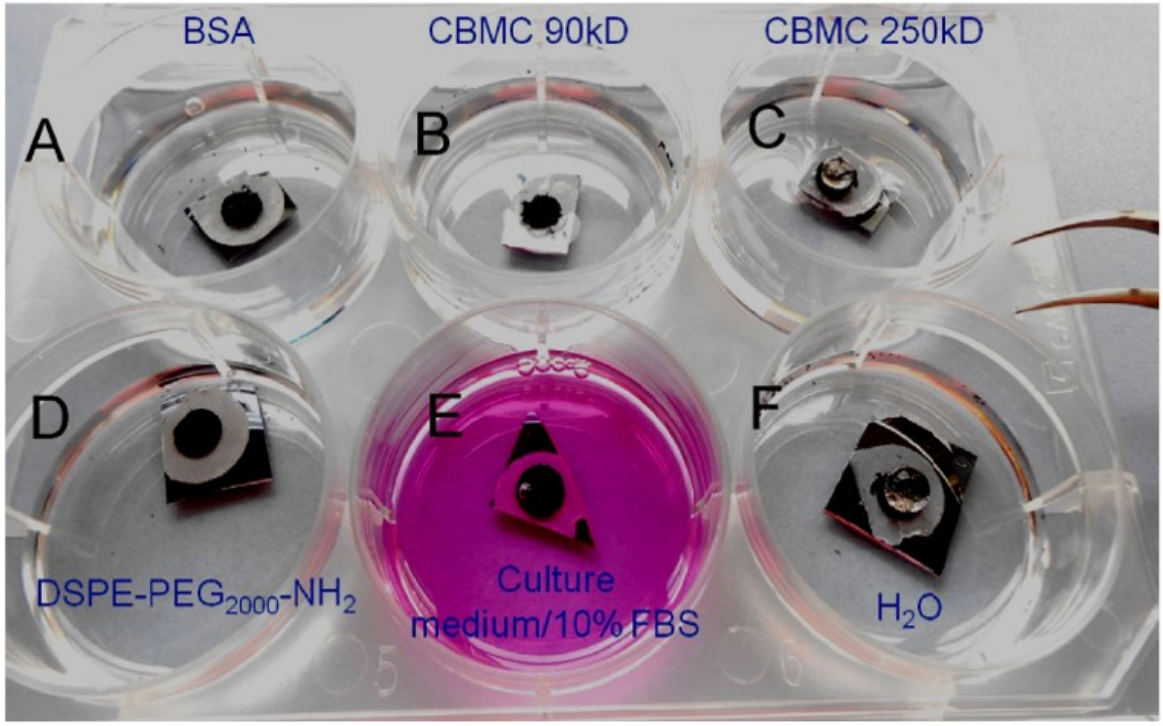

Figure S1: *Transfer of hydrophobic AG into aqueous media employing amphiphilic molecules as immersing agents. AG pellets of 8 mm diameter are fixed to silicon substrates and placed in wells containing aqueous suspensions of different agents. A) Bovine serum albumin (serum protein) The aqueous solution is strongly repelled by AG and collects around the Si-chip, whereas AG remains dry. B) Carboxymethyl cellulose with a molecular weight of 90 kD. The liquid is strongly repelled and collects in the top part of the well, and away from the Si-chip. C) Carboxymethyl cellulose with a molecular weight of 250 kD is repelled as demonstrated by the drop forming on the AG disk, similarly to plain water. D) 2-distearoyl-sn-glycero-3-phosphoethanolamine- N -[amine(PEG2000)] (DSPE-PEG2000-NH_2) readily wets AG and the Si-chip is entirely submerged in the liquid. E) Cell culture medium supplemented with 10% fetal bovine serum (proteins). F. Water as control sample to illustrate super-hydrophobicity of unmodified AG.*

Figure S1 illustrates the results of the series of experiments. BSA and CBMC at different molecular weight were not successful in improving immersion of AG. Cell culture medium supplemented with 10% FBS showed improved immersion of AG after a 2 days incubation period. DSPE-PEG2000-NH_2 has shown to readily immerse AG in

aqueous solutions and thus proven to be the most promising candidate for AG surface functionalization.

SI APPENDIX II: Additional SEM images of DSPE-PEG2000-NH_2 functionalized AG We employed SEM imaging to investigate the surface of biofunctionalized AG scaffolds at high resolution. Figure S2 shows a representative surface scan with different magnifications of DSPE-PEG2000-NH_2 functionalized AG. The sample was dehydrated by drying at ambient conditions and imaged without further surface treatment. The adsorbed molecules become visible at high magnification as fine hairy structures extending from the side walls (Figure S2 B) and as faint bright dots (Figure S2C). Pristine AG was subjected to Au sputtering as a control for scanning electron micrographs of biofunctionalized AG (Figure S3).

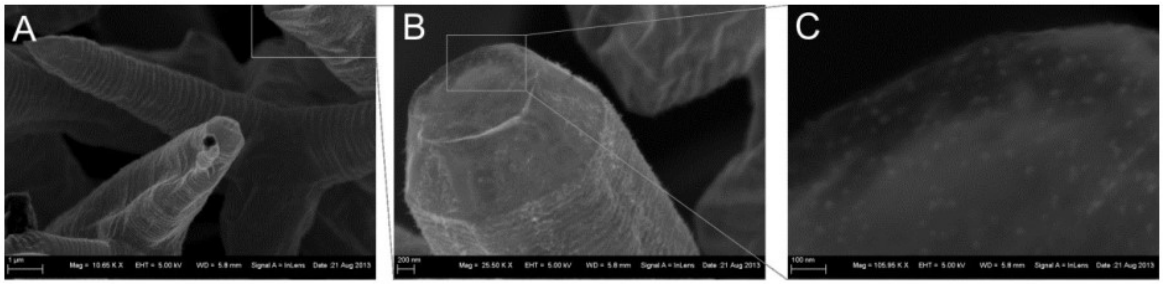

Figure S2: *Scanning electron micrographs of AG non-covalently functionalized with DSPEPEG2000-NH_2 without Au coating.*

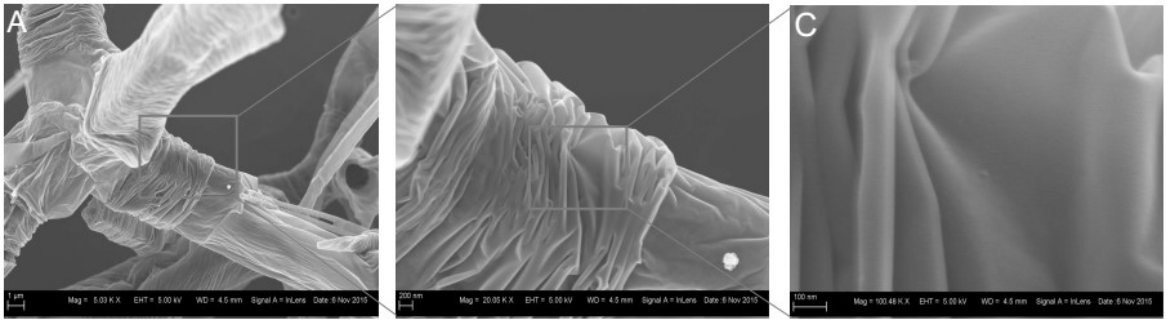

Figure S3: *Scanning electron micrographs of pristine AG with Au coating.*

SI APPENDIX III: Paraffin thin section of AG of different densities Three different AG structures C111, C107 and C116 of varying specific weight ranging from 0.2 mg/ccm to 1.5 mg/ccm were investigated. The CVD parameters influence the wall thickness of the graphitic shells and thus the density of the resulting AG samples. By varying the toluene injection rate various AG densities were obtained and estimated to be 0.2 0.4 mg/ccm for the most lightweight batch C111 (injection rate 5 ml/h per g(ZnO)), 0.5-0.7 mg/ccm for batch C107 (injection rate 5 ml/h per g(ZnO)) , and 1.0-1.2 mg/ccm for batch C116 (injection rate 6 ml/h per g(ZnO)). Figure S4

shows representative cross sections and a photograph of all 3 types in dry state. It is important to mention that all three types were produced based on a cylindrical ZnO template of 6 mm diameter and 3 mm height. In C107 and C106 the original size of the template is preserved with a minor gain in size of 1-2%. The ultra-lightweight structure of C111 - on the other hand - exhibits much reduced dimensions, as a consequence of compression under its own weight.

The samples were transferred into bi-distilled water through non-covalent surface modification by hydrophobic adsorption of PEG-lipids. For paraffin embedding dehydration was carried out by sequentially exchanging water for ethanol, subsequent transfer into xylene and soaking into liquid paraffin. During this procedure the samples were constantly kept in liquid to prevent collapse of the AG structure due to surface tension during evaporation. After solidification the paraffin blocks were trimmed down and either horizontal thin sections or vertical sections of 9 μm thickness were prepared for assessment of the network within the bulk material (Figure S4).

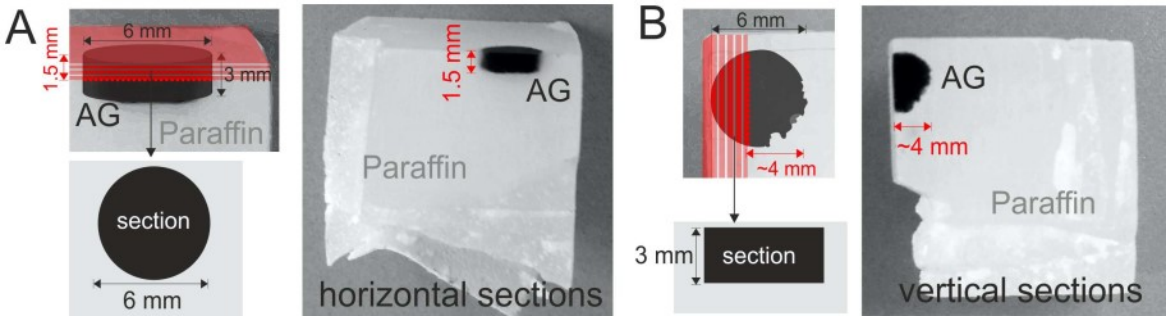

Figure S4: *Cartoons illustrating the preparation of horizontal and vertical sections from different paraffin embedded AG samples. Embedded AG disks were 6 mm in diameter and 3 mm in height. (A) Side view cartoon depicting the preparation of 9 μm thick horizontal cross sections to about the equatorial line of the AG disk at 1.5 mm. The photograph to the right shows what remains from the paraffin embedded AG disks after sectioning. (B) The top view cartoon on the left shows the preparation of vertical sections of 9 μm thickness and 3 mm height, which were were cut from the first 2 mm of the 6 mm AG sample. The top view photograph of the paraffin block shows the remaining sample.*

The sections were investigated under a light microscope to assess filament thickness, pore size, matrix connectivity, and homogeneity of these parameters (Figure S5A-C). Sections of the ultra- lightweight AG C111 generally revealed that the filament lengths and diameters, as well as the pore sizes ranged below typical structural parameters presented by natural extracellular matrix. Sections of AG C107 showed reduced connectivity of filaments, which might be an artificial result of the harsh treatment during paraffin embedding where paraffin was repeatedly filled and drained into and from the bulk sample, or may be related to structural problems of the ZnO template. Regions with disrupted network connectivity were much fewer in C116 with the highest specific weight of $>$ 1mg/ccm. Thus we assumed that interfilament connections were more robust, suggesting that this type of AG might be more suitable for future experiments.

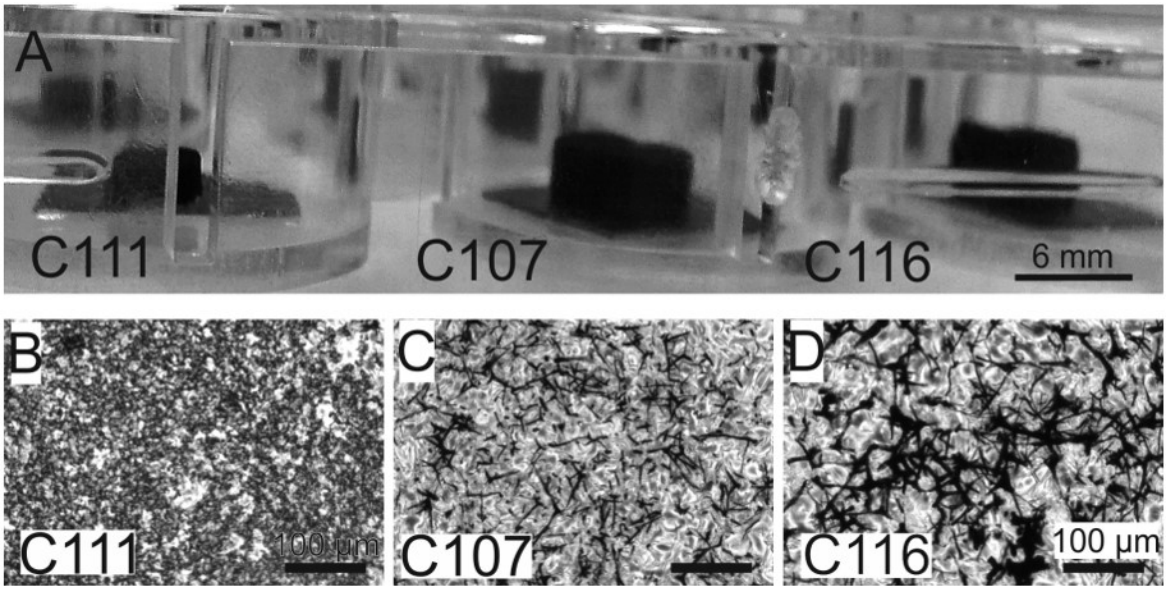

Figure S5: *(A) Photograph showing AG samples of different specific weight before paraffin embedding; C111 ultra-lightweight AG with average specific weight of 0.25 mg/cm^3, C107 AG with average specific weight of 0.6 mg/cm^3, C116 AG with average specific weight of 1.1 mg/cm^3. (B-C) Light microscopy images of paraffin sections revealing the network structure of carbon microfilaments within the bulk samples of C111, C107 and C116. Scale bars 100 µm.*

SI APPENDIX IV: Additional light microscopy images of haematoxylin and eosin stained AG sections

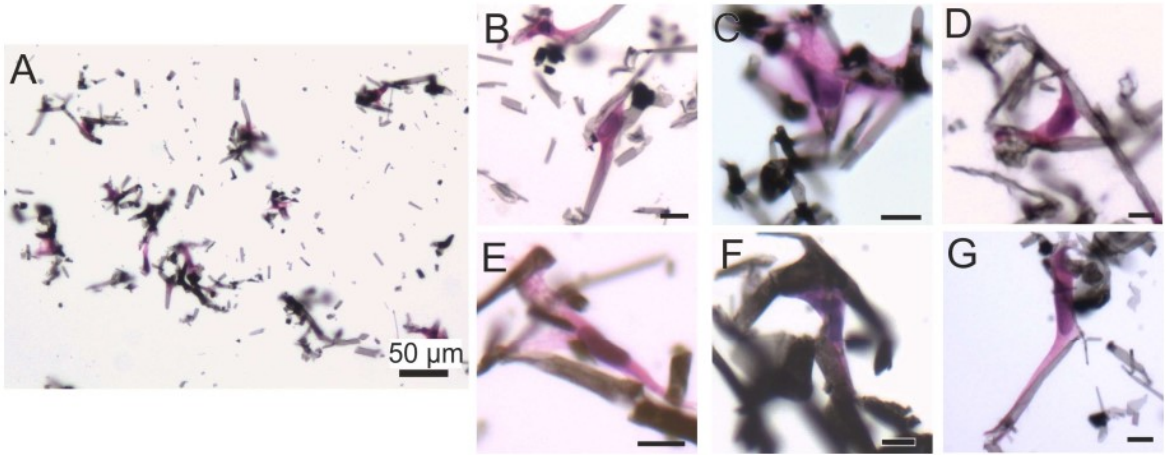

Figure Appendix-B.6: *(A) HE-staining makes REF52 YFP Pax cells visible by coloring the nuclei blue and the cytosol pink. Due to the vigorous de-waxing and staining treatment, the original section (Figure S5D) is disrupted and in part has been washed off the glass slide. B)-G) Higher magnification reveals cells that are well interfaced with AG filaments and illustrate morphologies typical for fibroblasts. Scale bars 10 µm.*

Appendix-C

C.1 Supporting information on publication 2

Biomimetic Carbon-Fiber Systems Engineering: A Modular Design Strategy to Generate Biofunctional Composites from Graphene and Carbon Nanofibers

Mohammadreza Taale, Fabian Schütt, Tian Carey, Janik Marx, Yogendra Kumar Mishra, Norbert Stock, Bodo Fiedler, Felice Torrisi, Rainer Adelung, Christine Selhuber-Unkel

Corresponding Author

Email: cse@tf.uni-kiel.de

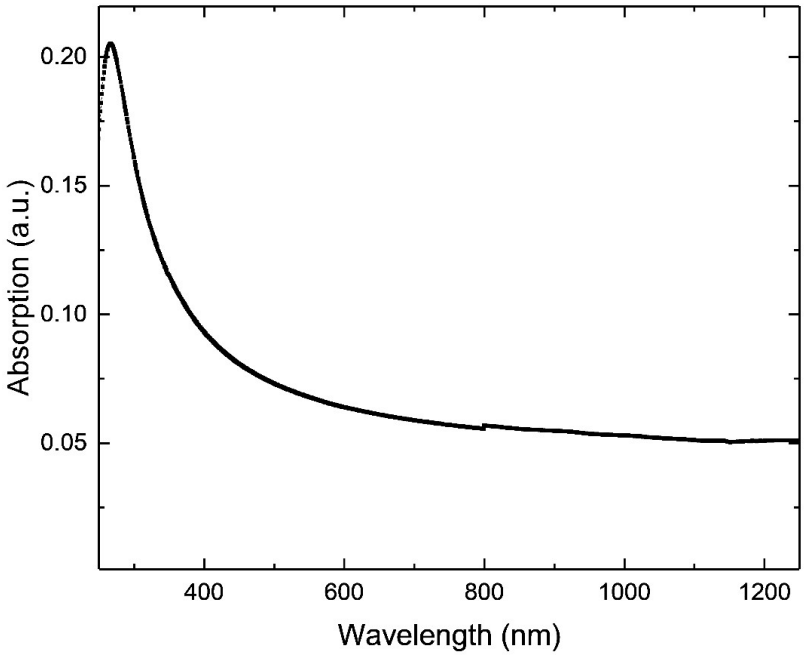

Figure S1: *Optical absorption spectrum of the graphene ink.*

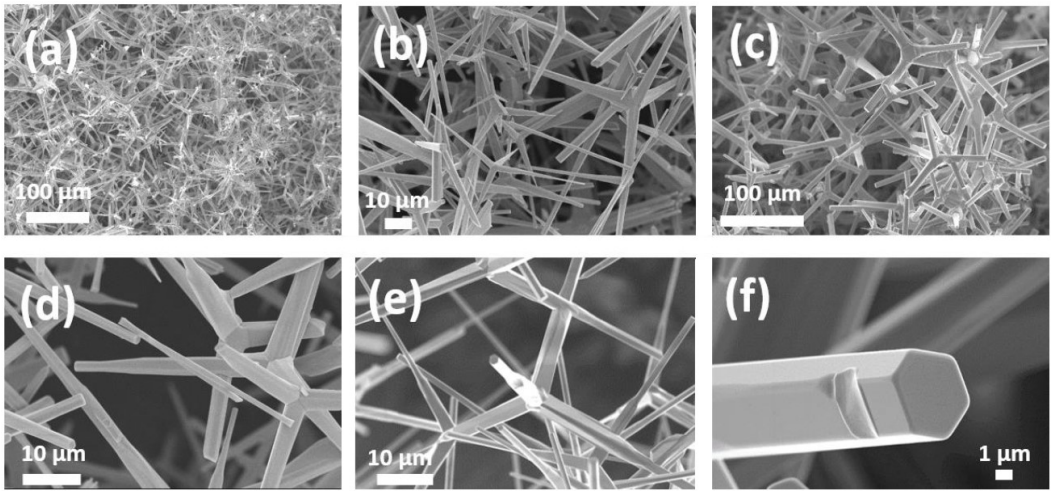

Figure S2: *Scanning electron micrographs showing the microstructure of ZnO tetrapod templates. a-c) Overview of the ZnO microstructure, d-f) zoom-in on ZnO tetrapods.*

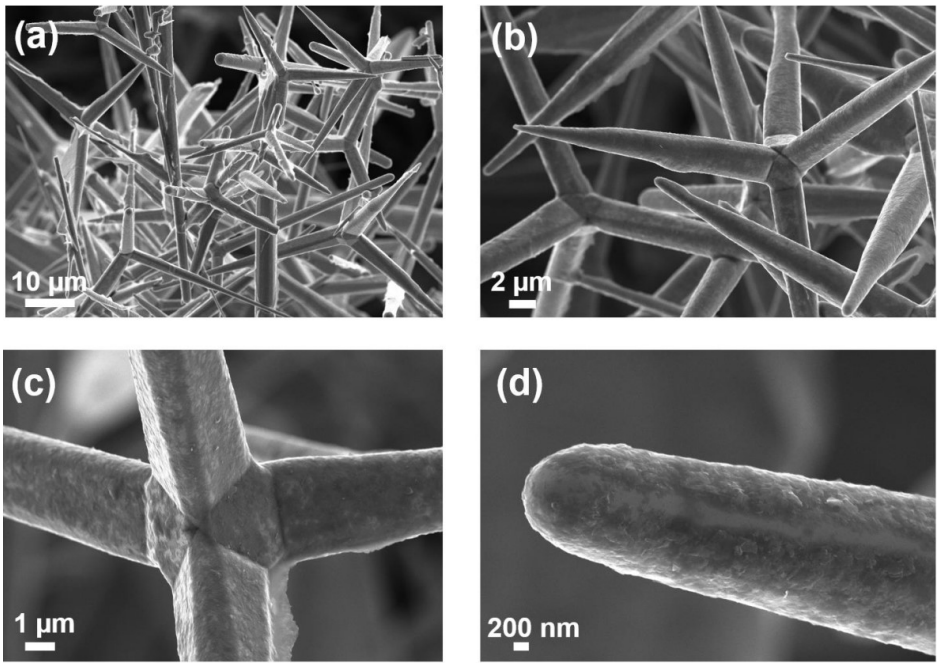

Figure S3: *Scanning electron micrograph of ZnO templates after infiltration with graphene. The ZnO tetrapods are coated by graphene. a, b) Overview of ZnO templates after infiltration with graphene. d, e) High magnification image of ZnO tetrapods after infiltration with graphene.*

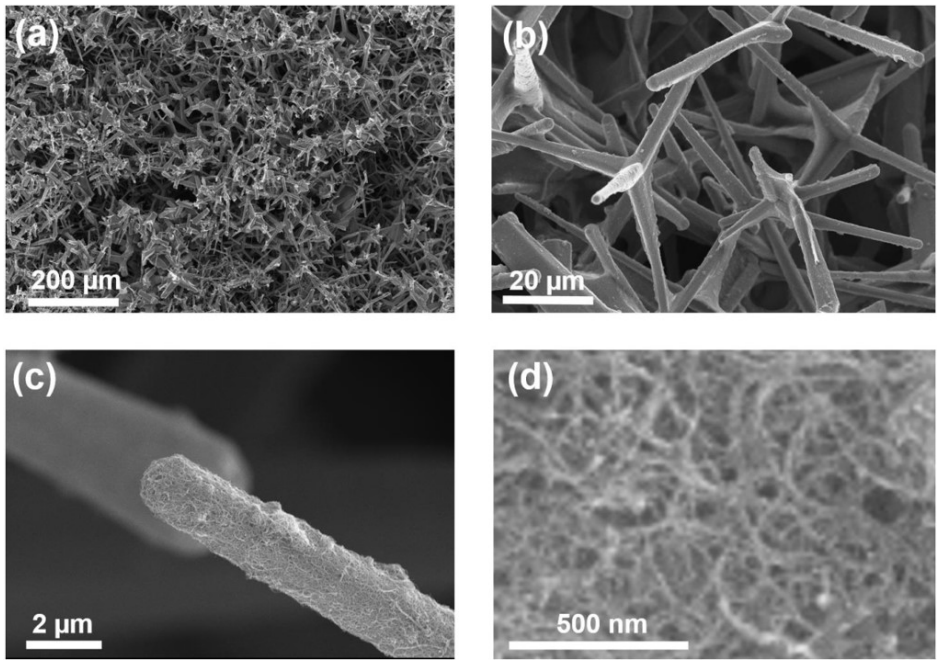

Figure S4: *Scanning electron micrograph of ZnO templates after infiltration with CNTs. The ZnO tetrapods are coated with self-entangled CNTs. a, b) Overview of ZnO templates after infiltration with CNTs. c, d) High magnification image of ZnO tetrapods after infiltration with CNTs.*

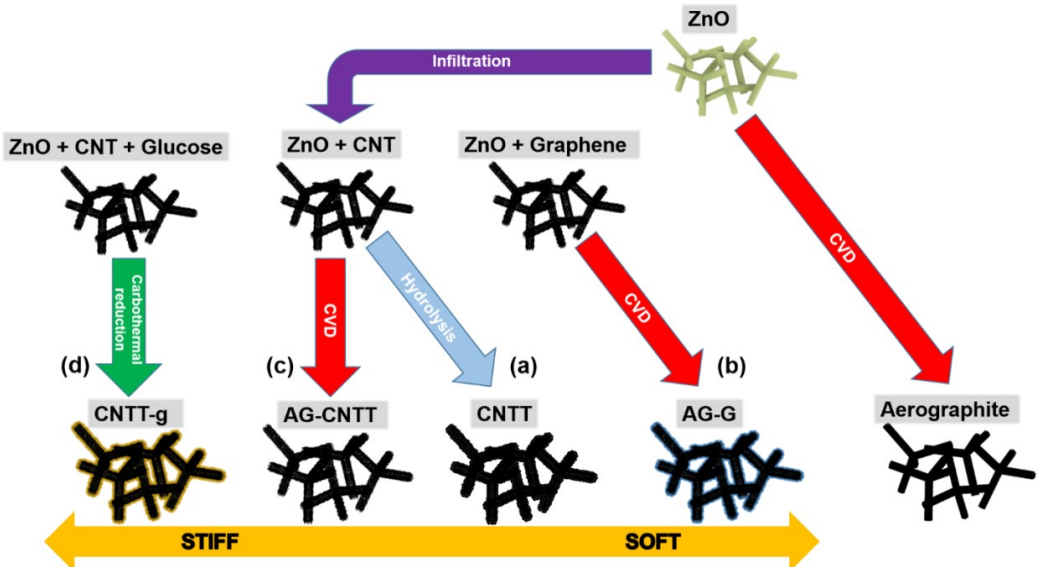

Figure S5: *Schematic illustration of the different 3D carbon tube structures. Brief description of abbreviations; a) Hydrolysis of CNT-decorated ZnO (CNTT), b) Conversion of graphenedecorated ZnO to aerographite (AG-G), c) Conversion of CNT-decorated ZnO to aerographite (AG-CNTT), d) Conversion of CNT- and glucose-decorated ZnO to aerographite via a carbothermal reduction process (CNTT-g).*

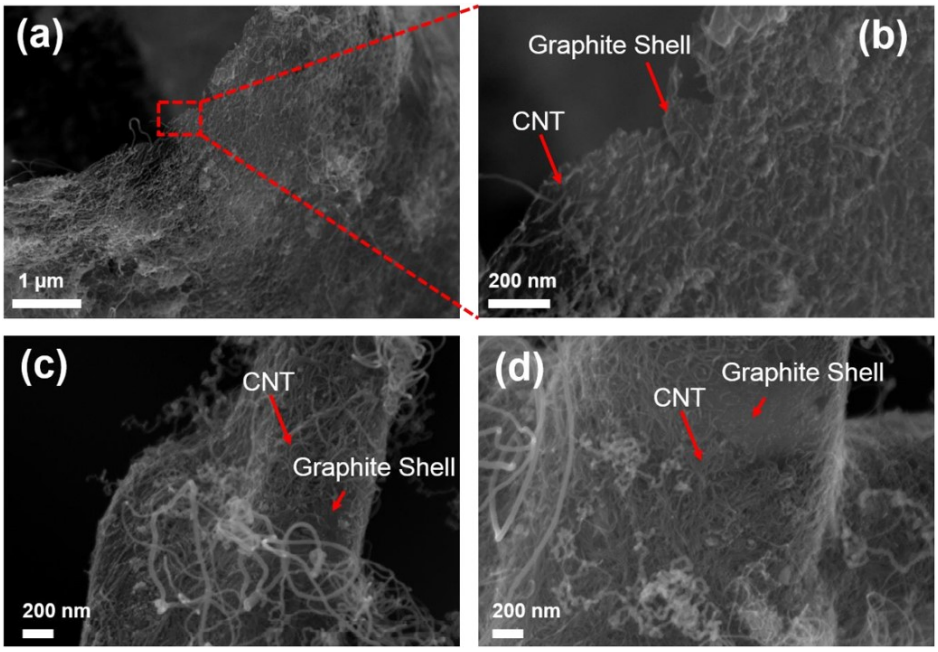

Figure S6: *Scanning electron micrographs of AG-CNTT structures, revealing the graphitic shell beneath entangled CNTs. a) Graphitic shell beneath entangled CNTs, b) Zoom-in on the graphitic shell beneath entangled CNTs, c, d) Medium sized overview showing the graphitic shell beneath entangled CNTs. (Red arrows show CNT and graphite shell in the SEM images)*

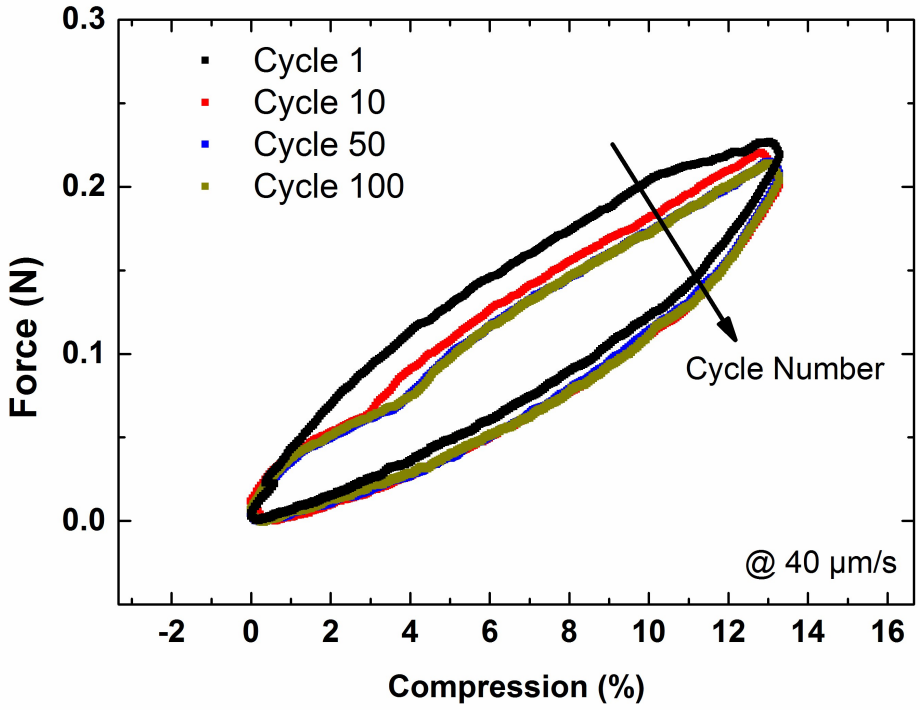

Figure S7: *Long-cycle compression test graph of AG-G scaffold. The graph presents the stressstrain curves at different cycles (i.e. 1, 10, 50, and 100) up to 100 times to 13.3 % at a deformation speed of 40 µm/s, with no waiting time between the individual compression cycles.*

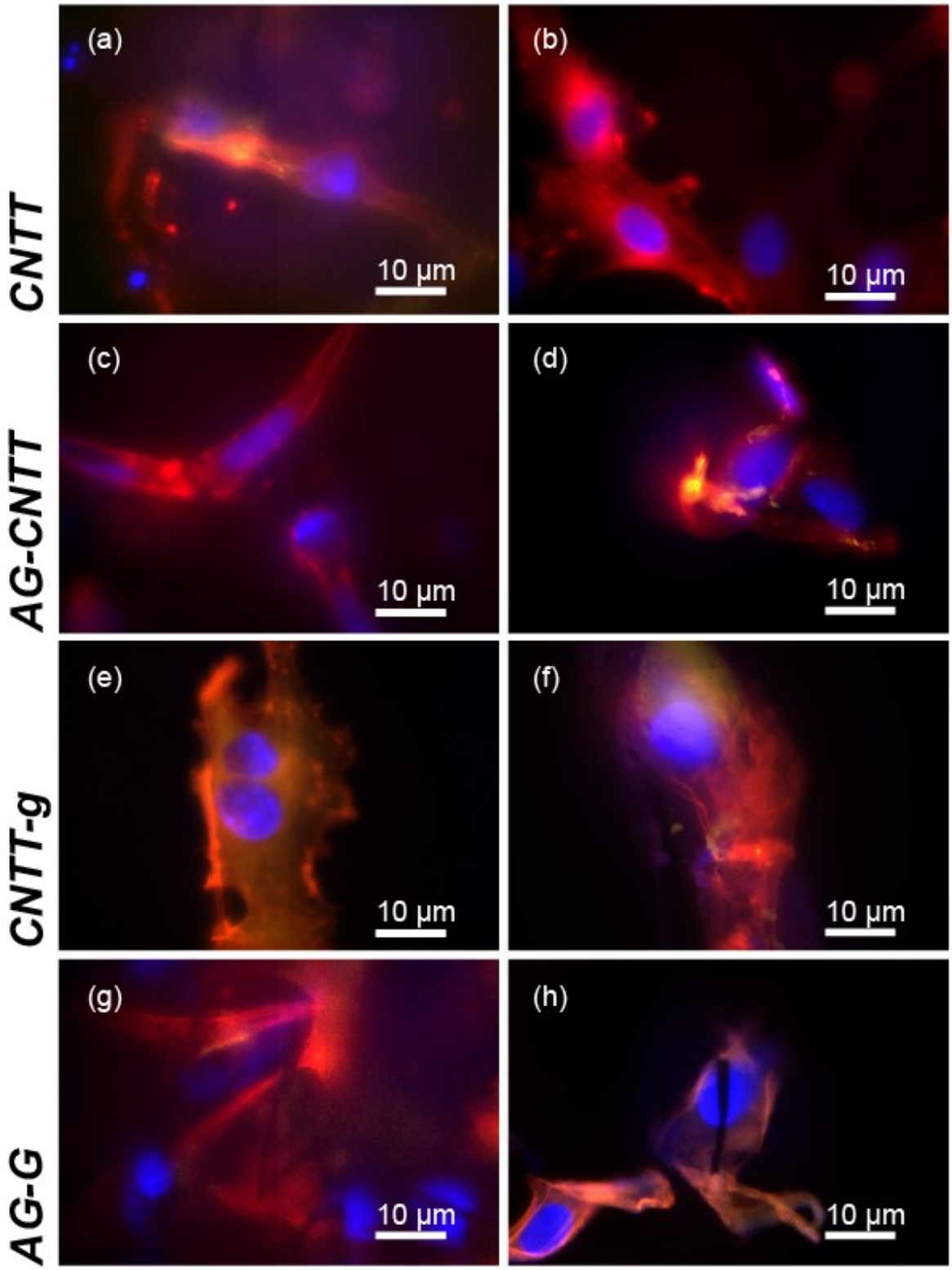

Figure S8: *High magnification fluorescence image of REF52 YFP-paxillin cells on 3D scaffolds a,b) CNTT, c,d) AG-CNTT, e,f) CNTT-g, g,h) AG-G. YFP-paxillin is mainly distributed in small adhesion sites (YFP; yellow), the nucleus was stained with Hoechst (DAPI; blue) and actin fibers were visualized by phalloidin (red). Fluorescent imaging took place in optical sections approximately between 50-100 µm from the surface of the material.*

Supporting discussion

1. Long cycle compression test on AG-G scaffold

The mechanical properties of our 3D carbon nanomaterial scaffolds, indeed play a crucial role in applications such as biomimetic scaffolds. As discussed in the manuscript, we are able to tailor the mechanical properties of the network structures by the incorporation of different nanomaterials into a graphitic shell. For example, the incorporation of CNTs results in an increase in the compression strength as well as the Youngs modulus of the bare graphitic scaffold, whereas this is rather brittle when compressed. In the case of non-CNT containing scaffolds (such as AG and AG-G) these exists elastic behavior under compression. In order to illustrate this point more in detail, we have measured the long-cycle compression behavior of an AG-G scaffold. This is the scaffold with the lowest stiffness among all the other presented scaffolds in our study. The scaffold was compressed 100 times to 13.3 % at a deformation speed of 40 μm/s, with no wait time between the individual compression cycles. Figure S7 shows the stress-strain curves at different cycles (i.e. 1, 10, 50, and 100). As a typical behavior of such highly porous foams 1 the first cycle (virgin curve) shows a deviation from the following cycles due to irreversible plastic deformation, indicating a change in the scaffold morphology into an energetically more favorable arrangement of the hollow microtubes. For the following 9 cycles the mechanical behavior is purely elastic and the stress-strain curves changing only slightly until a stable state is reached and almost no further change can be observed for the next 90 cycles.

Appendix-D

D.1 Supporting information on publication 3

Bioactive Carbon Based Hybrid 3D Scaffolds for Osteoblast Growth

Mohammadreza Taale, Fabian Schütt, Kai Zheng, Yogendra Kumar Mishra, Aldo R. Boccaccini, Rainer Adelung, Christine Selhuber-Unkel

Corresponding Author

Email: cse@tf.uni-kiel.de

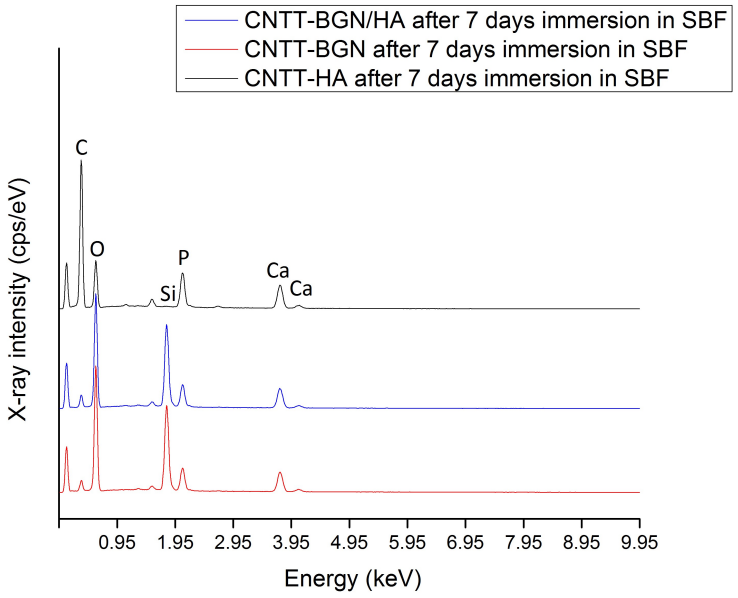

Figure S1: *EDS results of scaffolds after immersion in simulated body fluid (SBF). CNTT-BGN in SBF for 7 d (red graph); CNTT-HA in SBF for 7 d (black graph); CNTT-BGN/HA in SBF for 7d (blue graph).*

Table S1: *Density and porosity of the different scaffolds tested in this study. CNTT(y)-BGN(x): y and x correspond to the number of infiltrations of CNTs and ceramic (HA or BG) nanoparticles, respectively. For example, CNTT(3)-BGN(5) means a ZnO template was infiltrated 5 times with BG nanoparticles and 3 times with CNT dispersion.*

.

Scaffold	CNT concentration (mg/cm^3)	HA/BGN concentration (mg/cm^3)	Density/ g/cm^3	Porosity (%)
CNTT(3)-BGN(5)	32	214	0.246	87-94
CNTT(5)-BGN(5)	53	214	0.267	86-93
CNTT(7)-BGN(5)	75	214	0.289	85-92
CNTT(3)-HA(5)	32	214	0.246	87-94
CNTT(5)-HA(5)	53	214	0.267	86-93
CNTT(7)-HA(5)	75	214	0.289	85-92
CNTT(7)-BGN(3)/HA(3)	75	257	0.332	83-91

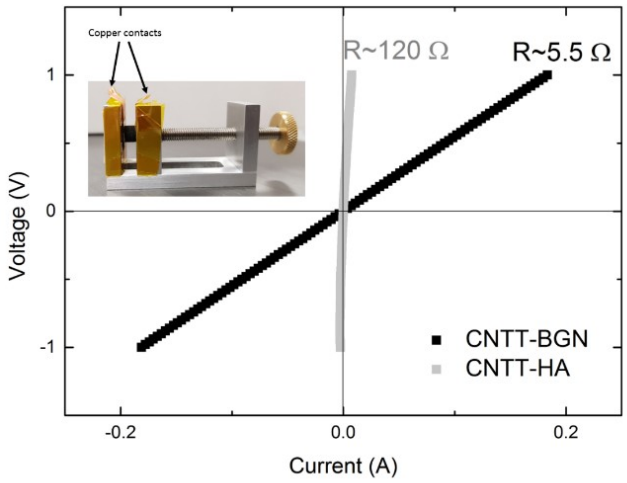

Figure S2: *Current-voltage (IV) curve of CNTT-HA and CNTT-BGN scaffolds, and the sample holder, which was used for electrical conductivity measurement.*

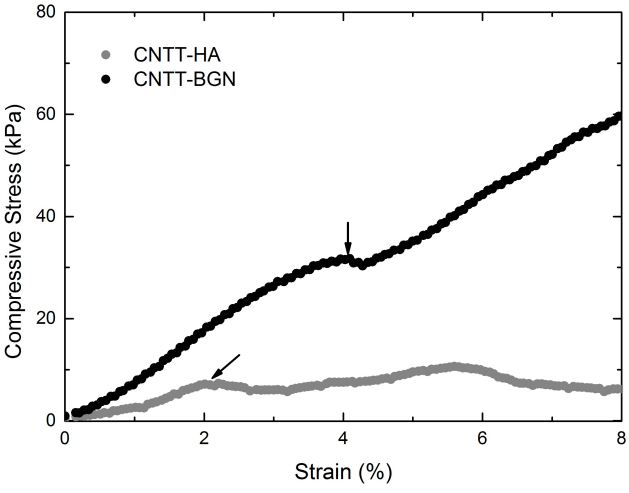

Figure S3: *Stress-strain curves for determining the compressive strength of CNTT-HA and CNTT-BGN scaffolds. The arrows mark the points of the maximum compressive stress (at which the sample breaks).*

Appendix-E

E.1 Supporting information on publication 4

Systematically designed periodic electrophoretic deposition for decorating 3D carbon-based scaffolds with bioactive nanoparticles

Mohammadreza Taale, Diana Krüger, Emmanuel Ossei-Wusu, Fabian Schütt, Muhammad Atiq Ur Rehman, Yogendra Kumar Mishra, Janik Marx, Norbert Stock, Bodo Fiedler, Aldo R Boccaccini, Regine Willumeit-Römer, Rainer Adelung, Christine Selhuber-Unkel

Corresponding Author

Email: cse@tf.uni-kiel.de

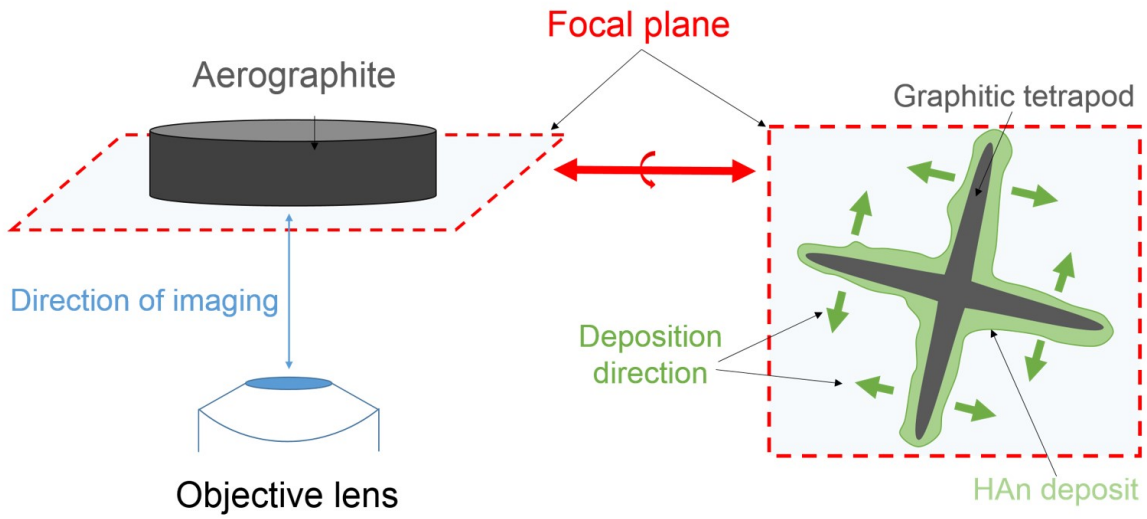

Figure S1: *Schematic of in situ filming during fluorescently labeled HAn deposition via EPD. The schematic reveals the meaning of lateral deposition. The focal plane of imaging is almost located on the surface of AG scaffolds, which is perpendicular to the direction of imaging. Due to the direction of imaging the deposit growth only is detectable among the focal plane, which is called lateral deposition in this study.*

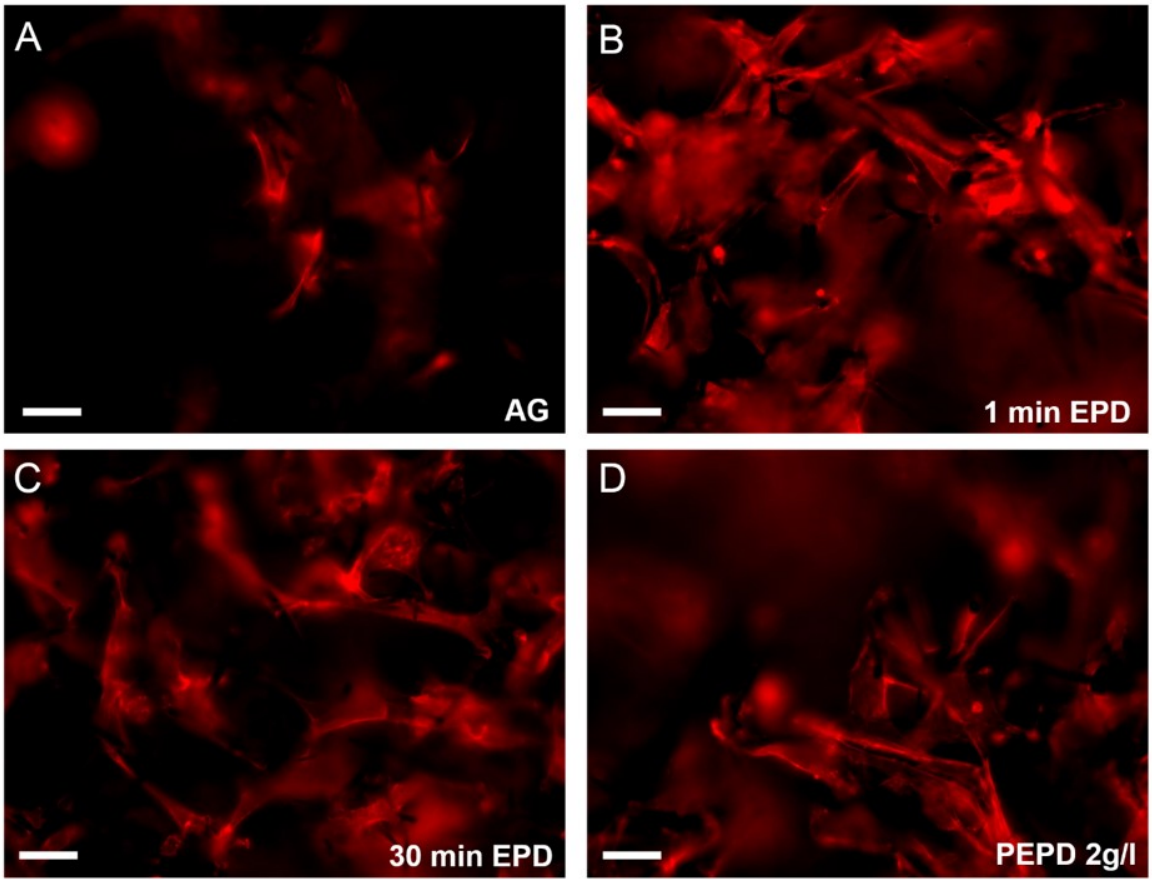

Figure S2: *High magnification fluorescence images of preosteoblast cells (MC3T3-E1) cells on 3D scaffolds A) AG, B) 1 min EPD, C) 30 min EPD, D) PEPD 2g/l. Actin fibers were visualized by phalloidin (red). Fluorescence imaging took place in optical sections up to 200 µm from the surface of the material.*

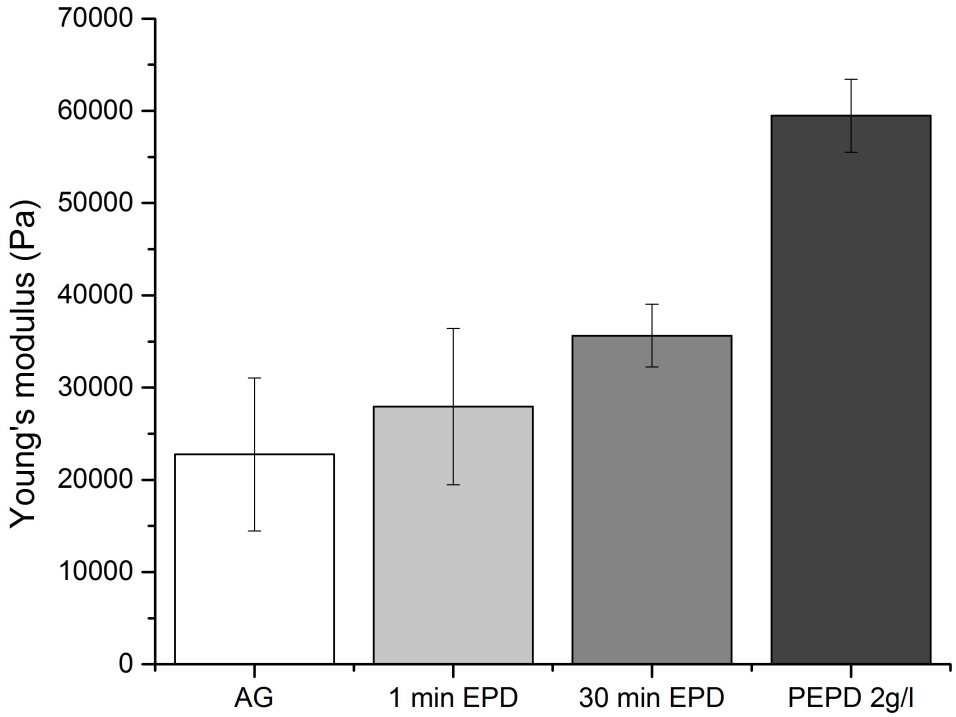

Figure S3: *Youngs moduli (measured under compression) of AG, 1 min EPD, 30 min EPD, and PEPD 2g/l scaffolds. The Youngs moduli of the scaffolds were measured using a home-built electromechanical testing setup. (Error bars represent the mean ± standard deviation, n = 3)*

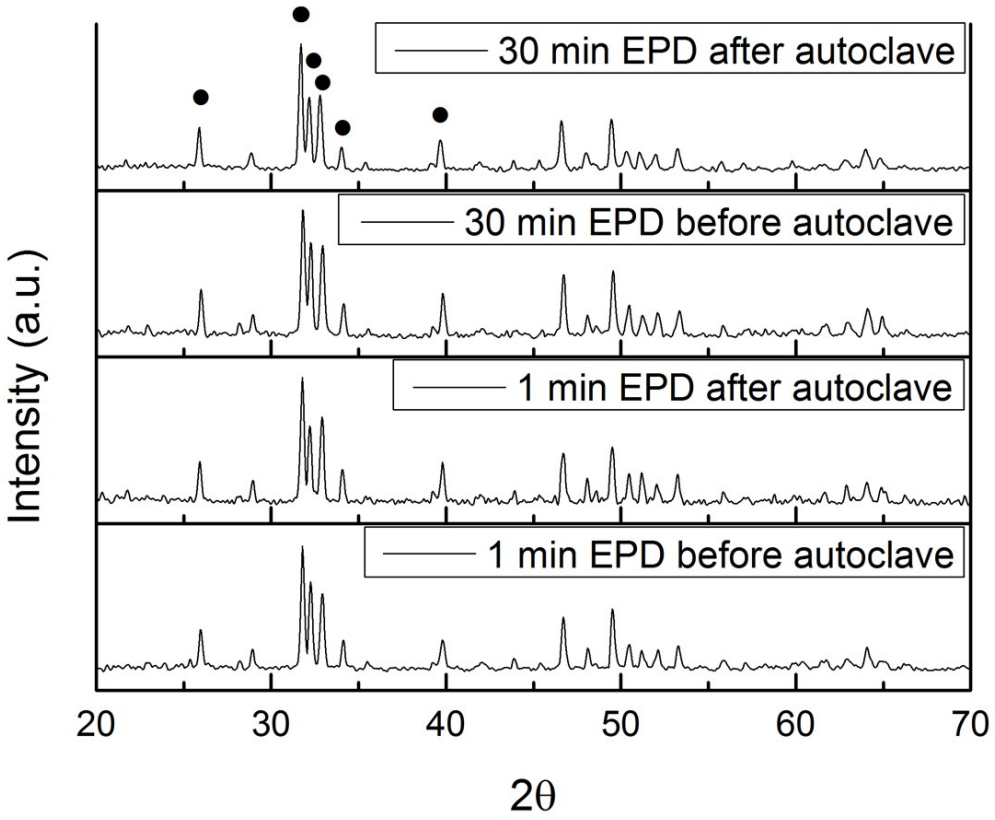

Figure S4: *XRD pattern of 1 min EPD and 30 min EPD scaffolds after and before autoclaving at 121 °C. The XRD pattern of the scaffolds show typical peaks for hydroxyapatite (•hydroxyapatite). The XRD patterns reveal no significant crystallinity difference between the scaffolds.*

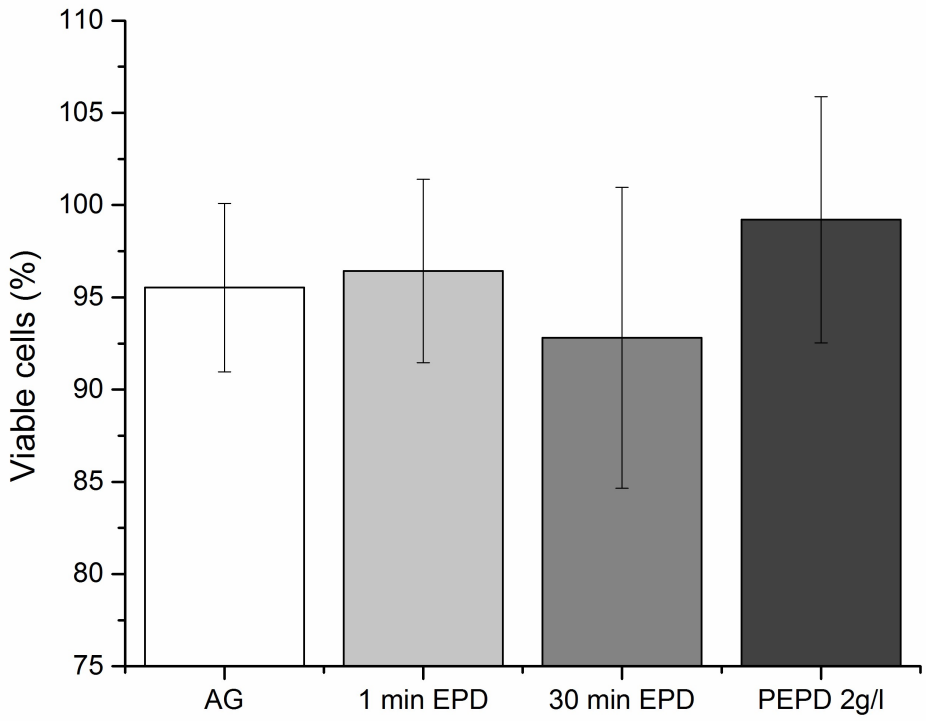

Figure S5: *Cell viability of preosteoblast cells (MC3T3-E1) treated with extracts of AG, 1 min EPD, 30 min EPD, and PEPD 2g/l, measured via an MTT-formazan absorbance assay. Fresh and untreated culture medium served as control. (Error bars represent the mean ± standard deviation, n = 5)*

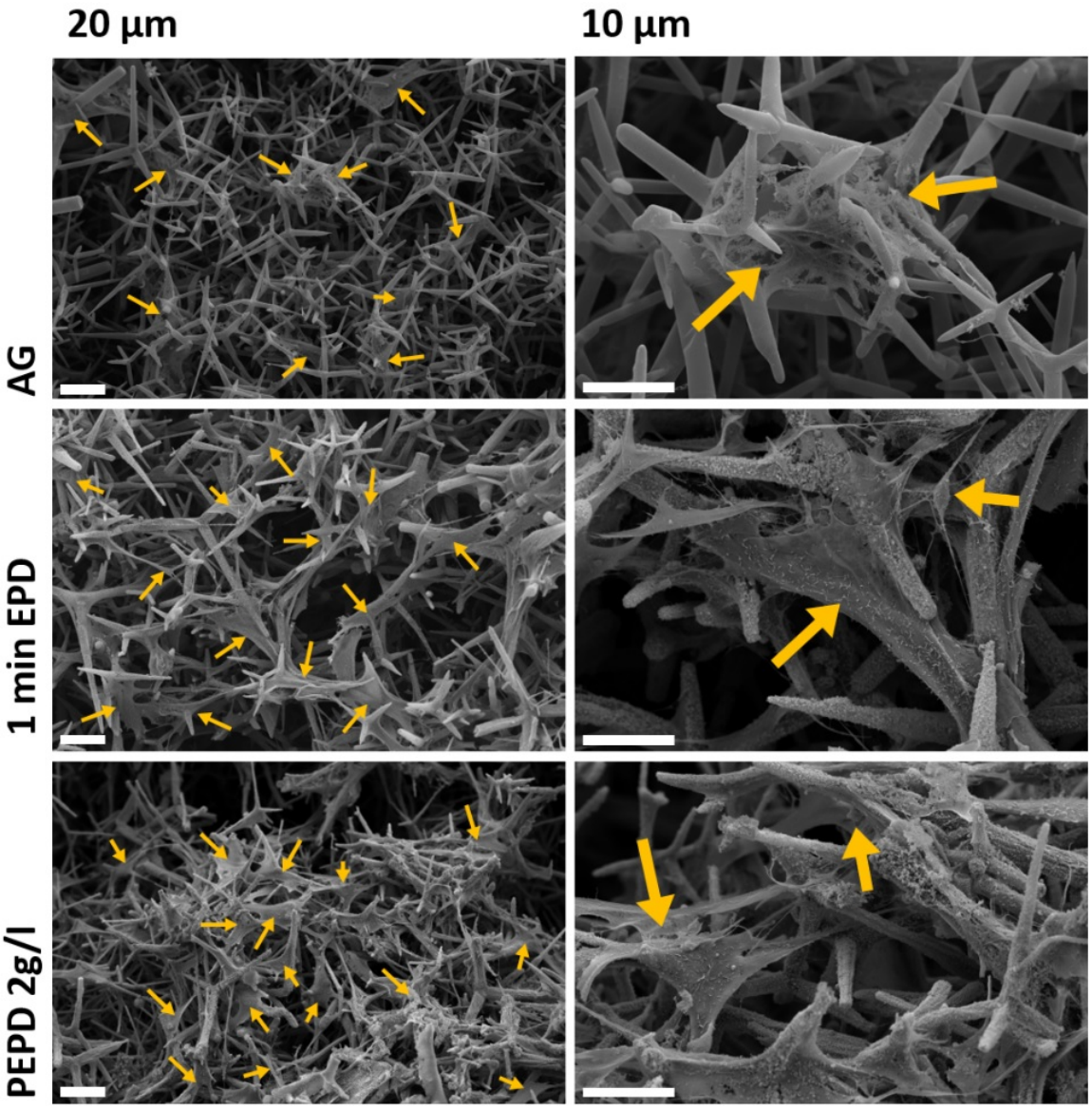

Figure S6: *SEM micrographs of preosteoblast cells (MC3T3-E1) cultivated for four days on AG and HAn-AG scaffolds. Scale bars are 20 µm for the column to the left, 10 µm for column to the right. SEM imaging took place deep inside the scaffolds (up to 3 mm). The yellow arrows point at osteoblast cells inside the scaffolds.*

Acknowledgments

At this point, I am deeply grateful to work on the project of carbon-based scaffolds for 3D cell growth and all the people who contributed in some way to accomplish this dissertation, which would have not been possible without their numerous helps.

Firstly, I would like to express sincere gratitude to my adviser Prof. Dr. Christine Selhuber-Unkel for giving me the opportunity to join her vibrant group and her continuous support of my Ph.D study and related research, for her patience, motivation, and immense knowledge. I am thankful for her guidance in all time of research and writing this thesis. I also appreciate a lot her helps in my personal life. I could not have imagined having a better advisor and mentor for my Ph.D study.

I would like to express my deepest gratitude to Dr. Constanze Lamprecht for sharing her research ideas and her non-stop supports prior and during the first year of my Ph.D. year. Without her dedication and motivation this work could never been granted.

I would like to acknowledge the funding of this project from Deutscher Akademischer Austauschdienst (DAAD) through a research grant for doctoral candidates (91526555-57048249) as well as supports by the European Research Council (ERC StG 336104 682 CELLINSPIRED, ERC PoC 768740 CHANNELMAT).

I would like to thank our project partners Prof. Dr. Rainer Adelung for sharing his ideas and interactive discussions throughout the joint projects. I admire him for providing high quality zinc oxide tetrapods and working area in his labs. His continuous attempts and contributions are the key point for the progress in this project.

I would like to thank Prof. Dr. Regine Willumeit-Römer and M.Sc. Diana Krüger for their assistance in X-ray microcomputed tomography.

I am very thankful to Dr. Fabian Schütt for his assistance in the development of carbon-based scaffolds.

I would like to thank Emmanuel Ossei-Wusu for his assistance in electrophoretic deposition process.

I would like to thank Prof. Dr. Aldo R Boccaccini for his support and patient guidance on the development of bioactive hybrid carbon-base scaffolds.

I would like to thank Diana Krüger and Steven Huth for their helps translating the

abstract of this dissertation.

I would like to sincerely thank all my friends and colleagues in the group of Biocompatible nanomaterials at Kiel University, Hendrikje Neumann, Steven Huth, Dr. Laith Kadem, Dr. Sören Gutekunst, Katharina Siemsen, Sandra Sindt, Christine Arndt, Michael Timmermann, Nils Lukat, Galen Ream , Ellen Riemer and Dr. Tina Kerby. I am also grateful to our technical staff Manuela Lieb for her technical assistance on cell culture.

I am very thankful to my dearest friends Dr. Ali Tavassolizadeh, Hendrikje Neumann and Mohammadhassan Emami for being always supportive and the wonderful times we had.

Finally, I wish to thank my lovely family for their endless encouragement and selfless supports over the past 25 years of my study.

Publications

Publications

- C. Lamprecht, M. Taale, I. Paulowicz, H. Westerhaus, C. Grabosch, A. Schuchardt, M. Mecklenburg, M. Böttner, R. Lucius, K. Schulte, R. Adelung, C. Selhuber-Unkel. A tunable scaffold of microtubular graphite for 3D cell growth. *ACS Appl. Mater. Interfaces*, 8:24, 14980-14985, 2016.
- M. Taale, F. Schütt, K. Zheng, Y. K. Mishra, A. R. Boccaccini, R. Adelung, C. Selhuber-Unkel. Bioactive carbon based hybrid 3D scaffolds for osteoblast growth. *ACS Appl. Mater. Interfaces*, 10:50, 43874-43886, 2018.
- M. Taale, F. Schütt, T. Carey, J. Marx, Y. K. Mishra, N. Stock, B. Fiedler, F. Torrisi, R. Adelung, C. Selhuber-Unkel. Biomimetic carbon-fiber systems engineering : A modular design strategy to generate biofunctional composites from graphene and carbon nanofibers. *ACS Appl. Mater. Interfaces*, 11:5, 5325-5335, 2019.
- M. Taale, D. Krüger, E. Ossei-Wusu, F. Schütt, M. A. U. Rehman, Y. K. Mishra, J. Marx, N. Stock, B. Fiedler, A. R. Boccaccini, R. Willumeit-Römer, R. Adelung, C. Selhuber-Unkel. Systematically designed periodic electrophoretic deposition for decorating 3D carbon-based scaffolds with bioactive nanoparticles. *ACS Biomater. Sci. Eng.*, 5:9, 4393-4404, 2019.
- M. Bremer, R. Reinke, B Hesseler, M. Taale, D Ingwersen, S. Schwarzer, C. Selhuber-Unkel, M. Gerken. Noncovalent spiropyran coatings for photoinduced wettability switching. *J. Nanomater.*, 1-6, 2017.

Bibliography

[1] Heungsoo Shin, Seongbong Jo, and Antonios G Mikos. Biomimetic materials for tissue engineering. *Biomaterials*, 24(24):4353–4364, 2003.

[2] MP Lutolf and JA Hubbell. Synthetic biomaterials as instructive extracellular microenvironments for morphogenesis in tissue engineering. *Nat. Biotechnol.*, 23(1):47, 2005.

[3] Byung-Soo Kim, In-Kyu Park, Takashi Hoshiba, Hu-Lin Jiang, Yun-Jaie Choi, Toshihiro Akaike, and Chong-Su Cho. Design of artificial extracellular matrices for tissue engineering. *Prog. Polym. Sci.*, 36(2):238–268, 2011.

[4] Molly M Stevens and Julian H George. Exploring and engineering the cell surface interface. *Science*, 310(5751):1135–1138, 2005.

[5] Janna K Mouw, Guanqing Ou, and Valerie M Weaver. Extracellular matrix assembly: A multiscale deconstruction. *Nat. Rev. Mol. Cell Biol.*, 15(12):771–785, 2014.

[6] Yogendra Kumar Mishra and Rainer Adelung. ZnO tetrapod materials for functional applications. *Mater. Today*, 21(6):631–651, 2018.

[7] Chaenyung Cha, Su Ryon Shin, Nasim Annabi, Mehmet R Dokmeci, and Ali Khademhosseini. Carbon-based nanomaterials: multifunctional materials for biomedical engineering. *ACS Nano*, 7(4):2891–2897, 2013.

[8] Benjamin S Harrison and Anthony Atala. Carbon nanotube applications for tissue engineering. *Biomaterials*, 28(2):344–353, 2007.

[9] Sumit Goenka, Vinayak Sant, and Shilpa Sant. Graphene-based nanomaterials for drug delivery and tissue engineering. *J. Control. Release*, 173:75–88, 2014.

[10] Constanze Lamprecht, Mohammadreza Taale, Ingo Paulowicz, Hannes Westerhaus, Carsten Grabosch, Arnim Schuchardt, Matthias Mecklenburg, Martina Bottner, Ralph Lucius, Karl Schulte, et al. A tunable scaffold of microtubular graphite for 3d cell growth. *ACS Appl. Mater. Interfaces*, 8(24):14980–14985, 2016.

[11] Changsheng Shan, Wenjie Zhao, X Lucas Lu, Daniel J O'Brien, Yupeng Li, Zeyuan Cao, Ana Laura Elias, Rodolfo Cruz-Silva, Mauricio Terrones, Bingqing Wei, and Jonghwan Suhr. Three-dimensional nitrogen-doped multiwall carbon nanotube sponges with tunable properties. *Nano Lett.*, 13(11):5514–5520, 2013.

[12] Xuchun Gui, Jinquan Wei, Kunlin Wang, Anyuan Cao, Hongwei Zhu, Yi Jia, Qinke Shu, and Dehai Wu. Carbon nanotube sponges. *Adv. Mater.*, 22(5):617–621, 2010.

[13] Kyu Hun Kim, Youngseok Oh, and Mohammad F Islam. Graphene coating makes carbon nanotube aerogels superelastic and resistant to fatigue. *Nat. Nanotechnol.*, 7(9):562–566, 2012.

[14] Mateusz B Bryning, Daniel E Milkie, Mohammad F Islam, Lawrence A Hough, James M Kikkawa, and Arjun G Yodh. Carbon nanotube aerogels. *Adv. Mater.*, 19(5):661–664, 2007.

[15] Marcus A Worsley, Peter J Pauzauskie, Tammy Y Olson, Juergen Biener, Joe H Satcher, and Theodore F Baumann. Synthesis of graphene aerogel with high electrical conductivity. *J. Am. Chem. Soc.*, 132(40):14067–14069, 2010.

[16] Cheng Zhu, T Yong-Jin Han, Eric B Duoss, Alexandra M Golobic, Joshua D Kuntz, Christopher M Spadaccini, and Marcus A Worsley. Highly compressible 3d periodic graphene aerogel microlattices. *Nat. Commun.*, 6:6962, 2015.

[17] Zhen Xu, Yuan Zhang, Peigang Li, and Chao Gao. Strong, conductive, lightweight, neat graphene aerogel fibers with aligned pores. *ACS Nano*, 6(8):7103–7113, 2012.

[18] Haiyan Sun, Zhen Xu, and Chao Gao. Multifunctional, ultra-flyweight, synergistically assembled carbon aerogels. *Adv. Mater.*, 25(18):2554–2560, 2013.

[19] Fabian Schütt, Stefano Signetti, Helge Krüger, Sarah Röder, Daria Smazna, Sören Kaps, Stanislav N Gorb, Yogendra Kumar Mishra, Nicola M Pugno, and Rainer Adelung. Hierarchical self-entangled carbon nanotube tube networks. *Nat. Commun.*, 8(1):1215, 2017.

[20] Miguel A Correa-Duarte, Nicholas Wagner, José Rojas-Chapana, Christian Morsczeck, Michael Thie, and Michael Giersig. Fabrication and biocompatibility of carbon nanotube-based 3d networks as scaffolds for cell seeding and growth. *Nano Lett.*, 4(11):2233–2236, 2004.

[21] Sharon L Edwards, Jeffrey S Church, Jerome A Werkmeister, and John A M Ramshaw. Tubular micro-scale multiwalled carbon nanotube-based scaffolds for tissue engineering. *Biomaterials*, 30(9):1725–1731, 2009.

[22] Gaurav Lalwani, Anu Gopalan, Michael D'Agati, Jeyantt Srinivas Sankaran, Stefan Judex, Yi-Xian Qin, and Balaji Sitharaman. Porous three-dimensional carbon nanotube scaffolds for tissue engineering. *J. Biomed. Mater. Res.*, 103(10):3212–3225, 2015.

[23] Ander Abarrategi, Maria C Gutierrez, Carolina Moreno-Vicente, María J Hortigüela, Viviana Ramos, Jose L Lopez-Lacomba, Maria L Ferrer, and Francisco del Monte. Multiwall carbon nanotube scaffolds for tissue engineering purposes. *Biomaterials*, 29(1):94–102, 2008.

[24] Erin Leigh Hopley, Shima Salmasi, Deepak M Kalaskar, and Alexander M Seifalian. Carbon nanotubes leading the way forward in new generation 3d tissue engineering. *Biotechnol. Adv.*, 32(5):1000–1014, 2014.

[25] Rajat Duggal, Fazle Hussain, and Matteo Pasquali. Self-assembly of single-walled carbon nanotubes into a sheet by drop drying. *Adv. Mater.*, 18(1):29–34, 2006.

[26] Yung Joon Jung, Swastik Kar, Saikat Talapatra, Caterina Soldano, Gunaranjan Viswanathan, Xuesong Li, Zhaoling Yao, Fung Suong Ou, Aditya Avadhanula, Robert Vajtai, et al. Aligned carbon nanotube- polymer hybrid architectures for diverse flexible electronic applications. *Nano Lett.*, 6(3):413–418, 2006.

[27] Alan B Dalton, Steve Collins, Edgar Munoz, Joselito M Razal, Von Howard Ebron, John P Ferraris, Jonathan N Coleman, Bog G Kim, and Ray H Baughman. Super-tough carbon-nanotube fibres. *Nature*, 423(6941):703, 2003.

[28] Ning Li, Qi Zhang, Song Gao, Qin Song, Rong Huang, Long Wang, Liwei Liu, Jianwu Dai, Mingliang Tang, and Guosheng Cheng. Three-dimensional graphene foam as a biocompatible and conductive scaffold for neural stem cells. *Sci. Rep.*, 3:1604, 2013.

[29] Scott J Hollister. Porous scaffold design for tissue engineering. *Nat. Mater.*, 4(7):518, 2005.

[30] Mahmood Aliofkhazraei, William I Milne, Cengiz S Ozkan, Stanislaw Mitura, Juana L Gervasoni, and Nasar Ali. *Graphene science handbook: electrical and optical properties*. CRC press, 2016.

[31] Jian-Hao Chen, Chaun Jang, Shudong Xiao, Masa Ishigami, and Michael S Fuhrer. Intrinsic and extrinsic performance limits of graphene devices on sio_2. *Nat. Nanotechnol.*, 3(4):206, 2008.

[32] Su Ryon Shin, Yi Chen Li, Hae Lin Jang, Parastoo Khoshakhlagh, Mohsen Akbari, Amir Nasajpour, Yu Shrike Zhang, Ali Tamayol, and Ali Khademhosseini. Graphene-based materials for tissue engineering. *Adv. Drug Deliv. Rev.*, 105:255–274, 2016.

[33] Sheng Tao Yang, Jianbin Luo, Qinghan Zhou, and Haifang Wang. Pharmacokinetics, metabolism and toxicity of carbon nanotubes for bio-medical purposes. *Theranostics*, 2(3):271–282, 2012.

[34] Seon Namgung, Ku Youn Baik, Juhun Park, and Seunghun Hong. Controlling the growth and differentiation of human mesenchymal stem cells by the arrangement of individual carbon nanotubes. *ACS Nano*, 5(9):7383–7390, 2011.

[35] Guang Jia, Haifang Wang, Lei Yan, Xiang Wang, Rongjuan Pei, Tao Yan, Yuliang Zhao, and Xinbiao Guo. Cytotoxicity of carbon nanomaterials: single-wall nanotube, multi-wall nanotube, and fullerene. *Environ. Sci. Technol.*, 39(5):1378–1383, 2005.

[36] Mohamed N Rahaman, Delbert E Day, B Sonny Bal, Qiang Fu, Steven B Jung, Lynda F Bonewald, and Antoni P Tomsia. Bioactive glass in tissue engineering. *Acta Biomater.*, 7(6):2355–2373, 2011.

[37] Tadashi Kokubo. Bioactive glass ceramics: properties and applications. *Biomaterials*, 12(2):155–163, 1991.

[38] Larry L Hench. Bioactive ceramics. *Ann. N. Y. Acad. Sci.*, 523(1):54–71, 1988.

[39] Paul Ducheyne and Qingqing Qiu. Bioactive ceramics: the effect of surface reactivity on bone formation and bone cell function. *Biomaterials*, 20(23-24):2287–2303, 1999.

[40] Ilaria Corni, Mary P Ryan, and Aldo R Boccaccini. Electrophoretic deposition: From traditional ceramics to nanotechnology. *J. Eur. Ceram. Soc.*, 28(7):1353–1367, 2008.

[41] Aldo R Boccaccini, Sigrid Keim, Renzhi Ma, Yang Li, and Igor Zhitomirsky. Electrophoretic deposition of biomaterials. *J. Royal Soc. Interface*, 7(suppl_5):S581–S613, 2010.

[42] Indrajit Roy, Tymish Y Ohulchanskyy, Haridas E Pudavar, Earl J Bergey, Allan R Oseroff, Janet Morgan, Thomas J Dougherty, and Paras N Prasad. Ceramic-based nanoparticles entrapping water-insoluble photosensitizing anticancer drugs: A novel drug- carrier system for photodynamic therapy. *J. Am. Chem. Soc.*, 125(26):7860–7865, 2003.

[43] Syuji Fujii, Masahiro Okada, Hidekatsu Sawa, Tsutomu Furuzono, and Yoshinobu Nakamura. Hydroxyapatite nanoparticles as particulate emulsifier: fabrication of hydroxyapatite-coated biodegradable microspheres. *Langmuir*, 25(17):9759–9766, 2009.

[44] Jiaxing Huang, Franklin Kim, Andrea R Tao, Stephen Connor, and Peidong Yang. Spontaneous formation of nanoparticle stripe patterns through dewetting. *Nat. Mater.*, 4(12):896, 2005.

[45] Salina Parvin, Jun Matsui, Eriko Sato, and Tokuji Miyashita. Side-chain effect on langmuir and langmuir–blodgett film properties of poly (n-alkylmethacrylamide)-coated magnetic nanoparticle. *J. Colloid Interface Sci.*, 313(1):128–134, 2007.

[46] Stephan T Dubas, Panittamat Kumlangdudsana, and Pranut Potiyaraj. Layer-by-layer deposition of antimicrobial silver nanoparticles on textile fibers. *Colloids Surf.*, 289(1-3):105–109, 2006.

[47] Daniela S Couto, Natália M Alves, and João F Mano. Nanostructured multilayer coatings combining chitosan with bioactive glass nanoparticles. *J. Nanosci. Nanotechnol.*, 9(3):1741–1748, 2009.

[48] C Jeffrey Brinker, Yunfeng Lu, Alan Sellinger, and Hongyou Fan. Evaporation-induced self-assembly: nanostructures made easy. *Adv. Mater.*, 11(7):579–585, 1999.

[49] Junhu Zhang, Yunfeng Li, Xuemin Zhang, and Bai Yang. Colloidal self-assembly meets nanofabrication: From two-dimensional colloidal crystals to nanostructure arrays. *Adv. Mater.*, 22(38):4249–4269, 2010.

[50] Mani Diba, Derrick WH Fam, Aldo R Boccaccini, and Milo SP Shaffer. Electrophoretic deposition of graphene-related materials: A review of the fundamentals. *Prog. Mater. Sci.*, 82:83–117, 2016.

[51] Aldo R Boccaccini, U. Schindler, and Horst G Krüger. Ceramic coatings on carbon and metallic fibres by electrophoretic deposition. *Mater. Lett.*, 51(3):225–230, 2001.

[52] David Zhitomirsky, Judith Roether, Aldo R Boccaccini, and Igor Zhitomirsky. Electrophoretic deposition of bioactive glass/polymer composite coatings with and without ha nanoparticle inclusions for biomedical applications. *J. Mater. Process. Technol.*, 209(4):1853–1860, 2009.

[53] Sarina Kay, Anil Thapa, Karen M Haberstroh, and Thomas J Webster. Nanostructured polymer/nanophase ceramic composites enhance osteoblast and chondrocyte adhesion. *Tissue Eng.*, 8(5):753–761, 2002.

[54] Ming Li, Qian Liu, Zhaojun Jia, Xuchen Xu, Yan Cheng, Yufeng Zheng, Tingfei Xi, and Shicheng Wei. Graphene oxide/hydroxyapatite composite coatings fabricated by electrophoretic nanotechnology for biological applications. *Carbon*, 67:185–197, 2014.

[55] Sandeep Tamrakar, Qi An, Erik T Thostenson, Andrew N Rider, Bazle Z Haque, and John W Gillespie Jr. Tailoring interfacial properties by controlling carbon nanotube coating thickness on glass fibers using electrophoretic deposition. *ACS Appl. Mater. Interfaces*, 8(2):1501–1510, 2016.

[56] BJC Thomas, Aldo R Boccaccini, and Milo SP Shaffer. Multi-walled carbon nanotube coatings using electrophoretic deposition (epd). *J. Am. Ceram. Soc.*, 88(4):980–982, 2005.

[57] A Chavez-Valdez, Milo SP Shaffer, and Aldo R Boccaccini. Applications of graphene electrophoretic deposition. a review. *J. Phys. Chem. B*, 117(6):1502–1515, 2012.

[58] Julián López-Viota, Subhra Mandal, Angel V Delgado, José Luis Toca-Herrera, Marco Möller, Francesco Zanuttin, Maurizio Balestrino, and Silke Krol. Electrophoretic characterization of gold nanoparticles functionalized with human

serum albumin (hsa) and creatine. *J. Colloid Interface Sci.*, 332(1):215–223, 2009.

[59] Paul Mulvaney, Michael Giersig, Thearith Ung, and Luis M Liz-Marzán. Direct observation of chemical reactions in silica-coated gold and silver nanoparticles. *Adv. Mater.*, 9(7):570–575, 1997.

[60] Maria J Santillán, Nancy Quaranta, and Aldo R Boccaccini. Titania and titania–silver nanocomposite coatings grown by electrophoretic deposition from aqueous suspensions. *Surf. Coat. Tech.*, 205(7):2562–2571, 2010.

[61] Gil-Sung Kim, Hyung-Kee Seo, VP Godble, Young-Soon Kim, O-Bong Yang, and Hyung-Shik Shin. Electrophoretic deposition of titanate nanotubes from commercial titania nanoparticles: application to dye-sensitized solar cells. *Electrochem. commun.*, 8(6):961–966, 2006.

[62] Lin Gao and Jiarui Lin. Electrophoretic coating of hydroxyapatite on pyrolytic carbon using glycol as dispersion medium. *J. Wuhan. Univ. Technol. Mat. Sci. Ed.*, 23(3):293–297, 2008.

[63] Vinayaraj Ozhukil Kollath, Qiang Chen, Steven Mullens, Jan Luyten, Karl Traina, Aldo R Boccaccini, and Rudi Cloots. Electrophoretic deposition of hydroxyapatite and hydroxyapatite–alginate on rapid prototyped 3d ti6al4v scaffolds. *J. Mater. Sci.*, 51(5):2338–2346, 2016.

[64] Aldo R Boccaccini, Florencia Chicatun, Johann Cho, Oana Bretcanu, Judith A Roether, Sasa Novak, and QZ Chen. Carbon nanotube coatings on bioglass-based tissue engineering scaffolds. *Adv. Funct. Mater.*, 17(15):2815–2822, 2007.

[65] Anthony Atala. Engineering organs. *Curr. Opin. Biotechnol.*, 20(5):575–592, 2009.

[66] Giuseppe Orlando, Kathryn J Wood, Robert J Stratta, James J Yoo, Anthony Atala, and Shay Soker. Regenerative medicine and organ transplantation: past, present, and future. *Transplantation*, 91(12):1310–1317, 2011.

[67] Toshiharu Shin'oka, Yasuharu Imai, and Yoshito Ikada. Transplantation of a tissue-engineered pulmonary artery. *N. Engl. J. Med.*, 344(7):532–533, 2001.

[68] Todd N McAllister, Marcin Maruszewski, Sergio A Garrido, Wojciech Wystrychowski, Nathalie Dusserre, Alicia Marini, Krzysztof Zagalski, Alejandro Fiorillo, Hernan Avila, Ximena Manglano, et al. Effectiveness of haemodialysis access with an autologous tissue-engineered vascular graft: a multicentre cohort study. *Lancet*, 373(9673):1440–1446, 2009.

[69] Harald C Ott, Thomas S Matthiesen, Saik-Kia Goh, Lauren D Black, Stefan M Kren, Theoden I Netoff, and Doris A Taylor. Perfusion-decellularized matrix: using nature's platform to engineer a bioartificial heart. *Nat. Med.*, 14(2):213, 2008.

[70] Edward A Ross, Matthew J Williams, Takashi Hamazaki, Naohiro Terada, William L Clapp, Christopher Adin, Gary W Ellison, Marda Jorgensen, and Christopher D Batich. Embryonic stem cells proliferate and differentiate when seeded into kidney scaffolds. *J. Am. Soc. Nephrol.*, 20(11):2338–2347, 2009.

[71] Pedro M Baptista, Giuseppe Orlando, Sayed-Hadi Mirmalek-Sani, Mohummad Siddiqui, Anthony Atala, and Shay Soker. Whole organ decellularization-a tool for bioscaffold fabrication and organ bioengineering. In *Engineering in medicine and biology society, 2009. EMBC 2009. Ann. Int. Conf. IEEE*, pages 6526–6529, 2009.

[72] Ravi Katari, Andrea Peloso, and Giuseppe Orlando. Tissue engineering and regenerative medicine: semantic considerations for an evolving paradigm. *Front. Bioeng. Biotechnol.*, 2:57, 2015.

[73] Abdallah S Daar and Heather L Greenwood. A proposed definition of regenerative medicine. *J. Tissue Eng. Regen. Med.*, 1(3):179–184, 2007.

[74] Robert Langer and Joseph P Vacanti. Tissue engineering. *Science*, 260(5110):920–926, 1993.

[75] Brendan Maher. Tissue engineering: How to build a heart. *Nature*, 499(7456):20, 2013.

[76] Robert Lanza, Robert Langer, and Joseph P Vacanti. *Principles of tissue engineering*. Academic press, 2011.

[77] Jeffrey A Hubbell. Materials as morphogenetic guides in tissue engineering. *Curr. Opin. Biotechnol.*, 14(5):551–558, 2003.

[78] Brahatheeswaran Dhandayuthapani, Yasuhiko Yoshida, Toru Maekawa, and D Sakthi Kumar. Polymeric scaffolds in tissue engineering application: a review. *Int. J. Polym. Sci.*, 2011.

[79] Valentina Miguez-Pacheco, Larry L. Hench, and Aldo R. Boccaccini. Bioactive glasses beyond bone and teeth: Emerging applications in contact with soft tissues. *Acta Biomater.*, 13:1–15, 2015.

[80] Larry L Hench. Bioceramics: from concept to clinic. *J. Am. Ceram. Soc.*, 74(7):1487–1510, 1991.

[81] Larry L Hench. Bioactive materials: the potential for tissue regeneration. *J. Biomed. Mater. Res. A*, 41(4):511–518, 1998.

[82] Constanze Lamprecht, J Torin Huzil, Marina V Ivanova, and Marianna Foldvari. Non-Covalent Functionalization of Carbon Nanotubes with Surfactants for Pharmaceutical Applications - A Critical Mini-Review. *Drug Deliv. Lett.*, 1(1):45–57, 2011.

[83] Matthias Mecklenburg, Arnim Schuchardt, Yogendra Kumar Mishra, Sören Kaps, Rainer Adelung, Andriy Lotnyk, Lorenz Kienle, and Karl Schulte. Aerographite: ultra lightweight, flexible nanowall, carbon microtube material with outstanding mechanical performance. *Adv. Mater.*, 24(26):3486–3490, 2012.

[84] Bruce Alberts, Dennis Bray, Julian Lewis, Martin Raff, Keith Roberts, and James D Watson. *Molecular Biology of the Cell*. Garland, 4th edition, 2002.

[85] Miguel Vicente-Manzanares, Colin Kiwon Choi, and Alan Rick Horwitz. Integrins in cell migration - the actin connection. *J. Cell Sci.*, 122(2):199–206, 2009.

[86] Christine Selhuber-Unkel, Mónica López-García, Horst Kessler, and Joachim P. Spatz. Cooperativity in adhesion cluster formation during initial cell adhesion. *Biophys. J.*, 95(11):5424–5431, 2008.

[87] Youhwan Kim, Hyojin Ko, Ik Keun Kwon, and Kwanwoo Shin. Extracellular matrix revisited: roles in tissue engineering. *Int. Neurourol. J.*, 20(Suppl 1):S23, 2016.

[88] Christian Frantz, Kathleen M Stewart, and Valerie M Weaver. The extracellular matrix at a glance. *J. Cell Sci.*, 123(24):4195–4200, 2010.

[89] R Dyche Mullins. Cytoskeletal mechanisms for breaking cellular symmetry. *Csh. Perspect. Biol.*, 2(1):a003392, 2010.

[90] Keith Burridge, Christopher E Turner, and Lewis H Romer. Tyrosine phosphorylation of paxillin and pp125fak accompanies cell adhesion to extracellular matrix: a role in cytoskeletal assembly. *J. Cell Biol.*, 119(4):893–903, 1992.

[91] Keith Burridge. Substrate adhesions in normal and transformed fibroblasts: organization and regulation of cytoskeletal, membrane and extracellular matrix components at focal contacts. *Cancer Rev.*, 4:18–78, 1986.

[92] William P Daley, Sarah B Peters, and Melinda Larsen. Extracellular matrix dynamics in development and regenerative medicine. *J. Cell Sci.*, 121(3):255–264, 2008.

[93] Christopher E Turner. Paxillin and focal adhesion signalling. *Nat. Cell Biol.*, 2(12):E231, 2000.

[94] Raymond W Sweet and Martin Rosenberg. Microinjection of the ras Oncogene Protein into Nonestablished Rat Embryo Fibroblasts1. *Cancer Res.*, 46(8):6427–6432, 1986.

[95] Jørgen Fogh, Jens M Fogh, and Thomas Orfeo. One hundred and twenty-seven cultured human tumor cell lines producing tumors in nude mice. *J. Natl. Cancer Inst.*, 59(1):221–226, 1977.

[96] Sevgi B Rodan, Yasuo Imai, Mark A Thiede, Gregg Wesolowski, David Thompson, Zvi Bar-Shavit, Susan Shull, Kenneth Mann, and Gideon A Rodan. Characterization of a human osteosarcoma cell line (saos-2) with osteoblastic properties. *Cancer Res.*, 47(18):4961–4966, 1987.

[97] Hiroko Sudo, Hiro-Ari Kodama, Yuji Amagai, Shigehisa Yamamoto, and Shiro Kasai. In vitro differentiation and calcification in a new clonal osteogenic cell line derived from newborn mouse calvaria. *J. Cell Biol.*, 96(1):191–198, 1983.

[98] Sook Hee Ku, Minah Lee, and Chan Beum Park. Carbon-based nanomaterials for tissue engineering. *Adv. Healthc. Mater.*, 2(2):244–260, 2013.

[99] Mercè Pacios Pujadó. *Carbon nanotubes as platforms for biosensors with electrochemical and electronic transduction*. Springer Science & Business Media, 2012.

[100] Riichiro Saito, Gene Dresselhaus, and Mildred S Dresselhaus. *Physical properties of carbon nanotubes*. World Scientific, 1998.

[101] Yi Lin, Shelby Taylor, Huaping Li, KA Shiral Fernando, Liangwei Qu, Wei Wang, Lingrong Gu, Bing Zhou, and Ya-Ping Sun. Advances toward bioapplications of carbon nanotubes. *J. Mater. Chem.*, 14(4):527–541, 2004.

[102] Kostya S Novoselov, Andre K Geim, Sergei V Morozov, D Jiang, Y_ Zhang, Sergey V Dubonos, Irina V Grigorieva, and Alexandr A Firsov. Electric field effect in atomically thin carbon films. *Science*, 306(5696):666–669, 2004.

[103] Hugh O Pierson. *Handbook of chemical vapor deposition: principles, technology and applications*. William Andrew, 1999.

[104] YI Zhang, Luyao Zhang, and Chongwu Zhou. Review of chemical vapor deposition of graphene and related applications. *Acc. Chem. Res.*, 46(10):2329–2339, 2013.

[105] Mukul Kumar and Yoshinori Ando. Chemical vapor deposition of carbon nanotubes: a review on growth mechanism and mass production. *J. Nanosci. Nanotechnol.*, 10(6):3739–3758, 2010.

[106] Matthew A Oehlschlaeger, David F Davidson, and Ronald K Hanson. Thermal decomposition of toluene: Overall rate and branching ratio. *Proc. Combust. Inst.*, 31(1):211–219, 2007.

[107] Sandhya Vardharajula, Sk Z Ali, Pooja M Tiwari, Erdal Eroğlu, Komal Vig, Vida A Dennis, and Shree R Singh. Functionalized carbon nanotubes: biomedical applications. *Int. J. Nanomed.*, 7:5361, 2012.

[108] Liang Yan, Feng Zhao, Shoujian Li, Zhongbo Hu, and Yuliang Zhao. Low-toxic and safe nanomaterials by surface-chemical design, carbon nanotubes, fullerenes, metallofullerenes, and graphenes. *Nanoscale*, 3(2):362–382, 2011.

[109] Sean C Smith and Debora F Rodrigues. Carbon-based nanomaterials for removal of chemical and biological contaminants from water: a review of mechanisms and applications. *Carbon*, 91:122–143, 2015.

[110] Elena Heister, Constanze Lamprecht, Vera Neves, Carmen Tîlmaciu, Lucien Datas, Emmanuel Flahaut, Brigitte Soula, Peter Hinterdorfer, Helen M Coley, S Ravi P Silva, et al. Higher dispersion efficacy of functionalized carbon nanotubes in chemical and biological environments. *ACS Nano*, 4(5):2615–2626, 2010.

[111] Kannan Balasubramanian and Marko Burghard. Chemically functionalized carbon nanotubes. *Small*, 1(2):180–192, 2005.

[112] Ying Wang, Zhaohui Li, Jun Wang, Jinghong Li, and Yuehe Lin. Graphene and graphene oxide: biofunctionalization and applications in biotechnology. *Trends Biotechnol.*, 29(5):205–212, 2011.

[113] David A Britz and Andrei N Khlobystov. Noncovalent interactions of molecules with single walled carbon nanotubes. *Chem. Soc. Rev.*, 35(7):637–659, 2006.

[114] Giuseppe Prencipe, Scott M Tabakman, Kevin Welsher, Zhuang Liu, Andrew P Goodwin, Li Zhang, Joy Henry, and Hongjie Dai. Peg branched polymer for functionalization of nanomaterials with ultralong blood circulation. *J. Am. Chem. Soc.*, 131(13):4783–4787, 2009.

[115] Vladimir A Sinani, Muhammed K Gheith, Alexander A Yaroslavov, Anna A Rakhnyanskaya, Kai Sun, Arif A Mamedov, James P Wicksted, and Nicholas A Kotov. Aqueous dispersions of single-wall and multiwall carbon nanotubes with designed amphiphilic polycations. *J. Am. Chem. Soc.*, 127(10):3463–3472, 2005.

[116] Samuel Zalipsky. Chemistry of polyethylene glycol conjugates with biologically active molecules. *Adv. Drug Deliv. Rev.*, 16(2-3):157–182, 1995.

[117] Ana Margarida Pereira, Raul Machado, André da Costa, Artur Ribeiro, Tony Collins, Andreia C Gomes, Isabel B Leonor, David L Kaplan, Rui L Reis, and Margarida Casal. Silk-based biomaterials functionalized with fibronectin type ii promotes cell adhesion. *Acta Biomater.*, 47:50–59, 2017.

[118] Antonio Cacchioli, Francesca Ravanetti, Andrea Bagno, Monica Dettin, and Carlo Gabbi. Human vitronectin–derived peptide covalently grafted onto titanium surface improves osteogenic activity: A pilot in vivo study on rabbits. *Tissue Eng. A*, 15(10):2917–2926, 2009.

[119] Erkki Ruoslahti. Fibronectin in cell adhesion and invasion. *Cancer Metastasis Rev.*, 3(1):43–51, 1984.

[120] Leyla V Valenick, Henry C Hsia, and Jean E Schwarzbauer. Fibronectin fragmentation promotes $\alpha 4\beta 1$ integrin-mediated contraction of a fibrin–fibronectin provisional matrix. *Exp. Cell Res.*, 309(1):48–55, 2005.

[121] Aiwu Zhou, James A Huntington, Navraj S Pannu, Robin W Carrell, and Randy J Read. How vitronectin binds pai-1 to modulate fibrinolysis and cell migration. *Nat. Struct. Mol. Biol.*, 10(7):541, 2003.

[122] Catarina M Alves, Rui L Reis, and John A Hunt. The competitive adsorption of human proteins onto natural-based biomaterials. *J. Royal Soc. Interface*, 7(50):1367–1377, 2010.

[123] Buddy D Ratner, Allan S Hoffman, Frederick J Schoen, and Jack E Lemons. Biomaterials science: an introduction to materials in medicine. *MRS Bull.*, 31:59, 2006.

[124] Paul Roach, David Farrar, and Carole C Perry. Interpretation of protein adsorption: surface-induced conformational changes. *J. Am. Chem. Soc.*, 127(22):8168–8173, 2005.

[125] Jingjing Guo, Xiaojun Yao, Lulu Ning, Qianqian Wang, and Huanxiang Liu. The adsorption mechanism and induced conformational changes of three typical proteins with different secondary structural features on graphene. *RSC Adv.*, 4(20):9953–9962, 2014.

[126] Cuicui Ge, Jiangfeng Du, Lina Zhao, Liming Wang, Ying Liu, Denghua Li, Yanlian Yang, Ruhong Zhou, Yuliang Zhao, Zhifang Chai, et al. Binding of blood proteins to carbon nanotubes reduces cytotoxicity. *Proc. Natl. Acad. Sci.*, 108(41):16968–16973, 2011.

[127] Xiang Wang, Tian Xia, Susana Addo Ntim, Zhaoxia Ji, Saji George, Huan Meng, Haiyuan Zhang, Vincent Castranova, Somenath Mitra, and André E Nel. Quantitative techniques for assessing and controlling the dispersion and biological effects of multiwalled carbon nanotubes in mammalian tissue culture cells. *ACS Nano*, 4(12):7241–7252, 2010.

[128] Rinaldo Florencio-Silva, Gisela Rodrigues da Silva Sasso, Estela Sasso-Cerri, Manuel Jesus Simões, and Paulo Sérgio Cerri. Biology of bone tissue: structure, function, and factors that influence bone cells. *BioMed Res. Int.*, 2015(1):421746, 2015.

[129] Steve Weiner, Wolfie Traub, and H Daniel Wagner. Lamellar bone: structure–function relations. *J. Struct. Biol.*, 126(3):241–255, 1999.

[130] Jae-Young Rho, Liisa Kuhn-Spearing, and Peter Zioupos. Mechanical properties and the hierarchical structure of bone. *Med. Eng. Phys.*, 20(2):92–102, 1998.

[131] Mehdi Tavassoli and Joseph Mendel Yoffey. *Bone marrow, structure and function.* AR Liss New York, 1983.

[132] António J Salgado, Olga P Coutinho, and Rui L Reis. Bone tissue engineering: state of the art and future trends. *Macromol. Biosci.*, 4(8):743–765, 2004.

[133] William J Whitehouse. Scanning electron micrographs of cancellous bone from the human sternum. *J. Pathol.*, 116(4):213–224, 1975.

[134] Eiichi Fukada and Iwao Yasuda. On the piezoelectric effect of bone. *J. Phys. Soc. Jpn.*, 12(10):1158–1162, 1957.

[135] Brad M Isaacson and Roy D Bloebaum. Bone bioelectricity: What have we learned in the past 160 years? *J. Biomed. Mater. Res.*, 95(4):1270–1279, 2010.

[136] James T Ryaby. Clinical effects of electromagnetic and electric fields on fracture healing. *Clin. Orthop. Relat. Res.*, 355:S205–S215, 1998.

[137] Shiyun Meng, Mahmoud Rouabhia, and Ze Zhang. Electrical stimulation modulates osteoblast proliferation and bone protein production through heparin-bioactivated conductive scaffolds. *Bioelectromagnetics*, 34(3):189–199, 2013.

[138] Carlos F Martino, Dmitry Belchenko, Virginia Ferguson, Sheila Nielsen-Preiss, and H Jerry Qi. The effects of pulsed electromagnetic fields on the cellular activity of saos-2 cells. *Bioelectromagnetics*, 29(2):125–132, 2008.

[139] Shiyun Meng, Ze Zhang, and Mahmoud Rouabhia. Accelerated osteoblast mineralization on a conductive substrate by multiple electrical stimulation. *J. Bone Miner. Metab.*, 29(5):535–544, 2011.

[140] Aref Shahini, Mostafa Yazdimamaghani, Kenneth J Walker, Margaret A Eastman, Hamed Hatami-Marbini, Brenda J Smith, John L Ricci, Sundar V Madihally, Daryoosh Vashaee, and Lobat Tayebi. 3d conductive nanocomposite scaffold for bone tissue engineering. *Int. J. Nanomed.*, 9:167, 2014.

[141] Alexander Jakovlevich Friedenstein, Klara Vasiljevna Petrakova, Alexandra Ivanovna Kurolesova, and Galina Petrovna Frolova. Heterotopic transplants of bone marrow. *Transplantation*, 6(2):230–247, 1968.

[142] Karen JL Burg, Scott Porter, and James F Kellam. Biomaterial developments for bone tissue engineering. *Biomaterials*, 21(23):2347–2359, 2000.

[143] Hiroshi Yoshimoto, Y.M. Shin, Hidetomi Terai, and Joseph P Vacanti. A biodegradable nanofiber scaffold by electrospinning and its potential for bone tissue engineering. *Biomaterials*, 24(12):2077–2082, 2003.

[144] Marc A Fernandez-Yague, Sunny Akogwu Abbah, Laoise McNamara, Dimitrios I Zeugolis, Abhay Pandit, and Manus J Biggs. Biomimetic approaches in bone tissue engineering: Integrating biological and physicomechanical strategies. *Adv. Drug Deliv. Rev.*, 84:1–29, 2015.

[145] Oana Bretcanu, Xanthippi Chatzistavrou, Konstantinos Paraskevopoulos, Reinhard Conradt, Ian Thompson, and Aldo R. Boccaccini. Sintering and crystallisation of 45S5 Bioglass® powder. *J. Eur. Ceram. Soc.*, 29(16):3299–3306, 2009.

[146] Antalya Ho-Shui-Ling, Johanna Bolander, Laurence E Rustom, Amy Wagoner Johnson, Frank P Luyten, and Catherine Picart. Bone regeneration strategies: Engineered scaffolds, bioactive molecules and stem cells current stage and future perspectives. *Biomaterials*, 2018.

[147] Alejandro A Gorustovich, Judith A Roether, and Aldo R Boccaccini. Effect of bioactive glasses on angiogenesis: a review of in vitro and in vivo evidences. *Tissue Eng. Part B Rev.*, 16(2):199–207, 2009.

[148] Kyung Mi Woo, Ji Hae Jun, Victor J Chen, Jihye Seo, Jeong Hwa Baek, Hyun Mo Ryoo, Gwan Shik Kim, Martha J Somerman, and Peter X Ma. Nano-fibrous scaffolding promotes osteoblast differentiation and biomineralization. *Biomaterials*, 28(2):335–343, 2007.

[149] Reading Shu, Roger McMullen, Melissa J Baumann, and Laura R McCabe. Hydroxyapatite accelerates differentiation and suppresses growth of MC3T3-E1 osteoblasts. *J. Biomed. Mater. Res.*, 67(4):1196–1204, 2003.

[150] Alexander Hoppe, Nusret S Güldal, and Aldo R Boccaccini. A review of the biological response to ionic dissolution products from bioactive glasses and glass-ceramics. *Biomaterials*, 32(11):2757–2774, 2011.

[151] Hongli Sun, Chengtie Wu, Kerong Dai, Jiang Chang, and Tingting Tang. Proliferation and osteoblastic differentiation of human bone marrow-derived stromal cells on akermanite-bioactive ceramics. *Biomaterials*, 27(33):5651–5657, 2006.

[152] Guobao Wei and Peter X Ma. Structure and properties of nano-hydroxyapatite/polymer composite scaffolds for bone tissue engineering. *Biomaterials*, 25(19):4749–4757, 2004.

[153] Huanan Wang, Yubao Li, Yi Zuo, Jihua Li, Sansi Ma, and Lin Cheng. Biocompatibility and osteogenesis of biomimetic nano-hydroxyapatite/polyamide composite scaffolds for bone tissue engineering. *Biomaterials*, 28(22):3338–3348, 2007.

[154] Kai Zheng, Nicola Taccardi, Ana Maria Beltrán, Baiyan Sui, Tian Zhou, VR Reddy Marthala, Martin Hartmann, and Aldo R Boccaccini. Timing of calcium nitrate addition affects morphology, dispersity and composition of bioactive glass nanoparticles. *RSC Adv.*, 6(97):95101–95111, 2016.

[155] Aldo R Boccaccini, Sigrid Keim, R Ma, Y Li, and Igor Zhitomirsky. Electrophoretic deposition of biomaterials. *J. Royal Soc. Interface*, 7(SUPPL. 5):S581–S613, 2010.

[156] Aldo R Boccaccini and Igor Zhitomirsky. Application of electrophoretic and electrolytic deposition techniques in ceramics processing. *Curr. Opin. Solid St. M.*, 6(3):251–260, 2002.

[157] Igor Zhitomirsky and L Gal-Or. Electrophoretic deposition of hydroxyapatite. *J. Mater. Sci.: Mater. Med.*, 8(4):213–219, 1997.

[158] Wei Yuan, Xin He, Xiaoshu Zhou, and Yue Zhu. Hydroxyapatite nanoparticle-coated 3d-printed porous ti6al4v and cocrmo alloy scaffolds and their biocompatibility to human osteoblasts. *J. Nanosci. Nanotechnol.*, 18(6):4360–4365, 2018.

[159] Yong Li, Wei Yang, Xiaokang Li, Xing Zhang, Cairu Wang, Xiangfei Meng, Yifeng Pei, Xiangli Fan, Pingheng Lan, Chunhui Wang, et al. Improving osteointegration and osteogenesis of three-dimensional porous ti6al4v scaffolds by polydopamine-assisted biomimetic hydroxyapatite coating. *ACS Appl. Mater. Interfaces*, 7(10):5715–5724, 2015.

[160] Vinayaraj Ozhukil Kollath, Qiang Chen, Steven Mullens, Jan Luyten, Karl Traina, Aldo R. Boccaccini, and Rudi Cloots. Electrophoretic deposition of hydroxyapatite and hydroxyapatitealginate on rapid prototyped 3D Ti6Al4V scaffolds. *J. Mater. Sci.*, 51(5):2338–2346, 2016.

[161] Laxmidhar Besra and Meilin Liu. A review on fundamentals and applications of electrophoretic deposition (EPD). *Prog. Mater. Sci.*, 52(1):1–61, 2007.

[162] Tatsumi Ishihara, Kuninobu Shimose, Takanari Kudo, Hiroyasu Nishiguchi, Taner Akbay, and Yusaku Takita. Preparation of yttria-stabilized zirconia thin films on strontium-doped lamno3 cathode substrates via electrophoretic deposition for solid oxide fuel cells. *J. Am. Ceram. Soc.*, 83(8):1921–1927, 2000.

[163] Józef Mazurkiewicz and Piotr Tomasik. Viscosity and dielectric properties of liquid binary mixtures. *J. Phys. Org. Chem.*, 3(8):493–502, 1990.

[164] Jonathan Black. *Biological performance of materials: fundamentals of biocompatibility*. CRC Press, 2005.

[165] Jean-Pierre Boutrand. *Biocompatibility and performance of medical devices*. Woodhead Pub, 2012.

[166] Yingying Zhang, Xin Chen, Cyril Gueydan, and Jiahuai Han. Plasma membrane changes during programmed cell deaths. *Cell Res.*, 28(1):9, 2018.

[167] Paresh Chandra Ray, Hongtao Yu, and Peter P Fu. Toxicity and environmental risks of nanomaterials: challenges and future needs. *J. Environ. Sci. Health C*, 27(1):1–35, 2009.

[168] Brian D Holt, Philip A Short, Andrew D Rape, Yu-li Wang, Mohammad F Islam, and Kris Noel Dahl. Carbon nanotubes reorganize actin structures in cells and ex vivo. *ACS Nano*, 4(8):4872–4878, 2010.

[169] Gunter Oberdörster, Juraj Ferin, and Bruce E Lehnert. Correlation between particle size, in vivo particle persistence, and lung injury. *Environ. Health Perspect.*, 102(suppl 5):173–179, 1994.

[170] Heike Papavlassopoulos, Yogendra K Mishra, Sören Kaps, Ingo Paulowicz, Ramzy Abdelaziz, Mady Elbahri, Edmund Maser, Rainer Adelung, and Claudia Röhl. Toxicity of functional nano-micro zinc oxide tetrapods: impact of cell culture conditions, cellular age and material properties. *PLOS ONE*, 9(1):e84983, 2014.

[171] Terry L Riss, Richard A Moravec, Andrew L Niles, Sarah Duellman, Hélène A Benink, Tracy J Worzella, and Lisa Minor. *Cell Viability Assays*, volume 1601. Eli Lilly & company and the national center for advancing translational sciences, 2017.

[172] Tim Mosmann. Rapid colorimetric assay for cellular growth and survival: Application to proliferation and cytotoxicity assays. *J. Immunol. Methods*, 65(1-2):55–63, 1983.

[173] Jörg M Wörle-Knirsch, Karin Pulskamp, and Harald F Krug. Oops they did it again! carbon nanotubes hoax scientists in viability assays. *Nano Lett.*, 6(6):1261–1268, 2006.

[174] Puriya Ngamwongsatit, Padmapriya P Banada, Watanalai Panbangred, and Arun K Bhunia. Wst-1-based cell cytotoxicity assay as a substitute for mtt-based assay for rapid detection of toxigenic bacillus species using cho cell line. *J. Microbiol. Methods*, 73(3):211–215, 2008.